frontiers | Research Topics

Innovations to improve screw fixation in traumatology and orthopedic surgery

Edited by
Jonas Widmer, Carl-Eric Aubin, Harry van Lenthe and Keitaro Matsukawa

Published in
Frontiers in Bioengineering and Biotechnology

ISSN 1664-8714
ISBN 978-2-83251-537-2
DOI 10.3389/978-2-83251-537-2

About Frontiers

Frontiers is more than just an open access publisher of scholarly articles: it is a pioneering approach to the world of academia, radically improving the way scholarly research is managed. The grand vision of Frontiers is a world where all people have an equal opportunity to seek, share and generate knowledge. Frontiers provides immediate and permanent online open access to all its publications, but this alone is not enough to realize our grand goals.

Frontiers journal series

The Frontiers journal series is a multi-tier and interdisciplinary set of open-access, online journals, promising a paradigm shift from the current review, selection and dissemination processes in academic publishing. All Frontiers journals are driven by researchers for researchers; therefore, they constitute a service to the scholarly community. At the same time, the *Frontiers journal series* operates on a revolutionary invention, the tiered publishing system, initially addressing specific communities of scholars, and gradually climbing up to broader public understanding, thus serving the interests of the lay society, too.

Dedication to quality

Each Frontiers article is a landmark of the highest quality, thanks to genuinely collaborative interactions between authors and review editors, who include some of the world's best academicians. Research must be certified by peers before entering a stream of knowledge that may eventually reach the public - and shape society; therefore, Frontiers only applies the most rigorous and unbiased reviews. Frontiers revolutionizes research publishing by freely delivering the most outstanding research, evaluated with no bias from both the academic and social point of view. By applying the most advanced information technologies, Frontiers is catapulting scholarly publishing into a new generation.

What are Frontiers Research Topics?

Frontiers Research Topics are very popular trademarks of the *Frontiers journals series*: they are collections of at least ten articles, all centered on a particular subject. With their unique mix of varied contributions from Original Research to Review Articles, Frontiers Research Topics unify the most influential researchers, the latest key findings and historical advances in a hot research area.

Find out more on how to host your own Frontiers Research Topic or contribute to one as an author by contacting the Frontiers editorial office: frontiersin.org/about/contact

Innovations to improve screw fixation in traumatology and orthopedic surgery

Topic editors

Jonas Widmer — Balgrist University Hospital, Switzerland
Carl-Eric Aubin — Polytechnique Montréal, Canada
Harry van Lenthe — KU Leuven, Belgium
Keitaro Matsukawa — Murayama Medical Center (NHO), Japan

Citation

Widmer, J., Aubin, C.-E., van Lenthe, H., Matsukawa, K., eds. (2023). *Innovations to improve screw fixation in traumatology and orthopedic surgery*. Lausanne: Frontiers Media SA. doi: 10.3389/978-2-83251-537-2

Table of contents

frontiers | Frontiers in Bioengineering and Biotechnology

TYPE Editorial
PUBLISHED 25 November 2022
DOI 10.3389/fbioe.2022.1094813

OPEN ACCESS

EDITED AND REVIEWED BY
Markus O. Heller,
University of Southampton,
United Kingdom

*CORRESPONDENCE
Jonas Widmer,
jonas.widmer@hest.ethz.ch

SPECIALTY SECTION
This article was submitted to Biomechanics, a section of the journal Frontiers in Bioengineering and Biotechnology

RECEIVED 10 November 2022
ACCEPTED 16 November 2022
PUBLISHED 25 November 2022

CITATION
Widmer J, Aubin C-E, van Lenthe GH and Matsukawa K (2022), Editorial: Innovations to improve screw fixation in traumatology and orthopedic surgery. *Front. Bioeng. Biotechnol.* 10:1094813. doi: 10.3389/fbioe.2022.1094813

Editorial: Innovations to improve screw fixation in traumatology and orthopedic surgery

Jonas Widmer[1]*, Carl-Eric Aubin[2], G. Harry van Lenthe[3] and Keitaro Matsukawa[4]

[1]Department of Orthopedics, Balgrist University Hospital, Zürich, Switzerland, [2]Polytechnique Montréal, Montreal, QC, Canada, [3]Biomechanics Section, KU Leuven, Leuven, Belgium, [4]Murayama Medical Center (NHO), Musashimurayama, Japan

KEYWORDS

spine fixaton, screw loosening, screw pull-out, bone screw, bone erosion, screw resilience

Editorial on the Research Topic
Innovations to improve screw fixation in traumatology and orthopedic surgery

Introduction

Although bony fixation with screws is a very common intervention and the technique has been refined in previous decades, insufficient screw hold and screw loosening still pose a relevant clinical problem with an incidence of about 10% in rigid fusion constructs. This rate is increased in motion-preserving instrumentations and in patients with low bone quality such as those with osteoporosis. In a recent study, the risk of screw loosening in vertebrae with low bone quality was found to be over 60% (Weiser et al., 2017). As a consequence, revision surgery is required in a substantial number of patients.

Improving screw fixation is a challenging field of research because a fundamental understanding of screw fixation in bone is still lacking. Conventional *in vitro* testing of the implant-bone structure using cadaveric bones is usually employed to evaluate the mechanical fixation of screws. Yet, the precise interplay between the screw thread and the intricate microstructure of trabecular bone is difficult to capture experimentally, especially right at the interface. Furthermore, experimental tests have demonstrated and quantified bone damage due to the screw insertion (Steiner et al., 2016), and microstructural finite element models have demonstrated that this can affect screw stability dramatically (Steiner et al., 2017). It is therefore an interplay of various factors that ultimately determine screw resilience in the bone.

Spine surgery is an area where screw fixation is particularly essential, but also particularly problematic. In the case of severe spinal deformity, a surgical instrumentation and fusion of the spine with implants anchored to the vertebrae and sometimes also to the pelvis is often

performed. Pedicle screws have become the state-of-the-art fixation constructs for spinal fusion surgery (Lenke et al., 2008), with two complementary mechanical roles: 1) to apply forces to correct or reduce the spinal deformity intraoperatively and to maintain correction subsequently; 2) to create the proper mechanical environment for bony fusion. Spinal instrumentation constructs are subject to high loads under which pedicle screw fixation failure may occur (Abul-Kasim and Ohlin, 2014; Wang et al., 2016).

Spinal fusion is and always has been a race between biology and biomechanics. If fusion fails, eventually all spinal instrumentation either loosens or breaks. The spine cycles several million times a year, and the loads applied to the instrumentation and its fixation are highly variable (Spirig et al., 2021). They also depend on the construct design (anchor density (Widmer et al., 2020), anchor rigidity (Cornaz et al., 2021; Cornaz et al., 2022) use or absence of anterior column support (Burkhard et al., 2021), which could influence the outcomes and affect the risks of mechanical complications such as fixation loosening, material breakage, and adding on problems such as proximal junctional kyphosis or proximal junctional failure. Optimal construct stiffness is unknown. Too stiff constructs result in decreased load sharing and may limit fusion mass development and maturation. Too flexible instrumentation results in pseudarthrosis formation or early fatigue failure. Instrumentation design, sagittal balance correction, and choice of proximal fusion level have significant effects on the resulting forces in the spinal instrumentation and the success of osteosynthesis. Planning and optimization are important and can be aided opportunistically using analytical modeling (Widmer et al., 2020; Marie-Rosa et al., 2021) and biomechanical analysis (Wang et al., 2012; Wang et al., 2016; Bianco et al., 2017).

Using a combination of experimental and computational methods, this Research Topic will present novel insights and techniques that directly address the high complication rate of screw loosening in traumatology and orthopedic surgery:

Spine fixations

Cornaz et al. quantified the contribution of the pedicle and corpus region in relation to bone quality and anchoring strength of pedicle screws. They demonstrated the importance of the pedicle region for screw hold, especially for reduced bone quality, and mentioned that selecting a larger screw diameter and augmenting the pedicle with bone cement may prevent screw loosening.

Similarly, Li et al. found that the regional bone property of screw holding plane mainly contribute to long-term screw fixation in anterior instrumentation in lateral lumbar interbody fusion technique. They emphasized the importance of optimizing screw trajectory and anti-osteoporosis therapy to reduce the risk of screw loosening.

In addition, Li et al. also illustrated the biomechanical effects of mismatch of the interbody support. According to their report, mismatch between the vertebral endplate and grafted bone caused mechanical stress around screws, suggesting the significance of modification of intervertebral cage design to maintain screw fixation, tailored to individual patient anatomy.

Meanwhile, Wang et al. reported a biomechanical study on interspinous process dynamic stabilization to reduce adjacent segment disorders, which is inevitable in spinal fusion surgery. This technology appears to alter kinematic motion less and has the potential to become an effective tool for spinal stabilization in the future.

Fixations in non-spine related orthopedic areas

Bone screws are also used for prophylactic fixation in adult patients with an aggressive benign femoral neck lesion. Although the insertion of three cannulated screws is an established treatment method for nondisplaced femoral neck fractures in adults, it carries the risk of epiphyseal arterial vascular injury. Fu et al. investigated whether a technique using only two cannulated screws is biomechanically adequate to treat the femoral neck and does not result in screw avulsion. They show that with this technique adequate biomechanical strength can be achieved when the entire anterior cortical bone is involved.

Similarly, the stability of different screw trajectories for complex proximal humerus fractures was investigated by Mischler et al. in this research topic. Since the failure rate of locked plates is very high with the current state of the art, a new method with computationally improved screw trajectories was evaluated. Both finite element analyses and cyclic biomechanical testing showed a significant reduction in cut-out failure with the novel, proposed technique.

In calcaneus fractures, avulsion fractures of the tuber calcanei are characterized by a solid bone fragment at the Achilles tendon insertion. In an experimental study by Jordan et al. using synthetic bone, failure rates under cyclic loading were analyzed for different plate groups and screw-based fixation techniques. Surprisingly, the authors found that the 5.0-mm cannulated compression screws provided reliable stability and were a viable alternative to the commonly used 6.5-mm screws.

In the clavicle, hook plates are commonly used for dislocations of the acromioclavicular joint and fractures of the distal clavicle. Common complications resulting from this surgical technique with hook plates are subacromial bone erosion and peri-implant clavicular fractures. Wang et al. studied the effect of different clavicular hook plates, such as short plates, long plates, and posteriorly offset hook plates with different number and position of screws using finite element simulations. Based on their results, the authors discuss and show the trade-off between few screws and high loads at the clavicula and more screw but a higher risk of bone plate failure.

The authors who contributed to this Research Topic give a broad overview of the topic and the problem of screw fixations with a range of applications. Even though the application of screws is very

diverse and covers a wide range of orthopedic specialty areas, the goal of achieving improved screw resilience is the same in all of them. Therefore, in the publication presented, we can also draw some overall conclusions from this Research Topic.

One major conclusion is that screws surrounded by higher bone density have higher resilience. This was shown in the study by Cornaz et al. who demonstrated increased retention in the pedicle at higher bone density for spine screws, in the study by Mischler et al. on the humerus who achieved better retention by adjusting the screw trajectory in areas of higher bone density, but also in the study by Fu et al. who indicated that anchoring of the screw in the cortex in the calcaneus is essential. Although this finding seems obvious, it appears to be of immense importance to incorporate it into current orthopedic techniques. Preoperative computer models that optimize and plan patient-specific screw trajectories, generic trajectories that lead to areas of higher bone quality, or implants that allow more targeted anchorage in cortical bone could therefore prevent problems with screws breaking out in the bone in the different areas.

Another conclusion is that the implant geometry of the screw going into the bone is very important. The implant geometry determines the resistance of the implant in the bone. This can be seen in our research topic, for example, in the study by Fu et al. in which different sizes and implants were tested and large differences in breakout force were found. Screws are primarily designed for an axial loading direction, but many of the load cases encountered in the application have a different primary loading direction, as shown by the many publications on our research topics from different fields. For example, Cornaz et al. and Li et al. point out that the loads acting on the screws during spinal fusion are mainly in the shear direction. New implant geometries such as nails and wedges that can be used as an alternative or in addition to screws could therefore be very promising to improve resilience. Much can therefore be achieved in the development of implants in the future.

Author contributions

JW coordinated the research topic, participated in the review processes, and co-wrote the editorial. C-EA, GHV, and KM participated in the review process and co-wrote and proofread the editorial.

Conflict of interest

The authors declare that the research was conducted in the absence of any commercial or financial relationships that could be construed as a potential conflict of interest.

Publisher's note

References

Abul-Kasim, K., and Ohlin, A. (2014). Evaluation of implant loosening following segmental pedicle screw fixation in adolescent idiopathic scoliosis: A 2 year follow-up with low-dose ct. *Scoliosis* 9 (1), 13. doi:10.1186/1748-7161-9-13

Bianco, R. J., Arnoux, P. J., Wagnac, E., Mac-Thiong, J. M., and Aubin, C. É. (2017). Minimizing pedicle screw pullout risks: A detailed biomechanical analysis of screw design and placement. *Clin. Spine Surg.* 30 (3), E226–E232. doi:10.1097/BSD.0000000000000151

Burkhard, M. D., Cornaz, F., Spirig, J. M., Wanivenhaus, F., Loucas, R., Fasser, M. R., et al. (2021). Posterior spinal instrumentation and decompression with or without cross-link? *North Am. Spine Soc. J.* 8, 100093. doi:10.1016/j.xnsj.2021.100093

Cornaz, F., Fasser, M. R., Snedeker, J. G., Spirig, J. M., Farshad, M., and Widmer, J. (2022). The biomechanical fundamentals of crosslink - augmentation in posterior spinal instrumentation. *Sci. Rep.* 12, 7621. doi:10.1038/s41598-022-11719-2

Cornaz, F., Widmer, J., Snedeker, J. G., Spirig, J. M., and Farshad, M. (2021). Cross-links in posterior pedicle screw- rod instrumentation of the spine: A systematic review on mechanical, biomechanical, numerical and clinical studies. *Eur. Spine J.* 30 (1), 34–49. doi:10.1007/s00586-020-06597-z

Lenke, L. G., Kuklo, T. R., Ondra, S., and Polly, D. W. (2008). Rationale behind the current state-of-the-art treatment of scoliosis (in the pedicle screw era). *Spine (Phila Pa 1976)* 33, 1051–1054. doi:10.1097/BRS.0b013e31816f2865

Marie-Rosa, F., Gerber, G., Passaplan, C., Cornaz, F., Snedeker, Jess G., Farshad, M., et al. (2021). Computational model predicts risk of spinal screw loosening in patients. *Eur. Spine J.* 31, 2639–2649. Unpublished Paper, currently under Review (the full text is attached in this document). doi:10.1007/s00586-022-07187-x

Spirig, J. M., Winkler, E., Cornaz, F., Fasser, M. R., Betz, M., Snedeker, J. G., et al. (2021). Biomechanical performance of bicortical versus pericortical bone trajectory (CBT) pedicle screws. *Eur. Spine J.* 30 (8), 2292–2300. doi:10.1007/s00586-021-06878-1

Steiner, J. A., Christen, P., Affentranger, R., Ferguson, S. J., and van Lenthe, G. H. (2017). A novel *in silico* method to quantify primary stability of screws in trabecular bone. *J. Orthop. Res.* 35 (11), 2415–2424. doi:10.1002/jor.23551

Steiner, J. A., Ferguson, S. J., and van Lenthe, G. H. (2016). Screw insertion in trabecular bone causes peri-implant bone damage. *Med. Eng. Phys.* 38 (4), 417–422. doi:10.1016/j.medengphy.2016.01.006

Wang, X., Aubin, C. E., Labelle, H., Parent, S., and Crandall, D. (2012). Biomechanical analysis of corrective forces in spinal instrumentation for scoliosis treatment. *Spine (Phila Pa 1976)* 37 (24), E1479–E1487. doi:10.1097/BRS.0b013e3182706745

Wang, X., Boyer, L., le Naveaux, F., Schwend, R. M., and Aubin, C. E. (2016). How does differential rod contouring contribute to 3-dimensional correction and affect the bone-screw forces in adolescent idiopathic scoliosis instrumentation? *Clin. Biomech.* 39, 115–121. doi:10.1016/j.clinbiomech.2016.10.002

Weiser, L., Huber, G., Sellenschloh, K., Viezens, L., Puschel, K., Morlock, M. M., et al. (2017). Insufficient stability of pedicle screws in osteoporotic vertebrae: Biomechanical correlation of bone mineral density and pedicle screw fixation strength. *Eur. Spine J.* 26 (11), 2891–2897. doi:10.1007/s00586-017-5091-x

Widmer, J., Fasser, M. R., Croci, E., Spirig, J., Snedeker, J. G., and Farshad, M. (2020). Individualized prediction of pedicle screw fixation strength with a finite element model. *Comput. Methods Biomech. Biomed. Engin.* 23 (4), 155–167. doi:10.1080/10255842.2019.1709173

frontiers | Frontiers in Bioengineering and Biotechnology

ORIGINAL RESEARCH
published: 08 April 2022
doi: 10.3389/fbioe.2022.862951

The Mismatch Between Bony Endplates and Grafted Bone Increases Screw Loosening Risk for OLIF Patients With ALSR Fixation Biomechanically

Jing-Chi Li[1†], *Tian-Hang Xie*[1†], *Zhuang Zhang*[1], *Zhe-Tao Song*[2], *Yue-Ming Song*[1*] and *Jian-Cheng Zeng*[1*]

[1]Department of Orthopedic Surgery and Orthopedic Research Institute, West China Hospital/West China School of Medicine for Sichuan University, Chengdu, China, [2]Department of Imaging, West China Hospital, Chengdu, China

OPEN ACCESS

Edited by:
Keitaro Matsukawa,
Murayama Medical Center (NHO),
Japan

Reviewed by:
Abdelwahed Barkaoui,
International University of Rabat,
Morocco
Riza Bayoglu,
NuVasive, United States

***Correspondence:**
Yue-Ming Song
sym_cd@163.com
Jian-Cheng Zeng
tomzeng5@126.com

[†]These authors have contributed equally to this work and share first authorship

Specialty section:
This article was submitted to Biomechanics, a section of the journal Frontiers in Bioengineering and Biotechnology

Received: 26 January 2022
Accepted: 24 March 2022
Published: 08 April 2022

Citation:
Li J-C, Xie T-H, Zhang Z, Song Z-T, Song Y-M and Zeng J-C (2022) The Mismatch Between Bony Endplates and Grafted Bone Increases Screw Loosening Risk for OLIF Patients With ALSR Fixation Biomechanically. Front. Bioeng. Biotechnol. 10:862951. doi: 10.3389/fbioe.2022.862951

The mismatch between bony endplates (BEPs) and grafted bone (GB) triggers several complications biomechanically. However, no published study has identified whether this factor increases the risk of screw loosening by deteriorating the local stress levels. This study aimed to illustrate the biomechanical effects of the mismatch between BEP and GB and the related risk of screw loosening. In this study, radiographic and demographic data of 56 patients treated by single segment oblique lumbar interbody fusion (OLIF) with anterior lateral single rod (ALSR) fixation were collected retrospectively, and the match sufficiency between BEP and GB was measured and presented as the grafted bony occupancy rate (GBOR). Data in patients with and without screw loosening were compared; regression analyses identified independent risk factors. OLIF with different GBORs was simulated in a previously constructed and validated lumbosacral model, and biomechanical indicators related to screw loosening were computed in surgical models. The radiographic review and numerical simulations showed that the coronal plane's GBOR was significantly lower in screw loosening patients both in the cranial and caudal vertebral bodies; the decrease in the coronal plane's GBOR has been proven to be an independent risk factor for screw loosening. In addition, numerical mechanical simulations showed that the poor match between BEP and GB will lead to stress concentration on both screws and bone-screw interfaces. Therefore, we can conclude that the mismatch between the BEP and GB will increase the risk of screw loosening by deteriorating local stress levels, and the increase in the GBOR by modifying the OLIF cage's design may be an effective method to optimize the patient's prognosis.

Keywords: oblique lumbar interbody fusion, grafted bony occupancy rate, screw loosening, biomechanical deterioration, anterior lateral single rod fixation

Abbreviations: ALSR, anterior lateral single rod; AUC, area under the curve; BEP, bony endplate; BMD, bone mineral density; CEP, cartilage endplate; CT, computational tomography; DC, disc compression; FCF, facet contact force; FEA, finite element analysis; GB, grafted bone; GBOR, grafted bony occupancy rate; HU, Hounsfield units; ICC, intraclass correlation efficiency; IDP, intradiscal pressure; OLIF, oblique lumbar interbody fusion; PEEK, polyether ether ketone; ROC, receiver operating characteristics; ROI, region of interest; ROM, range of motion; TI, titanium.

INTRODUCTION

The anterior lateral single rod (ALSR) fixation system can reconstruct instant postoperative stability in a single incision for oblique lumbar interbody fusion (OLIF) patients. As a hardware-related complication, screw loosening has been widely reported, negatively affecting patients' rehabilitation and deteriorating long-term prognosis (Bokov et al., 2019; Zou et al., 2020). The deterioration of stress levels was the most important risk factor for screw loosening (Tsuang et al., 2016; Pearson et al., 2017). Stress concentration on the bone-screw interfaces and screw rod systems will increase the risk of cancellous microdamage and resulting screw loosening (Nowak, 2019; Kanno et al., 2021). While discussing the risk factors for screw loosening, demographic characteristics are always assumed to be defined by some biomechanical pathogenesis. For instance, multiple studies have revealed that the incidence of screw loosening is high in senile patients with osteoporosis, which can be explained by the damage of bone-screw interface integration in vertebral bodies with low bone mineral density (BMD) (Bokov et al., 2019; Zou et al., 2020).

Clinical studies have shown that the mismatch between BEP and GB triggers complications, including nonunion and cage subsidence (Kim et al., 2012; Hu et al., 2021), and the mechanism of this phenomenon has been well explained. Specifically, biomechanical studies proved that the mismatch between BEP and GB changes the local load transmission pattern, and stress concentration can be observed on both the cranial and caudal sides of BEP and sub-BEP cancellous bone (Agarwal et al., 2013; Zhang et al., 2016). The risk of microdamage of bony structures and resulting cage subsidence should be increased (Mi et al., 2017; Lu and Lu, 2019). Meanwhile, the mismatch between BEP and GB can also lead to hypermobility of the surgical segment; resulting cage migration can also trigger cage subsidence, inhibit osteogenesis and increase the risk of nonunion (Agarwal et al., 2013; Zhang et al., 2016).

Studies proved that screw loosening was related to these complications, and insufficient anterior support was also reported as a risk factor for stress concentration in the bone-screw interfaces and resulting screw loosening (Kim et al., 2012; Bredow et al., 2016; Pearson et al., 2017; Hu et al., 2021). Considering that the mismatch between BEP and GB is a typical performance for insufficient anterior support, we hypothesize that it may also lead to the deterioration of stress levels and increase the risk of screw loosening. This study identifies whether the mismatch between BEP and GB will lead to local mechanical deterioration and resulting screw loosening from the perspective of radiographic observation and biomechanical research. This study collected imaging and demographic data from patients with single-segment OLIF fixed by the ALSR system. Biomechanical changes from OLIF models with different grades of contact sufficiency have been investigated in a calibrated and well-validated lumbosacral model. The published literature has not adequately clarified this issue.

In this study, we verified whether the mismatch between BEP and GB triggers a higher incidence of screw loosening and investigated the biomechanical effects of this phenomenon. Imaging data of OLIF patients fixed by ALSR have been retrospectively reviewed, and the biomechanical changes in ALSR and bone-screw interfaces have been computed in an anteriorly constructed numerical lumbo-sacral model. This study could provide theoretical guidance for understanding the screw loosening mechanism and optimizing the design of OLIF cages.

MATERIALS AND METHODS

Review of Prospectively Collected Radiographic and Demographic Data

Patient Collection

The ethics committees of West China Hospital reviewed and approved the protocol of this study (2020-554). Informed consent was waived for this retrospective study. We retrospectively reviewed patients who underwent single segment OLIF with ALSR screw fixation from May 2017 to August 2019. The age, sex, and BMI of these patients were recorded. A senior spine surgeon performed all operations. Screw types and sizes were identical in these patients. All screws were placed in a single attempt and penetrated the contralateral cortex.

Patients who underwent single segment OLIF with ALSR screw fixation for lumbar degenerative diseases, including spinal stenosis, grade 1 and grade 2 degenerative spondylolisthesis, and lumbar disc herniation, were included in this study. The exclusion criteria were as follows: 1) Patients with a history of lumbar surgery; 2) Patients with primary or metastatic spinal tumors, lumbar tuberculosis, rheumatic immune diseases, and secondary osteoporosis caused by medication or other metabolic diseases; 3) Patients with grade 3 and grade 4 degenerative spondylolisthesis or spondylolysis; 4) Patients who underwent lumbar revision surgery within the clinical follow-up period of 12 months for complications other than screw loosening; 5) Patients who underwent intraoperative screw replacement.

Collection Radiographic Data

All patients underwent lumbar computational tomography (CT) three times in the imaging center of our hospital, including 1 week before, 1 week after, and 1 year after OLIF surgery (tube voltage: 120 kV) (Mikula et al., 2019; Xi et al., 2020; Zou et al., 2020). The CT scan settings were uniform in all enrolled patients. An experienced spine surgeon independently measured the following radiographic parameters. The interobserver and intraobserver reliability of these measured parameters was verified in 10 randomly selected patients. One week after the imaging measurement, the spine surgeon and a senior radiologist independently remeasured the imaging parameters of these selected patients.

The screw loosening status of the cranial and caudal vertebral bodies was identified separately. In the postoperative 1-year CT imaging data, vertebral bodies with ≥1 mm width radiolucent zones around the screw were defined as screw loosening (Bredow et al., 2016; Bokov et al., 2019; Zou et al., 2020). The BMD of these patients was identified by measuring their Hounsfield unit (HU)

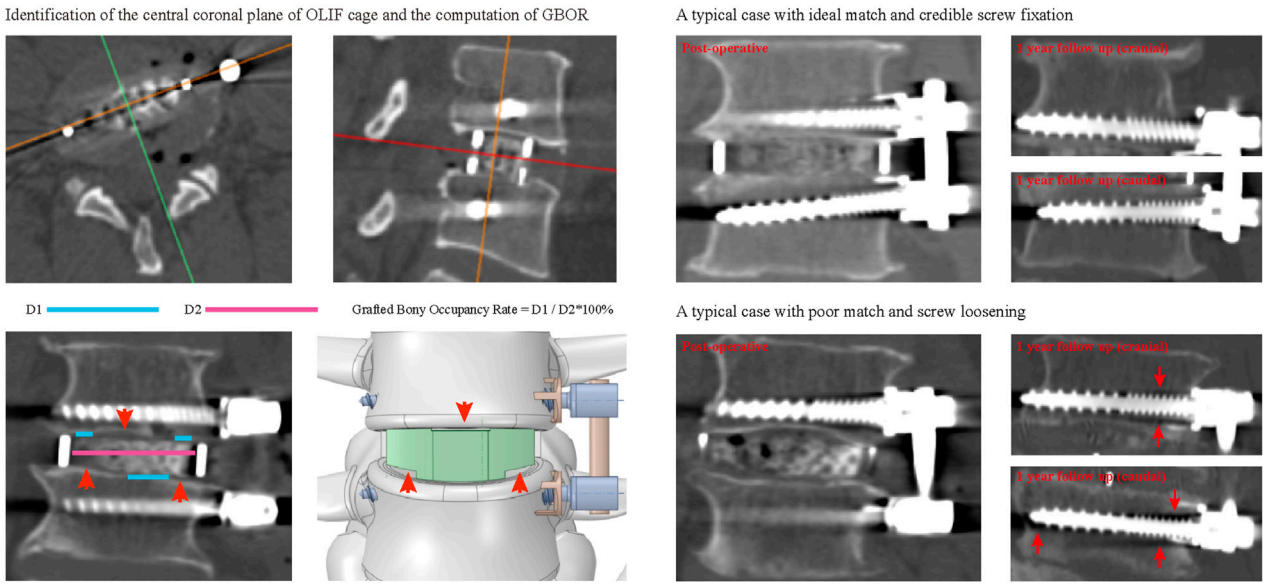

FIGURE 1 | The schematic of the definition and surgical simulations of GBOR, and typical cases for different contact sufficiency and resulting screw fixation status.

values. During HU measurement in vertebral bodies, the region of interest (ROI) was expanded to the largest within the cancellous bone but excluded other bony structures, such as cortical, BEP, and osteophytes (Schreiber et al., 2014; Xi et al., 2020; Zou et al., 2020). Values of HU were measured at the midsagittal plane, central transverse plane, transverse planes close to the superior and the inferior endplate separately, and the average value of these planes was set as the HU of the vertebral body (Pickhardt et al., 2013; Mikula et al., 2019; Xi et al., 2020; Zou et al., 2020). The sufficiency of contact between BEP and GB was quantified by calculating the grafted bony occupancy rate (GBOR) (Kim et al., 2012; Ushirozako et al., 2020). GBOR was measured in the cage's central sagittal and coronal planes (rather than the vertebral body) in the postoperative CT imaging data (**Figure 1**).

Statistical Analyses

Radiographic and demographic indicators are presented as the mean ± standard deviation for continuous variables and number (percentage) for categorical variables. We conducted statistical analyses in SPSS software. The intraclass correlation efficiency (ICC) was computed to identify the repeatability of continuous variables (ICC ≥ 0.8 represents excellent reliability) (Zou et al., 2019; Zou et al., 2020). The kappa values were computed to determine the repeatability of screw loosening (kappa values of 0.41–0.60 indicated moderate reliability; 0.61 to 0.80, substantial agreement; and 0.81 to 1.00, excellent or almost perfect agreement) (Oetgen et al., 2008; Yue et al., 2008; Li et al., 2021b).

Statistical analyses for cranial and caudal side screw loosening were performed separately. When comparing the difference between different groups, the independent samples Student's *t* test was used for continuous variables, and the chi-square test was used for the categorical variables. We performed binary logistic regression to identify independent risk factors for screw loosening. Univariate analyses of each potential risk factor were performed, and the variables that achieved a significance level of $p < 0.1$ were entered into multivariate analyses. Variables with $p < 0.05$ were considered independent risk factors in the multivariate analyses (Zhao et al., 2009; Park et al., 2017; Bagheri et al., 2019). A p value less than 0.05 indicated a significant difference.

Numerical Surgical Simulations and Finite Element Analyses (FEA)

Construction of the Intact Finite Element (FE) Model

Our published studies have constructed and validated a biomimetic lumbosacral FE model (L3-S1). Bone structures of the FE model include cortical, cancellous, and BEPs. The cortical thickness was set as 0.8 mm, and the thickness and morphology parameters (i.e., concave angles and depths) of BEPs were defined separately based on anatomic studies (Li et al., 2021a; Li et al., 2021b). Nonbony components include the intervertebral disc (IVD) and facet cartilages. The IVD consists of the nucleus, annulus, and cartilage endplates (CEPs). The nucleus's cross-sectional area accounted for 38% of the IVD (Li et al., 2021a; Li et al., 2021b). The outline of the BEP covers the entire IVD, and that of the CEP covers the nucleus and inner part of the annulus (Jacobs et al., 2014; DeLucca et al., 2016). Ligaments and facet capsules were defined as cable elements in the preprocessing process of FEA (Chuang et al., 2013; Dreischarf et al., 2014; Du et al., 2016; Li et al., 2019; Li et al., 2021a).

OLIF Simulations With Different Grades of Contact Sufficiency

The L4-L5 segment was selected to simulate oblique lumbar interbody fusion (OLIF) with ALSR screw fixation, and we

TABLE 1 | Construction of numerical models with different grades of contact sufficiency.

	Model1	Model2	Model3	Model4	Model5
Cranial	Ideal	Ideal	Poor	Acceptable	Poor
	GBOR = 100%	GBOR = 100%	GBOR = 60%	GBOR = 80%	GBOR = 60%
Caudal	Ideal	Poor	Ideal	Acceptable	Poor
	GBOR = 100%	GBOR = 60%	GBOR = 100%	GBOR = 80%	GBOR = 60%

performed surgical simulation according to a literature review and our surgical experience (Guo et al., 2020; Xi et al., 2020). In this process, lateral parts of the annulus, all of the nucleus, and CEPs were removed, and a polyether-ether-ketone (PEEK) OLIF cage (18 mm width and 50 mm length) filled with grafted bone was inserted into the interbody space. The lordotic angle and disc height of the postoperative models were identical to those of the intact model to eliminate the mechanical effects of these parameters (Kim et al., 2012; Wang et al., 2019; Guo et al., 2020).

Three different grades of contact sufficiency between the BEP and GB (including ideal, acceptable, and poor) were simulated by changing the GBOR in the coronal plane. The ideal contact was defined completely match between BEP and GB, GBOR in acceptable and poor contact models were defined as 80 and 60%, respectively. Based on the review of radiographic data, the mismatch on the superior side was mainly in the central region, while that on the inferior side was in the peripheral region. By combining different contact sufficiency grades between the GB and superior and inferior BEPs, five different OLIF models were constructed (**Table 1**; **Figures 1**, **5**).

During the simulation of ALSR screw fixation, two titanium alloy (TI) screws were inserted into the L4-L5 vertebral bodies and penetrated the contralateral cortex. The axes of the screws in the transverse plane were parallel to the OLIF cage, whereas those in the coronal plane were parallel to the BEPs (Guo et al., 2020; Xie et al., 2020). Screw threads were preserved, and the screw compaction effect was simulated by adjusting the material property of cancellous around the thread (Hsu et al., 2005; Matsukawa et al., 2016). The connection between the screw tulip, the nut, and the spacer was simplified to increase the computational efficiency.

Boundary and Loading Conditions

Finite element analyses in this study were performed in the "Ansys workbench 2020 r2 academic". Hybrid elements (e.g., tetrahedron and hexahedron elements) with different sizes were set in different components of the FE model. Mesh refinement was set in structures with low thickness and large deformation (e.g., BEP, facet cartilage, and posterior parts of the annulus) (Kim et al., 2010; Chuang et al., 2013; Dreischarf et al., 2014; Kang et al., 2017). The degrees of freedom of S1 inferior surfaces were fixed entirely. Different directional moments were applied on the superior BEP of L3 (DeLucca et al., 2016; Li et al., 2021a). Numerical simulations computed under flexion, extension, left and right bending, and axial rotation loading conditions (**Figure 3**). In the definition of material properties (**Table 2**), cortical and cancellous bone were defined by anisotropic law (Ferguson and Steffen, 2003; Morgan et al., 2003; Tsouknidas et al., 2015). The annulus was assumed to be hypoelastic material, and the nucleus was set as a semifluid incompressible material (Wu and Yao, 1976; Kim et al., 2010). The material properties of the surgical instrumented structure (i.e., PEEK and TI) were defined by isotropic law; the elastic modulus of the GB was calculated based on the HU values measured in the postoperative CT scan. By defining the friction coefficients between different contact surfaces, stress levels immediately after operation were computed (Chuang et al., 2012; Hsieh et al., 2017; Kang et al., 2017). The contact between facet cartilages was set as frictionless, the frictional coefficient between BEP and GB was 0.46, and that between BEP and cage and screw-cancellous interfaces was 0.2 (Lu and Lu, 2019; Rastegar et al., 2020).

Model Calibration and Validation

The stiffness of ligaments was seen as a calibrated indicator. By repeatedly computing the range of motions (ROMs) in the L4-L5 segment and adjusting ligament stiffness, the differences between computed ROMs and measured values from widely cited *in vitro* studies could be reduced (Schmidt et al., 2007a; Schmidt et al., 2007b; Du et al., 2016; Li et al., 2021a). As a result, current FE models could better represent real stress levels by model calibration. We performed a mesh convergence test on the calibrated intact model by evaluating the change in intradiscal pressure (IDP) with different mesh sizes. The model was considered converged if the change in the computed IDP was less than 3% (Ottardi et al., 2016; Fan et al., 2021). The computed ROM, IDP, disc compression (DC), and facet contact force (FCF) were compared with *in vitro* measured values in the multi-indicator model validation process (Wilson et al., 2006; Renner et al., 2007; Schilling et al., 2011).

RESULTS

Retrospectively Study of Prospectively Collected Data

Patient Collection and Screw Loosening Rates

A total of 56 patients (30 males and 26 females) with an average age of 56.57 ± 11.96 years treated by single segment OLIF with

TABLE 2 | Material properties of FE models' components.

Components	Elastic modulus (MPa)	Poisson's ratio	Cross-section (mm^2)	References
Cortical	E_{xx} = 11,300	V_{xy} = 0.484		Ferguson and Steffen (2003); Tsouknidas et al. (2015)
	E_{yy} = 11,300			
	E_{zz} = 22,000	V_{yz} = 0.203		
	G_{xy} = 3,800			
	G_{yz} = 5,400	V_{xz} = 0.203		
	G_{xz} = 5,400			
Cancellous	E_{xx} = 140	V_{xy} = 0.45		Morgan et al. (2003); Tsouknidas et al. (2015)
	E_{yy} = 140			
	E_{zz} = 200	V_{yz} = 0.315		
	G_{xy} = 48.3			
	G_{yz} = 48.3	V_{xz} = 0.315		
	G_{xz} = 48.3			
Bony endplates	12,000	0.3		Kang et al. (2017); Li et al. (2019)
Annulus	Hypoelastic material			Wu and Yao (1976); Kim et al. (2010)
Nucleus	1	0.49		Chuang et al. (2013); Qasim et al. (2014)
Cartilage endplates	10	0.4		Li et al. (2019); Li et al. (2021)
Anterior longitudinal ligaments	Calibrated load-deformation curved under different loading conditions	0.3	60	Du et al. (2016); Li et al. (2021)
Posterior longitudinal ligaments	Calibrated load-deformation curved under different loading conditions	0.3	21	Du et al. (2016); Li et al. (2021)
Ligamentum flavum	Calibrated load-deformation curved under different loading conditions	0.3	60	Du et al. (2016); Li et al. (2021)
Interspinous ligaments	Calibrated load-deformation curved under different loading conditions	0.3	40	Du et al. (2016); Li et al. (2021)
Supraspinous ligaments	Calibrated load-deformation curved under different loading conditions	0.3	30	Du et al. (2016); Li et al. (2021)
Intertransverse ligaments	Calibrated load-deformation curved under different loading conditions	0.3	10	Du et al. (2016); Li et al. (2021)
Capsular	7.5 (\25%) 32.9 ([25%)	0.3	67.5	Chuang et al. (2013); Li et al. (2019)
PEEK OLIF Cage	3,500	0.3		Hsieh et al. (2017); Kang et al. (2017)
Titanium alloy screw	110,000	0.3		Hsieh et al. (2017); Kang et al. (2017)

TABLE 3 | Validation of measured values repeatability.

	Interobserver	Intraobserver
ICCs of continuous variables	0.894	0.862
Kappa values of union status	0.778	0.759

ALSR screw fixation were recorded. The interobserver and intraobserver results during the judgment of screw loosening were substantial, with Kappa values of 0.778 and 0.759, respectively. The reliability of continuous variable measurement was excellent, with ICCs of 0.894 and 0.862, respectively (**Table 3**). The overall incidence rate of screw loosening was 35.71% (40/112), and the screw loosening rate of the vertebral body on the cranial side was 42.86% (24/56), which was significantly higher than that of the caudal vertebral body, which was 28.57% (16/56, p = 0.002). The cranial side's GBOR was significantly lower than that of the caudal side in coronal and sagittal planes (p = 0.009), and there were no significant differences in HU between cranial and caudal vertebral bodies (p = 0.519).

TABLE 4 | Logistic regression analysis of the cranial screw loosening.

	OR	95% CI		p
Univariate analysis				
Gender	2.333	0.791	6.885	0.125
Age	1.053	1.003	1.106	0.039[a]
BMI	0.972	0.83	1.138	0.723
Average HU	0.976	0.959	0.993	0.005[a]
GBOR (coronal plane)	0.971	0.949	0.995	0.017[a]
GBOR (Sagittal plane)	0.988	0.966	1.011	0.3
Multivariate analyses				
Age	1.028	0.971	1.089	0.341
Average HU	0.978	0.96	0.996	0.019[b]
GBOR (coronal plane)	0.973	0.948	0.999	0.043[b]

[a]*Variables that achieved a significance level of* p < *0.1 in the univariate analysis.*
[b]*Statistical significance in the multivariate regression analysis* (p < *0.05).*

Identification of Independent Risk Factors for Screw Loosening

The age of patients with cranial side screw loosening was significantly higher (p = 0.033) and had significantly lower

TABLE 5 | Logistic regression analysis of the caudal screw loosening.

	OR	95% CI		*p*
Univariate analysis				
Gender	1.739	0.54	5.604	0.354
Age	1.042	0.99	1.097	0.117
BMI	0.985	0.828	1.17	0.86
Average HU	0.957	0.933	0.982	0.001[a]
GBOR (coronal plane)	0.951	0.915	0.988	0.01[a]
GBOR (Sagittal plane)	0.974	0.946	1.002	0.071[a]
Multivariate analyses				
Average HU	0.953	0.927	0.98	0.001[b]
GBOR (coronal plane)	0.94	0.89	0.992	0.023[b]
GBOR (Sagittal plane)	0.996	0.956	1.038	0.852

[a]*Variables that achieved a significance level of* p < *0.1 in the univariate analysis.*
[b]*Statistical significance in the multivariate regression analysis* (p < *0.05).*

coronal plane GBOR and HU than those without screw loosening. The *p* value of HU was 0.003, and that of GBOR was 0.013. Based on the computational results of univariate logistic regression analyses, these three indicators were also entered into the multivariate analysis to identify independent risk factors. The results showed that reducing HU and coronal plane GBOR were independent risk factors for screw loosening on the cranial side (**Tables 4**, **5**). The *p* value of HU was 0.019, and that of GBOR was 0.043. In regard to caudal side screw loosening, differences in GBOR on the coronal plane and HU were significant in the screw loosening and nonloosening groups; the *p* value of HU was 0.000, and that of GBOR was 0.005. Based on univariate logistic regression analyses, HU and GBOR in coronal and sagittal planes were entered into the multivariate analysis. Consistent with the cranial vertebral body, reduced HU and coronal plane GBOR were also independent risk factors for

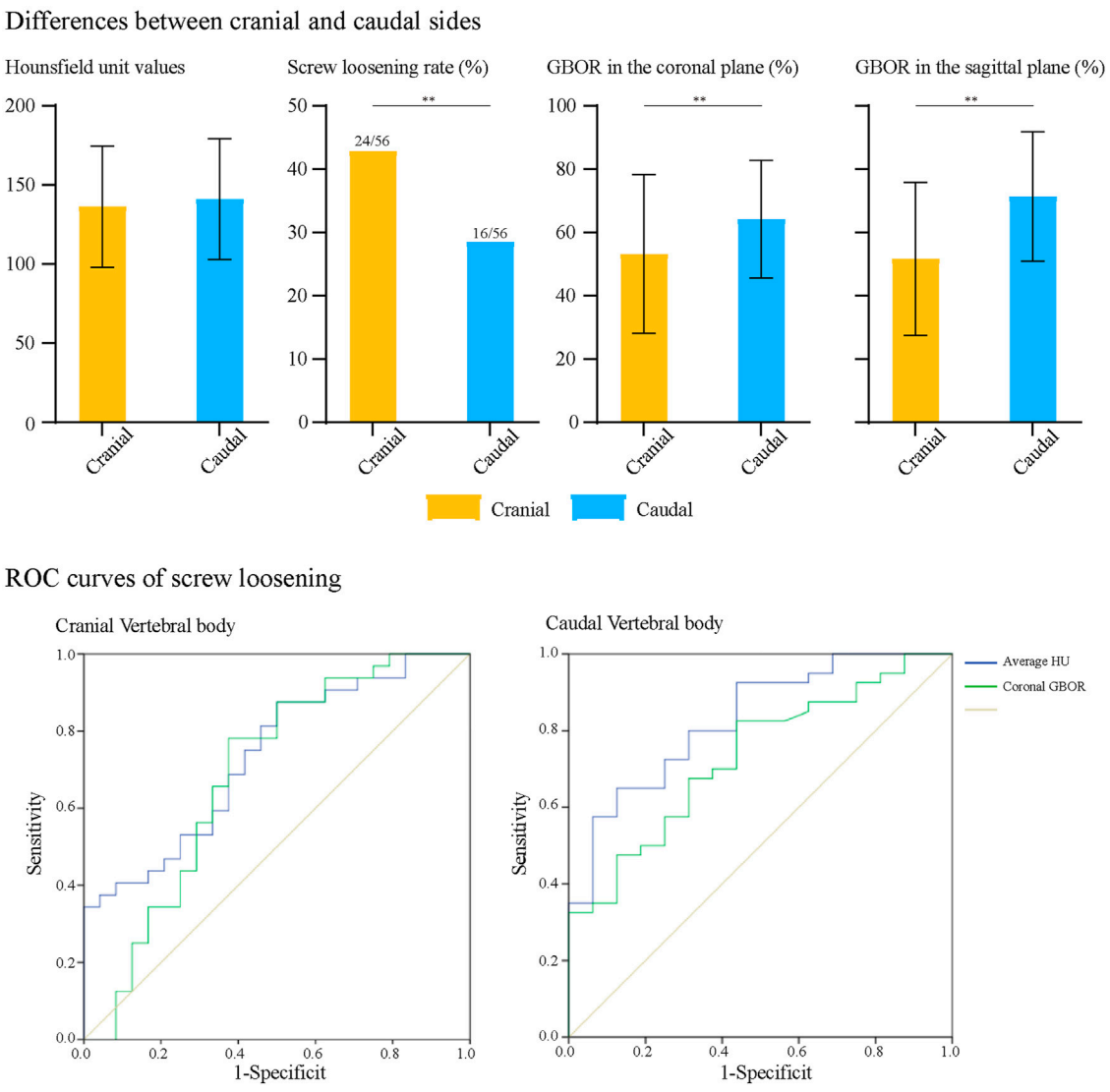

FIGURE 2 | ROC curves for cranial and caudal side screw loosening.

TABLE 6 | The cut-off value, sensitivity and specificity of four measurement methods for predicting screw loosening.

	Cut-off value	Sensitivity	Specificity	AUC
Cranial vertebral body				
Average HU	105.56	0.875	0.5	0.733
Coronal plane's GBOR (%)	55.27	0.656	0.6.67	0.686
Caudal vertebral body				
Average HU	107.3	0.925	0.562	0.83
Coronal plane's GBOR (%)	60.97	0.675	0.687	0.732

screw loosening in the caudal vertebral body (**Figure 2** and **Table 6**). The p value of HU was 0.001, and that of GBOR was 0.023.

Parameter Prediction Values for Screw Loosening

We performed ROC curve analyses to assess the predictive value of HU and coronal plane GBOR; the results are summarized in **Figure 2** and **Table 6**. Consistent with logistic regression analyses, HU values of vertebral bodies had the highest predictive ability. The AUCs of HU in the cranial and caudal vertebral bodies were 0.733 and 0.830, and those of the coronal plane's GBOR were 0.686 and 0.732, respectively.

Numerical Mechanical Surgical Simulations

Multi-Indicator Model Validation

Biomechanical indicators computed by the calibrated intact model were within ±1 standard deviation of the average values measured by *in vitro* studies. Thus, we believe that biomechanical changes identified by current FE models make good representations of actual stress levels (**Figure 3**).

Biomechanical Changes Caused by the Change in GBOR in the Coronal Plane

We computed the maximum von Mises stress of both cranial and caudal screws and the average stress of corresponding bone-screw interfaces to investigate the risk of screw loosening biomechanically (Ambati et al., 2015; Matsukawa et al., 2016; Fletcher et al., 2019; Kim et al., 2020); changes in computed biomechanical indicators can well explain the result from our review of radiographic data. Consistent with published studies, stress concentration can be observed in the screw head of both cranial and caudal screws (Chao et al., 2008; Amaritsakul et al., 2014). Compared to the model with ideal contact sufficiency, a slight stress concentration of the screw and corresponding bone-screw interfaces can be recorded with the acceptable (80%) contact model. In contrast, the stress values of the poor contact models dramatically increased under almost all body positions, especially under the left lateral bending and two-sided axial rotation loading conditions (**Figures 4**, **5**).

DISCUSSION

Stress concentration of the ALSR fixation system and bone-screw interfaces and the resulting loss of bone-screw integration are primary causes of screw loosening. Therefore, biomechanical changes should provide reasonable explanations for screw loosening-related clinically observed factors and provide theoretical references for optimizing treatment strategies. Taking the correlation between BMD reduction and the increased risk of screw loosening as an example: Consistent with the current study, clinical studies repeatedly proved that osteoporosis is an independent risk factor for predicting screw loosening (Bredow et al., 2016; Bokov et al., 2019). Biomechanical studies, including numerical simulations and *in vitro* mechanical tests, have also repeatedly proven that BMD reduction would lead to the deterioration of screw-bone integration and the resulting reduction of screw pull-out and fixation strength (Ohtori et al., 2013; Weidling et al., 2020; Zou et al., 2020). These findings have contributed to the updating of treatment principles. Regular anti-osteoporosis therapy has been promoted in osteoporosis patients requiring internal spinal fixation as an effective method to reduce the risk of screw loosening (Ohtori et al., 2013; Mikula et al., 2019).

Poor matches between BEP and GB biomechanically trigger complications. Clinical follow-up studies proved that a poor match would increase the risk of cage subsidence and nonunions (Kim et al., 2012; Hu et al., 2021); biomechanical studies presented that the poor match between BEP and GB triggers BEP stress concentration and hypermobility of the surgical segment (Agarwal et al., 2013; Zhang et al., 2016). These studies conclude that optimizing cage design based on the morphological difference of BEPs could reduce the risk of these complications by optimizing the local stress level. However, no studies have identified the effect of poor contact between the BEP and GB on the incidence of screw loosening. In patients fixed by the pedicle screw system, poor anterior column support was an essential trigger for biomechanical deterioration in the bone-screw interfaces, and the mismatch between BEP and GB can be seen as a typical instance of "poor anterior support" (Bredow et al., 2016; Pearson et al., 2017; Hu et al., 2021). Therefore, we proposed and verified the hypothesis that the mismatch between the BEP and GB may also increase the risk of screw loosening for ALSR fixation biomechanically. We believe this study's most significant innovation effectively combines radiographic

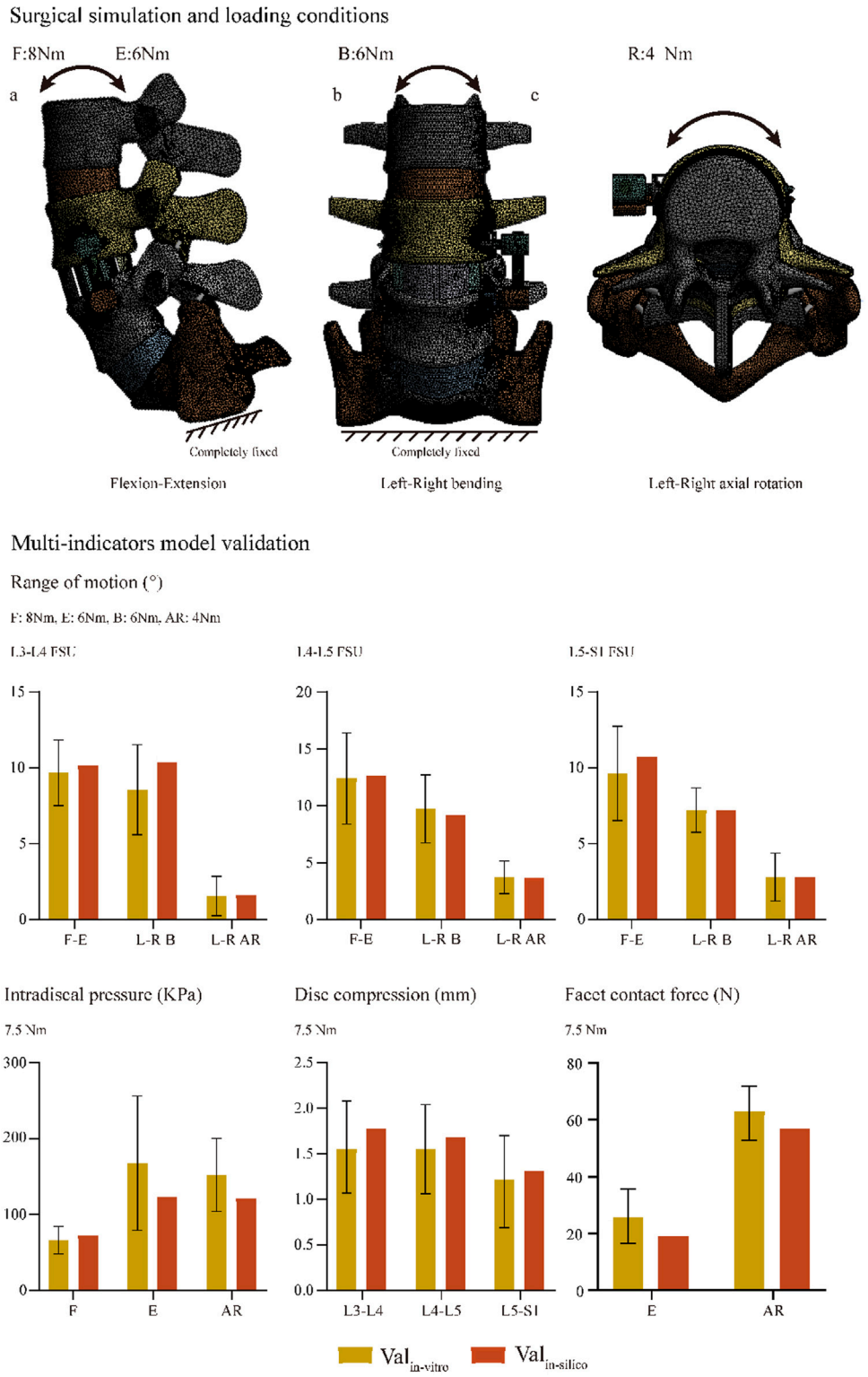

FIGURE 3 | Surgical simulations and multi-indicator model validations.

observation with numerical simulations compared with the same type of published studies. In these studies, clinical phenomena and biomechanical effects have been investigated separately (Kim et al., 2012; Agarwal et al., 2013; Zhang et al., 2016; Hu et al., 2021). In contrast, the current study constructs operative models to explore the biomechanical effects of clinically independent risk

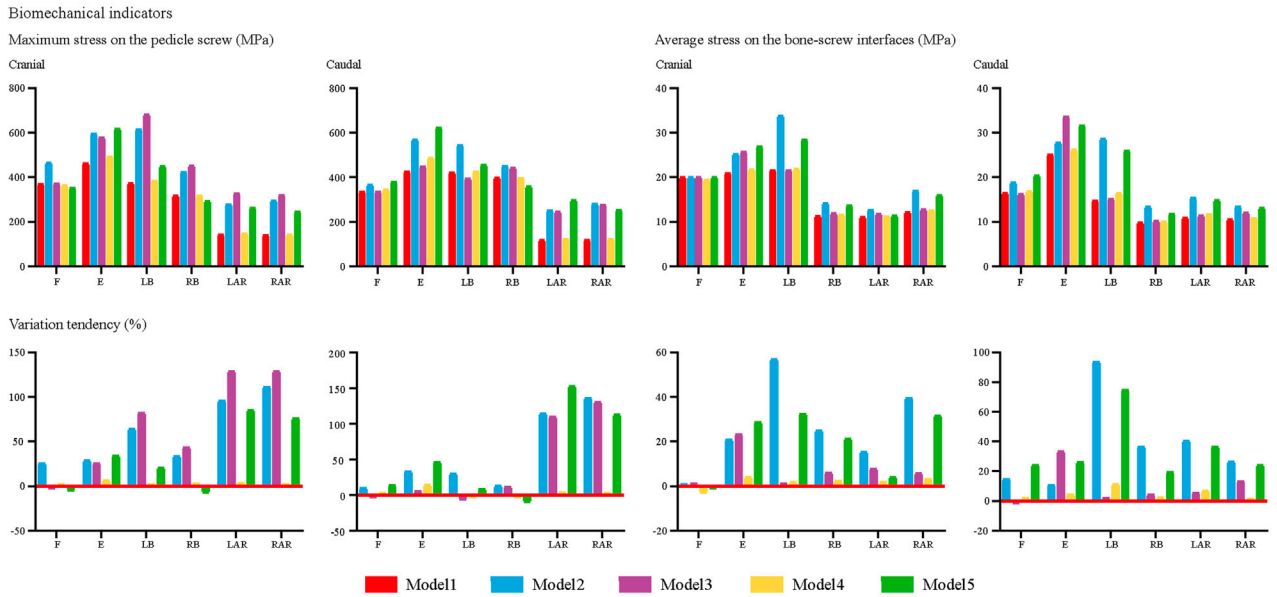

FIGURE 4 | Changes in biomechanical indicators.

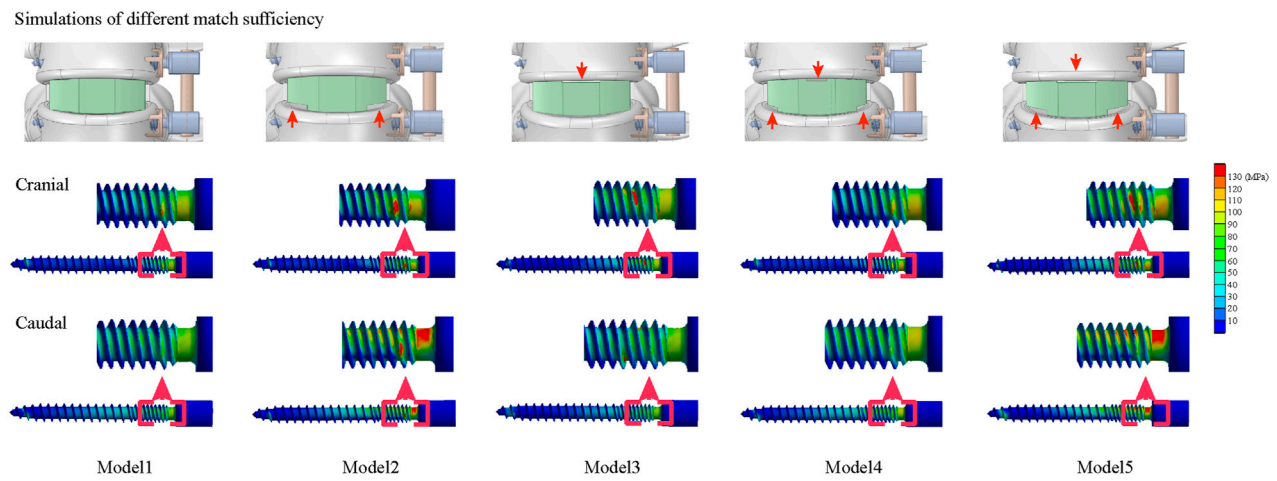

FIGURE 5 | Different match sufficiency and nephograms of screws.

factors. We believe that biomechanical parameters computed by these FE models could provide credible theoretical guidance for optimizing spinal instrumented devices (i.e., the OLIF cage).

Radiographic observations showed that reducing the GBOR in the coronal plane was also an independent risk factor for screw loosening in the cranial and caudal vertebral bodies. Biomechanical changes in screws and corresponding bone-screw interfaces in models with different match sufficiency have been computed in numerical surgical simulations (Ambati et al., 2015; Matsukawa et al., 2015; Fletcher et al., 2019; Kim et al., 2020). The effectiveness of these indicators in predicting the risk of screw loosening has been well demonstrated in previous biomechanical studies. Corresponding to the review of radiographic data, the poor match between BEP and GB increases the load transmitted by the ALSR system, and stress concentration on the bone-screw interfaces will lead to the microdamage of cancellous bone and resulting screw loosening. Therefore, the increase in match sufficiency by optimizing cage design should be significant for reducing screw loosening risk.

In vitro mechanical tests on fresh specimens, the "gold standard" of biomechanical studies, were not performed in this study for the following reasons. When using a particular type of OLIF cage, the contact sufficiency between the BEP and

GB mainly depends on the morphology parameters of the BEPs in different specimens. Considering that fresh specimens are very scarce and it is difficult to obtain sufficient specimens with different morphology parameters, it is unenforceable to perform the biomechanical test of this study by *in vitro* fresh specimen testing. Meanwhile, the mechanical effects of confounding factors (e.g., differences in BMD in different specimens) could not be excluded effectively in a small sample size study (Bredow et al., 2016; Bokov et al., 2019). In addition, the purpose of this study is to provide biomechanical references for the necessity of manufacturing OLIF cages that can match different BEP morphology parameters. Cage manufacturing is based on the results of mechanical tests, not the other way around. It is challenging to produce cages with different outlines to achieve different degrees of contact sufficiency with limited fresh specimens. Additionally, it is challenging to directly insert stress sensors into bone-screw interfaces. As a result, in fresh specimen mechanical tests, cancellous stress distribution can only be inferred by indirect measured indicators (e.g., displacement of the screw fixation system and deformation of vertebral bodies) (Nowak, 2019; Kanno et al., 2021).

In contrast, we believe FEA is more suitable for investigating the mechanical effects of contact sufficiency on the risk of screw loosening. In this study, surgical simulations were performed in a single intact model, and only the coronal plane's GBOR was adjusted in different FE models. This mechanical testing strategy can independently analyze the risk factor obtained from clinical observation, exclude the interference of other confounding factors, and obtain a more reliable conclusion (Dreischarf et al., 2014; Zhang and Gong, 2020). More significantly, details of the stress distribution on the bone-screw interfaces can be directly measured in FEA models (Xu et al., 2019; Takenaka et al., 2020). Without worrying about the difficulty of model sourcing, we can demonstrate the biomechanical effects of different match degrees between BEP and GB in the FEA study. By adjusting the cage outline to achieve different matching degrees, we can directly observe its biomechanical effects on the risk of screw loosening, which can provide a reliable reference for optimizing cage design.

Indeed, this study still has inherent limitations. Although screw loosening commonly occurred in the early stage (6 months) after spinal fixation, the variation tendency was evident at the 1-year clinical follow-up. As a radiographic review with limited sample sizes and a short follow-up period, we still should admit that the results of this study cannot be generalized to long-term clinical outcomes. In addition, in FEA, we did not identify the mechanical effects of the sagittal plane's GBOR. Although this factor is not an independent risk factor for screw loosening, it should be considered in our subsequent studies to evaluate the interaction of coronal and sagittal plane GBOR and their mechanical effects on the risk of screw loosening. Additionally, although this was the common method for the same type studies (Chuang et al., 2012; Kim et al., 2015; Hsieh et al., 2017; Kang et al., 2017; Li et al., 2021a), the multi-indicator model validation was only performed in the preoperative intact spine. The stress distribution of the ALSR system and bone-screw interfaces were computed in postoperative models without validation.

CONCLUSION

Based on the radiographic review and numerical surgical simulations, we can conclude that the mismatch between the BEP and GB will lead to stress concentration on the ALSR and bone-screw interfaces and increase the resulting risk of screw loosening. Cage design modification is of great significance for reducing screw loosening risk biomechanically.

DATA AVAILABILITY STATEMENT

The original contributions presented in the study are included in the article/Supplementary Material, further inquiries can be directed to the corresponding authors.

ETHICS STATEMENT

The studies involving human participants were reviewed and approved by Approval for the current study protocol was obtained from the ethics committees of West China Hospital (2020-554). Written informed consent for participation was not required for this study in accordance with the national legislation and the institutional requirements.

AUTHOR CONTRIBUTIONS

Conception and design: Y-MS, J-CZ, and J-CL; Acquisition of data: T-HX and J-CL. Analysis and interpretation of imaging data: J-CL, T-HX, Z-TS and ZZ; Statistical analysis: T-HX and ZZ, Manuscript modification: Y-MS, and J-CZ.

FUNDING

This work was supported by the Sichuan Science and Technology Major Program (No. 15 2018SZDZX0013-3).

ACKNOWLEDGMENTS

We acknowledge Xiao-Yu Zhang for the guidance of the figure preparation.

REFERENCES

Agarwal, A., Palepu, V., Agarwal, A. K., Goel, V. K., and Yildirim, E. D. (2013). Biomechanical Evaluation of an Endplate-Conformed Polycaprolactone-Hydroxyapatite Intervertebral Fusion Graft and its Comparison with a Typical Nonconformed Cortical Graft. *J. Biomech. Eng.* 135 (6), 61005–61009. doi:10.1115/1.4023988

Amaritsakul, Y., Chao, C.-K., and Lin, J. (2014). Biomechanical Evaluation of Bending Strength of Spinal Pedicle Screws, Including Cylindrical, Conical, Dual Core and Double Dual Core Designs Using Numerical Simulations and Mechanical Tests. *Med. Eng. Phys.* 36 (9), 1218–1223. doi:10.1016/j.medengphy.2014.06.014

Ambati, D. V., Wright, E. K., Jr., Lehman, R. A., Jr., Kang, D. G., Wagner, S. C., and Dmitriev, A. E. (2015). Bilateral Pedicle Screw Fixation Provides superior Biomechanical Stability in Transforaminal Lumbar Interbody Fusion: a Finite Element Study. *Spine J.* 15 (8), 1812–1822. doi:10.1016/j.spinee.2014.06.015

Bagheri, S. R., Alimohammadi, E., Zamani Froushani, A., and Abdi, A. (2019). Adjacent Segment Disease after Posterior Lumbar Instrumentation Surgery for Degenerative Disease: Incidence and Risk Factors. *J. Orthop. Surg. (Hong Kong)* 27 (2), 2309499019842378. doi:10.1177/2309499019842378

Bokov, A., Bulkin, A., Aleynik, A., Kutlaeva, M., and Mlyavykh, S. (2019). Pedicle Screws Loosening in Patients with Degenerative Diseases of the Lumbar Spine: Potential Risk Factors and Relative Contribution. *Glob. Spine J.* 9 (1), 55–61. doi:10.1177/2192568218772302

Bredow, J., Boese, C. K., Werner, C. M. L., Siewe, J., Löhrer, L., Zarghooni, K., et al. (2016). Predictive Validity of Preoperative CT Scans and the Risk of Pedicle Screw Loosening in Spinal Surgery. *Arch. Orthop. Trauma Surg.* 136 (8), 1063–1067. doi:10.1007/s00402-016-2487-8

Chao, C.-K., Hsu, C.-C., Wang, J.-L., and Lin, J. (2008). Increasing Bending Strength and Pullout Strength in Conical Pedicle Screws: Biomechanical Tests and Finite Element Analyses. *J. Spinal Disord. Tech.* 21 (2), 130–138. doi:10.1097/bsd.0b013e318073cc4b

Chuang, W.-H., Kuo, Y.-J., Lin, S.-C., Wang, C.-W., Chen, S.-H., Chen, Y.-J., et al. (2013). Comparison Among Load-, ROM-, and Displacement-Controlled Methods Used in the Lumbosacral Nonlinear Finite-Element Analysis. *Spine* 38 (5), E276–E285. doi:10.1097/brs.0b013e31828251f9

Chuang, W.-H., Lin, S.-C., Chen, S.-H., Wang, C.-W., Tsai, W.-C., Chen, Y.-J., et al. (2012). Biomechanical Effects of Disc Degeneration and Hybrid Fixation on the Transition and Adjacent Lumbar Segments. *Spine* 37 (24), E1488–E1497. doi:10.1097/brs.0b013e31826cdd93

Delucca, J. F., Cortes, D. H., Jacobs, N. T., Vresilovic, E. J., Duncan, R. L., and Elliott, D. M. (2016). Human Cartilage Endplate Permeability Varies with Degeneration and Intervertebral Disc Site. *J. Biomech.* 49 (4), 550–557. doi:10.1016/j.jbiomech.2016.01.007

Dreischarf, M., Zander, T., Shirazi-Adl, A., Puttlitz, C. M., Adam, C. J., Chen, C. S., et al. (2014). Comparison of Eight Published Static Finite Element Models of the Intact Lumbar Spine: Predictive Power of Models Improves when Combined Together. *J. Biomech.* 47 (8), 1757–1766. doi:10.1016/j.jbiomech.2014.04.002

Du, C.-F., Yang, N., Guo, J.-C., Huang, Y.-P., and Zhang, C. (2016). Biomechanical Response of Lumbar Facet Joints under Follower Preload: a Finite Element Study. *BMC Musculoskelet. Disord.* 17, 126. doi:10.1186/s12891-016-0980-4

Fan, W., Guo, L.-X., and Zhang, M. (2021). Biomechanical Analysis of Lumbar Interbody Fusion Supplemented with Various Posterior Stabilization Systems. *Eur. Spine J.* 30 (8), 2342–2350. doi:10.1007/s00586-021-06856-7

Ferguson, S. J., and Steffen, T. (2003). Biomechanics of the Aging Spine. *Eur. Spine J.* 12 (Suppl. 2), S97–s103. doi:10.1007/s00586-003-0621-0

Fletcher, J. W. A., Windolf, M., Grünwald, L., Richards, R. G., Gueorguiev, B., and Varga, P. (2019). The Influence of Screw Length on Predicted Cut-Out Failures for Proximal Humeral Fracture Fixations Predicted by Finite Element Simulations. *Arch. Orthop. Trauma Surg.* 139 (8), 1069–1074. doi:10.1007/s00402-019-03175-x

Guo, H.-z., Tang, Y.-c., Guo, D.-q., Luo, P.-j., Li, Y.-x., Mo, G.-y., et al. (2020). Stability Evaluation of Oblique Lumbar Interbody Fusion Constructs with Various Fixation Options: A Finite Element Analysis Based on Three-Dimensional Scanning Models. *World Neurosurg.* 138, e530–e538. doi:10.1016/j.wneu.2020.02.180

Hsieh, Y.-Y., Chen, C.-H., Tsuang, F.-Y., Wu, L.-C., Lin, S.-C., and Chiang, C.-J. (2017). Removal of Fixation Construct Could Mitigate Adjacent Segment Stress after Lumbosacral Fusion: A Finite Element Analysis. *Clin. Biomech.* 43, 115–120. doi:10.1016/j.clinbiomech.2017.02.011

Hsu, C.-C., Chao, C.-K., Wang, J.-L., Hou, S.-M., Tsai, Y.-T., and Lin, J. (2005). Increase of Pullout Strength of Spinal Pedicle Screws with Conical Core: Biomechanical Tests and Finite Element Analyses. *J. Orthop. Res.* 23 (4), 788–794. doi:10.1016/j.orthres.2004.11.002

Hu, Z., He, D., Gao, J., Zeng, Z., Jiang, C., Ni, W., et al. (2021). The Influence of Endplate Morphology on Cage Subsidence in Patients with Stand-Alone Oblique Lateral Lumbar Interbody Fusion (OLIF). *Glob. Spine J*, 2192568221992098. doi:10.1177/2192568221992098

Jacobs, N. T., Cortes, D. H., Peloquin, J. M., Vresilovic, E. J., and Elliott, D. M. (2014). Validation and Application of an Intervertebral Disc Finite Element Model Utilizing Independently Constructed Tissue-Level Constitutive Formulations that Are Nonlinear, Anisotropic, and Time-dependent. *J. Biomech.* 47 (11), 2540–2546. doi:10.1016/j.jbiomech.2014.06.008

Kang, K.-T., Koh, Y.-G., Son, J., Yeom, J. S., Park, J.-H., and Kim, H.-J. (2017). Biomechanical Evaluation of Pedicle Screw Fixation System in Spinal Adjacent Levels Using Polyetheretherketone, Carbon-Fiber-Reinforced Polyetheretherketone, and Traditional Titanium as Rod Materials. *Composites B: Eng.* 130 (dec), 248–256. doi:10.1016/j.compositesb.2017.07.052

Kanno, H., Aizawa, T., Hashimoto, K., and Itoi, E. (2021). Novel Augmentation Technique of Percutaneous Pedicle Screw Fixation Using Hydroxyapatite Granules in the Osteoporotic Lumbar Spine: a Cadaveric Biomechanical Analysis. *Eur. Spine J.* 30 (1), 71–78. doi:10.1007/s00586-020-06451-2

Kim, H., Lee, W., Choi, S., Kholinne, E., Lee, E., Alzahrani, W. M., et al. (2020). Role of Additional Inferomedial Supporting Screws in Osteoporotic 3-Part Proximal Humerus Fracture: Finite Element Analysis. *Geriatr. Orthop. Surg. Rehabil.* 11, 2151459320956958. doi:10.1177/2151459320956958

Kim, H.-J., Chun, H.-J., Moon, S.-H., Kang, K.-T., Kim, H.-S., Park, J.-O., et al. (2010). Analysis of Biomechanical Changes after Removal of Instrumentation in Lumbar Arthrodesis by Finite Element Analysis. *Med. Biol. Eng. Comput.* 48 (7), 703–709. doi:10.1007/s11517-010-0621-2

Kim, H.-J., Kang, K.-T., Chun, H.-J., Lee, C.-K., Chang, B.-S., and Yeom, J. S. (2015). The Influence of Intrinsic Disc Degeneration of the Adjacent Segments on its Stress Distribution after One-Level Lumbar Fusion. *Eur. Spine J.* 24 (4), 827–837. doi:10.1007/s00586-014-3462-0

Kim, H. S., Song, J. S., Heo, W., Cha, J. H., and Rhee, D. Y. (2012). Comparative Study between a Curved and a Wedge PEEK Cage for Single-Level Anterior Cervical Discectomy and Interbody Fusion. *Korean J. Spine* 9 (3), 181–186. doi:10.14245/kjs.2012.9.3.181

Li, J., Xu, C., Zhang, X., Xi, Z., Liu, M., Fang, Z., et al. (2021a). TELD with Limited Foraminoplasty Has Potential Biomechanical Advantages over TELD with Large Annuloplasty: an In-Silico Study. *BMC Musculoskelet. Disord.* 22 (1), 616. doi:10.1186/s12891-021-04504-1

Li, J., Xu, C., Zhang, X., Xi, Z., Sun, S., Zhang, K., et al. (2021b). Disc Measurement and Nucleus Calibration in a Smoothened Lumbar Model Increases the Accuracy and Efficiency of In-Silico Study. *J. Orthop. Surg. Res.* 16 (1), 498. doi:10.1186/s13018-021-02655-4

Li, J., Zhang, X., Xu, W., Xi, Z., and Xie, L. (2019). Reducing the Extent of Facetectomy May Decrease Morbidity in Failed Back Surgery Syndrome. *BMC Musculoskelet. Disord.* 20 (1), 369. doi:10.1186/s12891-019-2751-5

Lu, T., and Lu, Y. (2019). Comparison of Biomechanical Performance Among Posterolateral Fusion and Transforaminal, Extreme, and Oblique Lumbar Interbody Fusion: A Finite Element Analysis. *World Neurosurg.* 129, e890–e899. doi:10.1016/j.wneu.2019.06.074

Matsukawa, K., Yato, Y., Imabayashi, H., Hosogane, N., Abe, Y., Asazuma, T., et al. (2016). Biomechanical Evaluation of Fixation Strength Among Different Sizes of Pedicle Screws Using the Cortical Bone Trajectory: what Is the Ideal Screw Size for Optimal Fixation? *Acta Neurochir* 158 (3), 465–471. doi:10.1007/s00701-016-2705-8

Matsukawa, K., Yato, Y., Imabayashi, H., Hosogane, N., Asazuma, T., and Nemoto, K. (2015). Biomechanical Evaluation of the Fixation Strength of Lumbar Pedicle

Screws Using Cortical Bone Trajectory: a Finite Element Study. *Spi* 23 (4), 471–478. doi:10.3171/2015.1.spine141103

Mi, J., Li, K., Zhao, X., Zhao, C.-Q., Li, H., and Zhao, J. (2017). Vertebral Body Hounsfield Units Are Associated with Cage Subsidence after Transforaminal Lumbar Interbody Fusion with Unilateral Pedicle Screw Fixation. *Clin. Spine Surg.* 30 (8), E1130–e1136. doi:10.1097/bsd.0000000000000490

Mikula, A. L., Puffer, R. C., Jeor, J. D. S., Bernatz, J. T., Fogelson, J. L., Larson, A. N., et al. (2019). Teriparatide Treatment Increases Hounsfield Units in the Lumbar Spine Out of Proportion to DEXA Changes. *J. Neurosurg. Spine*, 1–6. doi:10.3171/2019.7.SPINE19654

Morgan, E. F., Bayraktar, H. H., and Keaveny, T. M. (2003). Trabecular Bone Modulus-Density Relationships Depend on Anatomic Site. *J. Biomech.* 36 (7), 897–904. doi:10.1016/s0021-9290(03)00071-x

Nowak, B. (2019). Experimental Study on the Loosening of Pedicle Screws Implanted to Synthetic Bone Vertebra Models and under Non-pull-out Mechanical Loads. *J. Mech. Behav. Biomed. Mater.* 98, 200–204. doi:10.1016/j.jmbbm.2019.06.013

Oetgen, M. E., Yue, J. J., La Torre, J. J. J.-d., and Bertagnoli, R. (2008). Does Vertebral Endplate Morphology Influence Outcomes in Lumbar Total Disc Arthroplasty? Part II: Clinical and Radiographic Results as Evaluated Utilizing the Vertebral Endplate Yue-Bertagnoli (VEYBR) Classification. *Int. J. Spine Surg.* 2 (2), 101–106. doi:10.1016/sasj-2007-0119-rr

Ohtori, S., Inoue, G., Orita, S., Yamauchi, K., Eguchi, Y., Ochiai, N., et al. (2013). Comparison of Teriparatide and Bisphosphonate Treatment to Reduce Pedicle Screw Loosening after Lumbar Spinal Fusion Surgery in Postmenopausal Women with Osteoporosis from a Bone Quality Perspective. *Spine* 38 (8), E487–E492. doi:10.1097/brs.0b013e31828826dd

Ottardi, C., Galbusera, F., Luca, A., Prosdocimo, L., Sasso, M., Brayda-Bruno, M., et al. (2016). Finite Element Analysis of the Lumbar Destabilization Following Pedicle Subtraction Osteotomy. *Med. Eng. Phys.* 38 (5), 506–509. doi:10.1016/j.medengphy.2016.02.002

Park, S.-J., Lee, C.-S., Chung, S.-S., Kang, S.-S., Park, H.-J., and Kim, S.-H. (2017). The Ideal Cage Position for Achieving Both Indirect Neural Decompression and Segmental Angle Restoration in Lateral Lumbar Interbody Fusion (LLIF). *Clin. Spine Surg.* 30 (6), E784–e790. doi:10.1097/bsd.0000000000000406

Pearson, H. B., Dobbs, C. J., Grantham, E., Niebur, G. L., Chappuis, J. L., and Boerckel, J. D. (2017). Intraoperative Biomechanics of Lumbar Pedicle Screw Loosening Following Successful Arthrodesis. *J. Orthop. Res.* 35 (12), 2673–2681. doi:10.1002/jor.23575

Pickhardt, P. J., Pooler, B. D., Lauder, T., Del Rio, A. M., Bruce, R. J., and Binkley, N. (2013). Opportunistic Screening for Osteoporosis Using Abdominal Computed Tomography Scans Obtained for Other Indications. *Ann. Intern. Med.* 158 (8), 588–595. doi:10.7326/0003-4819-158-8-201304160-00003

Qasim, M., Natarajan, R. N., An, H. S., and Andersson, G. B. (2014). Damage Accumulation Location Under Cyclic Loading in the Lumbar Disc Shifts from Inner Annulus Lamellae to Peripheral Annulus with Increasing Disc Degeneration. *J. Biomech.* 47 (1), 24–31.

Rastegar, S., Arnoux, P.-J., Wang, X., and Aubin, C.-É. (2020). Biomechanical Analysis of Segmental Lumbar Lordosis and Risk of Cage Subsidence with Different Cage Heights and Alternative Placements in Transforaminal Lumbar Interbody Fusion. *Comput. Methods Biomech. Biomed. Eng.* 23 (9), 456–466. doi:10.1080/10255842.2020.1737027

Renner, S. M., Natarajan, R. N., Patwardhan, A. G., Havey, R. M., Voronov, L. I., Guo, B. Y., et al. (2007). Novel Model to Analyze the Effect of a Large Compressive Follower Pre-load on Range of Motions in a Lumbar Spine. *J. Biomech.* 40 (6), 1326–1332. doi:10.1016/j.jbiomech.2006.05.019

Schilling, C., Krüger, S., Grupp, T. M., Duda, G. N., Blömer, W., and Rohlmann, A. (2011). The Effect of Design Parameters of Dynamic Pedicle Screw Systems on Kinematics and Load Bearing: an *In Vitro* Study. *Eur. Spine J.* 20 (2), 297–307. doi:10.1007/s00586-010-1620-6

Schmidt, H., Heuer, F., Drumm, J., Klezl, Z., Claes, L., and Wilke, H.-J. (2007a). Application of a Calibration Method Provides More Realistic Results for a Finite Element Model of a Lumbar Spinal Segment. *Clin. Biomech.* 22 (4), 377–384. doi:10.1016/j.clinbiomech.2006.11.008

Schmidt, H., Kettler, A., Heuer, F., Simon, U., Claes, L., and Wilke, H.-J. (2007b). Intradiscal Pressure, Shear Strain, and Fiber Strain in the Intervertebral Disc under Combined Loading. *Spine* 32 (7), 748–755. doi:10.1097/01.brs.0000259059.90430.c2

Schreiber, J. J., Hughes, A. P., Taher, F., and Girardi, F. P. (2014). An Association Can Be Found between Hounsfield Units and success of Lumbar Spine Fusion. *HSS Jrnl* 10 (1), 25–29. doi:10.1007/s11420-013-9367-3

Takenaka, S., Kaito, T., Ishii, K., Watanabe, K., Watanabe, K., Shinohara, A., et al. (2020). Influence of Novel Design Alteration of Pedicle Screw on Pull-Out Strength: A Finite Element Study. *J. Orthopaedic Sci.* 25 (1), 66–72. doi:10.1016/j.jos.2019.03.002

Tsouknidas, A., Sarigiannidis, S. O., Anagnostidis, K., Michailidis, N., and Ahuja, S. (2015). Assessment of Stress Patterns on a Spinal Motion Segment in Healthy versus Osteoporotic Bony Models with or without Disc Degeneration: a Finite Element Analysis. *Spine J.* 15 (3 Suppl. l), S17–s22. doi:10.1016/j.spinee.2014.12.148

Tsuang, F.-Y., Chen, C.-H., Wu, L.-C., Kuo, Y.-J., Lin, S.-C., and Chiang, C.-J. (2016). Biomechanical Arrangement of Threaded and Unthreaded Portions Providing Holding Power of Transpedicular Screw Fixation. *Clin. Biomech.* 39, 71–76. doi:10.1016/j.clinbiomech.2016.09.010

Ushirozako, H., Hasegawa, T., Ebata, S., Ohba, T., Oba, H., Mukaiyama, K., et al. (2020). Impact of Sufficient Contact between the Autograft and Endplate Soon after Surgery to Prevent Nonunion at 12 Months Following Posterior Lumbar Interbody Fusion. *J. Neurosurg. Spine* 33, 796–805. doi:10.3171/2020.5.SPINE20360

Wang, B., Hua, W., Ke, W., Lu, S., Li, X., Zeng, X., et al. (2019). Biomechanical Evaluation of Transforaminal Lumbar Interbody Fusion and Oblique Lumbar Interbody Fusion on the Adjacent Segment: A Finite Element Analysis. *World Neurosurg.* 126, e819–e824. doi:10.1016/j.wneu.2019.02.164

Weidling, M., Oefner, C., Schoenfelder, S., and Heyde, C.-E. (2020). A Novel Parameter for the Prediction of Pedicle Screw Fixation in Cancellous Bone - A Biomechanical Study on Synthetic Foam. *Med. Eng. Phys.* 79, 44–51. doi:10.1016/j.medengphy.2020.03.001

Wilson, D. C., Niosi, C. A., Zhu, Q. A., Oxland, T. R., and Wilson, D. R. (2006). Accuracy and Repeatability of a New Method for Measuring Facet Loads in the Lumbar Spine. *J. Biomech.* 39 (2), 348–353. doi:10.1016/j.jbiomech.2004.12.011

Wu, H.-C., and Yao, R.-F. (1976). Mechanical Behavior of the Human Annulus Fibrosus. *J. Biomech.* 9 (1), 1–7. doi:10.1016/0021-9290(76)90132-9

Xi, Z., Mummaneni, P. V., Wang, M., Ruan, H., Burch, S., Deviren, V., et al. (2020). The Association between Lower Hounsfield Units on Computed Tomography and Cage Subsidence after Lateral Lumbar Interbody Fusion. *Neurosurg. Focus* 49 (2), E8. doi:10.3171/2020.5.focus20169

Xie, T., Wang, C., Yang, Z., Xiu, P., Yang, X., Wang, X., et al. (2020). Minimally Invasive Oblique Lateral Lumbar Interbody Fusion Combined with Anterolateral Screw Fixation for Lumbar Degenerative Disc Disease. *World Neurosurg.* 135, e671–e678. doi:10.1016/j.wneu.2019.12.105

Xu, M., Yang, J., Lieberman, I. H., and Haddas, R. (2019). Finite Element Method-Based Study of Pedicle Screw-Bone Connection in Pullout Test and Physiological Spinal Loads. *Med. Eng. Phys.* 67, 11–21. doi:10.1016/j.medengphy.2019.03.004

Yue, J. J., Oetgen, M. E., Jaramillo-de la Torre, J. J., and Bertagnoli, R. (2008). Does Vertebral Endplate Morphology Influence Outcomes in Lumbar Disc Arthroplasty? Part I: an Initial Assessment of a Novel Classification System of Lumbar Endplate Morphology. *SAS J.* 2 (1), 16–22. doi:10.1016/s1935-9810(08)70013-6

Zhang, F., Xu, H.-c., Yin, B., Xia, X.-l., Ma, X.-s., Wang, H.-l., et al. (2016). Can an Endplate-Conformed Cervical Cage Provide a Better Biomechanical Environment Than a Typical Non-conformed Cage? *Orthop. Surg.* 8 (3), 367–376. doi:10.1111/os.12261

Zhang, M., and Gong, H. (2020). Translation of Engineering to Medicine: A Focus on Finite Element Analysis. *J. Orthopaedic Translation* 20, 1–2. doi:10.1016/j.jot.2019.12.001

Zhao, F.-D., Pollintine, P., Hole, B. D., Adams, M. A., and Dolan, P. (2009). Vertebral Fractures Usually Affect the Cranial Endplate Because it Is Thinner and Supported by Less-Dense Trabecular Bone. *Bone* 44 (2), 372–379. doi:10.1016/j.bone.2008.10.048

Zou, D., Li, W., Deng, C., Du, G., and Xu, N. (2019). The Use of CT Hounsfield Unit Values to Identify the Undiagnosed Spinal Osteoporosis in Patients with Lumbar Degenerative Diseases. *Eur. Spine J.* 28 (8), 1758–1766. doi:10.1007/s00586-018-5776-9

Zou, D., Sun, Z., Zhou, S., Zhong, W., and Li, W. (2020). Hounsfield Units Value Is a Better Predictor of Pedicle Screw Loosening Than the T-Score of DXA in Patients with Lumbar Degenerative Diseases. *Eur. Spine J.* 29 (5), 1105–1111. doi:10.1007/s00586-020-06386-8

Conflict of Interest: The authors declare that the research was conducted in the absence of any commercial or financial relationships that could be construed as a potential conflict of interest.

Publisher's Note: All claims expressed in this article are solely those of the authors and do not necessarily represent those of their affiliated organizations, or those of the publisher, the editors and the reviewers. Any product that may be evaluated in this article, or claim that may be made by its manufacturer, is not guaranteed or endorsed by the publisher.

frontiers | Frontiers in Bioengineering and Biotechnology

ORIGINAL RESEARCH
published: 23 June 2022
doi: 10.3389/fbioe.2022.919721

Locking Plates With Computationally Enhanced Screw Trajectories Provide Superior Biomechanical Fixation Stability of Complex Proximal Humerus Fractures

Dominic Mischler[1†], *Jana Felicitas Schader*[1†], *Jan Dauwe*[1,2], *Lara Tenisch*[1], *Boyko Gueorguiev*[1], *Markus Windolf*[1] *and Peter Varga*[1*]

[1]AO Research Institute Davos, Davos, Switzerland, [2]Department of Trauma Surgery, UZ Leuven, Leuven, Belgium

OPEN ACCESS

Edited by:
Jonas Widmer,
Balgrist University Hospital,
Switzerland

Reviewed by:
Uriel Zapata,
EAFIT University, Colombia
Francesc Levrero Florencio,
Developer, United Kingdom

***Correspondence:**
Peter Varga
peter.varga@aofoundation.org

[†]These authors have contributed equally to this work and share first authorship

Specialty section:
This article was submitted to Biomechanics, a section of the journal Frontiers in Bioengineering and Biotechnology

Received: 13 April 2022
Accepted: 03 June 2022
Published: 23 June 2022

Citation:
Mischler D, Schader JF, Dauwe J, Tenisch L, Gueorguiev B, Windolf M and Varga P (2022) Locking Plates With Computationally Enhanced Screw Trajectories Provide Superior Biomechanical Fixation Stability of Complex Proximal Humerus Fractures. Front. Bioeng. Biotechnol. 10:919721. doi: 10.3389/fbioe.2022.919721

Joint-preserving surgical treatment of complex unstable proximal humerus fractures remains challenging, with high failure rates even following state-of-the-art locked plating. Enhancement of implants could help improve outcomes. By overcoming limitations of conventional biomechanical testing, finite element (FE) analysis enables design optimization but requires stringent validation. This study aimed to computationally enhance the design of an existing locking plate to provide superior fixation stability and evaluate the benefit experimentally in a matched-pair fashion. Further aims were the evaluation of instrumentation accuracy and its potential influence on the specimen-specific predictive ability of FE. Screw trajectories of an existing commercial plate were adjusted to reduce the predicted cyclic cut-out failure risk and define the enhanced (EH) implant design based on results of a previous parametric FE study using 19 left proximal humerus models (Set A). Superiority of EH versus the original (OG) design was tested using nine pairs of human proximal humeri (N = 18, Set B). Specimen-specific CT-based virtual preoperative planning defined osteotomies replicating a complex 3-part fracture and fixation with a locking plate using six screws. Bone specimens were prepared, osteotomized and instrumented according to the preoperative plan *via* a standardized procedure utilizing 3D-printed guides. Cut-out failure of OG and EH implant designs was compared in paired groups with both FE analysis and cyclic biomechanical testing. The computationally enhanced implant configuration achieved significantly more cycles to cut-out failure compared to the standard OG design ($p < 0.01$), confirming the significantly lower peri-implant bone strain predicted by FE for the EH versus OG groups ($p < 0.001$). The magnitude of instrumentation inaccuracies was small but had a significant effect on the predicted failure risk ($p < 0.01$). The sample-specific FE predictions strongly correlated with the experimental results (R^2 = 0.70) when incorporating instrumentation inaccuracies. These findings demonstrate the power and validity of FE simulations in improving implant designs towards superior fixation stability of proximal humerus fractures. Computational optimization could be performed involving further implant features and

help decrease failure rates. The results underline the importance of accurate surgical execution of implant fixations and the need for high consistency in validation studies.

Keywords: bone fracture (MeSH ID: D050723), osteosynthesis, implant optimization, 3D-printing, finite element analysis, fixation failure

1 INTRODUCTION

Standardized fracture fixation implants provide good outcomes for most trauma applications. However, there are still problematic sites for osteosynthesis such as the proximal humerus. Besides intramedullary nailing, locking plate fixation has become one of the most commonly used joint-preserving surgical treatment options (Sudkamp et al., 2009). Nevertheless, even with state-of-the-art locked plating of proximal humerus fractures, the rate of mechanical fixation failures has been reported to range between 15% and 35% (Krappinger et al., 2011; Kralinger et al., 2014; Hengg et al., 2019; Panagiotopoulou et al., 2019), or even higher in the most endangered patient group of elderly osteoporotic women with complex and unstable fractures (Krappinger et al., 2011). The already high incidence is expected to further increase due to the aging population and prevalence of osteoporosis (Bahrs et al., 2014). Moreover, targeted studies reported no clear advantage of locked plating versus conservative treatment in terms of reoperation rate or functional outcomes (Olerud et al., 2011; Fjalestad et al., 2012; Rangan et al., 2015; Handoll et al., 2017). The potential reasons for mechanical fixation failures are manifold and include aspects related to the patient, complexity of the fracture, surgical execution, and the currently available implant designs that may not provide optimal fixation stability.

Conventional *in vitro* testing is the current gold standard method to evaluate biomechanical competence of implant fixations (Jabran et al., 2018), however, it is limited to the investigation of selected aspects, ideally in a paired study design, and therefore not well suited for analysis of complex multifactorial problems. Computational modeling enables rapid feedback on the implant stability under a wide variety of complicated conditions and can be used to investigate the effect of selected aspects in a systematic and efficient manner (Lewis et al., 2021). We have developed and validated a finite element (FE) simulation tool kit to analyze the virtual biomechanical behavior of locking plate fixations of proximal humerus fractures (Varga et al., 2017; Varga et al., 2018b). This "virtual testing machine" has been used to explore various aspects of locking plate fixations including the effects of configuration (Fletcher et al., 2019c), length (Fletcher et al., 2019a) and augmentation (Varga et al., 2020) of the locking screws, as well as positioning (Fletcher et al., 2019b) and type (Mischler et al., 2020a) of the plate. Beyond the analysis of existing implants, FE simulations can be utilized to explore the possibility of improving fixation stability by adapting design features. In recent *in silico* studies, the predicted cut-out failure risk could be significantly reduced by optimizing the screw trajectories of a fixed-angle locking plate (Mischler et al., 2020b) and further benefits were observed using patient-specific implants (Schader et al., 2021). The underlying FE analysis methodology was validated to predict experimental cyclic cut-out failure of locked plating of unstable three-part proximal humerus fractures (R^2 = 0.90, N = 19) (Varga et al., 2017). However, the validation has been performed for a given implant design and configuration only, and it has not been demonstrated whether the design improvements suggested by the simulations would indeed result in superior biomechanical outcomes, or whether this would be outside the validity scope. Further, it was unclear how accurately the planned configuration could be implemented experimentally and how potential instrumentation inaccuracies would affect the outcomes.

Therefore, the primary aim of this study was to evaluate the biomechanical benefit of a locking plate with computationally enhanced screw trajectories versus the standard implant design in a paired human cadaveric study. The second aim was to evaluate instrumentation accuracy and its potential influence on the FE predictions. The third aim was to quantify the specimen-specific predictive ability of FE simulations of both the planned and instrumented states.

2 MATERIALS AND METHODS

This study used a coupled computational and experimental approach, where FE simulations informed about how to

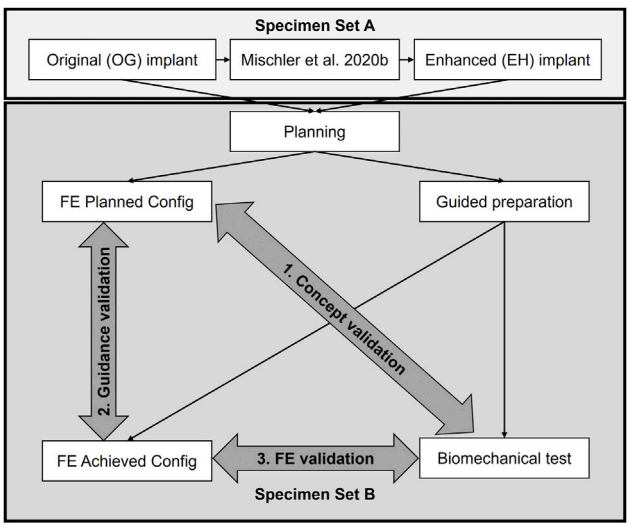

FIGURE 1 | Study overview. A computationally enhanced (EH) screw trajectory configuration was defined based on the results of a previous finite element (FE) analysis study (Set A) and compared with the original (OG) design *via* biomechanical testing on human cadaveric humerus specimens (Set B) to validate the concept of in silico design improvement (aim 1). The accuracies of the guided instrumentation (aim 2) and the specimen specific FE predictions (aim 3) were also validated based on the data of Set B.

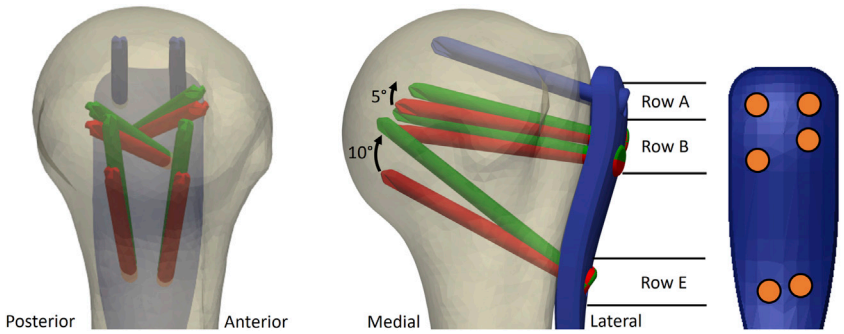

FIGURE 2 | Illustration of the original (OG, red) and the enhanced (EH, green) screw trajectories used for the experimental validation study. The most proximal screw row (blue) was the same for both OG and EH designs. Screws of row E were rotated proximally by 10° and screws of row B by 5°, respectively, compared to the OG configuration. Note that the intact bone is used only for illustration; the fixation was optimized in virtual fracture models. The screw distribution on the plate is illustrated with orange circles.

enhance the implant configuration, and the biomechanical tests evaluated whether the updated implant was superior to its original design, in line with the primary aim (**Figure 1**). Finally, FE models of the experimentally achieved constructs were created to determine the effect of potential instrumentation inaccuracies (second aim) and the specimen-specific predictive power (third aim). This was achieved in five steps (**Figure 1**): 1) the trajectories of the locking screws were varied compared to the original (OG) implant design of the PHILOS plate (DePuy Synthes, Zuchwil, Switzerland) in a previous parametric FE simulation study on 19 digital proximal humerus specimens (Set A) and used to define the enhanced (EH) configuration by reducing the predicted failure risk; 2) 18 paired bone specimens with high intra-donor symmetry (Set B) were osteotomized and fixed with 3D-printed metal plates featuring the OG or the EH screw trajectory designs based on preoperative planning, assisted by subject-specific 3D-printed guides; 3) the cyclic cut-out failure of the OG and EH fixations were assessed *via* biomechanical testing and compared between the groups; 4) instrumentation accuracy was evaluated by comparing the planned and experimentally achieved configurations; 5) FE simulations of both planned (FE-Planned) and experimentally achieved (FE-Achieved) configurations were performed and compared with the experimental results *via* correlation analysis.

2.1 Finite Element-Based Definition of the Enhanced Implant Configuration

The screw orientations of the EH implant design were defined based on the results of a previous parametric FE study (Mischler et al., 2020b). In short, FE models of nineteen low-density left proximal humerus specimens (Set A) of nine female and ten male elderly donors (mean ± standard deviation (SD) age: 83 ± 9 years) were created using a computational osteosynthesis tool (Varga et al., 2018b) to simulate an unstable three-part fracture AO/OTA 11-B3.2 instrumented with the PHILOS plate using six proximal locking screws occupying rows A, B and E (**Figure 2**). In a parametric analysis, the trajectories of these screws were individually varied in a grid-like pattern in both anterior-posterior and superior-inferior directions with 5° increments. Three physiologically relevant loading modes were applied. The average compressive principle strain in the cylindrical bone regions around the screws—a validated predictor for cyclic cut-out failure risk (Varga et al., 2017)—was evaluated for each new screw orientation configuration, compared to the OG design taken as baseline and finally averaged for all 19 samples.

These results were used in the current study to identify the combination of screw trajectories of the EH configuration that provided the largest overall observed decrease in the predicted cut-out risk compared with OG configuration while considering potential spatial restrictions of small humeral head sizes and anterior-posterior symmetry. The symmetry aspect was required for application of the same plate design to both left and right bones. Accordingly, compared with OG, the EH implant design was defined by proximally shifting the tips of screws in rows B and E by 5° and 10°, respectively, while keeping row A unchanged (**Figure 2**).

2.2 Specimen Selection for Set B

Human cadaveric humeri with low bone mineral density (BMD) and high pair symmetry (Set B) were identified from a larger pool in order to minimize the confounding effect of intra-donor differences. All donors gave their informed consent inherent within the donation of the anatomical gift statement during their lifetime. All experiments were carried out under the relevant guidelines and regulations. Additionally, internal review boards at Science Care (Phoenix, AZ, United States) and AO Research Institute Davos (Davos, Switzerland) approved the project. Thirty fresh-frozen (−20°C) humeral pairs from elderly donors were scanned using computed tomography (CT, GE Revolution, GE Healthcare, United States) with scanning settings of 120 kV voltage, 200 mA current and 0.625 mm slice thickness. The Hounsfield unit values of the CT image voxels were converted to BMD using a density calibration phantom (QRM-BDC/6, QRM GmbH, Moehrendorf, Germany). Humeri with high BMD (> 130 mgHA/cm^3) were excluded from the study. Radius and BMD

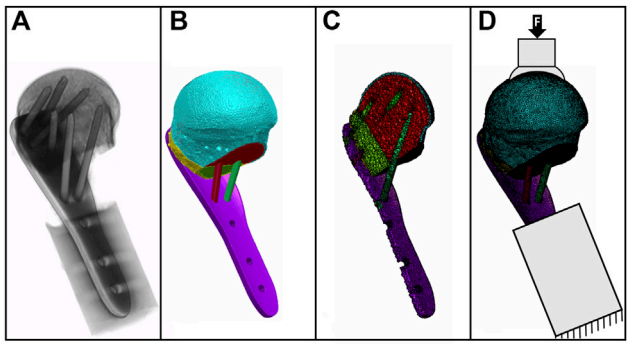

FIGURE 3 | Gray value image of a postoperative CT scan **(A)** with the underlying mask of bone fragments and implants **(B)**; the cross-sectional view of the FE mesh **(C)** and the specimen-specific FE model with boundary conditions are illustrated as fixed at the distal part and with load applied on the bone surface **(D)**.

of the humeral head were evaluated using previously developed methods (Varga et al., 2018a). In order to avoid confounding intra-donor differences, pair symmetry was evaluated in terms of humeral head radius (difference < 3%) and BMD (difference < 10%). Additionally, the humeral heads were required to be large enough to accommodate the calcar screws (Row E, **Figure 2**) of the OG configuration. The corresponding evaluation was performed on anterior-posterior C-arm images of the intact bones using an in-house developed implant navigation system (Windolf and Richards, 2021). Nine pairs (donor age: 85.3 ± 5.2 years, range: 73–91 years) fulfilled all criteria and were selected and scanned *via* high-resolution peripheral computed tomography (HR-pQCT, XtremeCT, Scanco Medical AG, Brüttisellen, Switzerland) with 60 kVp voltage, 900 µA current and 82 µM isotropic voxel size.

2.3 Preoperative Planning and Finite Element Simulations

The osteotomies and implant fixations were planned for each specimen of Set B based on the HR-pQCT images using Amira software (v2019, Thermo Fisher Scientific, Hillsboro, OR, United States) to maximize consistency and pair symmetry, thereby decreasing the effect of potential confounding factors. The detailed description of the planning procedure can be found in the **Supplementary Material**.

Specimen-specific FE models were created based on the planned osteotomy and implantation settings (**Figure 3**) using an established workflow (Varga et al., 2018b). Using Simpleware M-2017.06 (Simpleware Ltd., Exeter, United Kingdom), the bone fragment domains taken from the virtually osteotomized HR-pQCT images were combined with the computer-aided design (CAD) models of the plate and screws. The cortical and trabecular bone regions were separated using a special fill algorithm using Medtool v3.8 (Dr. Pahr Ingenieurs e.U., Pfaffstätten, Austria) (Medtool, 2014). The models were meshed with linear tetrahedral elements of 0.3–1.0 mm edge length. All material properties were isotropic and linear elastic. The screws and the 3D-printed metal plate (see **Section 2.4**) were modelled as made of titanium (modulus of elasticity 105 GPa) and steel (modulus of elasticity 210 GPa), respectively (Synthes, 2009). The elastic properties of the bone elements were scaled from the HR-pQCT-based BMD values (Dragomir-Daescu et al., 2011). Plate-screw and screw-bone interfaces were modeled as bonded. The FE models were aligned, and the boundary conditions were set according to the loading case of the planned experimental setup (**section 2.6**). The embedded portion of the plate was fully constrained and a static vertical force of 100 N was applied in a distributed manner on the proximal part of the humeral head (**Figure 3**). The FE analyses were performed using Abaqus (v2019, Simulia, Dassault Systemes, Velizy-Villacoublay, France). Average peri-implant strain was evaluated in cylindrical regions of the trabecular bone around the screws with a diameter of 8 mm and a total length of 50 mm, starting 5 mm in front of the screw tips (Varga et al., 2017).

Both OG and the EH configurations were simulated for each specimen. The two specimens of each pair were then stratified in the two groups based on the FE simulation results to avoid potential grouping bias.

2.4 Implant Manufacturing

Eighteen proximal humerus locking plates were fabricated with powder-based additive manufacturing *via* direct metal laser sintering from steel (1.2709, powder size of 15–45 µM) using an M2 device (CONCEPT Laser GmbH, GE Additive, Lichtenfels, Germany) at BSF Bünter AG (Heerbrugg, Switzerland). Printing settings were laser power of 200 W, layer thickness of 30 µM and thermal treatment at 540°C for 8 h to remove residual stresses and increase yield strength and hardness. The shape of the plates mimicked the PHILOS design with an increased wall thickness of 4 mm to eliminate potential plate bending during biomechanical testing. The screw holes with conical threads for the 3.5 mm locking screws were subsequently tapped by CNC machining. Trajectories of the six proximal screws followed the OG and EH designs for all nine plates in each group.

2.5 Specimen Preparation and Instrumentation Using 3D-Printed Guides

Individualized guides were designed and manufactured to aid the experimental execution of the planned specimen preparation procedures, including osteotomies, fragment reduction, implant positioning, pilot hole drilling, screw insertion, alignment of embedding and mounting on the testing machine (**Figure 4**). The guides were designed using a custom-developed semi-automated workflow in Amira (Supplementary Material) and 3D-printed from polylactide (Ultimaker 3, Ultimaker B.V., Utrecht, Netherlands).

Prior to processing, the bones were thawed at room temperature and purged of soft tissue. The fit of the humerus and the plate into the guides was then tested (**Figures 4A–D**). The surgical neck was osteotomized first using a bandsaw with blade thickness of 0.4 mm (**Figure 4E**). The second plane on the guide was used to cut the lateral fragment with the greater tuberosity

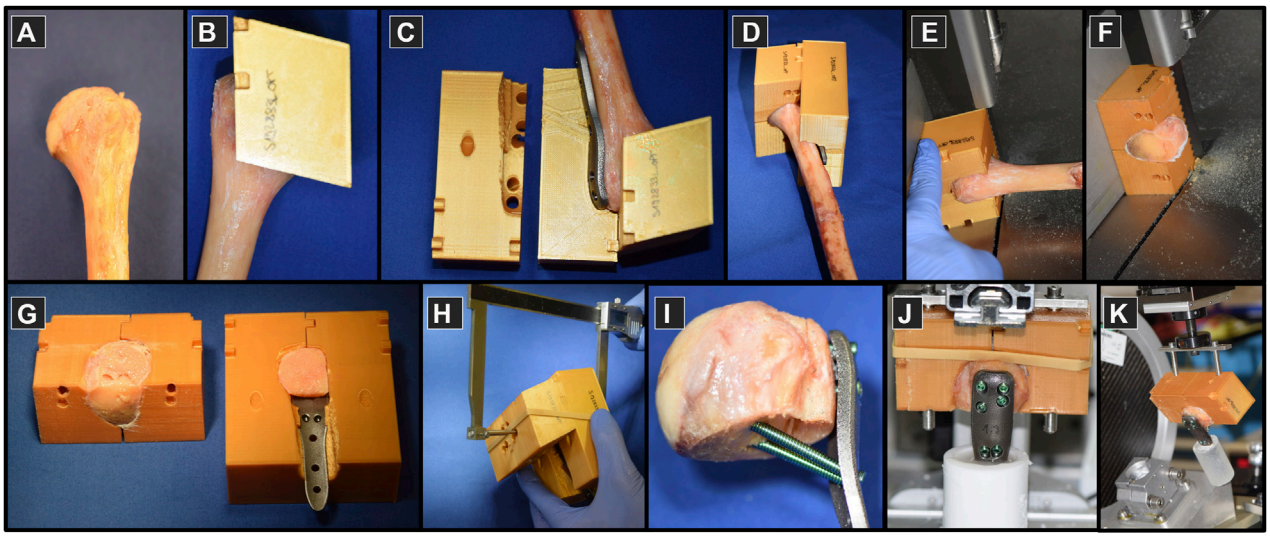

FIGURE 4 | Specimen preparation on proximal humeri **(A)** using custom 3D-printed plastic guides **(B–D)** used to assist the process of osteotomizing **(E,F)**, fragment reduction and implant positioning **(G)**, instrumentation **(H,I)**, embedding **(J)** and mounting to the experimental setup for biomechanical testing **(K)**.

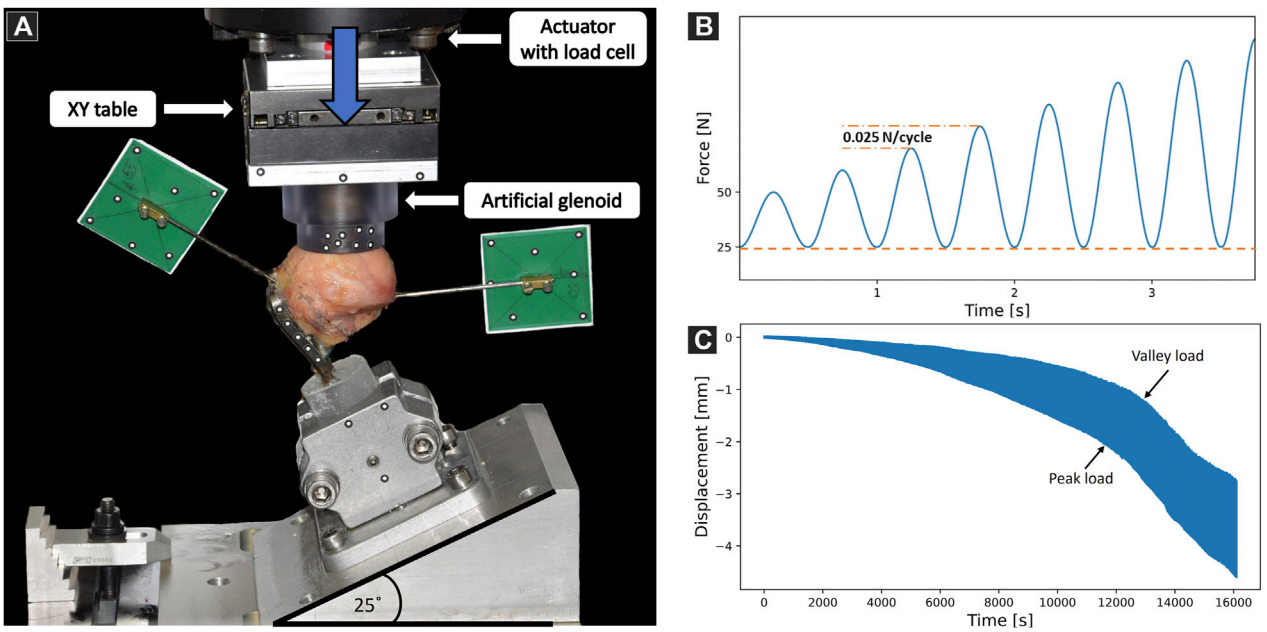

FIGURE 5 | (A) Biomechanical test setup with a specimen mounted on a metal wedge, inclined at 25° with respect to the machine base. Vertical arrow indicates loading direction. Motion tracking markers were attached to track the artificial glenoid, the plate, the mounting jig and the two bone fragments. **(B)** Biomechanical loading protocol consisting of sinusoidal curves with constant valley load (dashed line) and gradually increasing peak load (dashed-dotted line). **(C)** Exemplary results showing the evolution of humeral head center displacement along the anatomical shaft axis over time.

from the main head fragment (**Figure 4F**). The bone fragments were reduced and the construct was assembled, including the 3D-printed plate (**Figure 4G**). For each screw, the required drill depth and screw length were controlled using a custom caliper to provide approximately 6 mm tip-to-joint distance, considering the 2 mm increments of the commercial screws (**Figure 4H**). The pilot holes were drilled using the standard drill sleeves of the PHILOS instrument set. The fixation was instrumented by occupying all six holes of rows A, B and E with 3.5 mm titanium locking screws (DePuy Synthes, Zuchwil, Switzerland) (**Figure 4I**) using standard screw sleeves aligned by the guiding block holes. The distal part of the plates was embedded direct

distally to the calcar screws in Polymethylmethacrylate (PMMA, SCS-Beracryl, Suter-Kunststoffe AG, Fraubrunnen, Switzerland) with the guide utilized to align the construct along the humerus anatomical shaft axis (**Figure 4J**). In the final step, the guide ensured correct alignment of the specimen with respect to the loading axis of the biomechanical test setup while mounting it to the machine base (**Figure 4K**). Each specimen was CT-scanned after plating (post-operative scan) using the same device and settings as described above. Using these CT images, the deviation of the achieved instrumentation compared to the planned configuration was evaluated in terms of screw angles and tip-to-joint distances (**Supplementary Material**).

2.6 Biomechanical Testing

The setup for biomechanical testing was designed to provide a physiologically relevant loading mode of the proximal humerus and to ensure reproducibility according to the FE models. The bone-implant constructs were mounted to the machine base in a lateral angulation of 25° to replicate a physiologically relevant loading regime (Bergmann et al., 2011). To alleviate shear forces acting on the humeral head, a horizontal sliding table was attached to the machine actuator, allowing the artificial glenoid cup to continuously center itself on the humeral head during mechanical testing (**Figure 5A**). The specimens were cyclically tested to failure using an electrodynamic material testing machine (Acumen, MTS, Eden Prairie, MN, United States). The test protocol consisted of a sinusoidal loading curve with a constant valley load of 25 N and a gradually increasing peak load at a rate of 0.025 N/cycle, starting at 50 N (**Figure 5B**). The test was stopped at 6 mm actuator displacement. Stereographic motion tracking was used to measure the translational and rotational degrees of freedom of each component of both the setup and fixation construct using Aramis SRX camera system (GOM GmbH, Braunschweig, Germany). The head center was determined by fitting a sphere through digitized points on the head surface assessed with a touch probe device. The main parameter of interest was the displacement of the humeral head center along the humeral shaft axis relative to the plate (**Figure 5C**). Cut-out failure was defined as residual head fragment displacement at valley load; various failure threshold levels were evaluated, ranging from 0.25 mm to 1.5 mm with steps of 0.25 mm. The primary outcome measure of the experimental biomechanical testing was the number of cycles to cut-out failure.

2.7 Finite Element Modeling of the Experimentally Achieved Constructs

Subject-specific FE models of the plated specimens were created based on the postoperative CT scans to consider the experimentally achieved osteotomies, fracture reduction, implant positioning, screw orientation and embedding. The domain and position of the bone fragments were evaluated on the postoperative CT image in Amira. To avoid the effect of metal artefacts—present in the postoperative CT scan—on the BMD-based material properties, the image regions of the bone fragments were replaced by the spatially co-registered HR-pQCT image of the intact humerus. The experimentally achieved positioning of the plate and screws was replicated based on the postoperative scan by registering the CAD surfaces of the implants. The PMMA embedding of the distal part of the plate, determining specimen alignment and boundary conditions of the experimental test setup, was analyzed by fitting a cylinder to the embedding region in the postoperative scan. The FE-Achieved models of each specimen were then created and peri-implant strain was evaluated using the same simulation methodology as described in **section 2.3**.

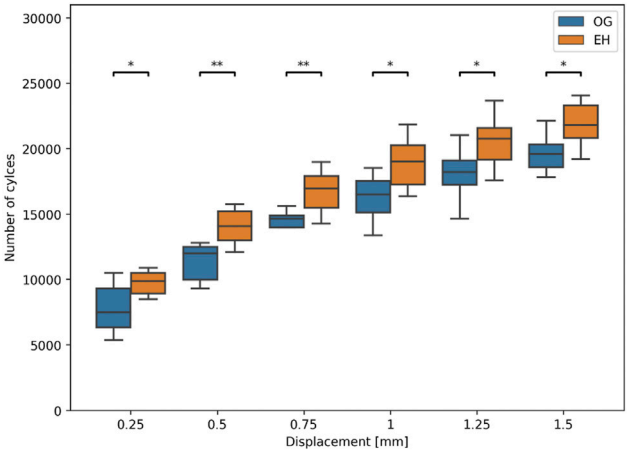

FIGURE 6 | Experimental number of cycles to cut-out failure at different levels of residual relative head fragment displacement with respect to the plate. Asterisks indicate significant differences between OG (blue) and EH (orange) implant designs. (*: $p \leq 0.05$; **: $p \leq 0.01$).

2.8 Statistical Analysis

Standard statistical methods were used for general data analysis using the SciPy package (Virtanen et al., 2020) in Python programming language (v3.7.4, Python Software Foundation, https://www.python.org/). Normality of data distribution was checked with Shapiro-Wilk test. Biomechanical stability was assessed by the number of cycles to cut-out failure and compared between the OG and EH groups by means of paired two-sided t-test or two-sided Wilcoxon Signed-Rank test in case of normally or non-normally distributed data, respectively. Linear regression analysis was performed and Pearson's correlation coefficient was computed to evaluate the strength of the relationship between the experimental number of cycles to failure and the peri-implant strain. Level of significance was set to 0.05 for all statistical tests.

3 RESULTS

3.1 Specimen Characteristics in the Study Groups

No significant differences were observed between the two groups of Set B in terms of BMD (OG mean ± SD: 112.0 ± 15.5 mgHA/cm^3, EH mean ± SD: 112.2 ± 13.7 mgHA/cm^3, $p > 0.94$, $N = 9$

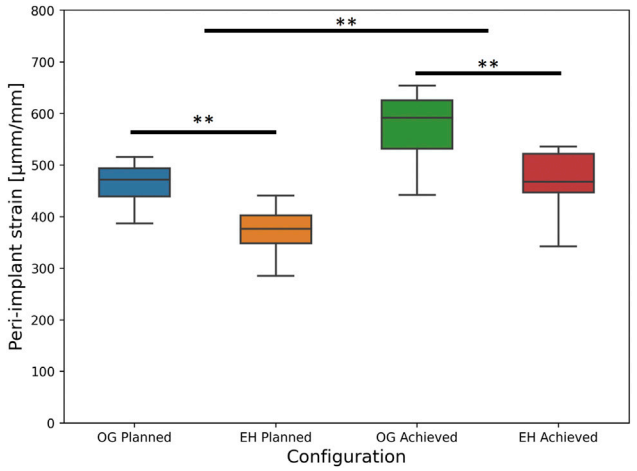

FIGURE 7 | FE-based peri-implant bone strain results, i.e., predicted risk of cut-out failure, for the planned (left) and achieved (right) model types, with the latter exhibiting significantly higher values versus the former; significant differences between the OG and EH screw configurations are demonstrated within each separate (planned or achieved) model type (**: $p \leq 0.01$).

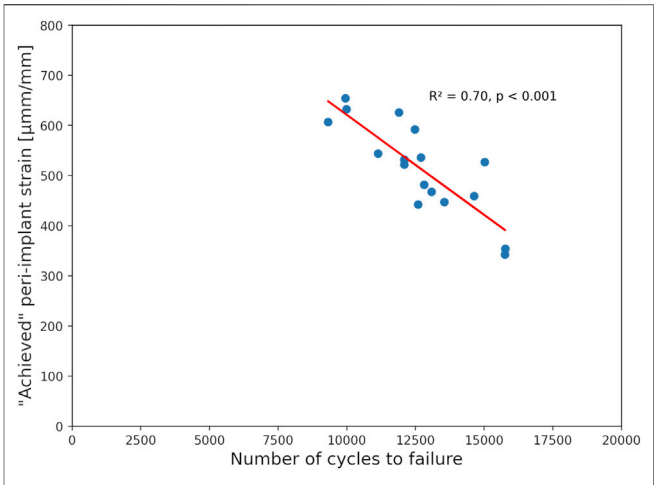

FIGURE 8 | Correlation of the experimental number of cycles until 0.5 mm cut-out failure and the peri-implant strain of the achieved FE models showing good prediction accuracy with high significance.

pairs) or head radius (OG: median: 21.5 mm, range: 20.6–23.7 mm; EH: median: 21.5 mm, range: 20.6–23.5 mm; $p = 0.07$, $N = 9$ pairs).

3.2 Concept Validation: Comparison Between Original and Enhanced

FE results of the FE-Planned configurations demonstrated that average peri-screw bone strain was significantly lower for the EH (mean ± SD: 367 ± 52 µmm/mm, range: 285–441 µmm/mm) versus the OG (mean ± SD: 460 ± 44 µmm/mm, range: 387–515 µmm/mm) implant designs, $p < 0.001$, $N = 9$ pairs.

During biomechanical testing, one pair was excluded due to issues with motion tracking data acquisition. Significantly higher cycles to failure were observed in the EH versus OG group for all levels of residual head fragment displacement, with the strongest significance being at 0.5 mm threshold (OG: mean ± SD: 11′368 ± 1′313 cycles, range: 9′320–12′814 cycles; EH: mean ± SD: 14′080 ± 1′414 cycles, range: 12′097–15′773 cycles), $p = 0.01$, $N = 8$ pairs (**Figure 6**).

3.3 Guidance Validation: Comparison Between Planned and Achieved Configurations

The deviation of the experimentally achieved screw trajectories compared with the planned state was 0.3 ± 1.3° (mean ± SD; range: −2.5–3.9°) in the proximal-distal direction and −1.7 ± 1.8° (range: −5.5–4.7°) in anterior-posterior directions. tip-to-joint distance deviations were −0.3 ± 1.1 mm (range: −3.1–2.2 mm). Detailed results are provided in the **Supplementary Material**. However, when replicating the instrumented state of the specimens with the FE simulations, significantly higher peri-screw bone strains were found for the FE-Achieved (mean ± SD: 514 ± 89 µmm/mm, range: 343–654 µmm/mm) compared with the FE-Planned analyses (mean ± SD: 414 ± 67 µmm/mm, range: 285–516 µmm/mm), $p < 0.01$, $N = 18$ specimens.

Nevertheless, the imperfections appeared to have similar influence on both groups and did not affect the statistical findings regarding the difference between the plate designs. In line with the FE-Planned simulations, the FE-Achieved models provided significantly lower peri-screw bone strains for the EH implant group (mean ± SD: 461 ± 71 µmm/mm, range: 343–536 µmm/mm) compared with the OG group (mean ± SD: 568 ± 73 µmm/mm, range: 441–654 µmm/mm), $p = 0.01$, $N = 9$ pairs (**Figure 7**).

3.4 Finite Element Validation Against Biomechanical Results

No significant correlations were found between the experimental biomechanical results and the FE-Planned simulations. In turn, results of the FE-Achieved models demonstrated a good correlation with the number of cycles to cut-out failure, providing $R^2 = 0.70$ at the 0.5 mm failure threshold ($p < 0.001$, $N = 17$ specimens, **Figure 8**).

4 DISCUSSION

Conventional validation studies aim to demonstrate that the computer models can reproduce previously observed experimental results. The present study took the more challenging inverse route to investigate whether the design changes suggested by the simulations would lead to experimentally measurable improvements. Indeed, this work demonstrated the feasibility and validity of the *in silico* approach for implant improvement as the computationally enhanced locking plate design provided significant increase in

the biomechanically assessed number of cycles to cut-out failure versus the standard design in a complex unstable proximal humerus fracture model. This was in line with the significantly lower peri-implant bone strain observed for the EH versus OG design in the FE simulations.

Improving primary stability of proximal humerus fracture fixations is not straightforward. Although the failure of single screws is strongly determined by the density of the surrounding bone region (Hepp et al., 2003; Steiner et al., 2015; Panagiotopoulou et al., 2021), FE simulations can provide improved predictions of stability for screws (Panagiotopoulou et al., 2021) and especially for entire bone-implant constructs (Varga et al., 2018a). FE analyses can incorporate the complex effects related to implants fixed with several screws, such as the importance of screw spread (Fletcher et al., 2019c). These benefits render computational tools optimal for investigation of implant improvement options in parametric analyses. Previous studies by Jabran et al. and Mischler et al. proposed FE-based optimization of screw trajectories of proximal humerus locking plates; however, without any biomechanical corroboration using human cadaveric specimens (Jabran et al., 2019; Mischler et al., 2020b). The present work filled this gap by demonstrating that an FE analysis methodology previously developed and validated to predict cyclic failure of a given implant design (Varga et al., 2017) remains valid to indicate design changes towards improved primary stability. This underlines the power and potential of validated computational methods that could be utilized towards tackling the challenging problem of fracture fixation failures.

The major change in the enhanced design providing biomechanical benefit found here was the elevation of the screw tips, i.e., proximal rotation of the screw trajectories. This is in line with the previous *in silico* optimization studies (Jabran et al., 2019; Mischler et al., 2020b). The present work used the same implant design for left and right humeri, in analogy with the PHILOS plate. Accordingly, the changes in screw trajectories compared with the original design were kept symmetric. Side-specific implants may achieve higher benefits and subject-specific designs may further improve performance (Schader et al., 2021). These were not considered in this study due to logistical challenges. Some commercially available implants feature side-specific designs to achieve benefits in fit and purchase, however, would require double stock to be kept available at hospitals. Towards subject-specificity, some plates utilize variable-angle locking designs, but even for these, the screw orientations providing optimal fixation stability remain unknown. Several studies have investigated the biomechanical behavior of locking plates with polyaxial screw holes, allowing a screw angulation range of 30–40° (Erhardt et al., 2009; Ruchholtz et al., 2011; Voigt et al., 2011; Zettl et al., 2011; Erhardt et al., 2012). However, the orientation of the screws within the humeral head were chosen by the surgeon during instrumentation based on intuition and thus the highest stability was potentially not achieved. This might be the reason why no superiority to fixed-angle locking plates could be demonstrated to date (Ockert et al., 2010; Voigt et al., 2011; Katthagen et al., 2016). The freedom of versatile configurations provided by these implants may not ensure the best stability. The selection of the case-specific screw arrangement and orientation of these implants can be arbitrary; it may not be reliable, reproducible, and mechanically optimal. Methodologies such as the FE analysis presented in this study, once developed further to the level of clinical application and high automation, could help in subject-specific screw trajectory selection.

Although reaching significance, the relative gain of the adjusted implant configuration compared with the original design remained moderate, approximately 19%. Further research could utilize the validated FE workflow for more generic optimization broadened to other features of the implant design. In future, this computer simulation methodology could be transferred to *in vivo* applications, to evaluate subject-specific fracture stability preoperatively for various implant choices and configurations, and guide the surgeon about the best possible individualized treatment option for the given patient. Nevertheless, biomechanical studies always represent an idealized scenario, while the clinical reality is more complex. Generally, biomechanical studies use osteotomies and anatomically correct fracture reductions. In clinics, the fracture pattern is usually more complex, and the planned reduction may not always be achieved, thus altering the construct behavior and making *in silico* optimizations more challenging. Further clinical validation would be required to evaluate whether the enhanced implant design would ensure lower clinical failure rates.

Besides the implant design, the quality and surgical accuracy of execution is of high importance. The small inaccuracies of instrumentation revealed by the postoperative analysis indicated that the specimen-specific 3D-printed guides were efficient. However, even these relatively small imperfections had a considerable effect on stability, as revealed by the FE analysis of the achieved state, demonstrating a significantly higher predicted failure risk compared to the planned configuration. While the statistical finding of the FE-Planned and FE-Achieved analyses was the same concerning the superiority of the EH versus the OG design, the simulations revealed similar results for the OG-Planned and EH-Achieved groups, indicating that the benefit of trajectory improvement was comparable to the loss of experimental imperfections. These findings emphasize the relevance of intraoperative navigation and guidance that could help surgeons to accurately execute the preoperative plan (Windolf and Richards, 2021). Such technologies are expected to help lowering complication rates of proximal humerus fracture fixations.

Another implication of the instrumentation inaccuracies was the lack of correlation between the FE-Planned simulations and the biomechanical results. However, when incorporating the instrumentation inaccuracies in the models, the FE-Achieved simulations were able to predict the cycles of cut-out failure with a good accuracy ($R^2 = 0.70$), confirming the validity of the used modeling approach in predicting biomechanical cut-out failure risk. These findings demonstrate the importance of incorporating exact details, including imperfections of the

instrumentation, into FE modeling when attempting to predict results of biomechanical testing. This is particularly important for studies aiming at validation of computer simulations.

Several limitations should be considered in this study which extend beyond the general limitations of biomechanical human cadaveric studies. The bone density of the specimens may not have reflected the most endangered highly osteoporotic population, but the range was reasonable compared with previous biomechanical studies. The complex physiological loading conditions of the shoulder joint could not be replicated experimentally, but the used test setup incorporated the most important aspect, i.e., the direction of glenohumeral loads acting *in vivo* (Bergmann et al., 2007; Bergmann et al., 2011). Furthermore, the used loading mode was designed to ensure its replication in the boundary conditions of the FE simulations. Several simplifications were used in the FE model. The bone-screw interfaces were defined as fully bonded and the properties of all materials were isotropic and linear elastic. However, the same simplifications were used in the previous validation study that confirmed that the FE simulations could well predict experimental cyclic cut-out failure and found no improvements with more sophisticated bone-screw interface models (Varga et al., 2017). The validated outcome measure, i.e., bone strain around the screw tips, can be computed with linear elastic models and does not require more sophisticated description of the material behavior of bone. The used osteotomy model mimicked a single and idealized fracture pattern, but it represented a challenging complex unstable three-part fracture including a comminuted calcar region. The 3D-printed guides are not feasible in a clinical setting and only intended for biomechanical studies. Finally, the fixation failures observed in the clinics are often of multifactorial nature. The failure mechanism investigated in the present study was screw cut-out and thus the results may not be applicable to other failure modes such as screw perforation.

To conclude, this study demonstrated that computationally enhanced screw trajectories in locking plates could reach significantly higher number of cycles to cut-out failure compared to the original implant design during biomechanical testing of unstable proximal humerus fractures. These findings confirmed the validity of the FE-based improvement approach and reinforced the power of computational simulations. The presented computational approach could be extended to other features of the design and help decrease the rate of fixation failures with improved implants, although clinical validation would be required first. Instrumentation of the planned configurations was achieved with good accuracy using the custom guides, but even the slight imperfections had a significant effect on the predicted failure risk. This underlines the importance of accuracy in surgical execution and implant placement that can be a more dominant factor than the implant design, potentially absorbing the benefit of optimization, and may require intraoperative navigation to achieve optimal outcomes. The FE models could predict the specimen-specific biomechanical results only when replicating the experimentally achieved construct including the inaccuracies, indicating the need for reproducing exact details in validation studies.

DATA AVAILABILITY STATEMENT

The raw data supporting the conclusions of this article will be made available by the authors, without undue reservation.

ETHICS STATEMENT

Ethical review and approval was not required for the study on human participants in accordance with the local legislation and institutional requirements. The donors have provided their written informed consent within the donation of the anatomical gift statement during their lifetime.

AUTHOR CONTRIBUTIONS

DM, BG, MW, and PV designed the study. DM, JS, JD, and PV planned and conducted the experimental testing. DM, LT, and PV performed the computational modeling and analyzed the data. DM and PV drafted the manuscript. All authors discussed the results, reviewed and commented on the manuscript.

FUNDING

This study was performed with the assistance of the AO Foundation *via* the AOTRAUMA Network (Grant No.: AR2019/07).

SUPPLEMENTARY MATERIAL

The Supplementary Material for this article can be found online at: https://www.frontiersin.org/articles/10.3389/fbioe.2022.919721/full#supplementary-material

REFERENCE

Bahrs, C., Tanja, S., Gunnar, B., Stig, B., Badke, A., Ulrich, S., et al. (2014). Trends in Epidemiology and Patho-Anatomical Pattern of Proximal Humeral Fractures. *Int. Orthop.* 38 (8), 1697–1704. doi:10.1007/s00264-014-2362-6

Bergmann, G., Graichen, F., Bender, A., Kaab, M., Rohlmann, A., and Westerhoff, P. (2007). *In Vivo* glenohumeral Contact Forces--Measurements in the First Patient 7 Months Postoperatively. *J. Biomech.* 40 (10), 2139–2149. doi:10.1016/j.jbiomech.2006.10.037

Bergmann, G., Graichen, F., Bender, A., Rohlmann, A., Halder, A., Beier, A., et al. (2011). *In Vivo* gleno-humeral Joint Loads during Forward Flexion and Abduction. *J. Biomech.* 44 (8), 1543–1552. doi:10.1016/j.jbiomech.2011.02.142

Dragomir-Daescu, D., Op Den Buijs, J., McEligot, S., Dai, Y., Entwistle, R. C., Salas, C., et al. (2011). Robust QCT/FEA Models of Proximal Femur Stiffness and Fracture Load during a Sideways Fall on the Hip. *Ann. Biomed. Eng.* 39 (2), 742–755. doi:10.1007/s10439-010-0196-y

Erhardt, J. B., Roderer, G., Grob, K., Forster, T. N., Stoffel, K., and Kuster, M. S. (2009). Early Results in the Treatment of Proximal Humeral Fractures with a Polyaxial Locking Plate. *Arch. Orthop. Trauma Surg.* 129 (10), 1367–1374. doi:10.1007/s00402-009-0924-7

Erhardt, J. B., Stoffel, K., Kampshoff, J., Badur, N., Yates, P., and Kuster, M. S. (2012). The Position and Number of Screws Influence Screw Perforation of the Humeral Head in Modern Locking Plates: a Cadaver Study. *J. Orthop. Trauma* 26 (10), e188–192. doi:10.1097/BOT.0b013e31823db922

Fjalestad, T., Hole, M. O., Hovden, I. A., Blucher, J., and Stromsoe, K. (2012). Surgical Treatment with an Angular Stable Plate for Complex Displaced Proximal Humeral Fractures in Elderly Patients: a Randomized Controlled Trial. *J. Orthop. Trauma* 26 (2), 98–106. doi:10.1097/BOT.0b013e31821c2e15

Fletcher, J. W. A., Windolf, M., Grunwald, L., Richards, R. G., Gueorguiev, B., and Varga, P. (2019a). The Influence of Screw Length on Predicted Cut-Out Failures for Proximal Humeral Fracture Fixations Predicted by Finite Element Simulations. *Arch. Orthop. Trauma Surg.* 139, 1069–1074. doi:10.1007/s00402-019-03175-x

Fletcher, J. W. A., Windolf, M., Richards, R. G., Gueorguiev, B., Buschbaum, J., and Varga, P. (2019b). Importance of Locking Plate Positioning in Proximal Humeral Fractures as Predicted by Computer Simulations. *J. Orthop. Res.* 37 (4), 957–964. doi:10.1002/jor.24235

Fletcher, J. W. A., Windolf, M., Richards, R. G., Gueorguiev, B., and Varga, P. (2019c). Screw Configuration in Proximal Humerus Plating Has Significant Impact on Fixation Failure Risk Predicted by Finite Element Models. *J. Shoulder Elb. Surg.* 28 (9), 1816–1823. in press. doi:10.1016/j.jse.2019.02.013

Handoll, H. H., Keding, A., Corbacho, B., Brealey, S. D., Hewitt, C., and Rangan, A. (2017). Five-year Follow-Up Results of the PROFHER Trial Comparing Operative and Non-operative Treatment of Adults with a Displaced Fracture of the Proximal Humerus. *Bone Jt. J.* 99-B (3), 383–392. doi:10.1302/0301-620X.99B3.BJJ-2016-1028

Hengg, C., Nijs, S., Klopfer, T., Jaeger, M., Platz, A., Pohlemann, T., et al. (2019). Cement Augmentation of the Proximal Humerus Internal Locking System in Elderly Patients: a Multicenter Randomized Controlled Trial. *Archives Orthop. Trauma Surg.* 139 (7), 927–942. doi:10.1007/s00402-019-03142-6

Hepp, P., Lill, H., Bail, H., Korner, J., Niederhagen, M., Haas, N. P., et al. (2003). Where Should Implants Be Anchored in the Humeral Head? *Clin. Orthop. Relat. Res.* 415, 139–147. doi:10.1097/01.blo.0000092968.12414.a8

Jabran, A., Peach, C., and Ren, L. (2018). Biomechanical Analysis of Plate Systems for Proximal Humerus Fractures: a Systematic Literature Review. *Biomed. Eng. Online* 17 (1), 47. doi:10.1186/s12938-018-0479-3

Jabran, A., Peach, C., Zou, Z., and Ren, L. (2019). Parametric Design Optimisation of Proximal Humerus Plates Based on Finite Element Method. *Ann. Biomed. Eng.* 47 (2), 601–614. doi:10.1007/s10439-018-02160-6

Katthagen, J. C., Schwarze, M., Warnhoff, M., Voigt, C., Hurschler, C., and Lill, H. (2016). Influence of Plate Material and Screw Design on Stiffness and Ultimate Load of Locked Plating in Osteoporotic Proximal Humeral Fractures. *Injury* 47 (3), 617–624. doi:10.1016/j.injury.2016.01.004

Kralinger, F., Blauth, M., Goldhahn, J., Kach, K., Voigt, C., Platz, A., et al. (2014). The Influence of Local Bone Density on the Outcome of One Hundred and Fifty Proximal Humeral Fractures Treated with a Locking Plate. *J. Bone Jt. Surg. Am.* 96 (12), 1026–1032. doi:10.2106/JBJS.M.00028

Krappinger, D., Bizzotto, N., Riedmann, S., Kammerlander, C., Hengg, C., and Kralinger, F. S. (2011). Predicting Failure after Surgical Fixation of Proximal Humerus Fractures. *Injury* 42 (11), 1283–1288. doi:10.1016/j.injury.2011.01.017

Lewis, G. S., Mischler, D., Wee, H., Reid, J. S., and Varga, P. (2021). Finite Element Analysis of Fracture Fixation. *Curr. Osteoporos. Rep.* 19 (4), 403–416. in press. doi:10.1007/s11914-021-00690-y

Medtool (2014). *Medtool User's Manual V3.8*. Pfaffstaetten, Austria: Dr. Pahr Ingenieurs e.U. 2511.

Mischler, D., Babu, S., Osterhoff, G., Pari, C., Fletcher, J., Windolf, M., et al. (2020a). Comparison of Optimal Screw Configurations in Two Locking Plate Systems for Proximal Humerus Fixation - a Finite Element Analysis Study. *Clin. Biomech. (Bristol, Avon)* 78, 105097. doi:10.1016/j.clinbiomech.2020.105097

Mischler, D., Windolf, M., Gueorguiev, B., Nijs, S., and Varga, P. (2020b). Computational Optimisation of Screw Orientations for Improved Locking Plate Fixation of Proximal Humerus Fractures. *J. Orthop. Transl.* 25, 96–104. doi:10.1016/j.jot.2020.02.007

Ockert, B., Braunstein, V., Kirchhoff, C., Korner, M., Kirchhoff, S., Kehr, K., et al. (2010). Monoaxial versus Polyaxial Screw Insertion in Angular Stable Plate Fixation of Proximal Humeral Fractures: Radiographic Analysis of a Prospective Randomized Study. *J. Trauma* 69 (6), 1545–1551. doi:10.1097/TA.0b013e3181c9b8a7

Olerud, P., Ahrengart, L., Ponzer, S., Saving, J., and Tidermark, J. (2011). Internal Fixation versus Nonoperative Treatment of Displaced 3-part Proximal Humeral Fractures in Elderly Patients: a Randomized Controlled Trial. *J. Shoulder Elb. Surg.* 20 (5), 747–755. doi:10.1016/j.jse.2010.12.018

Panagiotopoulou, V. C., Varga, P., Richards, R. G., Gueorguiev, B., and Giannoudis, P. V. (2019). Late Screw-Related Complications in Locking Plating of Proximal Humerus Fractures: a Systematic Review. *Injury* 50 (12), 2176–2195. doi:10.1016/j.injury.2019.11.002

Panagiotopoulou, V. C., Ovesy, M., Gueorguiev, B., Richards, R. G., Zysset, P., and Varga, P. (2021). Experimental and Numerical Investigation of Secondary Screw Perforation in the Human Proximal Humerus. *J. Mech. Behav. Biomed. Mater* 116, 104344. doi:10.1016/j.jmbbm.2021.104344

Rangan, A., Handoll, H., Brealey, S., Jefferson, L., Keding, A., Martin, B. C., et al. (2015). Surgical vs Nonsurgical Treatment of Adults with Displaced Fractures of the Proximal Humerus: the PROFHER Randomized Clinical Trial. *JAMA* 313 (10), 1037–1047. doi:10.1001/jama.2015.1629

Ruchholtz, S., Hauk, C., Lewan, U., Franz, D., Kuhne, C., and Zettl, R. (2011). Minimally Invasive Polyaxial Locking Plate Fixation of Proximal Humeral Fractures: a Prospective Study. *J. Trauma* 71 (6), 1737–1744. doi:10.1097/TA.0b013e31823f62e4

Schader, J. F., Mischler, D., Dauwe, J., Richards, R. G., Gueorguiev, B., and Varga, P. (2021). One Size May Not Fit All: Patient-Specific Computational Optimization of Locking Plates for Improved Proximal Humerus Fracture Fixation. *J. Shoulder Elb. Surg* 31 (1), 192–200. doi:10.1016/j.jse.2021.06.012

Steiner, J. A., Ferguson, S. J., and van Lenthe, G. H. (2015). Computational Analysis of Primary Implant Stability in Trabecular Bone. *J. Biomechanics* 48 (5), 807–815. doi:10.1016/j.jbiomech.2014.12.008

Sudkamp, N., Bayer, J., Hepp, P., Voigt, C., Oestern, H., Kaab, M., et al. (2009). Open Reduction and Internal Fixation of Proximal Humeral Fractures with Use of the Locking Proximal Humerus Plate. Results of a Prospective, Multicenter, Observational Study. *J. Bone Jt. Surg. Am.* 91 (6), 1320–1328. doi:10.2106/JBJS.H.00006

Synthes (2009). *Implant Materials*. Third Edition. West Chester: Synthes, Inc..

Varga, P., Grünwald, L., Inzana, J. A., and Windolf, M. (2017). Fatigue Failure of Plated Osteoporotic Proximal Humerus Fractures Is Predicted by the Strain Around the Proximal Screws. *J. Mech. Behav. Biomed. Mater.* 75, 68–74. doi:10.1016/j.jmbbm.2017.07.004

Varga, P., Grünwald, L., and Windolf, M. (2018a). The Prediction of Cyclic Proximal Humerus Fracture Fixation Failure by Various Bone Density Measures. *J. Orthop. Res.* 36 (8), 2250–2258. in press. doi:10.1002/jor.23879

Varga, P., Inzana, J. A., Gueorguiev, B., Suedkamp, N. P., and Windolf, M. (2018b). Validated Computational Framework for Efficient Systematic Evaluation of Osteoporotic Fracture Fixation in the Proximal Humerus. *Med. Eng. Phys.* 57, 29–39. doi:10.1016/j.medengphy.2018.04.011

Varga, P., Inzana, J. A., Fletcher, J. W. A., Hofmann-Fliri, L., Runer, A., Südkamp, N. P., et al. (2020). Cement Augmentation of Calcar Screws May Provide the Greatest Reduction in Predicted Screw Cut-Out Risk for Proximal Humerus Plating Based on Validated Parametric Computational Modelling: Augmenting Proximal Humerus Fracture Plating. *Bone Jt. Res.* 9 (9), 534–542. doi:10.1302/2046-3758.99.Bjr-2020-0053.R1

Virtanen, P., Gommers, R., Oliphant, T. E., Haberland, M., Reddy, T., Cournapeau, D., et al. (2020). SciPy 1.0: Fundamental Algorithms for Scientific Computing in Python. *Nat. Methods* 17 (3), 261–272. doi:10.1038/s41592-019-0686-2

Voigt, C., Geisler, A., Hepp, P., Schulz, A. P., and Lill, H. (2011). Are Polyaxially Locked Screws Advantageous in the Plate Osteosynthesis of Proximal Humeral Fractures in the Elderly? A Prospective Randomized Clinical Observational Study. *J. Orthop. Trauma* 25 (10), 596–602. doi:10.1097/BOT.0b013e318206eb46

Windolf, M., and Richards, R. G. (2021). Generic Implant Positioning Technology Based on Hole Projections in X-Ray Images. *J. Med. Device* 15 (2), 025002. doi:10.1115/1.4049979

Zettl, R., Muller, T., Topp, T., Lewan, U., Kruger, A., Kuhne, C., et al. (2011). Monoaxial versus Polyaxial Locking Systems: a Biomechanical Analysis of Different Locking Systems for the Fixation of Proximal Humeral Fractures. *Int. Orthop.* 35 (8), 1245–1250. doi:10.1007/s00264-011-1220-z

Conflict of Interest: The authors declare that the research was conducted in the absence of any commercial or financial relationships that could be construed as a potential conflict of interest.

frontiers | Frontiers in Bioengineering and Biotechnology

ORIGINAL RESEARCH
published: 07 July 2022
doi: 10.3389/fbioe.2022.891338

Two Cannulated Screws Provide Sufficient Biomechanical Strength for Prophylactic Fixation in Adult Patients With an Aggressive Benign Femoral Neck Lesion

Guangtao Fu[1†], *Guoqing Zhong*[1,2†], *Zehong Yang*[3†], *Shi Cheng*[1], *Limin Ma*[1*] and *Yu Zhang*[1*]

[1]Department of Orthopedics, Guangdong Provincial People's Hospital, Guangdong Academy of Medical Sciences, Guangzhou, China, [2]Shantou University Medical Colleges, Shantou, China, [3]Department of Radiology, Sun Yat-Sen Memorial Hospital, Sun Yat-Sen University, Guangzhou, China

OPEN ACCESS

Edited by:
Carl-Eric Aubin,
Polytechnique Montréal, Canada

Reviewed by:
Abdelwahed Barkaoui,
International University of Rabat, Morocco
Bohao Yin,
Shanghai Jiao Tong University, China

***Correspondence:**
Limin Ma
malimin7@126.com
Yu Zhang
luck_2001@126.com

[†]These authors have contributed equally to this work

Specialty section:
This article was submitted to Biomechanics, a section of the journal Frontiers in Bioengineering and Biotechnology

Received: 07 March 2022
Accepted: 27 May 2022
Published: 07 July 2022

Citation:
Fu G, Zhong G, Yang Z, Cheng S, Ma L and Zhang Y (2022) Two Cannulated Screws Provide Sufficient Biomechanical Strength for Prophylactic Fixation in Adult Patients With an Aggressive Benign Femoral Neck Lesion. Front. Bioeng. Biotechnol. 10:891338. doi: 10.3389/fbioe.2022.891338

Background: Two cannulated screws were proposed for prophylactic fixation in adult patients with an aggressive benign femoral neck lesion in recent literature. However, the biomechanical properties of this intervention have not yet been investigated.

Methods: After the evaluation of the heterogeneity of bone mineral density and geometry *via* quantitative computed tomography, 24 embalmed adult human cadaver femurs were randomized into the control, inferior half of the anterior cortical (25%) bone defect, entire anterior cortical (50%) bone defect, and the 50% bone defect and two cannulated screw group. Biomechanical analysis was conducted to compare the stiffness and failure load among the four groups when mimicking a one-legged stance. A CT-based finite element analysis (FEA) was performed to mimic the cortical and cancellous bone defect and the implantation of two cannulated screws of the four groups. Measurements of the maximal displacement and von Mises stress were conducted with the longitudinal load force and boundary conditions being established for a one-leg-standing status.

Results: We noted a significant improvement in the failure load after the insertion of two 6.5 mm cannulated screws in femurs with 50% bone defect (+95%, $p = 0.048$), and no significant difference was found between the screw group and the intact femur. Similar trends were also found in the measurements of stiffness (+23%, $p > 0.05$) *via* biomechanical testing and the von Mises stresses (–71%, $p = 0.043$) by FEA when comparing the screw group and the 50% bone defect group.

Conclusion: Our findings suggest that two cannulated screws provided sufficient biomechanical strength for prophylactic fixation in adult patients with an aggressive benign femoral neck lesion even when the entire anterior cortical bone is involved.

Keywords: femoral neck, benign lesion, cannulated screw, prophylactic fixation, biomechanical analysis

INTRODUCTION

The femur neck is one of the most common anatomical sites of benign and tumor-like bone lesions (Shin et al., 2013). Although those lesions in the femur neck are most commonly detected incidentally and asymptomatically, a high degree of concern is raised for pathological fracture due to loss of normal anatomical structure and less residual bone stock in this weight-bearing site (Shi et al., 2021). Furthermore, the economic and clinical value of prophylactic stabilization when performed on patients with painful lesions compromising the structural integrity of long bones has been well-proven (Blank et al., 2016). Thus, prophylactic internal fixation is currently preferred for aggressive benign femoral neck lesions in adults (Nakamura et al., 2015; Panchwagh et al., 2018). Several options of the internal implant for an aggressive benign femoral neck lesion were previously reported, including cannulated screws (Singh et al., 2015; Erol et al., 2016), intramedullary fixation (Zhang et al., 2017), and compression hip screw (Nakamura et al., 2015). However, there is still no agreed consensus on the optimal selection of the internal fixation implant which provides not only sufficient biomechanical strength but also a minimally invasive approach after curettage (Shi et al., 2021).

The insertion of three cannulated screws is a well-proven treatment for adult non-displaced femoral neck fractures (Filipov, 2019). However, the principal blood supply sources for the femoral head, the epiphyseal arterial network system (Zhao et al., 2017), are easily damaged when placing the third screw in the superior and posterior area, and this complication is difficult to evaluate using perioperative radiographs (Hoffmann et al., 2019). It was also reported that the first two cannulated screws provide not only sufficient biomechanical stability but also less trauma and lower risk (5% vs. 7%) of femoral head avascular necrosis in adult patients with non-displaced femoral neck fractures when compared with the traditional three cannulated screws (Krastman et al., 2006; Gupta et al., 2016; Widhalm et al., 2019). Consequently, prophylactic fixation with two cannulated screws was recently proposed by some surgeons for the treatment of aggressive benign lesions in the femoral neck due to the earlier mentioned benefits (Singh et al., 2015; Erol et al., 2016). But, the biomechanical properties of this intervention have not yet been investigated, although satisfied short-term clinical outcomes were reported in a limited sample size.

Thus, the present study aims to evaluate the biomechanical stability of using two 6.5 mm cannulated screws as prophylactic fixation for an aggressive benign femoral neck lesion *via* cadaveric biomechanical testing and finite element analysis.

METHODS AND MATERIALS

Specimen Preparation

Twenty-four embalmed adult human cadaver femurs were obtained from the Department of Anatomy, Southern Medical University in Guangzhou, China (average age: 77.8 years, range: 67–89 years; 15 males and nine females). The Institutional Review Board of Guangdong Provincial People's Hospital waived the informed consent procedure for this portion of the study. After removing soft tissue, anterior–posterior and lateral radiographs were taken for each femur to exclude pre-existing disease, deformity, or trauma.

Quantitative Computed Tomography Scanning

To evaluate the heterogeneity of bone density and geometry in the femur neck during the biomechanical testing, QCT scans were carried out using a clinical scanner (SIEMENS SOMATOM 64, 140 kV, 80 mAs, 0.5 * 0.5 mm/pixel resolution, and 1 mm slice thickness) for each cadaver femur. Using a calibration phantom (MINDWAYS Software, Inc., San Francisco, CA), grayscale values were mapped to K_2HPO_4 equivalent density (ρ_{KHP}) using five tubes with reference densities and Hounsfield Units (HUs) were calibrated. Segmentation of the bone hard tissue from its surroundings was performed for each slice. The raw QCT images (in DICOM format) were converted into a binary format, and a combination of user-defined threshold limits with an edge following scheme was used for generation of the hard-tissue contours and elimination of soft tissue. BMD (g/cm^3) of the femoral head, femoral neck, and intertrochanteric region was measured (**Figure 1A**).

Specific to geometric measurements, the femoral neck–shaft angle was defined as the angle formed between the femoral neck axis and the femoral shaft axis, and this angle was measured on QCT scout images for each patient (Lee et al., 2017). Hip axis length was defined as the length along the femoral neck axis, from the lateral aspect of the greater trochanter to the inner pelvic rim (Maeda et al., 2011). Neck width was also measured as described by Maeda et al. (2011).

Biomechanical Testing

After QCT scanning, 24 specimens were randomly and equally allocated to the following four groups: control group, 25% defect group, 50% defect group, and 50% defect + screw group (**Figures 2B1–B4**). The area of the bone defect was defined according to the description outlined by Çaypınar et al. (2016). Briefly, the femur neck is most likely a cylinder, and we adopted a cylinder with a 10 cm base (the circumference of the circle) and a height of 7 cm. For example, a 25% bone defect was obtained when we create a rectangle anterior cortical bone defect using a bone drill, with a 2.5 cm base and a 7.0 cm height. In the 50% defect + screw group, two 6.5 mm AO cannulated screws were inserted in parallel into the coronal plane at a 125° angle from the femoral shaft over the guiding K-wires. The two cannulated screws were inserted close to the superior and inferior margin of the femoral neck, and both screws advanced to within 5 mm of the subchondral bone to meet the requirements of the tip apex distance. The area of bone defect and the position of cannulated screws were further confirmed by X-ray (**Figures 2A1–A4**).

The specimens were then mounted with a fixed shaft in a servo-hydraulic test frame (ElectroForce 3500, TA instrument, United States). The angle between the loading axis and the proximal shaft was 15° during the mechanical testing to mimic

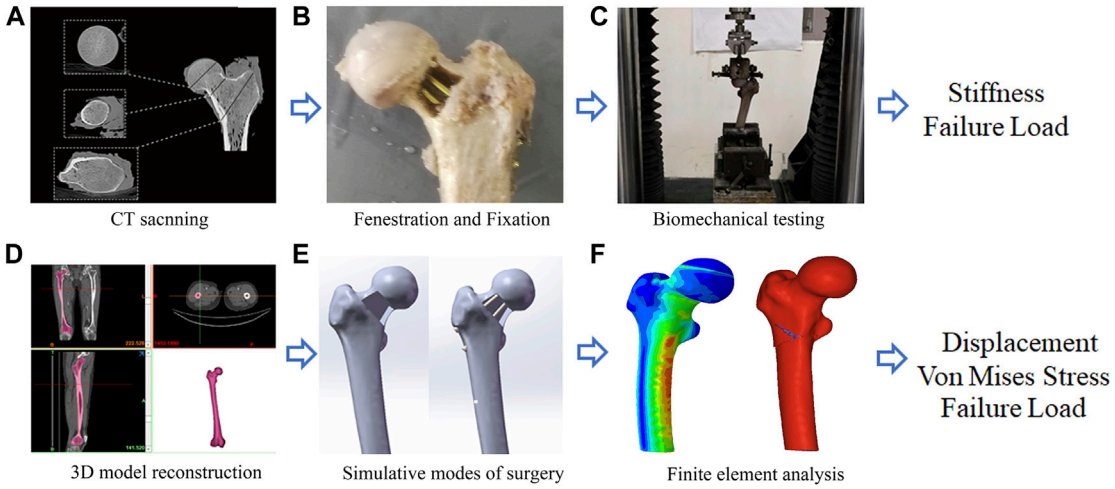

FIGURE 1 | A graphical overview of the present study design. **(A)** CT scanning; **(B)** Fenestration and Fixation; **(C)** Biomechanical testing; **(D)** Three-Dimension model reconstruction; **(E)** Simulative modes of surgery; **(F)** Finite element analysis.

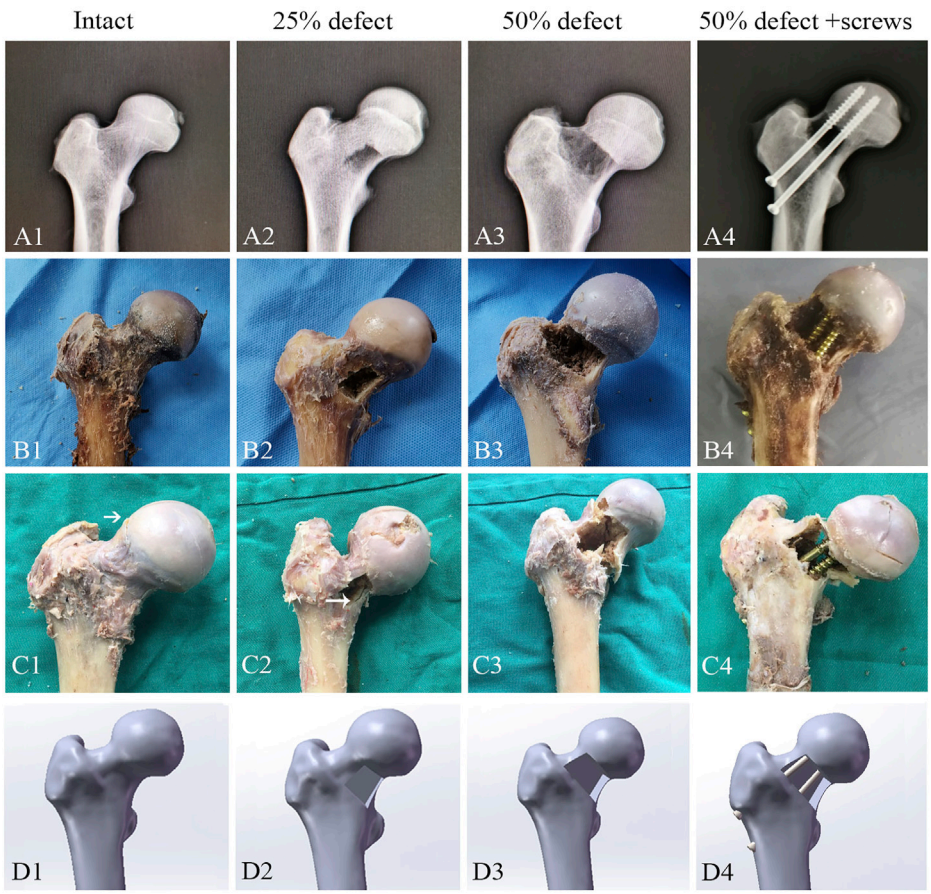

FIGURE 2 | Representative images for X-ray **(A1–A4)**, cadaveric tests **(B1–B4)**, femoral neck fracture **(C1–C4)**, and FEA **(D1–D4)** of the control group, 25%-defect group, 50%-defect group, and 50%-defect + two cannulated screw group.

TABLE 1 | Material properties are applied for the static and fracture analysis of finite element models.

Material properties	Cortical bone	Cancellous bone	Ti6Al–4V titanium
Young's modulus (E, MPa)	19,650	1,260	117,000
Poisson's ratio (μ)	0.3	0.2	0.3
Apparent density (ρ, g/cm3)	1.525	0.433	4.5
Yield stress (σ, Mpa)	136.728	3.434	1086
Failure strain (%)	0.70%	0.70%	-

the weight of the femur during a one-legged stance (**Figure 1C**) (Dou et al., 2019). The load was applied to the most cranial portion of the femoral head in the plane, spanned by the neck axis and the proximal femur axis. An axle bearing was inserted between the embedded femoral head and the test frame to allow rotation orthogonally to the loading axis through the femoral head. Before each test, all specimens were manually preloaded with a maximum of 100 N to avoid play between the embedded specimens and the test setup. The axial force was recorded *via* a 100-kN load cell (U3 force transducer; HBM, Darmstadt, Germany).

To keep the femora remained in the linear–elastic regime before the ultimate axial loading failure testing, a displacement range of 1 mm was chosen based on pre-tests, ensuring test conditions would not initiate plastic deformation and irreversible damage to the specimen. The axial stiffness was determined by vertically applying a vertical displacement of 1 mm maximum using displacement control 5 mm/min during the axial loading testing (Dou et al., 2019). Following a short relaxation period, a second compression cycle was applied with the same speed until the failure of load.

Three-Dimensional Model Construction

For a more detailed evaluation of the biomechanical property of the two cannulated screws, we also performed FEA. A healthy volunteer (male, 30-year-old) without previous history of surgery, trauma, and deformity in the lower limbs was recruited. Computerized tomography (CT) scan (SIEMENS SOMATOM 64) was performed on the lower limbs of the volunteer, with the slice thickness set at 0.5 mm. Image data of the right femur were imported into Mimics (version 21.0, Materialise NV, Leuven, Belgium) for three-dimensional (3D) reconstruction, which was based on the gray value of the tissue and segmentation of the region (**Figure 1D**). Subsequently, the model in STL format was imported into the Geomagic Wrap (version 2017, Geomagic Corporation, United States) for smoothing, meshing, and fitting surface processing.

A 3D computer-aided design software Solidworks (version 2017, Dassault Systèmes, Waltham, MA, United States) was then used to create the cortical and cancellous bone defect caused by the lesion and mimic the implantation of two cannulated screws (**Figure 1E**). Four models including control (intact), 25% bone defect, 50% bone defect, and 50% bone defect + two 6.5 mm cannulated screws were developed (**Figures 2D1–D4**). The 25% and 50% bone defects were obtained as outlined previously . To simulate the characteristics of the surgery more accurately, the position of the screws was strictly followed as per conventions of clinical practice, which we described in detail in the biomechanical analysis section.

Static Analysis

Data from the four models were imported into Abaqus 6.14 software (Dassault Systèmes S.A., France) to generate C3D10 tetrahedral elements. As per the study of Palumbo et al. (2014), Ti6Al-4V titanium was used as the internal fixation instruments, and the property parameters (Young's Modulus and Poisson's Ratio) of materials are listed in **Table 1**. The models were meshed to 1.0 mm, equal-sized facets, with >1,000,000 elements and ranging from 1,088,910 to 1,464,698. A mesh convergence test was conducted so that the deviation was less than 2%. In the current study, the cortical bone and cancellous bone interfaces were given with a tie feature. Regarding the interfaces between the screw thread and bone, the interfaces between the bone and metal were assigned as a sliding contact, with the frictional coefficient being 0.46 (Jiang et al., 2021).

It was reported that during static balance, approximately one-third of a person's body weight falls on each hip vertically (Çaypınar et al., 2016). Accordingly, a load of 700 N was applied straight down on the femoral head to simulate the one-leg-stance of an obese adult. Subsequently, the load force and boundary conditions were established for a one-leg-stance (**Figure 1F**). To mimic biomechanical testing, the area on the weight-bearing region of the femoral head, which intersects the mechanical axis, was set as the loading position, and the distal end of the femur was fixed. Measurements of von Mises stress were queried at 14 points of interest on the femoral neck that lay within the mid-coronal plane (**Figure 5A**). Von Mises stresses on the superior margin of the femoral neck were defined as the mean of von Mises stress from point 1 to point 7. The mean of von Mises stress from point 8 to point 14 was calculated as the Von Mises stresses on the inferior margin.

Fracture Mechanics Analysis

In order to test the failure loads, four models were imported to Hypermesh14.0 software (Altair, United States) to be meshed as tetrahedral with a size of 2 mm[21]. The mimic of the femoral neck fracture was established by Hypermesh and LS-DYNA software. An elastic–plastic material model (*MAT_03) in Hypermesh14.0 was used to simulate cortical and trabecular bone behaviors. According to previous studies (Li et al., 2010; Khor et al., 2018), the femoral fracture was defined by detecting a failure strain that was initiated and propagated by element deletion as long as the strain of an element reaches the limit. The fracture analyses were performed by LS-DYNA (LSTC, Livermore, CA) software to

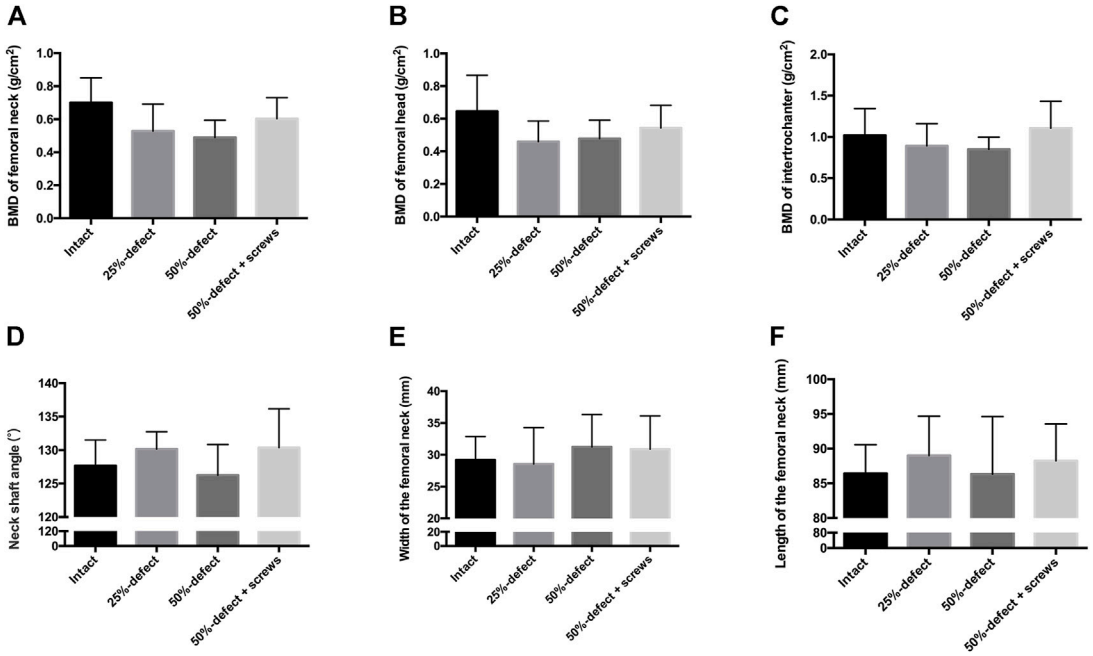

FIGURE 3 | QCT-based BMD of each group was measured at the femoral neck **(A)**, femoral head **(B)**, and intertrochanteric region **(C)** of the cadaver femurs. Measurements of the femoral geometry parameters include neck-shaft angle **(D)**, width of the femoral neck **(E)**, and length of the femoral neck **(F)**. All the data are presented as mean + std dev.

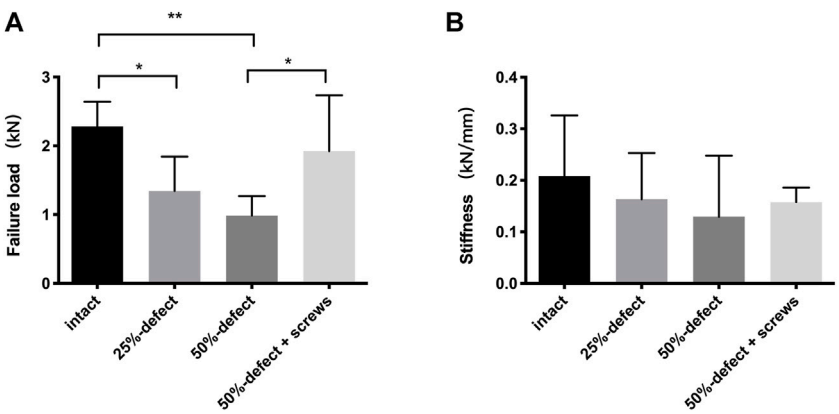

FIGURE 4 | Comparisons of failure load **(A)** and stiffness **(B)** within the four groups. * indicated $p < 0.05$, ** indicated $p < 0.01$, and all the data are presented as mean + std dev.

investigate the biomechanical effect of the failure test (Zheng et al., 2021). Material properties applied for fracture analysis are shown in **Table 1**. The density of cortical bone, cancellous, and Ti6Al–4V titanium was obtained from previous reports (Dhanopia and Bhargava, 2017; Zheng et al., 2021). According to the equations between bone density (ρ), Young's modulus (E), and yield stress (σ) (Morgan and Keaveny, 2001; Duchemin et al., 2008), cortical and cancellous bone's yield stress was calculated respectively. The contact settings between bone and screws were the same as those in the static analysis. Meanwhile, the loading settings were applied according to the biomechanics test of the cadaveric femurs until the failure of load.

Statistical Analysis

Continuous data were expressed as mean ± standard deviation or median with an interquartile range. Pearson's correlation analysis was conducted to test the correlation between maximum displacements of FEA and the stiffness of the mechanical test. The data of QCT measurement, biomechanical test, and FEA analysis of different groups were compared with one-way

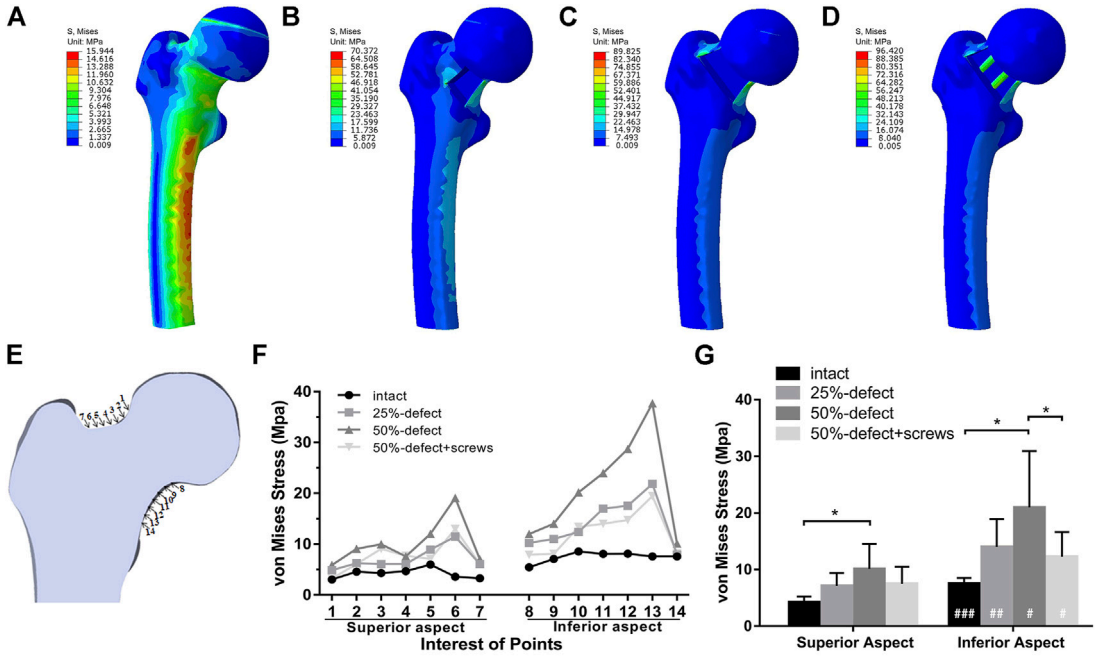

FIGURE 5 | Von Mises stress distribution of the intact femur **(A)**, 25%-defect **(B)**, 50%-defect **(C)**, and 50%-defect + two cannulated screws **(D)** under axial loading with 700 N. **(E)** Measurements of von Mises stress were queried at 14 different points on the femoral neck that lay within a single coronal plane. **(F)** Von Mises stresses of each point on the inferior and superior margin of the femoral neck were obtained. **(G)** Comparison of the mean von Mises stresses between the inferior and superior margin of the femoral neck in the circumstance of the intact femur, 25%-defect, 50%-defect, and 50%-defect + two cannulated screws. * indicated $p < 0.05$ when compared with other groups. # indicated $p < 0.05$, and ## indicated $p < 0.01$ when compared with the superior margin within each group. All the data are presented as mean + std.

ANOVA followed by the least significant difference (LSD) test for multiple comparisons. The two-sided Student's t-test was used to compare the von Mises stresses of the inferior margin and the superior margin of the femoral neck within the groups. Bonferroni correction was performed for multiple testing. Differences were considered significant if $p < 0.05$. SPSS 20.0 statistical software (Chicago, IL, United States) was used for these analyses.

RESULTS

Biomechanical Testing

No significant difference in BMD was measured at the femoral neck (**Figure 3A**), the femoral head (**Figure 3B**), or the intertrochanteric region (**Figure 3C**). Furthermore, no significant difference was observed between femoral geometry parameters including neck-shaft angle (**Figure 3D**), width of the femoral neck (**Figure 3E**), and length of the femoral neck (**Figure 3F**) of the cadaver femurs within the four groups. Thus, any potential bias caused by heterogeneity of bone density and geometry in the femur neck during the biomechanical testing is likely limited.

As illustrated by the cadaveric biomechanical testing, marked decreases in the failure load were observed in the 25% defect (−41.1%, $p = 0.038$) and 50% defect groups (−56.8%, $p = 0.004$) when compared with the intact femur (**Figure 4A**). There was a significant improvement in the failure load after insertion of two 6.5-mm cannulated screws in the 50% bone defect model (+95%, $p = 0.048$), and no significant difference was found when this group was compared to that of the intact femur (**Figure 4A**). As for stiffness measurements, a similar trend was found among the groups but did not reach statistical significance (**Figure 4B**). Moreover, as can be seen in **Figures 2C1–C4**, all of the fractures occurred in the femoral neck region.

FEA

The maximum displacement of the intact femur, 25% defect model, 50% defect model, and 50% defect + two cannulated screw model was 0.885 mm, 0.940 mm, 0.952 mm, and 0.938 mm, respectively. A significant linear correlation between the FEA stiffness and the stiffness of the cadaveric test ($r = 0.957$, $p = 0.04$) was observed, suggesting that our static analysis FEA models were valid.

The von Mises stress distributions of the four models are shown in **Figures 5A–D**. The quantitative von Mises stresses of selected points on the inferior and superior margin of the femoral neck are given in **Figures 5E,F**. When compared with the intact femur, the 50% defect model showed significantly higher mean von Mises stresses on both the inferior aspect (+140%, $p = 0.001$) and superior aspect (+180%, $P < 0.001$) of the femoral neck (**Figure 5G**). Insertion of the two screws significantly reduced the mean von Mises stresses on the inferior aspect in the 50% bone defect model (−71%, $p = 0.043$), while no significant

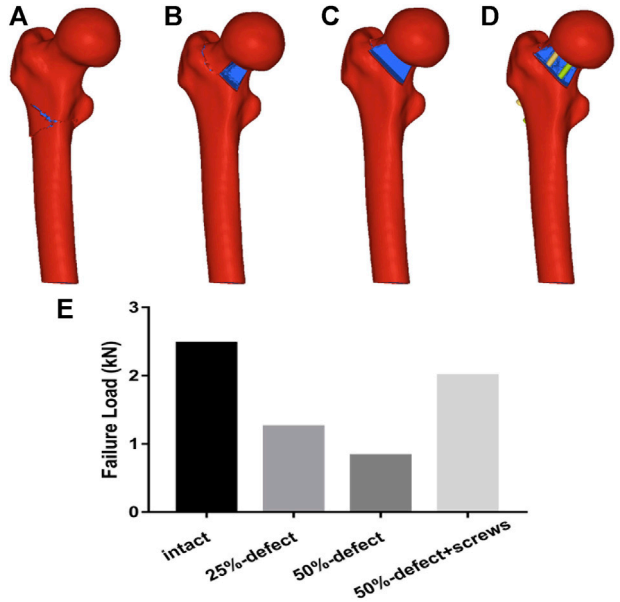

FIGURE 6 | Fracture lines of the four models are shown in **Figures 6A–D**. **Figure 6E**. Comparisons of failure load within the four groups are made *via* FEA.

difference was found when compared with the control group (**Figure 5G**). As shown in **Figure 5G**, there were more significant increases in the von Mises stress measurements on the inferior aspect of the femoral neck than on the superior aspect, in both the 25%-bone defect group (p = 0.006) and 50%-bone defect group (p = 0.024).

Regarding the failure load testing, the fracture lines of the four models are shown in **Figures 6A–D**. As illustrated in **Figure 6E**, there was a marked improvement in the failure load after insertion of two 6.5-mm cannulated screws in the 50% bone defect model. A statistically significant linear correlation of the failure load between FEA and cadaveric tests was also found (r = 0.953, p = 0.047).

DISCUSSION

In the present study, we observed a significant improvement in bone strength after the insertion of two 6.5-mm cannulated screws under the condition of a 50%-bone defect in the femoral neck as determined by cadaveric biomechanical tests and FEA. Similarly, another cadaveric study found that two cannulated screws provided increased axial stiffness and torsional stiffness in an anterior cortical bone defect adult femur sample but without a clear definition of the bone defect area (Dou et al., 2019). To the best of our knowledge, our study represents the first time to investigate the biomechanical stability of two cannulated screws as prophylactic fixation under the condition of an entire anterior cortical bone defect in the femoral neck, which is commonly encountered in adult patients with an aggressive benign femoral neck lesion.

Although no significant difference in the biomechanical properties was found between the two groups, two cannulated screws in a 50% femoral neck cortical bone defect sample did not provide increased biomechanical stability when compared with the intact femur as expected. However, it is important to note that the mean failure load of the two cannulated screw group in our study was approximately 1600 N. During static balance, approximately one-third of a person's body weight falls on each hip vertically (Çaypınar et al., 2016). Accordingly, 300 N falls vertically on each hip with 600 N on both hips in a 90 kg man during static standing, and 900 N falls on each hip during a one-legged stance. Thus, we suggest that the strength of two cannulated screw fixation was sufficient for full-weight standing and walking, especially in patients with normal body weight. However, our fixation strategy might be insufficient in all circumstances as up to 10 times a person's body weight can be exerted on the hips during running or intense activities (Çaypınar et al., 2016). Previous clinical studies also reported that no periprosthetic fracture was reported at either 6 months (Singh et al., 2015) or 48 months (Erol et al., 2016) after local curettage and prophylactic fixation using two cannulated screws in benign femoral neck lesion adult patients, with a restriction of intense activities before bone healing. Overall, we suggested that the application of two cannulated screws for prophylactic fixation is feasible for an aggressive benign femoral neck lesion in adult patients, even with an entire anterior cortical bone defect.

In the present study, significant decreases in the biomechanical properties of the femur neck were found in the 25% bone defect and 50% bone defect groups as determined by biomechanical analysis and FEA. A previous cadaver study showed that the failure load significantly decreased when the area of the bone defect increased from 35% to 55% in the femoral neck (Çaypınar et al., 2016). It was also reported that a bone defect located in the femoral neck was associated with worse biomechanical properties in both sideways fall and stance-loading conditions when compared with a bone defect located in the proximal diaphysis (Rajapakse et al., 2019). Clinical studies further confirmed these conclusions as patients with more than 54% bone defect in the femoral neck displayed a higher risk of pathological fractures during follow-up (Jeys et al., 2006; Günther et al., 2007). As we mentioned before, prophylactic fixation for an impending pathologic fracture in patients with painful lesions was associated with higher economic and clinical values when compared with an established fracture (Blank et al., 2016). Consequently, we recommend surgical intervention if the cortical bone is involved, although there remains no guideline for prophylactic bone fixation in patients with benign and tumor-like bone lesions in the femoral neck (Shih et al., 1996; Shin et al., 2013; Erol et al., 2016).

We also observed that there were more significant increases in the von Mises stress measurements on the inferior aspect of the femoral neck than on the superior aspect, in both 25%- and 50%-bone defect groups. Similarly, Benca et al. (2017); Benca et al. (2019) showed stiffness and failure load were significantly lower in specimens with inferior femoral neck lesions than with superior femoral neck lesions. The destruction of cortical bone in the calcar and principal compressive trabeculae might be a reasonable

explanation for this observation (Rudman et al., 2006). Thus, we suggest that the site of the lesion in the femoral neck has a potentially large effect on reducing biomechanical properties, and more caution should be applied when lesions are located in the inferior margin of the femoral neck.

The present study has several limitations. First, biomechanical measurements based on FEA and cadaveric tests did not evaluate the strength of two cannulated screw fixation in the circumstance of side-fall as only static standing was simulated. Determining the failure load in a simulated one-legged stance setup cannot be representative for all real-life fracture mechanisms which are inherently different from one patient to another and must account for different pathologies and load inductions (Benca et al., 2017). Nevertheless, the experimental setup and methodology used in this study provided highly reproducible experimental conditions and results comparable to those of previously published work in this field (Çaypınar et al., 2016; Benca et al., 2017; Benca et al., 2019; Dall'Ara et al., 2013). Second, neither cadaveric biomechanical testing nor FEA took into consideration soft tissues including the capsular ligament and periosteum, and this might partially limit the applicability of this testing in *in vivo* situations. Moreover, FEA with homogenous material properties is not based on specimen-specific femur models but on a healthy subject, and the bone defect in our testing was created artificially with only one defined lesion geometry that is consistent with previous studies (Çaypınar et al., 2016; Rajapakse et al., 2019). However, in the clinical setting, bone lesions often affect multiple regions and the cortex. Furthermore, conditions where more than 50% defect of the cortical bone in the femoral neck were not investigated in this study. Nevertheless, as it was reported that under such conditions, there would be insufficient bone to hold the screws, and internal fixation or total hip arthroplasty might be more appropriate approaches in this situation (Zhang et al., 2008). Last, it is necessary to compare the two cannulated screws with other internal fixation methods in order to highlight the advantages of this surgical method and support its clinical application, which we plan to fulfill in future studies.

CONCLUSION

Based on cadaveric biomechanical testing and FEA, we found that two 6.5-mm cannulated screws provided sufficient biomechanical strength for prophylactic fixation in adult patients with an aggressive benign femoral neck lesion, where even the entire anterior cortical bone is involved. The current study also provides preliminary evidence for the clinical application of two cannulated screws in the former-mentioned clinical scenario, although the strength of the evidence was limited by the fact that only the circumstance of static standing was mimicked and the FEA was based on one healthy subject. Future biomechanical studies mimicking the circumstance of side-fall and stair climbing, biomechanical testing compared with other internal fixation methods, and long-term clinical follow-up with adequate sample size are needed to further validate our findings.

DATA AVAILABILITY STATEMENT

The raw data supporting the conclusions of this article will be made available by the authors, without undue reservation.

ETHICS STATEMENT

The studies involving human participants were reviewed and approved by Guangdong Provincial People's Hospital. Written informed consent for participation was not required for this study in accordance with the national legislation and the institutional requirements.

AUTHOR CONTRIBUTIONS

Data curation—GF, GZ, and ZY. QCT analysis—ZY. Biomechanical test—GF and SC. FEA—GZ and LM. Writing of the original draft—GF and GZ. Writing—review and editing—YZ and LM. YZ takes responsibility for the integrity of the data analysis.

FUNDING

This work was also supported by the Guangdong Basic and Applied Basic Research Foundation (2022A1515011103 and 2021A1515110458).

REFERENCES

Benca, E., Reisinger, A., Patsch, J. M., Hirtler, L., Synek, A., Stenicka, S., et al. (2017). Effect of Simulated Metastatic Lesions on the Biomechanical Behavior of the Proximal Femur. *J. Orthop. Res.* 35 (11), 2407–2414. doi:10.1002/jor.23550

Benca, E., Synek, A., Amini, M., Kainberger, F., Hirtler, L., Windhager, R., et al. (2019). QCT-based Finite Element Prediction of Pathologic Fractures in Proximal Femora with Metastatic Lesions. *Sci. Rep.* 9 (1), 10305. doi:10.1038/s41598-019-46739-y

Blank, A. T., Lerman, D. M., Patel, N. M., and Rapp, T. B. (2016). Is Prophylactic Intervention More Cost-Effective Than the Treatment of Pathologic Fractures in Metastatic Bone Disease? *Clin. Orthop. Relat. Res.* 474 (7), 1563–1570. doi:10.1007/s11999-016-4739-x

Çaypınar, B., Erol, B., Topkar, M., and Başçı, O. (2016). Biomechanical Determination of the Relationship between Femoral Neck Lesion Size and the Risk of Pathological Fracture. *Hip Int.* 26 (2), 158–163. doi:10.5301/hipint.5000309

Dall'Ara, E., Luisier, B., Schmidt, R., Kainberger, F., Zysset, P., and Pahr, D. (2013). A Nonlinear QCT-Based Finite Element Model Validation Study for the Human Femur Tested in Two Configurations *In Vitro*. *Bone* 52 (1), 27–38. doi:10.1016/j.bone.2012.09.006

Dhanopia, A., and Bhargava, M. (2017). Finite Element Analysis of Human Fractured Femur Bone Implantation with PMMA Thermoplastic Prosthetic Plate. *Procedia Eng.* 173, 1658–1665. doi:10.1016/j.proeng.2016.12.190

Dou, B., Zhang, F., Ni, M., Ni, M., Dai, Y., Wang, Z., et al. (2019). Biomechanical and Finite Element Study of Drilling Sites for Benign Lesions in Femoral Head and Neck with Curettage, Bone-Grafting and Internal Fixation. *Math. Biosci. Eng.* 16 (6), 7808–7828. doi:10.3934/mbe.2019392

Duchemin, L., Bousson, V., Raossanaly, C., Bergot, C., Laredo, J. D., Skalli, W., et al. (2008). Prediction of Mechanical Properties of Cortical Bone by Quantitative Computed Tomography. *Med. Eng. Phys.* 30 (3), 321–328. doi:10.1016/j.medengphy.2007.04.008

Erol, B., Topkar, M. O., Aydemir, A. N., Okay, E., Caliskan, E., and Sofulu, O. (2016). A Treatment Strategy for Proximal Femoral Benign Bone Lesions in Children and Recommended Surgical Procedures: Retrospective Analysis of 62 Patients. *Arch. Orthop. Trauma Surg.* 136 (8), 1051–1061. doi:10.1007/s00402-016-2486-9

Filipov, O. B. (2019). Biplane Double-Supported Screw Fixation of Femoral Neck Fractures. *J. Am. Acad. Orthop. Surg.* 27 (11), e507–e515. doi:10.5435/jaaos-d-17-00117

Günther, K.-P., Hartmann, A., Aikele, P., Aust, D., and Ziegler, J. (2007). Large Femoral-Neck Cysts in Association with Femoroacetabular Impingement. *J. Bone & Jt. Surg.* 89 (4), 863–870. doi:10.2106/jbjs.f.00885

Gupta, M., Arya, R. K., Kumar, S., Jain, V. K., Sinha, S., and Naik, A. K. (2016). Comparative Study of Multiple Cancellous Screws versus Sliding Hip Screws in Femoral Neck Fractures of Young Adults. *Chin. J. Traumatology* 19 (4), 209–212. doi:10.1016/j.cjtee.2015.11.021

Hoffmann, J. C., Kellam, J., Kumaravel, M., Clark, K., Routt, M. L. C., and Gary, J. L. (2019). Is the Cranial and Posterior Screw of the "Inverted Triangle" Configuration for Femoral Neck Fractures Safe? *J. Orthop. Trauma* 33 (7), 331–334. doi:10.1097/bot.0000000000001461

Jeys, L. M., Suneja, R., Chami, G., Grimer, R. J., Carter, S. R., Tillman, R. M., et al. (2006). Impending Fractures in Giant Cell Tumours of the Distal Femur: Incidence and Outcome. *Int. Orthop.* 30, 135. doi:10.1007/s00264-005-0061-z

Jiang, D., Zhan, S., Wang, L., Shi, L. L., Ling, M., Hu, H., et al. (2021). Biomechanical Comparison of Five Cannulated Screw Fixation Strategies for Young Vertical Femoral Neck Fractures. *J. Orthop. Res.* 39 (8), 1669–1680. doi:10.1002/jor.24881

Khor, F., Cronin, D. S., Watson, B., Gierczycka, D., and Malcolm, S. (2018). Importance of Asymmetry and Anisotropy in Predicting Cortical Bone Response and Fracture Using Human Body Model Femur in Three-point Bending and Axial Rotation. *J. Mech. Behav. Biomed. Mater.* 87, 213–229. doi:10.1016/j.jmbbm.2018.07.033

Krastman, P., van den Bent, R. P., Krijnen, P., and Schipper, I. B. (2006). Two Cannulated Hip Screws for Femoral Neck Fractures: Treatment of Choice or Asking for Trouble? *Arch. Orthop. Trauma Surg.* 126 (5), 297–303. doi:10.1007/s00402-006-0143-4

Lee, S. H., Lee, Y. H., and Suh, J.-S. (2017). Lateral Cortical Thickening and Bone Heterogeneity of the Subtrochanteric Femur Measured with Quantitative CT as Indicators for Early Detection of Atypical Femoral Fractures in Long-Term Bisphosphonate Users. *Am. J. Roentgenol.* 209 (4), 867–873. doi:10.2214/ajr.17.17938

Li, Z., Kindig, M. W., Kerrigan, J. R., Untaroiu, C. D., Subit, D., Crandall, J. R., et al. (2010). Rib Fractures under Anterior-Posterior Dynamic Loads: Experimental and Finite-Element Study. *J. Biomechanics* 43 (2), 228–234. doi:10.1016/j.jbiomech.2009.08.040

Maeda, Y., Sugano, N., Saito, M., and Yonenobu, K. (2011). Comparison of Femoral Morphology and Bone Mineral Density between Femoral Neck Fractures and Trochanteric Fractures. *Clin. Orthop. Relat. Res.* 469 (3), 884–889. doi:10.1007/s11999-010-1529-8

Morgan, E. F., and Keaveny, T. M. (2001). Dependence of Yield Strain of Human Trabecular Bone on Anatomic Site. *J. Biomechanics* 34 (5), 569–577. doi:10.1016/s0021-9290(01)00011-2

Nakamura, T., Matsumine, A., Asanuma, K., Matsubara, T., and Sudo, A. (2015). Treatment of the Benign Bone Tumors Including Femoral Neck Lesion Using Compression Hip Screw and Synthetic Bone Graft. *SICOT-J* 1, 15. doi:10.1051/sicotj/2015009

Palumbo, B. T., Nalley, C., Gaskins, R. B., 3rd, Gutierrez, S., Alexander, G. E., Anijar, L., et al. (2014). Biomechanical Analysis of Impending Femoral Neck Fractures: the Role of Percutaneous Cement Augmentation for Osteolytic Lesions. *Clin. Biomech.* 29 (3), 289–295. doi:10.1016/j.clinbiomech.2013.12.001

Panchwagh, Y., Joshi, S. K., and Sancheti, P. K. (2018). Benign Aggressive Lesions of Femoral Head and Neck: Is Salvage Possible? *Ijoo* 52 (1), 51–57. doi:10.4103/ortho.ijortho_209_17

Rajapakse, C. S., Gupta, N., Evans, M., Alizai, H., Shukurova, M., Hong, A. L., et al. (2019). Influence of Bone Lesion Location on Femoral Bone Strength Assessed by MRI-Based Finite-Element Modeling. *Bone* 122, 209–217. doi:10.1016/j.bone.2019.03.005

Rudman, K., Aspden, R., and Meakin, J. (2006). Compression or Tension? the Stress Distribution in the Proximal Femur. *Biomed. Eng. Online* 5, 12. doi:10.1186/1475-925x-5-12

Shi, J., Zhao, Z., Yan, T., Guo, W., Yang, R., Tang, X., et al. (2021). Surgical Treatment of Benign Osteolytic Lesions in the Femoral Head and Neck: a Systematic Review. *BMC Musculoskelet. Disord.* 22 (1), 549. doi:10.1186/s12891-021-04442-y

Shih, H.-N., Cheng, C.-Y., Chen, Y.-J., Huang, T.-J., and Hsu, R. W.-W. (1996). Treatment of the Femoral Neck and Trochanteric Benign Lesions. *Clin. Orthop. Relat. Res.* 328 (328), 220–226. doi:10.1097/00003086-199607000-00034

Shin, S. H., Yeo, I., and Seo, S. W. (2013). Can Certain Benign Lesions of the Proximal Femur Be Treated without Surgery? *Clin. Orthop. Relat. Res.* 471 (10), 3319–3325. doi:10.1007/s11999-013-3048-x

Singh, P., Kejariwal, U., and Chugh, A. (2015). A Rare Occurrence of Enchondroma in Neck of Femur in an Adult Female: A Case Report. *J. Clin. Diagn Res.* 9 (12), Rd01–3. doi:10.7860/JCDR/2015/16555.6938

Widhalm, H. K., Arnhold, R., Beiglböck, H., Munteanu, A., Lang, N. W., and Hajdu, S. (2019). A Comparison of Dynamic Hip Screw and Two Cannulated Screws in the Treatment of Undisplaced Intracapsular Neck Fractures-Two-Year Follow-Up of 453 Patients. *Jcm* 8 (10), 1670. doi:10.3390/jcm8101670

Zhang, C.-l., Zeng, B.-f., Dong, Y., Terrell, D. b., and Malawer, M. M. (2008). Dynamic Condylar Screw or Hip Joint (Spanning) External Fixator for Treatment of Pathological Fractures of Femoral Neck and Trochanter Secondary to Benign Lesions. *Chin. Med. J.* 121 (2), 178–180. doi:10.1097/00029330-200801020-00017

Zhang, Y., Li, J.-z., Lu, X.-c., Zhang, Y., Zhang, H.-s., Shi, H.-l., et al. (2017). Intramedullary Nailing Combined with Bone Grafting for Benign Lesions of the Proximal Femur. *Orthop. Surg.* 9 (1), 97–102. doi:10.1111/os.12311

Zhao, D., Qiu, X., Wang, B., Wang, Z., Wang, W., Ouyang, J., et al. (2017). Epiphyseal Arterial Network and Inferior Retinacular Artery Seem Critical to Femoral Head Perfusion in Adults with Femoral Neck Fractures. *Clin. Orthop. Relat. Res.* 475 (8), 2011–2023. doi:10.1007/s11999-017-5318-5

Zheng, L., Chen, X., Zheng, Y., He, X., Wu, J., and Lin, Z. (2021). Cement Augmentation of the Proximal Femoral Nail Antirotation for the Treatment of Two Intertrochanteric Fractures - a Comparative Finite Element Study. *BMC Musculoskelet. Disord.* 22 (1), 1010. doi:10.1186/s12891-021-04878-2

Conflict of Interest: The authors declare that the research was conducted in the absence of any commercial or financial relationships that could be construed as a potential conflict of interest.

frontiers | Frontiers in Bioengineering and Biotechnology

ORIGINAL RESEARCH
published: 04 August 2022
doi: 10.3389/fbioe.2022.896790

Surgical Fixation of Calcaneal Beak Fractures—Biomechanical Analysis of Different Osteosynthesis Techniques

*Martin C. Jordan *, Lukas Hufnagel, Miriam McDonogh, Mila M. Paul, Jonas Schmalzl, Eva Kupczyk, Hendrik Jansen, Philipp Heilig, Rainer H. Meffert and Stefanie Hoelscher-Doht*

Julius-Maximilian-University of Würzburg, Würzburg, Germany

The calcaneal beak fracture is a rare avulsion fracture of the tuber calcanei characterized by a solid bony fragment at the Achilles tendon insertion. Treatment usually requires osteosynthesis. However, lack of biomechanical understanding of the ideal fixation technique persists. A beak fracture was simulated in synthetic bones and assigned to five different groups of fixation: A) 6.5-mm partial threaded cannulated screws, B) 4.0-mm partial threaded cannulated screws, C) 5.0-mm headless cannulated compression screws, D) 2.3-mm locking plate, and E) 2.8-mm locking plate. Different traction force levels were applied through an Achilles tendon surrogate in a material-testing machine on all stabilized synthetic bones. Outcome measures were peak-to-peak displacement, total displacement, plastic deformation, stiffness, visual-fracture-line displacement, and mode of implant failure. The 2.3- and 2.8-mm plating groups showed a high drop-out rate at 100 N tension force and failed under higher tension levels of 200 N. The fracture fixation using 4.0-mm partial threaded screws showed a significantly higher repair strength and was able to withhold cyclic loading up to 300 N. The lowest peak-to-peak displacement and the highest load-to-failure and stiffness were provided by fracture fixation using 6.5-mm partial threaded cannulated screws or 5.0-mm headless cannulated compression screws. As anticipated, large 6.5-mm screw diameters provide the best biomechanical fixation. Surprisingly, the 5.0-mm headless cannulated compression screws yield reliable stability despite the absent screw head and washer. When such large screws cannot be applied, 4.0-mm screws also allow reasonable fixation strength. Plate fixation should be implemented with precaution and in combination with a restrictive postoperative motion protocol. Finally, clinical cases about the surgical application and recovery are included.

Keywords: foot, ankle, Achilles, tendon, fracture

OPEN ACCESS

Edited by:
Jonas Widmer, Balgrist University Hospital, Switzerland

Reviewed by:
Samuel Haupt, Spital Oberengadin, Switzerland
Christos Tsagkaris, University of Crete, Greece

****Correspondence:***
Martin C. Jordan
jordan_m@ukw.de

Specialty section:
This article was submitted to Biomechanics, a section of the journal Frontiers in Bioengineering and Biotechnology

Received: *15 March 2022*
Accepted: *17 June 2022*
Published: *04 August 2022*

Citation:
Jordan MC, Hufnagel L, McDonogh M, Paul MM, Schmalzl J, Kupczyk E, Jansen H, Heilig P, Meffert RH and Hoelscher-Doht S (2022) Surgical Fixation of Calcaneal Beak Fractures—Biomechanical Analysis of Different Osteosynthesis Techniques. Front. Bioeng. Biotechnol. 10:896790. doi: 10.3389/fbioe.2022.896790

BACKGROUND

The beak fracture is a rare calcaneal fracture subtype of the posterior calcaneal tuberosity (Warrick and Bremner, 1953; Carnero-Martín de Soto et al., 2019). The available data indicate that elderly patients with osteopenic or osteoporotic bones are more likely to be affected by this fracture (Carnero-Martín de Soto et al., 2019; Beavis et al., 2008; Lee et al., 2012). Beavis et al. (2008) described three different fracture types based on the extent to which the tendon insertion is affected at the tuber calcanei. In type I fractures, a shell of bone avulses from the posterior tuberosity. Type II describes fractures with a solid bone fragment, where an oblique fracture line runs toward the posterior end of the posterior facet (**Figures 1**, **2**, and

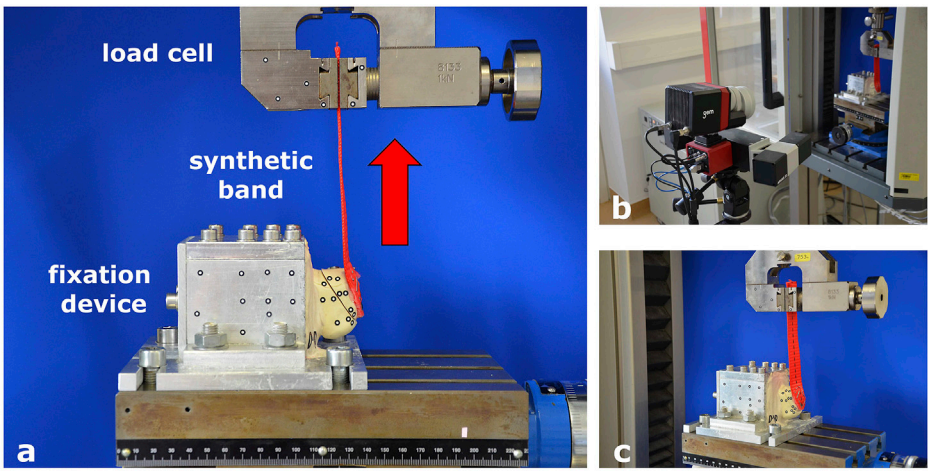

FIGURE 1 | Test set-up and fixation in the material testing machine. **(A)** Fixation device for synthetic bone specimens to the material testing machine. **(B)** Optical measuring machine. **(C)** Band mimicking the Achilles tendon to apply tension to the fragment.

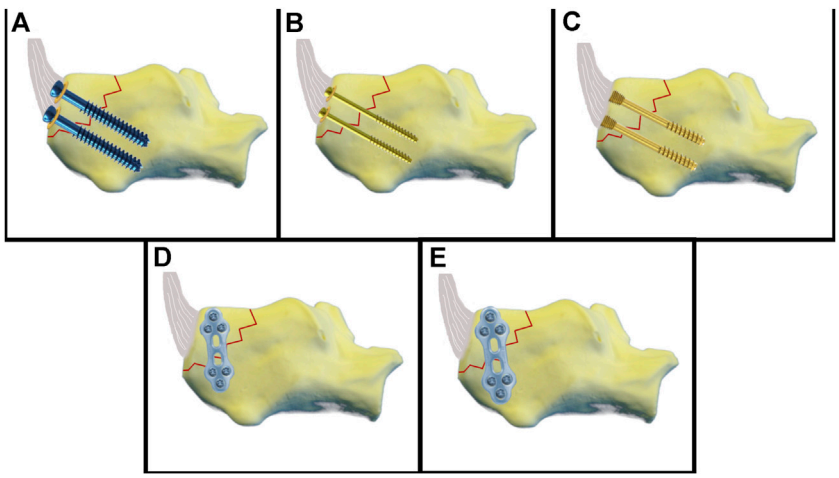

FIGURE 2 | Schematic illustration of the fixation techniques. **(A)** 6.5-mm partial threaded cannulated screw. **(B)** 4.0-mm partial threaded cannulated screw. **(C)** 5.0 headless cannulated compression screw. **(D)** 2.3-mm plate fixation. **(E)** 2.8-mm plate fixation.

Figure 7A). Type III fractures are infrabursal avulsions from the middle third of the posterior tuberosity. The injury itself is usually the result of sudden and disproportional muscular contractions, where the Achilles tendon rips a solid bony fragment out of the tuberosity. These fractures require urgent treatment because the pressure on the thin soft tissue coverage can cause severe necrosis (Banerjee et al., 2012; Mitchell et al., 2019). The small osseous fragments in type I and III fractures are typically refixed using suture anchors or transosseous sutures (Banerjee et al., 2012; Wakatsuki et al., 2016). For type II fractures, the literature recommends open reduction and fixation using 4.5- or 6.5-mm partially threaded screws (Banerjee et al., 2012; Gitajn et al., 2015). What remains unclear, however, is which type of screw is least likely to result in complications such as screw pull-out or screw cut-out (Banerjee et al., 2012; Lee et al., 2012; Carnero-Martín de Soto et al., 2019). The purpose of this study was to perform a comprehensive biomechanical comparison of currently available operative fixation techniques and to demonstrate their application in selected clinical cases. Given the high potential of failure with some of these methods, this study should help elucidate the most reliable technique (Gitajn et al., 2015).

MATERIALS AND METHODS

Specimens and Fracture Generation

A total of 50 synthetic bone specimens of the calcaneus (LD 9118; Synbone, Zizers, Switzerland) were used in this study. Previous studies have shown that the biomechanical properties of synthetic bone and human specimens are similar, and our pre-tests

TABLE 1 | Different groups tested.

Group	Fixation	Implant	Company
A	2 × cannulated screws 6.5 mm and washer	Length 45 mm, partial threaded, REF 408.431; washer 13 mm, REF 419.990	DePuy Synthes
B	2 × cannulated screws 4.0 mm and washer	Length 44 mm, partial threaded, REF 407.644; washer 7 mm, REF 419.980	DePuy Synthes
C	2 × 5.0 mm headless cannulated compression screws	Length 45 mm, REF A-8211.45X	Medartis
D	Plate fixation 2.3 mm	2.0/2.3 TriLock GridPl 3 + 3 hole, 37 mm, t1.3, APTUS, REF A-4655.69 + 2 × 16 mm + 2 × 18 mm + 2 × 20 mm locking screws	Medartis
E	Plate fixation 2.8 mm	2.8 TriLock Grid Pl 3 + 3 hole, 43 mm, t1.6, APTUS, REF A-4850.69 + 2 × 14 mm + 2 × 16 mm + 2 × 20 mm locking screws	Medartis

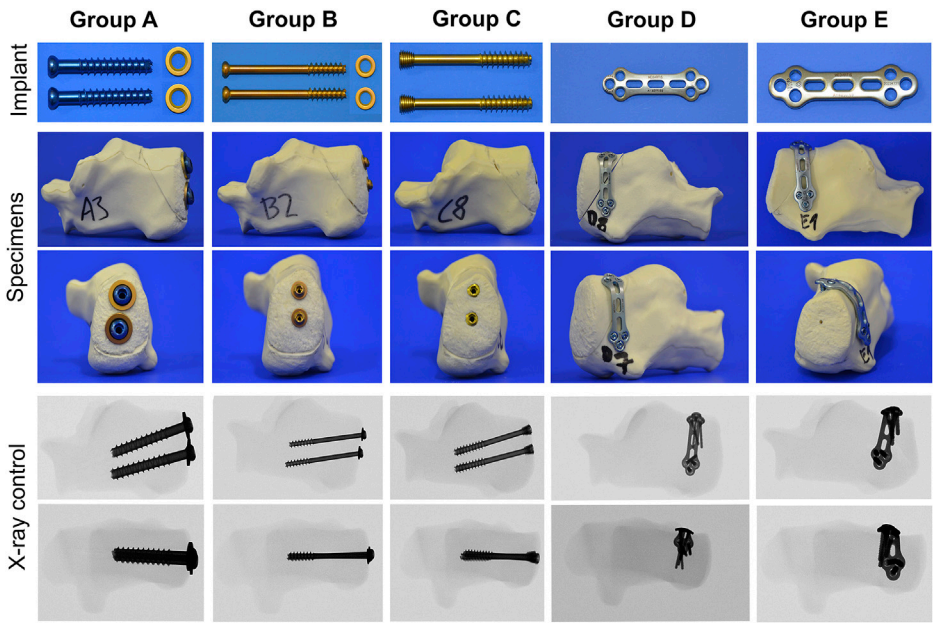

FIGURE 3 | Overview of the fixation techniques tested, including the implant material, stabilized synthetic bones, and fluoroscopic imaging.

confirmed these findings. A comparison of different synthetic bone models showed that Synbone most closely mimics the bone structure of elderly patients (Hoelscher-Doht et al., 2014; Fuchs et al., 2020). A Beavis type II fracture was induced using an oscillating saw. The size of the triangular fragment was 2.0 × 3.2 × 4.2 mm. The Achilles tendon was simulated by a braided synthetic band (kwb Germany GMBH, LC 1500 daN, Art.-Nr. 772,395) attached to the fragment (EPO-X-Y, Roxolid, Germany and staples).

Test Set-Up

A custom-made aluminum fixation device was developed to fit into the testing machine. Two-thirds of the bone specimen was embedded in the fixation device using calcium sulfate Ca $[SO_4]$ $2H_2O$, leaving the tuber calcanei free. The fixation device was mounted to the bottom of the testing machine, and the synthetic band simulating the Achilles tendon was affixed to a clamp connected to the load cell. Visual markers for video capturing were placed on the synthetic bone, with six markers on either side of the fracture. More markers were attached to the fixation device as reference points (**Figure 1**).

Experimental Groups

The fragment in Group A was fixed using two cannulated 6.5 mm threaded screws with underlying washers (length 45 mm, REF 408.431, b7, DePuy Synthes, Johnson & Johnson, United States). First, the fracture was reduced and fixated with two 2.8 mm k-wires. Using a cannulated 5.0 mm drill bit, the cannulated screws were inserted over the k-wires and underlaid with round washers (REF 419.990). Group B was stabilized with two cannulated 4.0 mm partially threaded screws and washers (length 44 mm, REF 407.644, DePuy Synthes). The fracture was reduced and fixed with two 1.25 mm k-wires. Using a cannulated 2.7 mm drill bit, the cannulated screws and washers (REF

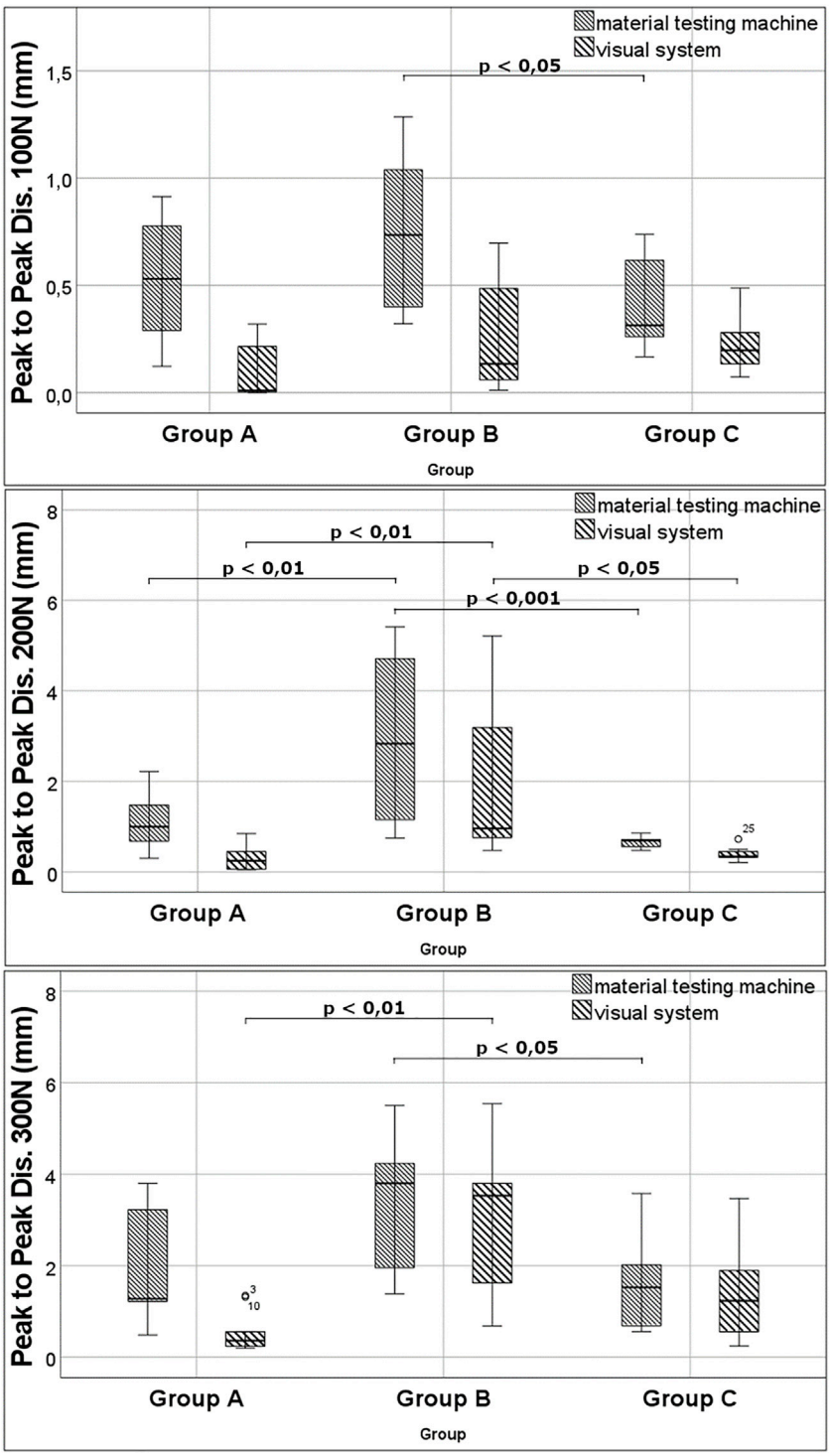

FIGURE 4 | Results for peak-to-peak displacement at different load levels.

419.980) were inserted over the k-wires. Group C was fixed with two 5.0 mm headless cannulated compression screws (length 45 mm, A-8211.45X, Medartis). Headless cannulated compression screws were inserted *via* priorly placed k-wires until the screw head was buried on the bone level. Group D was fixed by a lateral 2.0/2.3 mm locking plate (TriLock Grid Plate 3 + 3 hole, 37 mm, t1.3, APTUS, REF A-4655.69, Medartis). Reposition was achieved by a pointed reduction clamp and temporarily fixed by k-wires. Bending pliers were used to contour the plate. Locking screws from 14–20 mm were used.

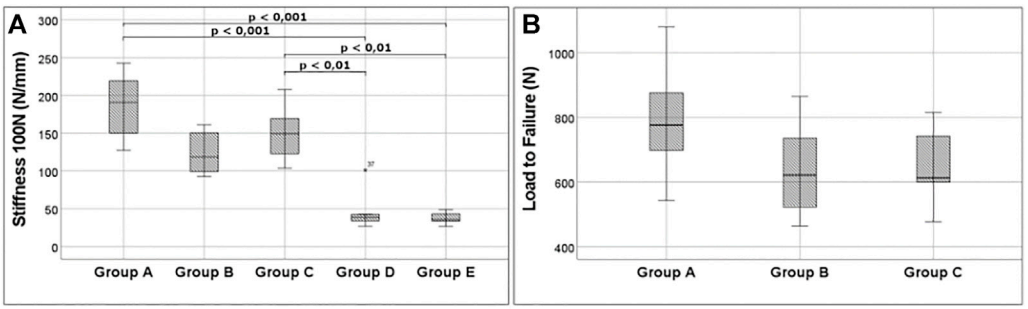

FIGURE 5 | Important outcome. **(A)** Stiffness at 100 N for all groups analyzed. A very low stiffness is noticeable for groups D and E, underlining the weakness of plating. **(B)** Boxplots show the high fixation strength of 6.5-mm partial threaded cannulated screw screws. 5.0 headless cannulated compression screw, and 4.0-mm partial threaded cannulated screw can also resist high tension forces.

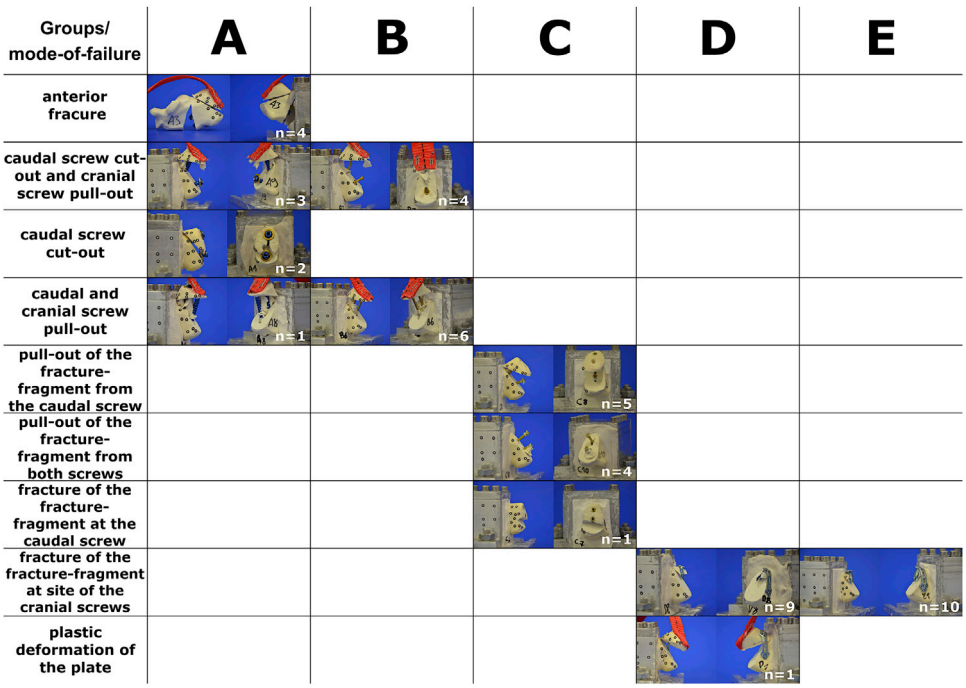

FIGURE 6 | Type of implant failure sorted by groups. The horizontal column represents the groups tested **(A–E)**. The vertical column describes the different modes of failure. Please see also **Supplementary Material** at the end.

Group E was stabilized by a lateral 2.8 mm locking plate (2.8 TriLock Grid Plate 3 + 3 hole, 43 mm, t1.6, APTUS, REF A-4850.69, Medartis) and locking screws (14–20 mm) (**Figures 2**, **3**, and **Table 1**). In each group, ten synthetic bone specimens of the calcaneus were used.

Biomechanical Protocol

Testing was conducted using a material-testing machine (Zwick/Roell Z020; Zwick GmbH & Co., Ulm, Germany) and the corresponding software (testXpert version 3.6; Zwick/Roell). The test protocol was determined according to our own pretests (load range 10–400 N; number of test cycles 10–8000). The final test protocol encompassed a 10 N preload followed by 10 setting cycles between 10 and 40 N. Following this, the test started with a cyclic loading from 10 to 100 N for 1,000 repetitive cycles. The next load level was 10–200 N for 1,000 cycles, and the third load level was 10–300 N for 1,000 load repeats: a static "ultimate strength" test was performed after cyclic testing. This measured load-to-failure and failure mode. For optical 3D metrology, a camera system (Pontos live, GOM, Germany) was placed in front of the material testing machine. The integrated software (Correlate Professional, 2018; GOM) captured marker displacement. The most caudally positioned marker on the fragment was used for visual analysis of the displacement. Parameters measured were *peak-to-peak displacement* for 100, 200, and 300 N in mm, *stiffness* (N/mm)

and *plastic deformation* (mm), *total displacement* (mm), *load-to-failure* (N), and *mode of failure* (anterior fracture, caudal screw cut-out and cranial screw pull-out, caudal screw cut-out, caudal and cranial screw pull-out, pull-out of the fracture-fragment from the caudal screw, pull-out of the fracture fragment from both screws, fracture of the fracture-fragment at the caudal screw, fracture of the fracture fragment at the site of the cranial screws, and plastic deformation of the plate).

Statistical Analysis

Microsoft Excel 2010 (Microsoft Corp. Redmond, WA, United States) was used for data collection. The data were analyzed using SPSS Statistics 27/28 (IBM Corp. Armonk, NY, United States). A power analysis was performed in previous tests using a power of 80% and a significance level of 5%, which showed that the sample size was adequate. The results are presented as the mean with standard deviation. All data were statistically analyzed for normal distribution using the Shapiro–Wilk test. Normally distributed data were compared using analysis of variance and the Bonferroni correction. Non normally distributed data were analyzed using the Kruskal–Wallis test and Dunn–Bonferroni correction. A p-value of <0.05 was considered statistically significant.

RESULTS

Results were grouped into biomechanical data gained by the material testing machine and visual data by the optical system.

Drop-Out

Specimens in groups D and E were not able to bear the 200 and 300 N tensions and, therefore, could not progress to load-to-failure tests. Three specimens in Group D and one in Group E lasted the 1,000 cycles at 100 N. This rendered a sufficient statistical analysis of these groups impossible. Drop-out occurred during the cyclic loading at 300 N for one specimen in Group A, three specimens in Group B, and one specimen in Group C.

Peak-to-Peak Displacement

Biomechanical data: Means at the load level of 100 N were 0.5 ± 0.3 mm in Group A, 0.8 mm ± 0.4 mm in Group B, and 0.4 mm ± 0.2 mm in Group C. There was a significant difference between Group B and C with $p = 0.023$. For 200 N, means were 1.1 ± 0.6 mm in Group A, 3.0 ± 1.8 mm in Group B, and 0.7 ± 0.1 mm in Group C. At this level, statistical differences could be seen between groups A and B with $p = 0.002$ and between groups B and C with $p < 0.001$. For cyclic testing at 300 N, means were 1.8 ± 1.2 mm in Group A, 3.3 mm ± 1.6 mm in Group B, and 1.6 ± 1.0 mm in Group C. Data showed a significant difference between groups B and C with $p = 0.048$. Visual data: Means at the load level of 100 N were 0.09 ± 0.12 mm in Group A, 0.26 ± 0.25 mm in Group B, and 0.22 ± 0.13 mm in Group C. At this level, there was no statistical difference. Means for cyclic testing at 200 N were 0.30 ± 0.26 mm in Group A, 1.99 ± 1.66 mm in Group B, and 0.38 ± 0.15 mm in Group C. Significant differences could be seen between groups A and B with $p = 0.001$ and between groups B and C with $p = 0.016$. For the load level of 300 N, the means were 0.56 ± 0.45 mm in Group A, 2.94 ± 1.73 mm in Group B, and 1.34 ± 1.06 mm in Group C. The difference between groups A and B was statistically significant, with $p = 0.008$ (**Figure 4**).

Total Displacement

Biomechanical data: the means were 3.9 ± 1.3 mm in Group A, 6.8 ± 1.5 mm in Group B, and 4.4 ± 1.2 mm in Group C. Statistical analysis showed significant differences between groups A and B with $p = 0.001$ and between groups B and C with $p = 0.007$. Visual data: the means were 1.11 ± 0.731 mm in Group A, 5.31 ± 2.94 mm in Group B, and 3.04 ± 1.44 mm in Group C. There was a significant difference between groups A and B with $p = 0.002$.

Plastic Deformation

For the load level of 100 N, means were 0.1 ± 0.1 mm in Group A, 0.3 ± 0.2 mm in Group B, and 0.2 ± 0.1 mm in Group C. There was no significant difference. At 200 N load, the means were 0.4 ± 0.3 mm in Group A, 2.1 ± 2.1 mm in Group B, and 0.5 ± 0.2 mm in Group C. Data showed a significant difference between groups A and B with $p = 0.013$. Means for cyclic testing at 300 N were 0.7 ± 0.6 mm in Group A, 3.1 ± 2.3 mm in Group B, and 1.4 ± 1.1 mm in Group C. There was a significant difference between groups A and B with $p = 0.006$.

Stiffness

At a load of 100 N, means were 185 N/mm ± 42 N/mm in Group A, 124 N/mm ± 28 N/mm in Group B, 148 N/mm ± 31 N/mm in Group C, 44 N/mm ± 23 N/mm in Group D, and 37 N/mm ± 7 N/mm in Group E. Statistical analysis showed differences between groups C and E with $p = 0.006$, between groups C and D with $p = 0.006$, between groups A and E with $p < 0.001$, and between groups A and D with $p < 0.001$. Means at 200 N were 206 N/mm ± 48 N/mm in Group A, 121 N/mm ± 26 N/mm in Group B, and 151 N/mm ± 29 N/mm in Group C. There was a significant difference between groups A and B with $p = 0.002$. For cyclic testing at 300 N, the means were 202 N/mm ± 25 N/mm in Group A, 114 N/mm ± 15 N/mm in Group B, and 134 N/mm ± 22 N/mm in Group C. The data showed significant differences between groups A and B and groups A and C with $p < 0.001$ (**Figure 5**).

Load-to-Failure

Means were 787 ± 184 N in Group A, 638 N ± 147 N in Group B, and 651 N ± 113 N in Group C. No significant difference was found for the maximum load (**Figure 5**).

Implant Failure

In Group A, four specimens developed an anterior fracture at the screw ends. Three specimens failed by a simultaneous cut-out of the caudal screw and pull-out of the cranial screw. In two cases, cut-out of the caudal screw occurred without pull-out of the cranial screw. One specimen failed by pull-out of both the caudal and cranial screws. In Group B, six specimens failed through the pull-out of both screws. Four specimens sustained a cut-out of the caudal screw and a pull-out of the cranial screw. In Group C, modes of failure were different to the ones described for groups A and B. Five specimens failed by pull-out of the fracture-fragment

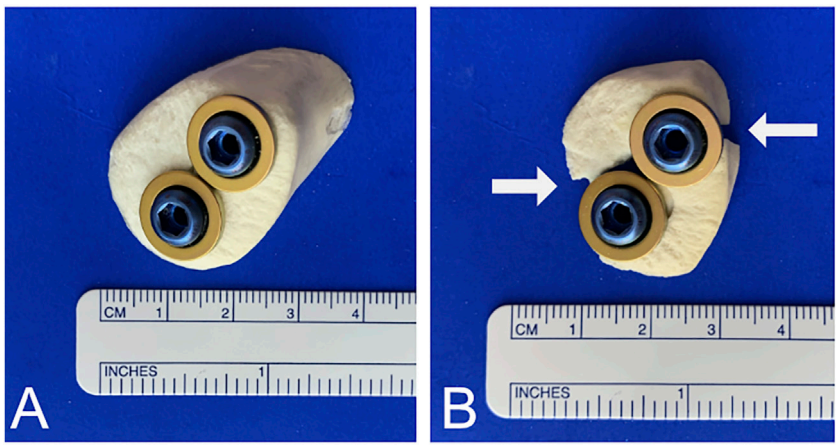

FIGURE 7 | Screw-to-bone ratio. **(A)** To avoid burst of the fracture caused by oversized screws, a 1:2 screw-to-bone ratio is recommended. **(B)** Cracks and bursts of the fracture can occur when the screw size is not appropriate. White arrows indicate fracture.

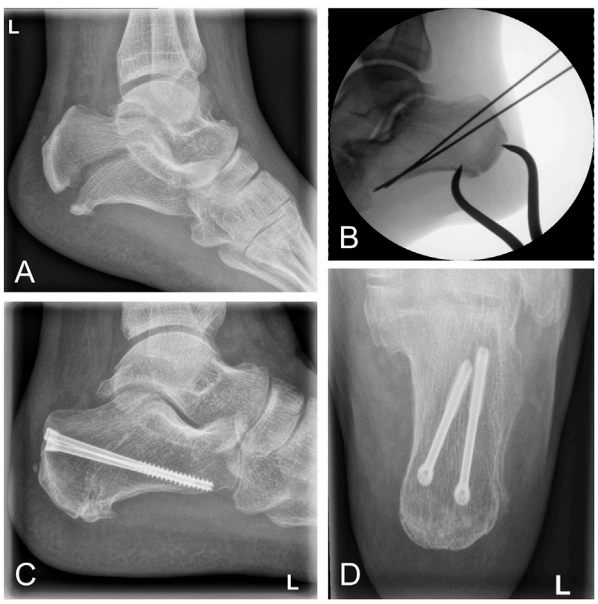

FIGURE 8 | Clinical case of a calcaneal avulsion fracture successfully treated using 5.0-mm headless cannulated compression screws. **(A)** Lateral x-ray showing a fracture gap caused by tension of the Achilles tendon. **(B)** Intraoperative fluoroscopy demonstrating percutaneous reduction by a pointed reduction clamp. **(C** and **D)** Postoperative x-ray after 12 months demonstrating osseous healing in lateral and ap views.

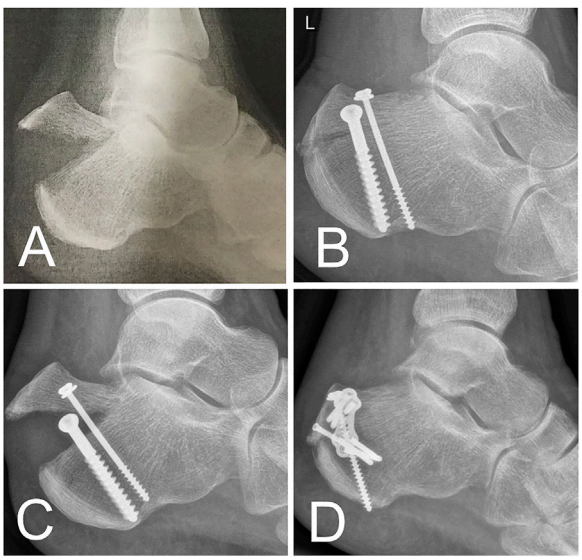

FIGURE 9 | Clinical case. **(A)** Beak fracture characterized by a solid bone part in a 61-year-old female patient. **(B)** X-ray after urgent reduction and screw fixation. **(C)** Early fracture dislocation after mobilization of the patient. **(D)** Revision performed using a combination of screw and plate osteosynthesis.

from the caudal screw. In four specimens, pull-out of the fracture-fragment occurred in both the caudal and cranial screw. One specimen failed by fracture at the level of the caudal screw. In Group D, almost all specimens failed by breakout of the fragment at the site of the screws. Failure due to plate deformation was only observed once. In Group E, the same mode of failure could be seen as in the majority of Group D. All objects failed by breakout of the fragment at the site of the screws (**Figure 6**; **Supplementary Video S1**).

DISCUSSION

Our data confirm the biomechanical stability of 4.0- and 6.5-mm cannulated partially threaded screws with round washers. Despite the absence of a washer, the 5.0 headless cannulated compression screws also demonstrated a surprisingly high stiffness and low displacement as compared to the other screws. In contrast, the stability of plate fixation was disappointing. None of the plates was able to tolerate loads above 100 N. In terms of overall stability, the best results were observed with 6.5-mm cannulated partially threaded screws, followed by 5.0 headless cannulated

compression screws and 4.0-mm cannulated partially threaded screws, respectively. Plate fixation was found to be significantly weaker. In calcaneal beak fractures, the skin and soft tissue cover over the heel is at risk and should be handled with great caution (Banerjee et al., 2012; Gitajn et al., 2015; Mitchell et al., 2019). The advantage of the percutaneous operative technique is the very low risk of soft tissue trauma compared to open techniques. The screw fixation methods presented here allow percutaneous fixation with minimal soft tissue irritation. When using conventional screws, the screw head and washer can be placed at the level of the Achilles tendon insertion, usually without interfering with the surrounding tissue. From a clinical point of view, the risk of soft tissue irritation can be further reduced through the use of the headless cannulated compression screws, which enables the burial of the screw head in the bone. This method may also reduce the necessity of implant removal. However, screw revision may be more difficult due to the challenge of finding the screw head under the bone level. But the clinical advantage of these headless cannulated compression screws requires evaluation through clinical studies and cannot be confirmed by our biomechanical study. In addition, in cases where the fragment does not adapt well, conversion to open exposure and fixation may become necessary. In these and in revision cases, plate fixation may be an option. To our knowledge, no biomechanical study has been conducted regarding the use of 2.3- or. 2.8-mm plates. As mentioned previously, our results raise concerns about the fixation of beak-type fractures using plate osteosynthesis. The stability is inferior compared to screws. In cases where plates are used for surgical revision, limited postoperative mobilization is vital. Despite our poor biomechanical results, successful reports of plate fixation for beak fractures exist (Agni and Fearon, 2016). A combination of plate and screw fixation is also possible (Yu et al., 2013).

Careful selection of screw sizes is vital and screw size is limited by the dimensions of the fragment. To avoid an iatrogenic burst of the bony fragment through the use of inadequate screws, we recommend a screw-bone ratio of roughly 1:2 (**Figure 7**). Although suture anchors were not included in the test protocol, they may also be used to augment screw fixation for bony fragments (Khazen et al., 2007; Yoshida et al., 2016).

Clinical cases further underline our findings. Based on the results of this biomechanical study, we implemented headless cannulated compression screws in a clinical case of a calcaneal avulsion fracture with critical soft tissue findings. The fracture healed completely, and the clinical function was excellent after 6 months (**Figure 8**). Despite this success, an open exposure and visually controlled reduction to ascertain anatomic fixation of the fragment may be necessary for more complex fractures and may be superior to percutaneous fixation (Banerjee et al., 2012; Blum et al., 2019). In another clinical case, a screw cut-out caused a re-dislocation of the fragment. The use of an additional plate enabled the fixation of a fragment too small for 6.5-mm or 4.0-mm diameter screws. The fracture healed well following the first revision using a restrictive postoperative motion protocol (**Figure 9**). Despite this, we do not recommend plating of beak fractures as a first-line treatment.

Despite this, results for the most promising fixation techniques require follow-up confirmation in a biomechanical setting with cadaver specimens. Furthermore, while fixation of the tension band on the tuber calcanei was challenging, the simple test set-up does not mimic the properties of *in vivo* Achilles tendons. This became most obvious under high loads. Load vectors may also be different under real-life conditions. In addition, the small proportions of the plates used may be responsible for their poor biomechanical performance compared to screws. Despite these limitations, this study represents the largest biomechanical study to date regarding this uncommon injury.

CONCLUSION

1) Generally, 6.5-mm partially threaded screws and 5.0-mm headless cannulated compression screws have the best overall stability for beak fracture fixation.
2) Whenever the fragment size does not allow one of the screws mentioned earlier, two 4.0-mm partially threaded screws are a good alternative.
3) In general, 2.3-mm or 2.8-mm bend plates cannot be recommended. If used, a combination of screws, suture anchors, or other fixation techniques and a very restrictive postoperative rehabilitation protocol is recommended.
4) Screw cut-out is mode-of-failure in partially threaded screws. Fragment pull-out occurred in 5.0-mm headless cannulated compression screws. Breakout of the fragment happens when plates are used.

DATA AVAILABILITY STATEMENT

The original contributions presented in the study are included in the article/**Supplementary Material**; further inquiries can be directed to the corresponding author.

AUTHOR CONTRIBUTIONS

MJ: study design, establishing the test set-up, conducting biomechanical tests, funding, and manuscript development. LH: conducting biomechanical tests, statistics, and data processing. MM: manuscript development and language editing. MP: manuscript revision and data processing. JS: manuscript revision and figure modification. EK: data collection and processing. HJ: clinical case assembling and manuscript revision. PH: conducting biomechanical tests (optical system). RM: manuscript revision, clinical input, and data interpretation. SH-D: manuscript revision, clinical input, data interpretation, biomechanical testing, and supervision.

SUPPLEMENTARY MATERIAL

The Supplementary Material for this article can be found online at: https://www.frontiersin.org/articles/10.3389/fbioe.2022.896790/full#supplementary-material

REFERENCES

Agni, N., and Fearon, P. (2016). Calcaneal Tuberosity Fixation Using a Locking Compression Hook Plate. *J. Foot Ankle Surg.* 55, 891–893. doi:10.1053/j.jfas.2016.03.012

Banerjee, R., Chao, J. C., Taylor, R., and Siddiqui, A. (2012). Management of Calcaneal Tuberosity Fractures. *J. Am. Acad. Orthop. Surg.* 20, 253–258. doi:10.5435/JAAOS-20-04-253

Beavis, R. C., Rourke, K., and Court-Brown, C. (2008). Avulsion Fracture of the Calcaneal Tuberosity: a Case Report and Literature Review. *Foot Ankle Int.* 29, 863–866. doi:10.3113/FAI.2008.0000

Blum, L. E., Hundal, R., Walton, D., and Hake, M. E. (2019). Percutaneous Fixation of Calcaneal Tuberosity Avulsion Fracture. *J. Orthop. Trauma* 33 (Suppl. 1), S44–S45. doi:10.1097/BOT.0000000000001533

Carnero-Martín de Soto, P., Bautista-Enrique, D., Gómez-Cáceres, A., Rodríguez-León, A., Bravo-Zurita, M. J., and Santos-Maraver, M. T. (2019). Avulsion Fractures of Posterior Calcaneal Tuberosity: Identification of Prognostic Factors and Classification. *J. Foot Ankle Surg.* 58, 423–426. doi:10.1053/j.jfas.2018.09.002

Elfar, J. J., Menorca, R. M. G., Reed, J. D., and Stanbury, S. (2014). Composite Bone Models in Orthopaedic Surgery Research and Education. *J. Am. Acad. Orthop. Surg.* 22, 111–120. doi:10.5435/00124635-201402000-00006

Fuchs, K. F., Heilig, P., McDonogh, M., Boelch, S., Gbureck, U., Meffert, R. H., et al. (2020). Cement-augmented Screw Fixation for Calcaneal Fracture Treatment: a Biomechanical Study Comparing Two Injectable Bone Substitutes. *J. Orthop. Surg. Res.* 15, 533. doi:10.1186/s13018-020-02009-6

Gitajn, I. L., Abousayed, M., Toussaint, R. J., Vrahas, M., and Kwon, J. Y. (2015). Calcaneal Avulsion Fractures. *Foot Ankle Specialist* 8, 10–17. doi:10.1177/1938640014548323

Hoelscher-Doht, S., Jordan, M. C., Bonhoff, C., Frey, S., Blunk, T., and Meffert, R. H. (2014). Bone Substitute First or Screws First? A Biomechanical Comparison of Two Operative Techniques for Tibial-Head Depression Fractures. *J. Orthop. Sci.* 19, 978–983. doi:10.1007/s00776-014-0613-4

Khazen, G. E., Wilson, A. N., Ashfaq, S., Parks, B. G., and Schon, L. C. (2007). Fixation of Calcaneal Avulsion Fractures Using Screws with and without Suture Anchors: a Biomechanical Investigation. *Foot Ankle Int.* 28, 1183–1186. doi:10.3113/FAI.2007.1183

Lee, S.-M., Huh, S.-W., Chung, J.-W., Kim, D.-W., Kim, Y.-J., and Rhee, S.-K. (2012) Avulsion Fracture of the Calcaneal Tuberosity: Classification and its Characteristics. *Clin. Orthop. Surg.* 4:134–138. doi:10.4055/cios.2012.4.2.134

Mitchell, P. M., O'Neill, D. E., Branch, E., Mir, H. R., Sanders, R. W., and Collinge, C. A. (2019). Calcaneal Avulsion Fractures: A Multicenter Analysis of Soft-Tissue Compromise and Early Fixation Failure. *J. Orthop. Trauma* 33, e422–e426. doi:10.1097/BOT.0000000000001582

Wakatsuki, T., Imade, S., and Uchio, Y. (2016). Avulsion Fracture of the Calcaneal Tuberosity Treated Using a Side-Locking Loop Suture (SLLS) Technique through Bone Tunnels. *J. Orthop. Sci.* 21, 690–693. doi:10.1016/j.jos.2015.06.011

Warrick, C. K., and Bremner, A. E. (1953). Fractures of the Calcaneum. *J. Bone Jt. Surg. Br. volume* 35-B, 33–45. doi:10.1302/0301-620x.35b1.33

Yoshida, K., Kasama, K., and Akahane, T. (2016). Avulsion Fracture of the Calcaneus Treated with a Soft Anchor Bridge and Lag Screw Technique: A Report of Two Cases. *J. Foot Ankle Surg.* 55, 310–313. doi:10.1053/j.jfas.2014.09.038

Yu, G.-r., Pang, Q.-j., Yu, X., Chen, D.-w., Yang, Y.-f., Li, B., et al. (2013). Surgical Management for Avulsion Fracture of the Calcaneal Tuberosity. *Orthop. Surg.* 5, 196–202. doi:10.1111/os.12058

Conflict of Interest: Implant material was purchased from DePuy Synthes with a 30% research discount. Medartis provided the implant material without cost. RM is president of the International Bone and Research Association. SH-D received funding from Medartis for biomechanical projects not related to this work.

The remaining authors declare that the research was conducted in the absence of any commercial or financial relationships that could be construed as a potential conflict of interest.

frontiers | Frontiers in Bioengineering and Biotechnology

TYPE Original Research
PUBLISHED 19 August 2022
DOI 10.3389/fbioe.2022.943092

OPEN ACCESS

EDITED BY
Keitaro Matsukawa,
Murayama Medical Center (NHO), Japan

REVIEWED BY
Alessio Gizzi,
Campus Bio-Medico University, Italy
Xinhua Li,
Shanghai General Hospital, China
Qiang Yang,
Tianjin Hospital, China

*CORRESPONDENCE
Baoqing Pei,
pbq@buaa.edu.cn
Shibao Lu,
spinelu@163.com

SPECIALTY SECTION
This article was submitted to Biomechanics, a section of the journal Frontiers in Bioengineering and Biotechnology

RECEIVED 13 May 2022
ACCEPTED 18 July 2022
PUBLISHED 19 August 2022

CITATION
Wang W, Kong C, Pan F, Wang Y, Wu X, Pei B and Lu S (2022), Biomechanical comparative analysis of effects of dynamic and rigid fusion on lumbar motion with different sagittal parameters: An in vitro study. *Front. Bioeng. Biotechnol.* 10:943092. doi: 10.3389/fbioe.2022.943092

Biomechanical comparative analysis of effects of dynamic and rigid fusion on lumbar motion with different sagittal parameters: An *in vitro* study

Wei Wang[1,2], Chao Kong[1,2], Fumin Pan[1,2], Yu Wang[1,2], Xueqing Wu[3], Baoqing Pei[3]* and Shibao Lu[1,2]*

[1]Department of Orthopedics, Xuanwu Hospital, Capital Medical University, Beijing, China, [2]National Clinical Research Center for Geriatric Diseases, Beijing, China, [3]Beijing Key Laboratory for Design and Evaluation Technology of Advanced Implantable and Interventional Medical Devices, Beijing Advanced Innovation Center for Biomedical Engineering, School of Biological Science and Medical Engineering, Beihang University, Beijing, China

Background: Although the management of the lumbar disease is highly dependent on the severity of the patient's condition, optimal surgical techniques to reduce the risk of adjacent degeneration disease (ADS) remain elusive. Based on *in vitro* biomechanical tests of the cadaver spine, this study aimed to comparatively analyze the kinematic responses of the spine with dynamic and rigid fixations (i.e., Coflex fixation and posterolateral fusion) after single-or double-level lumbar fusion in daily activities.

Methods: Six human lumbar specimens (L1-S1) were selected for this experiment, and the sagittal parameters of each lumbar specimen were measured in the 3D model. The specimens were successively reconstructed into five groups of models: intact model, single-level L4-5 Coflex fixation model, single-level L4-5 Fusion (posterior pedicle screw fixation) model, double-level L4-5 Coflex + L5-S1 Fusion model; and double-level L4-5 Fusion + L5-S1 Fusion model. The pure moment was applied to the specimen model to simulate physiological activities in daily life through a custom-built robot testing device with an optical tracking system.

Results: For single-level lumbar fusion, compared to the traditional Fusion fixation, the Coflex dynamic fixation mainly restricted the extension of L4-L5, partially retained the range of motion (ROM) of the L4-L5 segment, and reduced the motion compensation of the upper adjacent segment. For the double-level lumbar fixation, the ROM of adjacent segments in the Coflex + Fusion was significantly decreased compared to the Fusion + Fusion fixation, but there was no significant difference. In addition, PT was the only sagittal parameter of the preoperative lumbar associated with the ROM under extension loading. The Coflex fixation had little effect on the original sagittal alignment of the lumbar spine.

Conclusion: The Coflex was an effective lumbar surgical technique with a less altering kinematic motion of the lumbar both at the index segment and adjacent

segments. However, when the Coflex was combined with the fusion fixation, this ability to protect adjacent segments remained elusive in slowing the accelerated degradation of adjacent segments.

KEYWORDS

Coflex interspinous stabilization, lumbar fusion, range of motion, sagittal parameter, adjacent segment degeneration

Introduction

Lumbar fusion with posterior instrumentation has been the gold standard for lumbar spine intervention treatment. Traditional lumbar fusion has intrinsic issues in some cases, such as longer operational time, higher blood loss, and greater stiffness, and may result in over-treatment of the patient. The longitudinal retrospective investigation of lumbar fusion, on the other hand, found that rigid fixation accelerated secondary degeneration of adjacent segments (Whitecloud et al., 1994; Louie et al., 2019; Wang et al., 2021). Spine fusions disrupt the mechanical environment inside the vertebral body, affect blood oxygen and nourishment delivery, and cause postoperative complications of adjacent segments after spinal fusion (Zhou et al., 2016). The high incidence of secondary accelerated degenerative diseases at adjacent levels after lumbar fusion is still a problem for orthopedic surgeons.

To overcome the limits of traditional fusion, emerging non-fusion techniques with motion preservation are designed to achieve sufficient stability and slow the degeneration process by restoring partially segmental kinematics, allowing for more physiological load transmission (Sangiorgio et al., 2011; Zhou et al., 2020; Zheng et al., 2021). A Coflex interspinous stabilization, as the third joint offloads the two facets, provides neutral equilibrium of lumbar disorders and minimizes stress concentration in adjacent segments, preventing the occurrence of ASD. Several previous studies have suggested that the Coflex system is safe and effective (Zhao et al., 2018; Shen et al., 2021). Zheng et al. (2021) compared the radiographic outcomes of patients after single-level Coflex stabilization and traditional posterior fusion for a minimum of 8 years and found no significant difference between the two groups at each time point. The superiority of that dynamic, flexible surgical stabilization over traditional fusions, however, remains elusive, especially considering that the selection of surgery is highly dependent on the severity of the patient's condition.

The key to maintaining the static and dynamic balance of the human body is sagittal spine alignment, which minimizes the energy consumption of the trunk in daily activities. Clinical studies have suggested that sagittal balance is important in developing therapeutic strategies for a variety of spinal disorders (Ferrero et al., 2016; Sebaaly et al., 2018; Sebaaly et al., 2020). Spinopelvic radiographs have gradually become the standard in clinic for giving information on pathological diagnosis or preoperative planning (Roussouly et al., 2005; Bari et al., 2020; Sebaaly et al., 2020). Roussouly et al. (2005) proposed four types of sagittal alignment of the normal spine, which was defined by several sagittal parameters of the lumbar spine, such as pelvic incidence (PI), sacral inclination (SS), pelvic tilt (PT), lumbar lordosis (LL), etc. The optimum spinal surgery treatment should alleviate focal segmental illness and restore lumbar spine stability. Simultaneously, surgical procedures aim to minimize

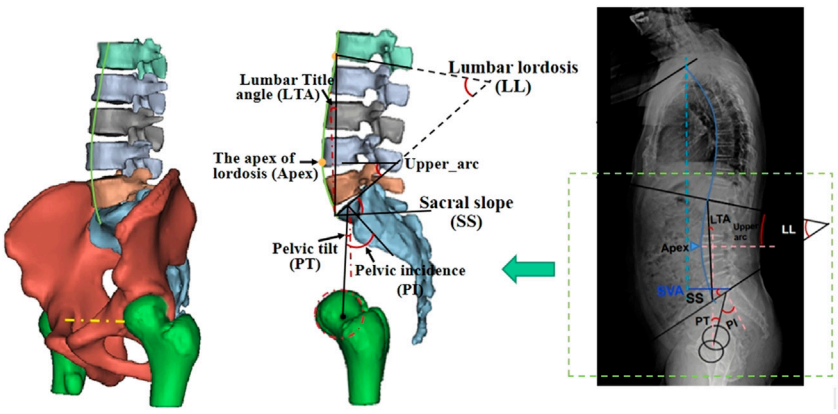

FIGURE 1
Measurement of sagittal parameters in the 3D lumbo-pelvic model.

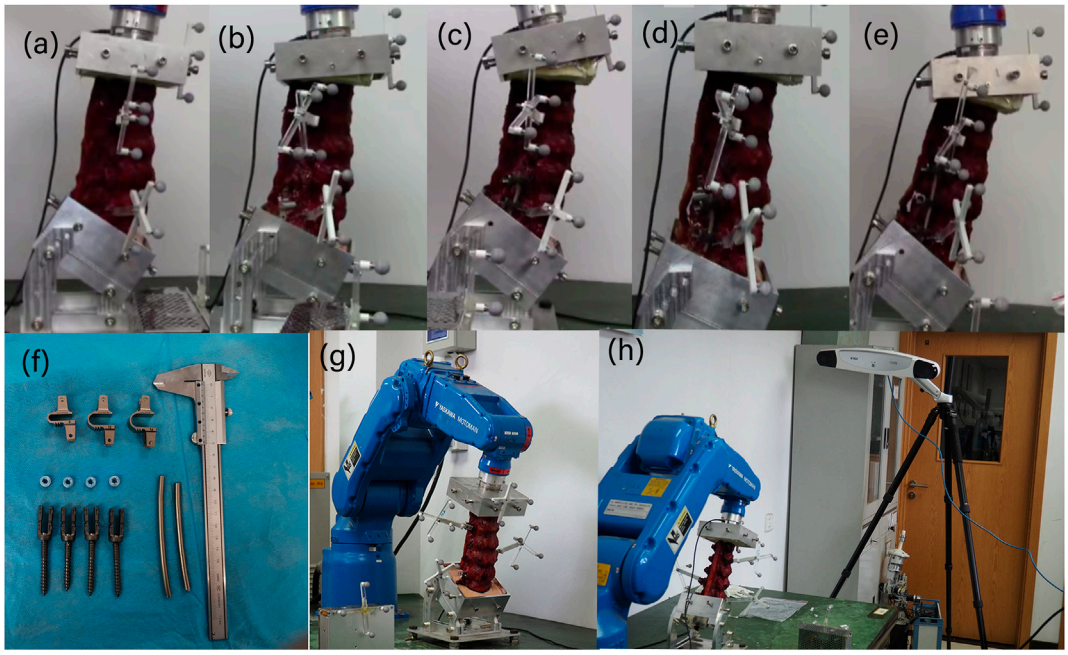

FIGURE 2
Schematic diagram of the *in vitro* experimental sample. **(A)** Normal; **(B)** L4-L5 Coflex; **(C)** L4-L5 Fusion; **(D)** Coflex + Fusion (L4-L5 Coflex + L5-S1 Fusion); **(E)** Fusion + Fusion (L4-L5 Fusion + L5-S1 Fusion). There were six samples in each group. **(F)** Implanted devices; **(G)** the robotic testing device; **(H)** 3D optoelectronic camera system.

the impact on the overall biomechanical stability of the lumbar spine, especially in adjacent segments. Many patients with lumbar degeneration have some degree of movement instability and obstacles (Kettler et al., 2012; Pieler-Bruha, 2016). The *in vivo* and *in vitro* kinematic study of the human spine is still a challenging task. There have been few studies on assessing the effect of dynamic or rigid fixation on spinal motion on a laboratory platform considering the sagittal alignment of the spine due to a shortage of human donor cadaver spines and complicated experimental procedures.

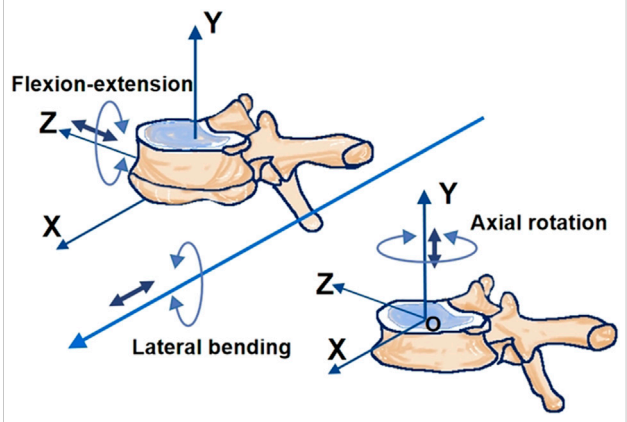

FIGURE 3
The coordinate system of two adjacent vertebral bodies.

The goal of this study was to establish an experimental assessment method for spinal biomechanics research after lumbar fusion, considering spinal kinematics and sagittal alignment. We investigated how the dynamic Coflex and traditional fusions and fixed segments (single or double-level lumbar fusion) influenced the range of motion (ROM) of the lumbar, especially on adjacent segments. This study also tried to find out whether normal sagittal parameters before fusion correlated with the ROM of the spine after different lumbar fusions. These results partially bridged the gap in understanding the biomechanical response of the spine to dynamic and traditional fixation devices and provide references for understanding the accelerated degeneration of adjacent segments and optimizing the application of spinal internal fixation.

Materials and methods

Specimen preparation

Approved by the Bioethics and Medical Ethics Committee, Beihang University (No.: BM20190009), Six donated human lumbar spines (L1–S1 segments, three females, three males,

TABLE 1 Sample information.

	Sex	Age	PI (°)	PT (°)	SS (°)	LL (°)	Upper arc (°)	LTA (°)	Apex	NVL
Sample 1	Female	53	36.9	9.4	27.5	40.3	14	−5.2	Upper L5	4.3
Sample 2	Male	32	39.6	10.2	29.4	43.2	13.9	−4.4	Base L4	4.6
Sample 3	Male	55	44.2	11.4	32.8	48.2	15.4	−4.2	Base L4	4.9
Sample 4	Female	64	47.5	10.1	37.4	52.4	14.8	−5.7	Middle L4	5
Sample 5	Male	59	54.1	10.7	43.4	53.9	14.7	−5.9	Middle L4	4.8
Sample 6	Female	42	59	12.2	46.8	58.2	16.6	−3.07	Base L3	5

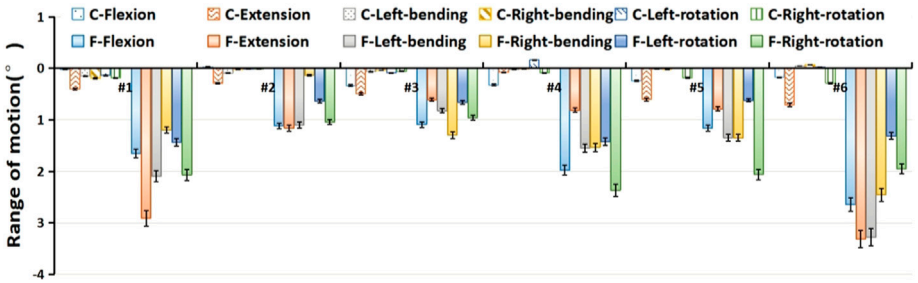

FIGURE 4
Preoperative and postoperative differences in the overall range of motion of each specimen. C: L4-L5 Coflex fixation group; F: L4-L5 Fusion fixation group.

32–64 years of age) were enrolled in the experimental study. The spiral computed tomography (CT) with a slice thickness of 0.6 mm (Light Speed Pro16, GE, Waukesha, WI, United States) was conducted to exclude the lumbar spines with disc degeneration, bony defects, scoliosis, tumors, a history of back surgery, or prolonged bed rest before death. Muscles around the lumbar spine were removed to gain the osteoligamentous structure, but be careful to preserve discs, facets and ligaments (Wilke et al., 1998). The specimens were partially frozen and wrapped in cling film before testing to reduce water loss.

Parameters measurement

A 3D model of the lumbar was reconstructed using CT images to measure the sagittal parameters. Duval-Beaupère et al. (1992), Roussouly et al. (2005) defined sagittal

TABLE 2 Significant difference in the range of motion of single-level fusion under different loading.

	Normal VS. L4-L5 Coflex	Normal VS. L4-L5 Fusion	L4-L5 Coflex VS. L4-L5 Fusion
Flexion	0.036*	0.001*	0.003*
Extension	0.006*	0.022*	0.052
Left-bending	0.152	0.005*	0.007*
Right-bending	0.388	0.007*	0.01*
Left-rotation	0.93	0.002*	0.003*
Right-rotation	0.54	0.001*	0.001*

*Significant difference $p < 0.05$.

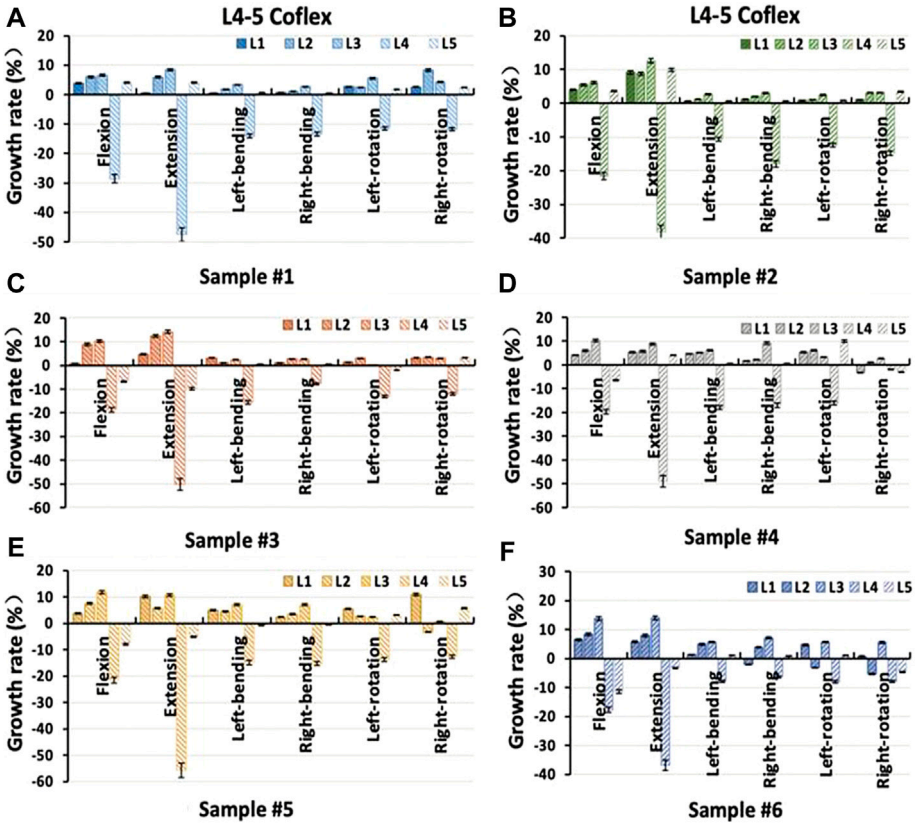

FIGURE 5
Percentage increment of the range of motion in each segment of samples after single-level L4-L5 Coflex fixation **(A)** Sample # 1; **(B)** Sample # 2; **(C)** Sample # 3; **(D)** Sample # 4; **(E)** Sample # 5 and **(F)** Sample # 6.

parameters. The lumbo-pelvic sagittal parameters included pelvic incidence (PI), sacral slope (SS), pelvic tilt (PT), lumbar lordosis (LL), the apex of lordosis (Apex), lumbar title angle (LTA), upper_arc, and the number of vertebrae in lordosis (NVL), as shown in Figure 1. The five observers measured each radiograph twice with 1 week between rounds.

Construction of the lumbar fusion model

Each specimen was successively reconstructed into five groups of models, as shown in Figure 2. 1) Normal: intact model; 2) L4-L5 Coflex: single-level L4-5 Coflex fixation model; 3) L4-L5 Fusion: single-level L4-5 pedicle screw fixation model; 4) Coflex + Fusion: double-level L4-5 Coflex + L5-S1 pedicle screw fixation model; 5) Fusion + Fusion: double-level L4-5 Coflex™ + L5-S1 pedicle screw fixation model. All the above models were made by experienced orthopedic doctors in Xuanwu Hospital.

Testing protocol and device

A robotic testing device (NX100MH6, Kabushiki-gaisha Yasukawa Denki, Kitakyushu, Japan) published in our previous literature was performed to measure the force-displacement behavior of lumbar segments (Kong et al., 2015) (Figure 2). A force-moment sensor (Gamma, ATI Industrial Automation, Ontario, Canada) was mounted on the robot's arm to record force and then provide feedback. Polymethylmethacrylate (PMMA) was used to fix both the L1 and S1 vertebra ends for installation in the custom-made containers (Figure 2). The 3D optoelectronic camera system (Optotrak Certus, Northern Digital Inc., Waterloo, Canada) recorded the vertebrae movement by tracking the location of five markers. The markers were attached to L1, L2, L3, L4, and L5 vertebrae, respectively.

According to the International Society of Biomechanics (ISB), the coordinating axes between adjacent vertebral bodies as shown in Figure 3. The test protocol consisted of six pure

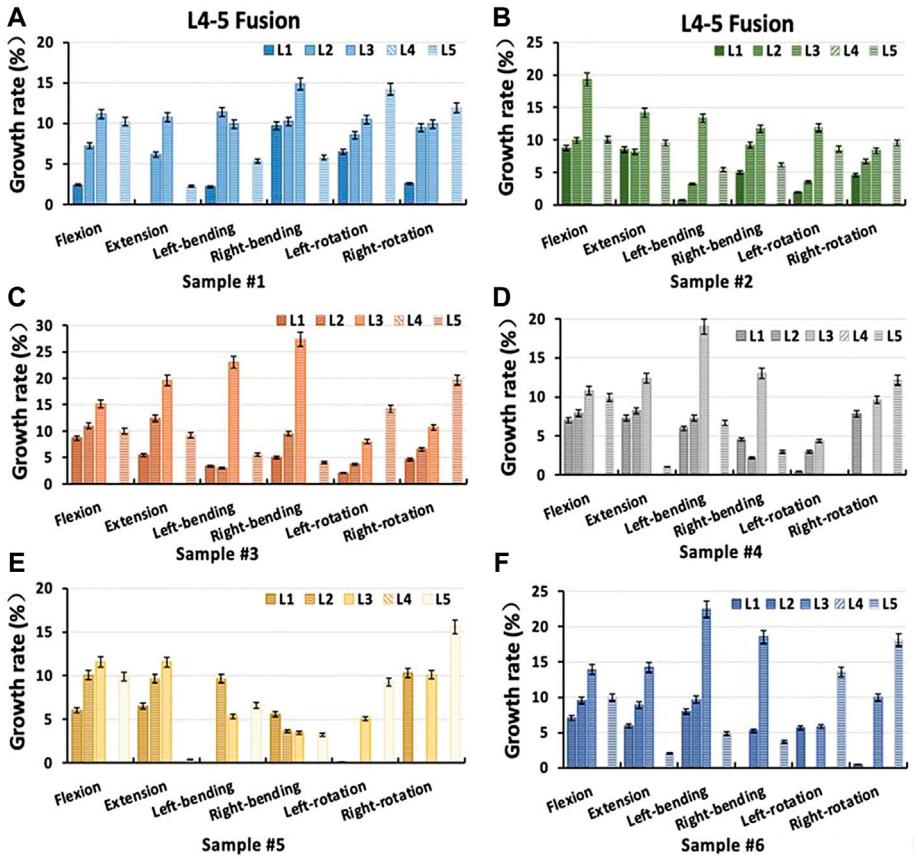

FIGURE 6
Percentage increment of the range of motion in each segment of samples after single-level L4-L5 Fusion fixation **(A)** Sample # 1; **(B)** Sample # 2; **(C)** Sample # 3; **(D)** Sample # 4; **(E)** Sample # 5 and **(F)** Sample # 6.

moment loads at a constant loading rate of 1.0°/s (Panjabi et al., 1992), including the flexion and extension load of 7.5 Nm, a lateral bending load of 7.5 Nm and axial rotation of 5 Nm. The robotic system automatically optimized the loading path, increasing the target load by 10% (7.5/5 Nm). In order to minimize the viscoelastic effect (Panjabi, 1998; Panjabi, 2007), the first 1.5 loading cycles were used and the following three loading cycles were recorded for analysis. During the test, the specimens were kept moist with saline (0.9%). First, Normal specimens were tested using the above method and then soaked in 0.9% saline water for 30 min. The normal specimen was implanted with the Coflex at the L4-5 segment to reconstruct the L4-5 Coflex specimen. The L4-5 Coflex specimen then repeated the above experimental steps and recovered. Similarly, L4-L5 Fusion, Coflex + Fusion, and Fusion + Fusion specimens were sequentially reconstructed and tested. In this study, the same spine specimen was reused five times. O'Connell et al. (2007) demonstrated that, in the *in vitro* tests, the original mechanical properties of the spine could be restored when soaking in a physiological saline bath for 3–4 times longer than the loading time.

Data analysis

Data analysis was performed using SPSS software (IBM Corp, Armonk, NY, United States). Inter-rater and intra-rater reliability was assessed using intra-class correlation (ICC) coefficients. The ROM of the specimens in all the groups was measured under different loading conditions. Paired t-tests were used to compare the ROM of the same specimens in the different model groups. Spearman's correlations were used to compare the relationships between the sagittal parameters and the ROM in the different Model groups under all loading conditions. Correlations were assumed to be strong (r = 0.80–1.00), moderate (r = 0.50–0.79), weak (r = 0.20–0.49), or not relevant (r < 0.20). $p < 0.05$ was considered statistically significant.

TABLE 3 Significant difference in the range of motion of adjacent segments after single-level fusion under different loading.

	Normal VS. Coflex	Normal VS. Fusion	Coflex VS. Fusion		Normal VS. Coflex	Normal VS. Fusion	Coflex VS. Fusion
L3-L4				L5-S1			
Extension	0.006*	0.002*	0.017*	Extension	0.963	0.717	0.281
Left-bending	0.004*	0.007*	0.015*	Left-bending	0.939	0.398	0.004*
Right-bending	0.001*	0.002*	0.029*	Right-bending	0.051	0.55	0.001*
Left-rotation	0.023*	0.004*	0.058	Left-rotation	0.841	0.624	0.503
Right-rotation	0.015*	0.001*	0.001*	Right-rotation	0.945	0.17	0.091
L2-L3				L2-L1			
Flexion	0.001*	0.001*	0.008*	Flexion	0.009*	0.003*	0.064
Extension	0.004*	0.003*	0.116	Extension	0.014*	0.013*	0.75
Left-bending	0.019*	0.006*	0.016*	Left-bending	0.12	0.121	0.626
Right-bending	0.001*	0.001*	0.045*	Right-bending	0.11	0.068	0.034*
Left-rotation	0.334	0.375	0.754	Left-rotation	0.23	0.062	0.833
Right-rotation	0.78	0.843	0.957	Right-rotation	0.162	0.007*	0.204

*Significant difference $p < 0.05$.

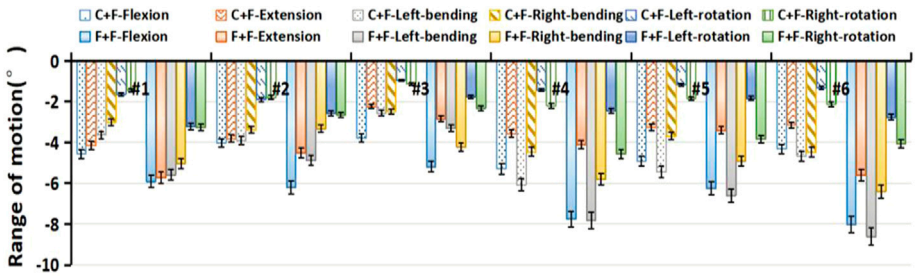

FIGURE 7
Preoperative and postoperative differences in the overall range of motion of each sample. C+F: L4-L5 Coflex + L5-S1 Fusion fixation group; F+F: L4-L5 Fusion + L5-S1 Fusion fixation group.

Results

Sagittal parameters

The sagittal parameters of the intact specimens before fusion were shown in Table 1. The average value of LL, PI, PT SS, Upper_arc and LTA was 46.88 ± 7.74°, 10.67 ± 0.92°, 36.22 ± 7.06°, 49.37 ± 6.18°, 14.90 ± 0.91°, and −4.75 ± 0.97°, respectively. The inflection point from kyphosis to lordosis almost appeared at the T12-L1 segments with an NVL of 5.01. The Apex of lumbar lordosis was located near the lower endplate L3 to the upper endplate S1. The ICC of all the parameters ranged from 0.83 to 0.97.

Overall range of motion in a single-level lumbar fixation model

Under different loading conditions, the overall ROM of L1-S1 segments in the two single-level lumbar fixation models (L4-L5 Coflex and L4-L5 Fusion) was shown in Figure 4. The overall ROM change in the L4-5 Coflex was minimal, essentially less than 0.3°. As shown in Table 2, the single-level Coflex fixation had a significant effect on the ROM in flexion and extension ($p < 0.05$), compared to the ROM in the Normal, but there was no significant change in the ROM in lateral bending and axial rotation loading ($p > 0.05$). For the

TABLE 4 Significant difference in the range of motion of two-level fusion under different loading.

	Normal VS. Coflex + Fusion	Normal VS. Fusion + Fusion	Coflex + Fusion VS. Fusion + Fusion
Flexion	0.002*	0.001*	0.007*
Extension	0.001*	0.001*	0.001*
Left-bending	0.004*	0.001*	0.002*
Right-bending	0.015*	0.002*	0.004*
Left-rotation	0.004*	0.002*	0.009*
Right-rotation	0.013*	0.006*	0.013*

*Significant difference $p < 0.05$.

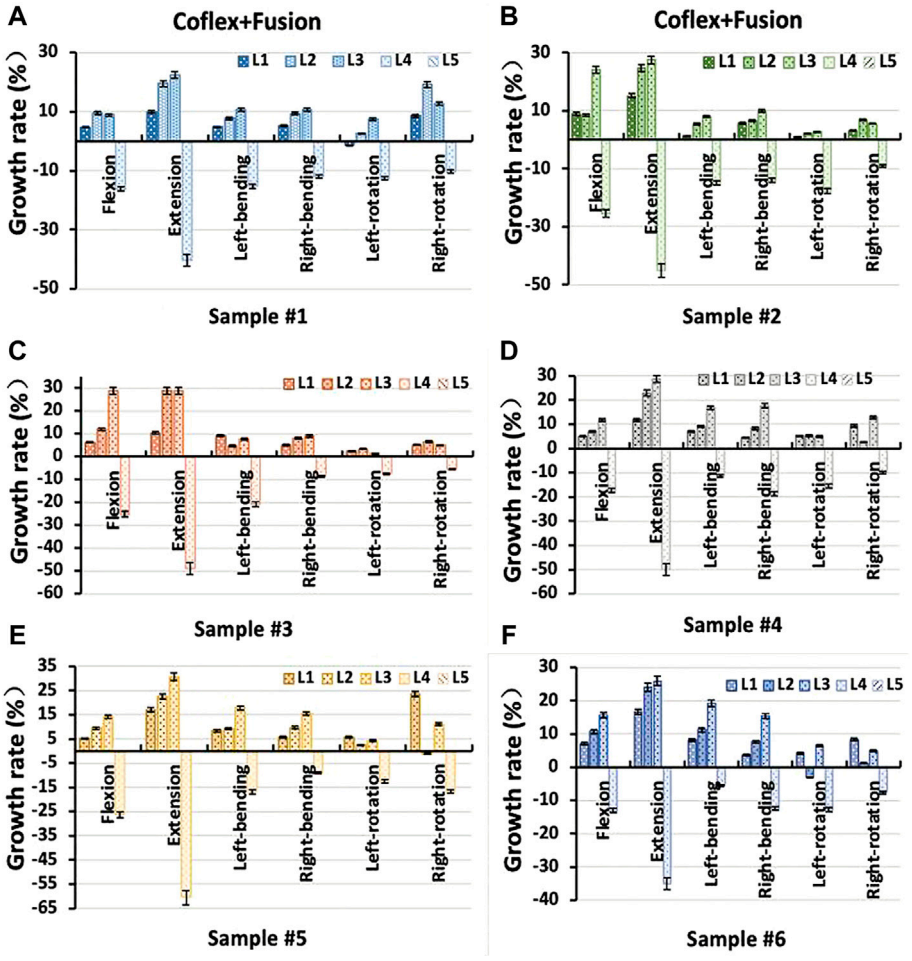

FIGURE 8
Percentage increment of the range of motion in each segment of samples after two-level Coflex + Fusion fixation **(A)** Sample # 1; **(B)** Sample # 2; **(C)** Sample # 3; **(D)** Sample # 4; **(E)** Sample # 5 and **(F)** Sample # 6.

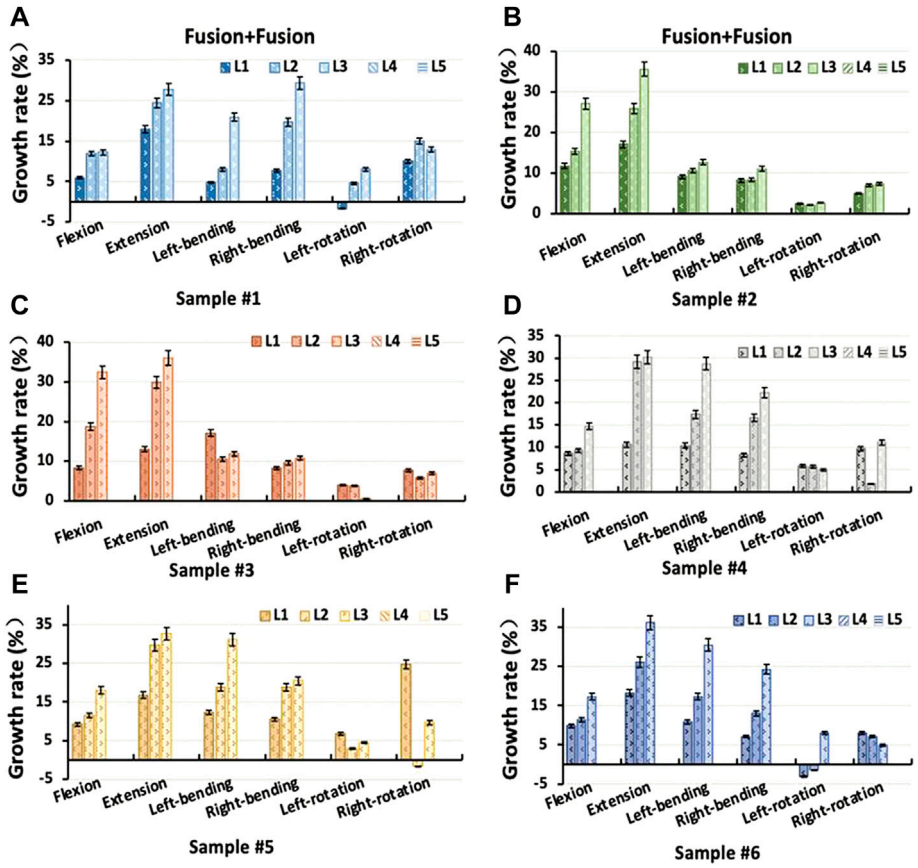

FIGURE 9
Percentage increment of the range of motion in each segment of samples after two-level Fusion + Fusion fixation **(A)** Sample # 1; **(B)** Sample # 2; **(C)** Sample # 3; **(D)** Sample # 4; **(E)** Sample # 5 and **(F)** Sample # 6.

L4-L5 Fusion model, the overall ROM decreased significantly under all loading conditions ($p < 0.05$). The ROM decreased from 1.19° to 2.91° in flexion, 0.13°–1.16° in extension, 0.60°–2.37° in lateral bending, and 0.61°–3.31° in axial rotation, respectively. The L4-L5 Fusion had a larger effect on the ROM than the L4-L5 Coflex in flexion, lateral bending, and axial rotation ($p < 0.05$). Although the decrease in ROM in the L4-L5 Fusion was larger than that in the L4-L5 Coflex under extension loading, there was no significant difference between them ($p > 0.05$).

Intervertebral rotation distribution in a single-level fixation model

The distribution of the ROM of each vertebra in the L4-L5 Coflex and L4-L5 Fusion was shown in Figure 5. The Coflex dynamic fixation reduced ROM from 36.71% to 55.68% in extension, 17.73%–28.61% in flexion, and about 10% in lateral bending and axial rotation at the L4-L5 level. The increase in ROM in adjacent segments of the specimens after L4-L5 Coflex was minimal, ranging from 0.06% to 14.19%. In extension, the increase in ROM of adjacent segments was significantly greater than that under other loading conditions, indicating that the Coflex implant greatly inhibited extension movement. In the L4-L5 Fusion, the ROM of adjacent segments increased much more than in the L4-L5 Coflex, ranging from 0.05% to 27.34%.

Under all loading conditions, the ROM significantly increased in the L4-L5 Coflex and the L4-L5 Fusion for the upper L3-L4 adjacent segment ($p < 0.05$), with an increase in the L4-L5 Fusion being much greater than that in the L4-L5 Coflex ($p < 0.05$), as shown in Figure 6 and Table 3. For the L2-L3 adjacent segments, the ROM in the L4-L5 Coflex and the L4-L5 Fusion increased significantly in flexion, extension, and lateral bending $p < 0.05$), and there was a significant difference between the two single-level fixation models ($p < 0.05$). However, for the L1-L2 adjacent segment, both single-level

TABLE 5 Significant difference in the range of motion of adjacent segments after single-level fusion under different loading.

	Normal VS. C+F	Normal VS. F+F	C+F VS. F+F		Normal VS. C+F	Normal VS. F+F	C+F VS. F+F
L3-L4				L2-L3			
Flexion	0.001*	0.001*	0.001*	Flexion	0.001*	0.001*	0.017*
Extension	0.001*	0.003*	0.052	Extension	0.002*	0.002*	0.066
Left-bending	0.005*	0.005*	0.006*	Left-bending	0.003*	0.003*	0.01*
Right-bending	0.001*	0.003*	0.044*	Right-bending	0.001*	0.002*	0.011*
Left-rotation	0.013*	0.02*	0.32	Left-rotation	0.282	0.102	0.085
Right-rotation	0.003*	0.001*	0.767	Right-rotation	0.061	0.053	0.611
L2-L1							
Flexion	0.002*	0.001*	0.003*	Extension	0.007*	0.054*	0.113
Left-bending	0.005*	0.001*	0.021*	Right-bending	0.001*	0.001*	0.081
Left-rotation	0.055	0.861	0.389	Right-rotation	0.051	0.071	0.082

*Significant difference $p < 0.05$; C+F: L4-L5 Coflex + L5-S1 Fusion fixation group; F+F: L4-L5 Fusion + L5-S1 Fusion fixation group.

fixations had a significant effect on ROM in flexion and extension, with no significant difference ($p > 0.05$). Furthermore, neither the L4-L5 Coflex nor the L4-L5 Fusion had a significant effect on the ROM of the inferior L5-S1 adjacent segment.

Range of motion in a two-level lumbar fixation model

Under different loading conditions, the overall ROM of L1-S1 segments in the double-level lumbar fixation models (L4-L5 Coflex and L4-L5 Fusion) was shown in Figure 7. Both the Coflex + Fusion and Fusion + Fusion showed no significant influence on the ROM of the inferior L5-S1 adjacent segment ($p < 0.05$), with the former having less effect in flexion, lateral bending, and axial rotation than the latter ($p < 0.05$) (Table 4). The ROM differences between the two fixation models were as follows: 1.31°–3.68° in flexion, 0.36°–2.45° in extension, 0.29°–3.93° in lateral bending, and 0.65°–1.99° in axial rotation.

3.5 Intervertebral rotation distribution in a two-level fixation model

The Coflex dynamic fixation maintained the partial ROM at the L4-L5 level, with a decrease in extension of 40.28%–60.01%, in flexion of 13.09%–26.30%, in lateral bending of 5.48%–20.89%, and in axial rotation of 5.54%–17.59% (Figure 8). In the Coflex + Fusion, the ROM of adjacent segments increased by 4.79%–28.88% in flexion, 1.28%–19.25% in lateral bend, and −3.08% to 12.80% in axial rotation, respectively. In extension, the increase in ROM of adjacent segments was significantly larger than that in other loading conditions, ranging from 9.96% to 30.60%. In the Fusion + Fusion, the ROM of adjacent segments increased by 10.57%–36.17% in flexion, 5.92%–32.40% in extension, 4.78%–29.31% in lateral bend, and −3.12% to 24.70% in axial rotation, respectively. The ROM of adjacent segments in the Fusion + Fusion was significantly larger than that of adjacent segments in the Coflex + Fusion ($p < 0.05$).

For the upper L3-L4 adjacent segment, the ROM significantly increased in the Coflex + Fusion and the Fusion + Fusion under all loading conditions ($p < 0.05$), while there was a significant difference only in flexion and lateral bending ($p < 0.05$), as shown in Figure 9 and Table 5. Similarly, for the L1-L2 and L2-L3 adjacent segments, the double-level fixation had a significant effect on the ROM in flexion, extension and lateral bending, with a significant difference only in flexion and lateral bending ($p > 0.05$).

Correlation analysis

The correlation between the original sagittal parameters of the lumbar-pelvis and the ROM in the different fixation models under different loading conditions was shown in Table 6. Only in the L4-L5 Coflex in flexion, the ROM was correlated with four parameters, including PI ($r = 0.943$), SS ($r = 0.943$), LL ($r = 0.943$) and Apex ($r = -0.883$). In extension, PT had a strong correlation with the ROM both

TABLE 6 Correlation between the lumbar-pelvic parameter and the range of motion after fusion under different loading.

Fusion	Loading	PI	PT	SS	LL	Apex	Upper arc	LTA	NVL
L4-L5 Coflex	Flexion	**0.943***	0.600	**0.943***	**0.943***	**−0.883***	0.771	0.029	0.725
	Extension	0.371	**0.886***	0.371	0.371	−0.294	0.543	0.714	0.406
	Left-bending	0.600	−0.086	0.600	0.600	−0.618	0.086	−0.657	0.290
	Right-bending	0.600	−0.086	0.600	0.600	−0.706	0.086	−0.543	0.493
	Left-rotation	0.143	−0.143	0.143	0.143	−0.265	0.143	0.257	0.145
	Right-rotation	−0.14	0.143	−0.143	−0.143	0.088	0.143	0.771	−0.087
L4-L5 Fusion	Flexion	−0.086	0.543	−0.086	−0.086	0.118	−0.086	0.600	−0.174
	Extension	0.371	**0.886***	0.371	0.371	−0.294	0.543	0.714	0.406
	Left-bending	0.200	0.543	0.200	0.200	−0.206	0.714	0.771	0.638
	Right-bending	−0.029	0.371	−0.029	−0.029	0.088	0.657	0.771	0.319
	Left-rotation	−0.714	−0.143	−0.714	−0.714	0.706	−0.543	0.429	−0.725
	Right-rotation	0.371	0.600	0.371	0.371	−0.147	0.600	0.143	0.203
Coflex + Fusion	Flexion	0.143	0.714	0.143	0.143	−0.088	0.257	0.600	0.203
	Extension	0.771	**0.829***	0.771	0.771	−0.736	**0.943***	0.543	**0.899***
	Left-bending	0.771	0.257	0.771	0.771	−0.794	0.371	−0.143	0.435
	Right-bending	0.543	−0.200	0.543	0.543	−0.618	0.143	−0.600	0.435
	Left-rotation	0.029	−0.371	0.029	0.029	−0.088	0.029	−0.086	−0.058
	Right-rotation	−0.200	**−0.829***	−0.200	−0.200	0.088	−0.429	−0.771	−0.145
Fusion + Fusion	Flexion	0.086	0.600	0.086	0.086	0.000	0.086	0.314	0.058
	Extension	0.543	**0.943***	0.543	0.543	−0.500	0.600	0.771	0.493
	Left-bending	0.714	0.143	0.714	0.714	−0.706	0.200	−0.429	0.290
	Right-bending	0.029	−0.371	0.029	0.029	−0.088	0.029	−0.086	−0.058
	Left-rotation	0.174	−0.232	0.174	0.174	−0.239	0.145	0.000	0.074
	Right-rotation	−0.543	−0.943*	−0.543	−0.543	0.500	−0.600	−0.771	−0.493

*Significant difference $p < 0.05$. PI: pelvic incidence; PT, pelvic tilt; SS, sacral slope; LL, lumbar lordosis; Apex, the apex of lordosis; LTA, lumbar title angle; NVL, the number of vertebrae in lordosis.

in the single- and double-level fusions. There was no correlation between other sagittal parameters of the normal specimens and the ROM under all loading conditions.

Discussion

In this study, we evaluated the kinetic response of the lumbar after different fusion techniques and fixed segments, especially adjacent segments, in combination with *in vitro* biomechanical testing and spinopelvic radiographic parameters. Both single or double-level spinal fusion had the greatest effect on the ROM of the lumbar under flexion loading, followed by lateral bending, extension and axial rotation loading. The upper adjacent segment was the most influenced by the implant in all fusion models, with the most significant compensatory movement, while the effect diminished as the distance between the adjacent segments increased. The implant, it was thought, altered the geometry of the spine and reconstructed the sagittal parameters match. As a result, neither after single-level lumbar fusion nor after double-level lumbar fusion, most sagittal parameters in the normal spine before fusion correlated with the ROM of the spine.

The Coflex dynamic implantation for single-level fixation remained partial movement of the target segment, affecting only the range of movement under extension loading. These findings were consistent with the previous research. Wilke et al. (1998) demonstrated that Coflex dynamic fixation reduced the ROM in the posterior extension of the lumbar spine by approximately 50% compared to the intact lumbar spine, and the ROM was not significantly affected in flexion, lateral bending, and rotation. Pan et al. (2016) also found no significant effects on adjacent segments in the lumbar model after Coflex fixation. The Fusion fixation had a greater effect on the ROM than that of the Coflex fixation, but both limited the extension movement. The ROM of the upper L3-l4 adjacent segment was affected by both fusion methods, however, there was no significant effect on the ROM of the inferior L5-S1 adjacent segment. The result was consistent with the clinical cases, that upper adjacent segments were more prone to secondary accelerated degeneration.

For double-segment internal fixation, although Coflex + Fusion fixation had less effect on the motion of adjacent segments than that of Fusion + Fusion fixation, the ROM of adjacent segments also significantly increased. Similar results were reported by Mageswaran et al. (2012) that the ROM of adjacent segments in an *in vitro* experimental model significantly increased in flexion, extension, and axial rotation after L3-L4 semi-rigid screw dynamic fixation + L4-L5 fusion fixation. Strube et al. (2010) also showed that, after dynamic fixation combined with fusion fixation, the ROM of the upper adjacent segments still increased significantly. It was worth noting that the protection of adjacent segments by this dynamic fixation method may not delay the degeneration of adjacent segments in the case of double-segment fixation.

Sagittal alignment plays a critical role in the biomechanical adaptation and compensation of the spine. Our previous study suggested that sagittal parameters were mainly correlated to the ROM response of the lumbar spine under sagittal (flexion and extension) loading, but had little effect on the ROM under lateral flexion and axial rotation loads. In this study, the preoperative lumbar PT was the only sagittal parameter associated with the overall ROM after single or double-level spinal fusions under extension loading. Roussouly and Nnadi (2010), Roussouly and Pinheiro-Franco (2011) advised that PT reflected the ability of the pelvis to rotate around the femoral head. Our results found that most sagittal parameters of the original lumbar before fusion did not correlated with the ROM after both single or double-level lumbar fusion. Traditional internal fixation with stiffness higher than vertebrae completely alters the original structure and shape of the lumbar, putting patients at risk of overtreatment. For the Coflex dynamic fixation, the ROM after fusion was still associated with PI, SS, LL, and Apex in flexion. That indicated that Coflex dynamic fixation had less interference with the original morphology of the lumbar spine, but, in the Coflex + Fusion fixation, such retention of the original morphology disappeared.

There were several limitations to the current study. Firstly, the number of samples in this study was limited due to the difficulty in obtaining qualified lumbar spine specimens. These data did not support a correlation analysis between the lumbar sagittal classification of lumbar vertebrae and ROM. Secondly, *in vitro* testing protocols and facilities for similar studies are complex and diverse. Our data cannot be directly compared with published results from other experiments. Thirdly, muscles and other soft tissues of the spine were not considered in this biomechanical testing. The results are somewhat different from the real state of the human lumbar spine. Despite these limitations, our study can provide insights into how single or double-level spinal fusion affects lumbar motion and a better understanding of the correlation between preoperative sagittal parameters and lumbar movements after different lumbar internal fixation techniques.

Conclusion

Our findings revealed the different kinetic characteristics of the dynamic Coflex and rigid fusion devices for single and double-level lumbar fusion. The Coflex exhibited its advantage in single-level lumbar fusion that preserved partial movement of the target segment and lowered motion compensation in the upper adjacent segment. For the double-level lumbar fixation, although the range of motion of adjacent segments in the Coflex + Fusion fixation was smaller than that in the Fusion + Fusion fixation, there was no significant difference. PT was the only preoperative lumbar sagittal parameter associated with the range of motion after single and double-level fusions in extension. Coflex dynamic fixation showed the ability to reduce interference in the lumbar spine's original shape. This study proposed a preliminary experimental assessment approach for studying the effects of various surgical implants on the biomechanical response of patients with a range of preoperative lumbar sagittal parameters.

Data availability statement

The original contributions presented in the study are included in the article/supplementary material, further inquiries can be directed to the corresponding authors.

Ethics statement

The studies involving human participants were reviewed and approved by Bioethics and Medical Ethics Committee, Beihang

University (No.: BM20190009). The patients/participants provided their written informed consent to participate in this study.

Author contributions

Conceptualization, WW; methodology, CK; validation, XW; formal analysis, FP; writing—original draft preparation, YW; writing—review and editing, BP; supervision, SL.

Funding

This research was funded by National Natural Science Foundation of China, grant numbers 81672201, 81871794, and 11972065.

Conflict of interest

The authors declare that the research was conducted in the absence of any commercial or financial relationships that could be construed as a potential conflict of interest.

Publisher's note

All claims expressed in this article are solely those of the authors and do not necessarily represent those of their affiliated organizations, or those of the publisher, the editors and the reviewers. Any product that may be evaluated in this article, or claim that may be made by its manufacturer, is not guaranteed or endorsed by the publisher.

References

Bari, T. J., Hansen, L. V., and Gehrchen, M. (2020). Surgical correction of adult spinal deformity in accordance to the roussouly classification: Effect on postoperative mechanical complications. *Spine Deform.* 8, 1027–1037. doi:10.1007/s43390-020-00112-6

Duval-Beaupère, G., Schmidt, C., and Cosson, P. (1992). A barycentremetric study of the sagittal shape of spine and pelvis: The conditions required for an economic standing position. *Ann. Biomed. Eng.* 20, 451–462. doi:10.1007/BF02368136

Ferrero, E., Vira, S., Ames, C. P., Kebaish, K., Obeid, I., O'Brien, M. F., et al. (2016). Analysis of an unexplored group of sagittal deformity patients: Low pelvic tilt despite positive sagittal malalignment. *Eur. Spine J.* 25, 3568–3576. doi:10.1007/s00586-015-4048-1

Kettler, A., Rohlmann, F., Ring, C., Mack, C., and Wilke, H. J. (2012). Erratum: Do early stages of lumbar intervertebral disc degeneration really cause instability? Evaluation of an *in vitro* database. *Eur. Spine J.* 21, 1414. doi:10.1007/s00586-012-2160-z

Kong, C., Lu, S., Hai, Y., and Zang, L. (2015). Biomechanical effect of interspinous dynamic stabilization adjacent to single-level fusion on range of motion of the transition segment and the adjacent segment. *Clin. Biomech. (Bristol, Avon.* 30, 355–359. doi:10.1016/j.clinbiomech.2015.02.012

Louie, P. K., Haws, B. E., Khan, J. M., Markowitz, J., Movassaghi, K., Ferguson, J., et al. (2019). Comparison of stand-alone lateral lumbar interbody fusion versus open laminectomy and posterolateral instrumented fusion in the treatment of adjacent segment disease following previous lumbar fusion surgery. *Spine* 44, E1461–E1469. doi:10.1097/BRS.0000000000003191

Mageswaran, P., Techy, F., Colbrunn, R. W., Bonner, T. F., and McLain, R. F. (2012). Hybrid dynamic stabilization: A biomechanical assessment of adjacent and supraadjacent levels of the lumbar spine: Laboratory investigation. *J. Neurosurg. Spine* 17, 232–242. doi:10.3171/2012.6.SPINE111054

O'Connell, G. D., Vresilovic, E. J., and Elliott, D. M. (2007). Comparison of animals used in disc research to human lumbar disc geometry. *Spine* 32, 328–333. doi:10.1097/01.brs.0000253961.40910.c1

Pan, A., Hai, Y., Yang, J., Zhou, L., Chen, X., and Guo, H. (2016). Adjacent segment degeneration after lumbar spinal fusion compared with motion-preservation procedures: A meta-analysis. *Eur. Spine J.* 25, 1522–1532. doi:10.1007/s00586-016-4415-6

Panjabi, M. M. (1998). Cervical spine models for biomechanical research. *Spine* 23, 2684–2699. doi:10.1097/00007632-199812150-00007

Panjabi, M. M., Goel, V., Oxland, T., Takata, K., Duranceau, J., Krag, M., et al. (1992). Human lumbar vertebrae: Quantitative three-dimensional anatomy. *Spine (Phila. pa. 1976)* 17, 299–306. doi:10.1097/00007632-199203000-00010

Panjabi, M. M. (2007). Hybrid multidirectional test method to evaluate spinal adjacent-level effects. *Clin. Biomech.* 22 (3), 257–265. doi:10.1016/j.clinbiomech.2006.08.006

Pieler-Bruha, E. (2016). Paraspinal muscle, facet joint, and disc problems: Risk factors for adjacent segment degeneration after lumbar fusion. *J. fur Min.* 23, 102–103.

Roussouly, P., Gollogly, S., Berthonnaud, E., and Dimnet, J. (2005). Classification of the normal variation in the sagittal alignment of the human lumbar spine and pelvis in the standing position. *Spine* 30, 346–353. doi:10.1097/01.brs.0000152379.54463.65

Roussouly, P., and Nnadi, C. (2010). Sagittal plane deformity: An overview of interpretation and management. *Eur. Spine J.* 19, 1824–1836. doi:10.1007/s00586-010-1476-9

Roussouly, P., and Pinheiro-Franco, J. L. (2011). Biomechanical analysis of the spino-pelvic organization and adaptation in pathology. *Eur. Spine J.* 20 (5), 609–618. doi:10.1007/s00586-011-1928-x

Sangiorgio, S. N., Sheikh, H., Borkowski, S. L., Khoo, L., Warren, C. R., and Ebramzadeh, E. (2011). Comparison of three posterior dynamic stabilization devices. *Spine* 36, 1251–1258. doi:10.1097/BRS.0b013e318206cd84

Sebaaly, A., Gehrchen, M., Silvestre, C., Kharrat, K., Bari, T. J., Kreichati, G., et al. (2020). Mechanical complications in adult spinal deformity and the effect of restoring the spinal shapes according to the roussouly classification: A multicentric study. *Eur. Spine J.* 29, 904–913. doi:10.1007/s00586-019-06253-1

Sebaaly, A., Grobost, P., Mallam, L., and Roussouly, P. (2018). Description of the sagittal alignment of the degenerative human spine. *Eur. Spine J.* 27, 489–496. doi:10.1007/s00586-017-5404-0

Shen, J., Wang, Q., Wang, Y., Min, N., Wang, L., Wang, F., et al. (2021). Comparison between fusion and non-fusion surgery for lumbar spinal stenosis: A meta-analysis. *Adv. Ther.* 38, 1404–1414. doi:10.1007/s12325-020-01604-7

Strube, P., Tohtz, S., Hoff, E., Gross, C., Perka, C., and Putzier, M. (2010). Dynamic stabilization adjacent to single-level fusion: Part I. Biomechanical effects on lumbar spinal motion. *Eur. Spine J.* 19, 2171–2180. doi:10.1007/s00586-010-1549-9

Wang, M., Xu, L., Chen, X., Zhou, Q., Du, C., Yang, B., et al. (2021). Optimal reconstruction of sagittal alignment according to global alignment and proportion score can reduce adjacent segment degeneration after lumbar fusion. *Spine (Phila. pa. 1976)* 46, E257–E266. doi:10.1097/BRS.0000000000003761

Whitecloud, T. S., Davis, J. M., and Olive, P. M. (1994). Operative treatment of the degenerated segment adjacent to a lumbar fusion. *Spine (Phila. pa. 1976)* 19, 531–536. doi:10.1097/00007632-199403000-00007

Wilke, H.-J., Wenger, K., and Claes, L. (1998). Testing criteria for spinal implants: Recommendations for the standardization of *in vitro* stability testing of spinal implants. *Eur. Spine J.* 7, 148–154. doi:10.1007/s005860050045

Zhao, H., Duan, L. J., Gao, Y. S., Yang, Y. D., Zhao, D. Y., Tang, X. S., et al. (2018). Retraction Note: Comparison of two FDA-approved interspinous spacers for treatment of lumbar spinal stenosis: Superion versus X-STOP-a meta-analysis from five randomized controlled trial studies. *J. Orthop. Surg. Res.* 13 (1), 138. doi:10.1186/s13018-018-0845-7

Zheng, X., Chen, Z., Yu, H., Zhuang, J., Yu, H., and Chang, Y. (2021). A minimum 8-year follow-up comparative study of decompression and coflex stabilization with decompression and fusion. *Exp. Ther. Med.* 21, 595. doi:10.3892/etm.2021.10027

Zhou, C., Cha, T., Wang, W., Guo, R., and Li, G. (2020). Investigation of alterations in the lumbar disc biomechanics at the adjacent segments after spinal fusion using a combined *in vivo* and in silico approach. *Ann. Biomed. Eng.* 1, 601–616. doi:10.1007/s10439-020-02588-9

Zhou, C., Jin, S., and Willing, R. (2016). Simulation of extracellular matrix remodeling by fibroblast cells in soft three-dimensional bioresorbable scaffolds. *Biomech. Model. Mechanobiol.* 15, 1685–1698. doi:10.1007/s10237-016-0791-4

frontiers | Frontiers in Bioengineering and Biotechnology

TYPE Original Research
PUBLISHED 30 August 2022
DOI 10.3389/fbioe.2022.922848

OPEN ACCESS

EDITED BY
Keitaro Matsukawa,
Murayama Medical Center (NHO),
Japan

REVIEWED BY
Xin Zhao,
Shanghai Jiao Tong University, China
Panagiotis Chatzistergos,
Staffordshire University,
United Kingdom
Wen Yuan,
Shanghai Changzheng Hospital, China
Yun Peng,
NuVasive, United States

*CORRESPONDENCE
Yue-Ming Song,
sym_cd@163.com
Jian-Cheng Zeng,
tomzeng5@126.com

†These authors have contributed equally to this work and share first authorship

SPECIALTY SECTION
This article was submitted to Biomechanics,
a section of the journal
Frontiers in Bioengineering and Biotechnology

RECEIVED 18 April 2022
ACCEPTED 29 July 2022
PUBLISHED 30 August 2022

CITATION
Li J-C, Yang Z-Q, Xie T-H, Song Z-T, Song Y-M and Zeng J-C (2022), Deterioration of the fixation segment's stress distribution and the strength reduction of screw holding position together cause screw loosening in ALSR fixed OLIF patients with poor BMD. *Front. Bioeng. Biotechnol.* 10:922848. doi: 10.3389/fbioe.2022.922848

Deterioration of the fixation segment's stress distribution and the strength reduction of screw holding position together cause screw loosening in ALSR fixed OLIF patients with poor BMD

Jing-Chi Li[1†], Zhi-Qiang Yang[1†], Tian-Hang Xie[1], Zhe-Tao Song[2], Yue-Ming Song[1*] and Jian-Cheng Zeng[1*]

[1]Department of Orthopedic Surgery and Orthopedic Research Institute, West China Hospital/West China School of Medicine for Sichuan University, Chengdu, China, [2]Department of Imaging, West China Hospital, Chengdu, China

The vertebral body's Hounsfield unit (HU) value can credibly reflect patients' bone mineral density (BMD). Given that poor bone-screw integration initially triggers screw loosening and regional differences in BMD and strength in the vertebral body exist, HU in screw holding planes should better predict screw loosening. According to the stress shielding effect, the stress distribution changes in the fixation segment with BMD reduction should be related to screw loosening, but this has not been identified. We retrospectively collected the radiographic and demographic data of 56 patients treated by single-level oblique lumbar interbody fusion (OLIF) with anterior lateral single rod (ALSR) screw fixation. BMD was identified by measuring HU values in vertebral bodies and screw holding planes. Regression analyses identified independent risk factors for cranial and caudal screw loosening separately. Meanwhile, OLIF with ALSR fixation was numerically simulated; the elastic modulus of bony structures was adjusted to simulate different grades of BMD reduction. Stress distribution changes were judged by computing stress distribution in screws, bone-screw interfaces, and cancellous bones in the fixation segment. The results showed that HU reduction in vertebral bodies and screw holding planes were independent risk factors for screw loosening. The predictive performance of screw holding plane HU is better than the mean HU of vertebral bodies. Cranial screws suffer a higher risk of screw loosening, but HU was not significantly different between cranial and caudal sides. The poor BMD led to stress concentrations on both the screw and bone-screw interfaces. Biomechanical deterioration was more severe in the cranial screws than in

Abbreviations: ALSR, anterior lateral single rod; BEP, bony endplate; BMD, bone mineral density; BMI, body mass index; CEP, cartilage endplate; CT, computational tomography; FEA, finite element analysis; HU, Hounsfield units; ICC, intraclass correlation efficiency; IDP, intradiscal pressure; IVD, intervertebral disc; OLIF, oblique lumbar interbody fusion; PEEK, polyether ether ketone; ROC, receiver operating characteristics; ROM, range of motion; SL, segmental lordotic.

the caudal screws. Additionally, lower stress can also be observed in fixation segments' cancellous bone. Therefore, a higher proportion of ALSR load transmission triggers stress concentration on the screw and bone-screw interfaces in patients with poor BMD. This, together with decreased bony strength in the screw holding position, contributes to screw loosening in osteoporotic patients biomechanically. The trajectory optimization of ALSR screws based on preoperative HU measurement and regular anti-osteoporosis therapy may effectively reduce the risk of screw loosening.

KEYWORDS

oblique lumbar interbody fusion, screw loosening, biomechanical deterioration, anterior lateral single rod fixation, screw holding plane, stress distribution

1 Introduction

Anterior lateral single rod (ALSR) fixation can provide sufficient instant postoperative stability for oblique lumbar interbody fusion (OLIF) patients without the need for other surgical incisions (Zhao et al., 2022a; Zhao et al., 2022b). As a hardware-related complication, screw loosening has been widely reported, negatively affecting patients' rehabilitation and deteriorating long-term prognosis (Bokov et al., 2019; Zou et al., 2020). Osteoporosis is an essential risk factor for this complication. Bone-screw integration was aggravated with the reduction in bone mineral density (BMD); this was proven to be the primary mechanism for the higher risk of screw loosening in osteoporotic patients (Bokov et al., 2019; Zou et al., 2020).

Traditionally, the dual-energy X-ray absorptiometry is the gold standard for diagnosing osteoporosis. However, this imaging examination cannot eliminate pathological bone formation during lumbar degenerative diseases (e.g., osteophytes, endplate sclerosis, and zygapophyseal joint osteoarthritis). This leads to an underestimation of the severity of osteoporosis in patients with lumbar degenerative diseases (Mikula et al., 2019; Zou et al., 2020). The vertebral Hounsfield unit (HU) value measured by computed tomography (CT) has been widely used to diagnose osteoporosis (Bredow et al., 2016; Gausden et al., 2017). The confounding effect of pathological bone formation can be eliminated during the measurement of HU in the vertebral body by adjusting the region of interest (Mi et al., 2017; Zou et al., 2019). Thus, HU has become a credible indicator in BMD judgment.

Presently, the HU value of the vertebral body is defined by the average value of four planes, including the midsagittal plane, central transverse plane, and transverse planes close to the superior and inferior bony endplates (Figure 1) (Bredow et al., 2016; Zou et al., 2019). Although this HU definition method is commonly used in BMD judgment and screw loosening risk prediction for patients with lumbar screw fixation, it still has inherent defects: it cannot directly reflect the BMD in the screw holding plane. As mentioned above, the yield strength reduction of cancellous bone is the main biomechanical mechanism for poor bone-screw integration and resulting screw loosening in osteoporotic patients, and regional differences in BMD and strength in cancellous bone exist (Smit et al., 1997; Wegrzyn et al., 2010). We hypothesize that the HU measurement of the screw holding plane can better reflect changes in these local effects.

As above mentioned, surgeons believe that the decreased bony strength is the main reason for the increased risk of screw loosening in osteoporotic patients. Meanwhile, studies illustrated that stress concentration on the bone-screw interfaces and fixation screws would aggravate poor bone-screw integration and result in screw loosening (Tsuang et al., 2016; Pearson et al., 2017; Nowak, 2019; Kanno et al., 2021). Specifically, according to the stress shielding effect, the reduction of BMD will aggravate the stiffness differences between bony structures and titanium screws (Agarwal et al., 2016; Hsieh et al., 2020). As a result, a higher proportion of stress should be transported by the screw fixation system. Therefore, we hypothesize that this may be the potential mechanism for the stress concentration of screw and bone screw interfaces. In other words, a higher risk of screw loosening in osteoporotic patients may not be limited to poor bone quality but also biomechanical deterioration in bone-screw interfaces, but this has still not been verified.

In this study, to verify these hypotheses, we investigated whether the HU in the screw holding plane is a better predictor during the judgment of screw loosening and investigated changes in the load transmission proportion between the vertebral body and ALSR screw system with BMD stepwise reduction. The prospectively collected radiographic and demographic data of OLIF patients fixed by ALSR were retrospectively reviewed. Changes in the stress distribution of the ALSR fixation segment were investigated by computing biomechanical changes in fixation screws, bone-screw interfaces, and cancellous bones of vertebral bodies in an anteriorly constructed and validated lumbosacral model. This study could provide theoretical guidance for understanding the screw loosening mechanism and feasible methods to reduce the risk of screw loosening.

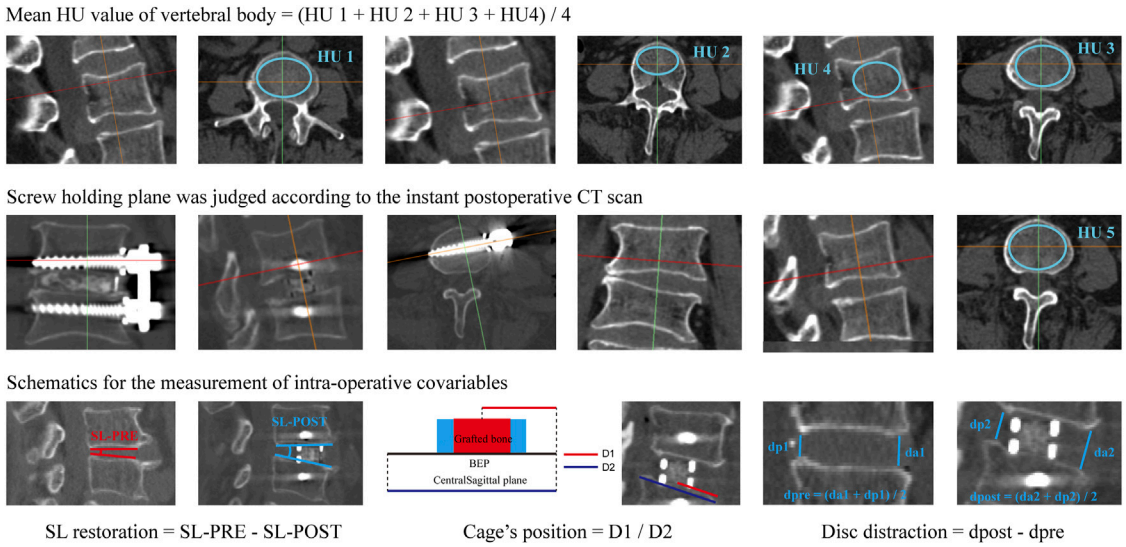

FIGURE 1
Schematic of different HU measurement methods and the measurement of intraoperative covariables. HU1, HU in the transverse plane close to the superior BEP; HU2, HU in the central transverse plane; HU3, HU in the transverse plane close to the inferior BEP; HU4, HU in the midsagittal plane; The mean value of HU1 to HU4 was defined as the mean HU of the vertebral body; HU5, HU value of the screw holding plane.

2 Materials and methods

2.1 Review of prospectively collected radiographic and demographic data

2.1.1 Patient collection

The ethics committees of West China Hospital approved the protocol of this study (2020-554). Informed consent was waived for this retrospective study. We retrospectively reviewed the radiographic and demographic data of OLIF patients with ALSR screw fixation from May 2017 to August 2019. Their age, sex, and body mass index (BMI) were recorded. A senior spine surgeon performed all operations. Screw types and sizes were identical in these patients. All screws were placed in a single attempt and penetrated the contralateral cortex.

Patients who underwent single segment OLIF with ALSR screw fixation for patients with lumbar degenerative diseases, including spinal stenosis, grade 1 and grade 2 degenerative spondylolisthesis, and lumbar disc herniation, were included in this study. The exclusion criteria were as follows: 1) Patients with a history of lumbar surgery; 2) Patients with primary or metastatic spinal tumors, lumbar tuberculosis, rheumatic immune diseases, and secondary osteoporosis caused by medication or other metabolic diseases; 3) Patients with grade 3 and grade 4 degenerative spondylolisthesis or spondylolysis; 4) Patients who underwent lumbar revision surgery within the clinical follow-up period of 12 months for complications other than screw loosening; 5) Patients who underwent intraoperative screw replacement.

2.1.2 Radiographic data collections

Patients underwent lumbar computational tomography (CT) three times in the imaging center of West China Hospital, including 1 week before, 1 week after, and 1 year after OLIF surgery. The tube voltage was set to 120 kV, and all CT scan setting parameters were uniform in all enrolled patients (Mikula et al., 2019; Xi et al., 2020; Zou et al., 2020). An experienced spine surgeon independently measured the screw loosening status and radiographic parameters mentioned in the Figure 1. The interobserver and intraobserver reliability of these measured parameters was verified in 10 randomly selected patients. One week after the imaging measurement, the spine surgeon and a senior radiologist independently remeasured the imaging parameters of these selected patients. These measurement results were recorded separately to verify intraobserver and interobserver consistency.

The screw loosening status of the cranial and caudal vertebral bodies was judged separately. In the postoperative 1 year CT imaging data, vertebral bodies with ≥1 mm width radiolucent zones around the screw were defined as screw loosening (Figure 2) (Bredow et al., 2016; Bokov et al., 2019; Zou et al., 2020). The BMD of these patients was identified by measuring their Hounsfield unit (HU) values in the preoperative CT imaging data. During HU measurement in vertebral bodies, the region of interest was expanded to the largest within the cancellous bone but excluded other bony structures, such as **cortical shell**, BEP, and osteophytes (Schreiber et al., 2014; Xi et al., 2020; Zou et al., 2020). As

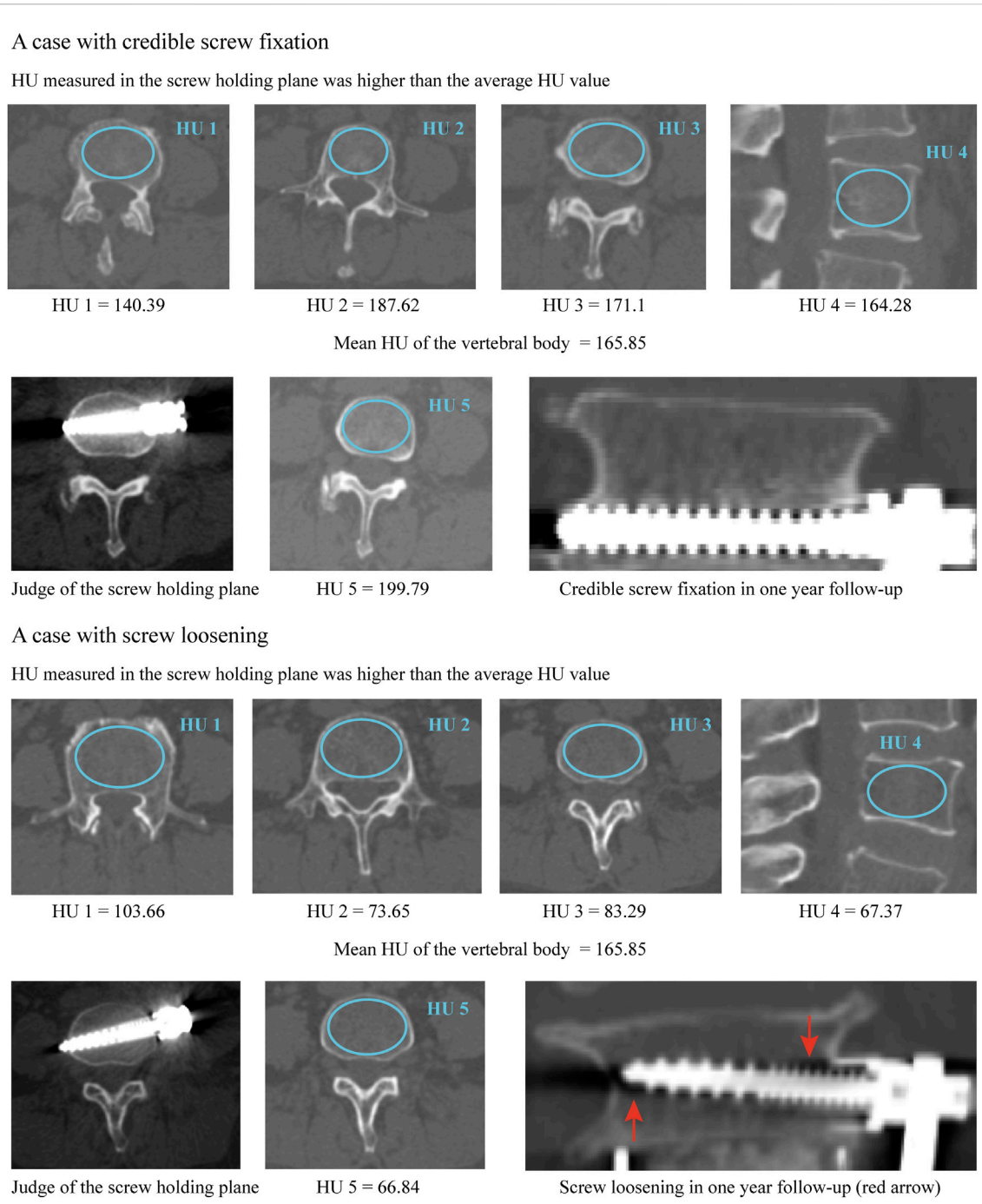

FIGURE 2
Typical cases for the better predictive performance of screw holding plane HU when predicting the risk of screw loosening.

mentioned above, HU was measured separately at the midsagittal plane, central transverse plane, and transverse planes close to the superior and inferior endplates. These HU values were defined as HU1 to HU4. The average value of these planes was set as the HU of the vertebral body (Pickhardt et al., 2013; Mikula et al., 2019; Xi et al., 2020; Zou et al., 2020). The screw holding plane was identified based on the instant postoperative CT imaging data (Ishikawa et al., 2018; Sakai et al., 2018; Xu et al., 2020). The HU value measured on the corresponding transverse plane in preoperative CT was defined as HU5 to represent the BMD of the screw holding cancellous bone (Figure 1).

Meanwhile, considering that disc distraction, segmental lordotic (SL) angle restoration, and cage position could affect local transmission patterns, these values were regarded as covariables and were also been measured in this study (Okuda et al., 2006; Landham et al., 2017). Disc height was measured on the central sagittal plane, and its value was defined as the average value of the anterior and posterior disc height. The difference in disc height between pre- and postoperation was defined as the value of disc distraction (Kaito et al., 2011; Havey et al., 2012). The SL angle was also measured on the central sagittal plane, and differences in SL between pre- and postoperation were defined as the value of SL restoration. The cage's position was identified in the instant postoperative CT scan (Figure 1) (Labrom et al., 2005; Landham et al., 2017; Park et al., 2017; He et al., 2021).

2.1.3 Statistical analyses

Radiographic and demographic indicators are presented as the mean ± standard deviation for continuous variables and the number (percentage) for categorical variables. We conducted statistical analyses in SPSS 23.0 software. The intraclass correlation efficiency (ICC) was computed to identify the repeatability of continuous variables (ICC ≥0.8 represents excellent reliability) (Zou et al., 2019; Zou et al., 2020). The kappa values were computed to determine the repeatability of screw loosening (kappa values of 0.41–0.60 indicated moderate reliability; 0.61–0.80, substantial agreement; and 0.81–1.00, excellent or almost perfect agreement) (Oetgen et al., 2008; Yue et al., 2008). ICC values were also computed to identify the consistency between HU values of the vertebral body and holding plane.

Statistical analyses for cranial and caudal side screw loosening were performed separately. When comparing the difference between different groups, the independent samples Student`s *t* test was used for continuous variables, and the chi-square test was used for the categorical variables. When comparing the significant difference between two groups by the Student's *t*-test, all indexes from random samples were normal distribution, and all parameters of the experimental and control groups had homogeneity of variance. We performed binary logistic regression to identify independent risk factors for screw loosening. When using the binary logistic regression, the dependent variable (screw loosening status) is a binary classification variable (which is from different patients and therefore fully independent); its classification is complete and exclusive (screw loosening or not). In the multivariate analysis, all factors had no significant collinearity, and there are no obvious outliers and strong influence points for all included parameter values. Univariate analyses of each potential risk factor were performed, and the variables that achieved a significance level of $p < 0.1$ were entered into multivariate analyses. Variables with $p < 0.05$ were considered independent risk factors in the multivariate analyses (Zhao et al., 2009; Park et al., 2017; Bagheri et al., 2019; Pisano et al., 2020; Zou et al., 2020). Regarding the sample size in this study, we declare that this was a retrospective study, and all patients who meet the inclusive criteria were enrolled in it. In the multivariate analysis, the sample size is more than 20 times the number of independent variables. Therefore, we believe that the sample size in this study is sufficient to investigate potential risk factors for screw loosening. A *p* value less than 0.05 indicated a significant difference.

2.2 Numerical biomechanical simulations of changes in stress distribution

2.2.1 Study design protocol of the surgical simulation

FEA is considered a reliable method for evaluating biomechanical changes related to screw loosening for its ability to accurately qualify the stress level of special components (Hsu et al., 2005; Kang et al., 2014; Guvenc et al., 2019). The most maligned limitation of numerical biomechanical simulations (i.e., FEA) is that FEA could not investigate the biomechanical significance of several covariables based on a single calibrated intact model. Adimittednly, the current FEA models have not simulated covariables, including SL restorations, cage positions, and disc distractions (i.e., changes in postoperative disc height) (Labrom et al., 2005; Kaito et al., 2010; Havey et al., 2012; Landham et al., 2017). Therefore, these models cannot identify the biomechanical significance of factors related to these covariables (e.g., changes in tensile stress of ligaments and muscles).

To demonstrate the reliability of numerical simulations (i.e., prove that the covariables mentioned above could not affect the screw loosening risk), these covariables have been included in regression analyses to judge the risk of screw loosening. Since these covariables did not differ significantly between the credible screw fixation group and the group of screw loosening and were not independent risk factors for screw loosening, we believe that not simulating these covariables will not affect the reliability of the numerical simulation results in this study. Therefore, when investigating the biomechanical significance of a particular variable, we believe researchers should eliminate the interference of covariables by reviewing radiographic and demographic data, and this may be a feasible method to optimize the credibility of FEA studies.

2.3 Model construction strategy

2.3.1 Construction of the intact model

Simulation of OLIF with ALSR fixation was performed in a previously constructed and validated biomimetic lumbosacral FE model (L3-S1) (Li et al., 2021b; Xu et al., 2022b). Bone structures of the FE model include cortical shell, cancellous, and BEPs. The

cortical thickness was set as 0.8 mm, and the thickness and morphology parameters (i.e., concave angles and depths) of BEPs were defined separately based on anatomic studies. Nonbony components include the intervertebral disc (IVD) and facet cartilages. The IVD consists of the nucleus, annulus, and cartilage endplates (CEPs). On the basis of imaging data measurements, the nucleus's cross-sectional area accounted for 38% of the IVD (Li et al., 2021b). The annulus was divided into four different layers; the outline of the BEP covers the entire IVD, and that of the CEP covers the nucleus and inner part of the annulus (Jacobs et al., 2014; Delucca et al., 2016). Ligaments and facet capsules were defined as cable elements in the preprocessing process of finite element analysis (FEA) (Dreischarf et al., 2014; Li et al., 2021a). To optimize the computational accuracy of the FEA model, model calibration was performed by adjusting the annulus average radius and nucleus positions in our previously published studies (Li et al., 2021b; Xu et al., 2022b). Specifically, by repeatedly computing the range of motions (ROMs) in the L4-L5 segment and adjusting these calibrated parameters, the differences between computed ROMs and measured values from widely cited *in vitro* studies could be reduced, and the computational stress values can make a good representation of real biomechanical situations.

2.3.2 Construction of the OLIF model with ALSR fixation

The L4-L5 segment was selected to simulate ALSR fixed OLIF. Surgical simulations were performed based on a literature review and our surgical experience. In this process, lateral parts of the annulus, all of the nucleus, and CEPs were removed, and a polyether-ether-ketone (PEEK) OLIF cage (18 mm width and 50 mm length) filled with grafted bone was inserted into the interbody space (Guo et al., 2020; Xi et al., 2020). The lordotic angle and disc height of the postoperative models were identical to those of the intact model to eliminate the mechanical effects of these parameters (Kim et al., 2015b; Wang et al., 2019; Guo et al., 2020).

The three-dimensional model of the fixation screw was reversely constructed based on the outline of the screw used in ALSR fixation in our clinical practice. During the simulation of ALSR screw fixation, two titanium alloy screws were inserted into the L4-L5 vertebral bodies and penetrated the contralateral cortex. The axes of the screws in the transverse plane were parallel to the OLIF cage, whereas those in the coronal plane were parallel to the BEPs (Guo et al., 2020; Xie et al., 2020). Screw threads were preserved, and the screw compaction effect was simulated by adjusting the material property of cancellous around the thread (Hsu et al., 2005; Matsukawa et al., 2016). The connection between the screw tulip, the nut, and the spacer was simplified to increase the computational efficiency (Xu et al., 2022a).

2.4 Boundary and loading conditions

2.4.1 Mesh generations and model validations

FEA in this study was performed in the "Ansys workbench 2020 r2 academic". Hybrid elements (e.g., tetrahedron and hexahedron elements) with different sizes were set in different components of the FE model. Mesh refinement was set in structures with low thickness and large deformation (e.g., BEP, facet cartilage, posterior parts, and the outer layer of the annulus) (Chuang et al., 2013; Dreischarf et al., 2014; Xu et al., 2022b). To eliminate the confounding effect of mesh sizes on computational results, we performed a mesh convergence test on the calibrated intact model by evaluating the change in intradiscal pressure (IDP) with different mesh sizes. The model was considered converged if the change in the computed IDP was less than 3% (Ottardi et al., 2016; Fan et al., 2021). The degrees of freedom of S1 inferior surfaces were fixed entirely. Different directional moments were applied to the superior BEP of L3 (Delucca et al., 2016; Xu et al., 2022a). Additionally, we performed a multi-indicator model validation in the calibrated intact model. The computed ROM, IDP, disc compression, and facet contact force were compared within *in vitro* measured values (Wilson et al., 2006; Renner et al., 2007; Schilling et al., 2011). When the difference between the computed biomechanical value and the *in vitro* measured mean value is less than one standard deviation, the intact model is considered to be validated (Kim et al., 2013; Kim et al., 2015a; Kim et al., 2015b).

2.5 Material properties and contact types definition, and indicators selection.

In the definition of material properties (Table 1), **cortical shell** and cancellous bone were defined by anisotropic law. The annulus was assumed to be hypoelastic material, and the nucleus was set as a semifluid incompressible material (Li et al., 2021b; Xu et al., 2022b). The material properties of the surgical instrumented structure (i.e., PEEK and titanium alloy) were defined by isotropic law (Chuang et al., 2012; Hsieh et al., 2017). By defining the friction coefficients between different contact surfaces, stress levels immediately after operation were computed. Consistent with published studies, the contact between facet cartilages was set as frictionless. Moreover, given the screw loosening occurred in the short postoperative period, the instant postoperative biomechanical environment has been simulated by setting the frictional coefficient between BEP and GB as 0.46, and that between BEP and cage and screw-cancellous interfaces as 0.2 (Lu and Lu, 2019; Rastegar et al., 2020). The simulation of stepwise BMD reduction was performed by modifying the stiffness of bony tissues. In this process, the morphological features of different models remain identical. The material properties of bony tissues with different BMDs are

TABLE 1 Material properties of FE models' components.

Components	Elastic modulus (MPa)	Poisson's ratio	Cross-section (mm^2)	References
Cortical (Normal BMD)	E_{xx} = 11,300	V_{xy} = 0.484		Ferguson and Steffen (2003), Tsouknidas et al. (2015)
	E_{yy} = 11,300	V_{yz} = 0.203		
	E_{zz} = 22,000	V_{xz} = 0.203		
	G_{xy} = 3,800			
	G_{yz} = 5,400			
	G_{xz} = 5,400			
Cancellous (Normal BMD)	E_{xx} = 140	V_{xy} = 0.45		Morgan et al. (2003), Tsouknidas et al. (2015)
	E_{yy} = 140	V_{yz} = 0.315		
	E_{zz} = 200	V_{xz} = 0.315		
	G_{xy} = 48.3			
	G_{yz} = 48.3			
	G_{xz} = 48.3			
Bony endplates (Normal BMD)	12,000	0.3		Li et al. (2019), Kang et al. (2014)
Cortical (Slight reduction of BMD)	Exx = 9,436	Vxy =0.484		Ferguson and Steffen (2003), Tsouknidas et al. (2015)
	Eyy = 9,436	Vyz =0.203		
	Ezz = 18,370	Vxz =0.203		
	Gxy = 3,173			
	Gyz = 4,509			
	Gxz = 4,509			
Cancellous (Slight reduction of BMD)	Exx = 93.8	Vxy = 0.45		Morgan et al. (2003), Tsouknidas et al. (2015)
	Eyy = 93.8	Vyz =0.315		
	Ezz = 150	Vxz =0.315		
	Gxy = 32.36			
	Gyz = 36.23			
	Gxz = 36.23			
Bony endplates (Slight reduction of BMD)	10,035	0.3		Li et al. (2019), Kang et al. (2014)
Cortical (Significant reduction of BMD)	Exx = 7,571	Vxy =0.484		Ferguson and Steffen (2003), Tsouknidas et al. (2015)
	Eyy = 7,571	Vyz =0.203		
	Ezz = 14,740	Vxz =0.203		
	Gxy = 2,546			
	Gyz = 3,618			
	Gxz = 3,618			
Cancellous (Significant reduction of BMD)	Exx = 47.6	Vxy = 0.45		Morgan et al. (2003), Tsouknidas et al. (2015)
	Eyy = 47.6	Vyz =0.315		
	Ezz = 100	Vxz =0.315		
	Gxy = 16.42			
	Gyz = 24.15			
	Gxz = 24.15			
Bony endplates (Significant reduction of BMD)	8,070	0.3		Li et al. (2019), Kang et al. (2014)
Annulus	Hypoelastic material			Kim et al. (2013), Wu and Yao (1976)
Nucleus	1	0.49		Chuang et al. (2013), Qasim et al. (2014)
Cartilage endplates	10	0.4		Li et al. (2019), Li et al. (2021a)
Anterior longitudinal ligaments	Calibrated load-deformation curved under different loading conditions	0.3	60	Du et al. (2016), Li et al. (2021b)

(Continued on following page)

TABLE 1 (*Continued*) Material properties of FE models' components.

Components	Elastic modulus (MPa)	Poisson's ratio	Cross-section (mm^2)	References
Posterior longitudinal ligaments	Calibrated load-deformation curved under different loading conditions	0.3	21	Du et al. (2016), Li et al. (2021a)
Ligamentum flavum	Calibrated load-deformation curved under different loading conditions	0.3	60	Du et al. (2016), Li et al. (2021b)
Interspinous ligaments	Calibrated load-deformation curved under different loading conditions	0.3	40	Du et al. (2016), Li et al. (2021a)
Supraspinous ligaments	Calibrated load-deformation curved under different loading conditions	0.3	30	Du et al. (2016), Li et al. (2021b)
Intertransverse ligaments	Calibrated load-deformation curved under different loading conditions	0.3	10	Du et al. (2016), Li et al. (2021a)
Capsular	7.5 (\25%)	0.3	67.5	Chuang et al. (2013), Li et al. (2019)
	32.9 ([25%)			
PEEK OLIF Cage	3500	0.3		Hsieh et al. (2017), Kang et al. (2014)
Titanium alloy screw	1,10,000	0.3		Hsieh et al. (2017), Kang et al. (2014)

presented in Table 1 (Morgan et al., 2003; Tsouknidas et al., 2015; Li et al., 2019). Finally, when it comes to the selection of computational indicators, the average stress of bone-screw interfaces and cancellous bone and the maximum stress of the screw could credibly judge changes in screw loosening risk (Tsuang et al., 2016; Pearson et al., 2017; Guvenc et al., 2019).

3 Results

3.1 Retrospectively study of prospectively collected data

3.1.1 Patient collection and screw loosening rates

A total of 56 patients (30 males and 26 females) with an average age of 56.57 ± 11.96 years treated by single segment OLIF with ALSR screw fixation were recorded. The interobserver and intraobserver results during the judgment of screw loosening were substantial, with Kappa values of 0.778 and 0.759, respectively. The reliability of continuous variable measurement was excellent, with ICCs of 0.867 and 0.835, respectively (Table 2). The overall incidence rate of screw loosening was 35.71% (40/112), the screw loosening rate of the vertebral body on the cranial side was 42.86% (24/56) and that of the caudal vertebral body was 28.57% (16/56). There were no significant differences in HU between the cranial and caudal sides, whether the HU was measured by the mean value of vertebral bodies (p = 0.525) or in the screw holding plane (p = 0.707). Excellent consistency between vertebral bodies' HU and HU of screw holding planes can be observed in cranial and caudal vertebral bodies and groups with credible screw fixation and screw loosening (Table 3). Although there were no significant differences, the HU of the screw holding planes was higher than the vertebral bodies' HU in the credible screw fixation group and was lower than the mean HU of the vertebral bodies in the screw loosening group (Figures 2, 3).

TABLE 2 Validation of measured values repeatability.

	Interobserver	Intraobserver
ICCs of continuous variables	0.867	0.835
Kappa values of union status	0.789	0.746

TABLE 3 Validation of consistency between HU values of the vertebral body and holding plane.

	Credible screw fixation	Screw loosening
Cranial	0.897	0.958
Caudal	0.966	0.961

3.1.2 Identification of independent risk factors for screw loosening

The age of patients with cranial side screw loosening was significantly higher (p = 0.033). The HU values in the credible screw fixation group (i.e., without screw loosening) were significantly higher than those in the screw loosening group, whether the HU was measured by the mean value of vertebral bodies or in the screw holding plane (Figure 2). Based on the results of univariate logistic regression analyses, these three indicators were also entered into the multivariate analysis to

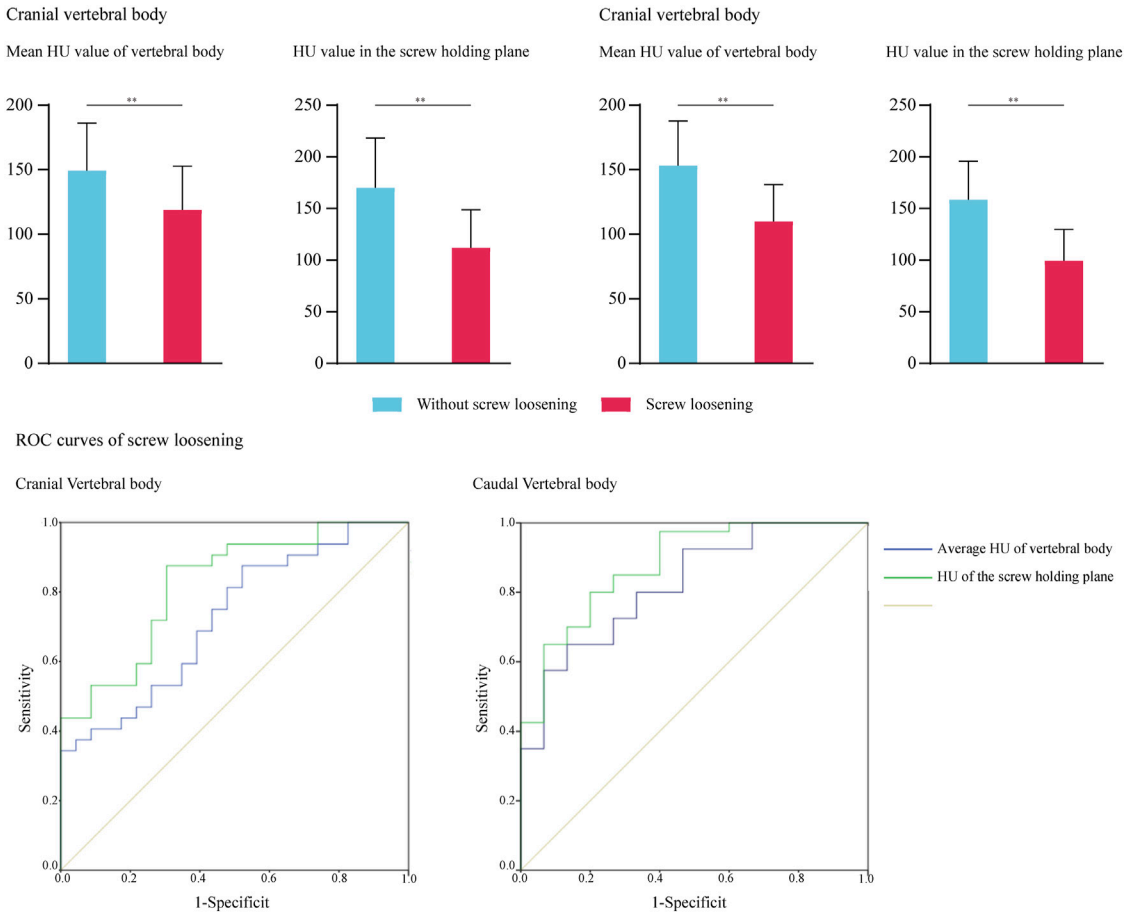

FIGURE 3
ROC curves for cranial and caudal side screw loosening and significant difference for HU in groups with credible screw fixation and screw loosening.

identify independent risk factors. Considering the excellent consistency between vertebral bodies' HU and HU of screw holding planes, the multivariate analysis of vertebral bodies' HU and HU in screw holding planes was performed separately. The results showed that reducing HU, both measured by these two methods, was an independent risk factor for screw loosening on the cranial side (Tables 3, 4); the p value of vertebral bodies' HU was 0.005, and that of HU in screw holding planes was 0.000.

Concerning the caudal side, there were no significant age differences between patients with credible fixation and screw loosening ($p = 0.117$). The variation tendency of HU changes was consistent with the cranial vertebral body. Considering that only the p values of vertebral body HU and screw holding plane HU reduction were <0.1 in the univariate logistic regression analysis, multivariate analysis was not performed. The reduction of vertebral bodies' HU and screw holding planes' HU were regarded as independent risk factors for screw loosening in the caudal vertebral body (Figure 3 and Table 5); the p value of vertebral bodies' HU was 0.001, of HU in screw holding planes, was 0.000, separately. Other covariables, including sex, BMI, SL restoration, disc distraction, and cage positions, did not significantly affect the risk of screw loosening. Additionally, the values of intraoperative covariables (i.e., cage position, SL restoration, disc distraction) were not significantly different between the credible screw fixation group and the screw loosening groups. These covariables were not independent risk factors for screw loosening on either the cranial or caudal sides.

3.1.3 Parameter prediction values for screw loosening

We performed ROC curve analyses to assess the predictive value of vertebral body HU and HU measured in the screw holding plane; the results are summarized in Figure 3 and Table 6. Consistent with logistic regression analyses, HU values measured in the screw holding plane had the highest

TABLE 4 Logistic regression analysis of the cranial screw loosening.

	OR	95% CI		*p*
Univariate analysis				
Gender	2.333	0.791	6.885	0.125
Age	1.053	1.003	1.106	0.039[a]
BMI	0.972	0.83	1.138	0.723
SL restoration	1.1	0.949	1.275	0.208
Cage's position	0.979	0.909	1.054	0.568
Disc distraction	1.152	0.829	1.601	0.399
HU (Mean value of vertebral body)	0.976	0.959	0.993	0.005[b]
HU (Screw holding plane)	0.969	0.952	0.986	0.000[b]
Multivariate analyses				
Age	1.038	0.984	1.095	0.172
HU (Mean value of vertebral body)	0.978	0.960	0.996	0.015[b]
Age	1.032	0.969	1.098	0.329
HU (Screw holding plane)	0.971	0.954	0.988	0.001[b]

[a]variables that achieved a significance level of $p < 0.1$ in the univariate analysis.
[b]statistical significance in the multivariate regression analysis ($p < 0.05$).

TABLE 5 Logistic regression analysis of the caudal screw loosening.

	OR	95% CI		p
Univariate analysis				
Gender	1.739	0.54	5.604	0.354
Age	1.042	0.99	1.097	0.117
BMI	0.985	0.828	1.17	0.86
SL restoration	1.058	0.91	1.229	0.463
Cage's position	0.986	0.91	1.068	0.734
Disc distraction	0.89	0.605	1.31	0.555
HU (Mean value of vertebral body)	0.957	0.933	0.982	0.001[b]
HU (Screw holding plane)	0.95	0.923	0.977	0.000[b]

[b]Statistical significance in the multivariate regression analysis ($p < 0.05$).

predictive ability. The area under the curves of screw holding plane HU in the cranial and caudal vertebral bodies were 0.828 and 0.88, respectively, and those of the vertebral body HU were 0.733 and 0.83, respectively. The sensitivity and specificity of the vertebral body's HU were 0.875 and 0.5 in the cranial, 0.925 and 0.562 in the caudal vertebral body. The screw holding plane's HU values were 0.875 and 0.652 in the cranial, 0.8 and 0.667 in the caudal vertebral body (Table 6).

3.2 Numerical mechanical surgical simulations

3.2.1 Multi-indicator model validation

Biomechanical indicators computed by the calibrated intact model were within ± 1 standard deviation of the average values measured by fresh specimens in widely cited *in vitro* studies. Thus, we believe that biomechanical changes identified by current FE models make good representations of actual stress levels (Figure 3).

3.2.2 Biomechanical changes caused by bone mineral density reductions.

Numerical simulations were performed under flexion, extension left and right bending, and axial rotation loading conditions (Figure 4). Loading conditions were identical to the calibration and validation of ROMs. Biomechanical changes in the cranial and caudal sides were computed separately. The maximum equivalent stress of screws and the average equivalent stress of bone-screw interfaces were computed and recorded to investigate local biomechanical changes in the screw holding position (Ambati et al., 2015; Matsukawa et al., 2016; Fletcher et al., 2019; Kim et al., 2020). The average equivalent stress of vertebral bodies was computed to investigate stress distribution changes (i.e., the proportion of load transportation in vertebral bodies and ALSR screw systems) in postoperative models with different BMDs.

Changes in computed biomechanical indicators can explain the result from our radiographic and demographic data review. Consistent with published studies, stress concentration can be observed in the screw head of both cranial and caudal screws (Chao et al., 2008; Amaritsakul et al., 2014). With a stepwise reduction of BMD, higher equivalent stress of bone-screw interfaces can be observed under all loading conditions. The

TABLE 6 The cut-off value, sensitivity and specificity of four measurement methods for predicting screw loosening.

	Cut-off value	Sensitivity	Specificity	AUC
Cranial vertebral body				
HU (Mean value of vertebral body)	105.56	0.875	0.5	0.733
HU (Screw holding plane)	123.35	0.875	0.652	0.828
Caudal vertebral body				
HU (Mean value of vertebral body)	107.3	0.925	0.562	0.83
HU (Screw holding plane)	120.81	0.8	0.667	0.88

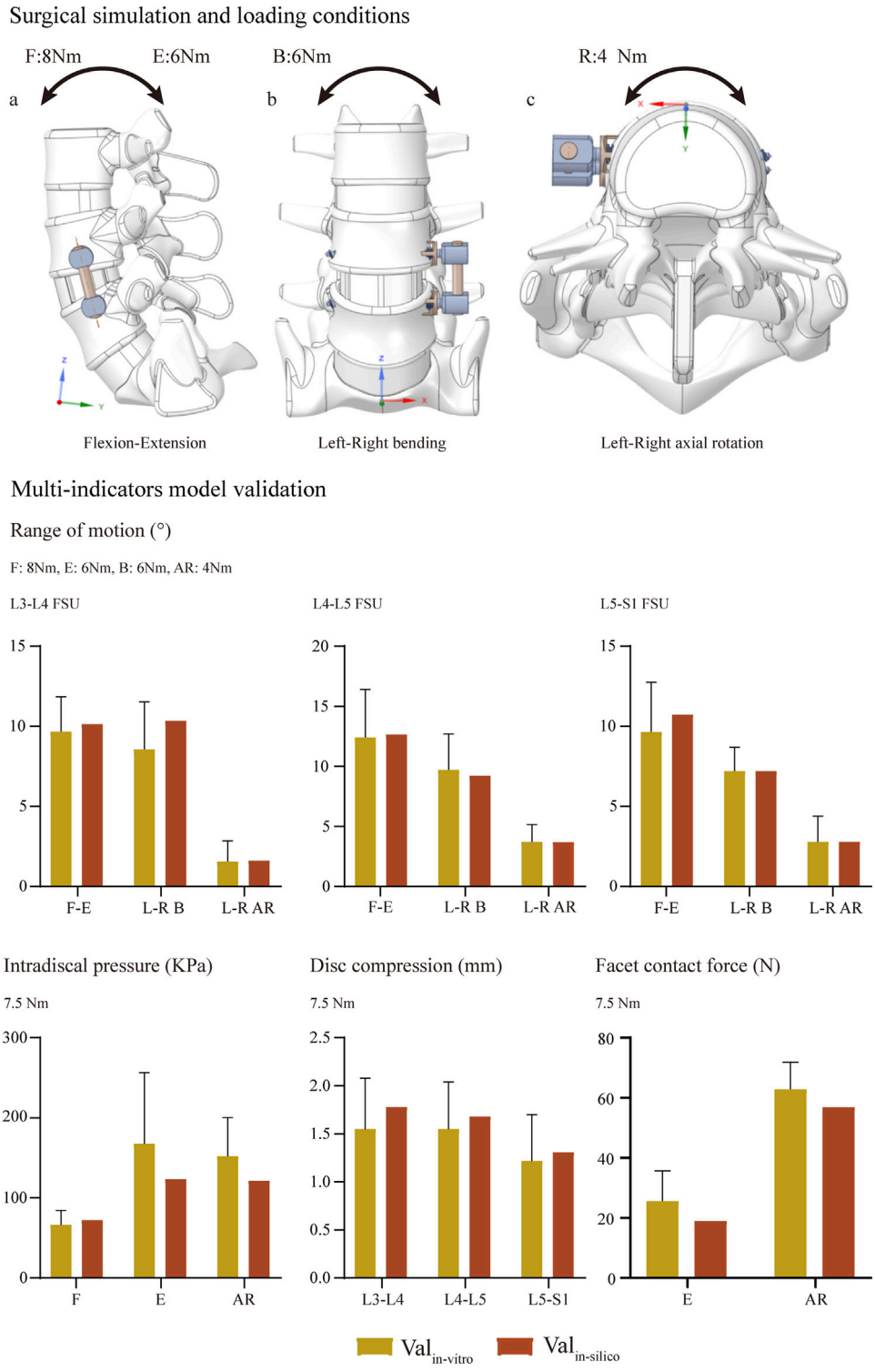

FIGURE 4
Surgical simulations and multi-indicator model validations (Wilson et al., 2006; Renner et al., 2007; Schilling et al., 2011).

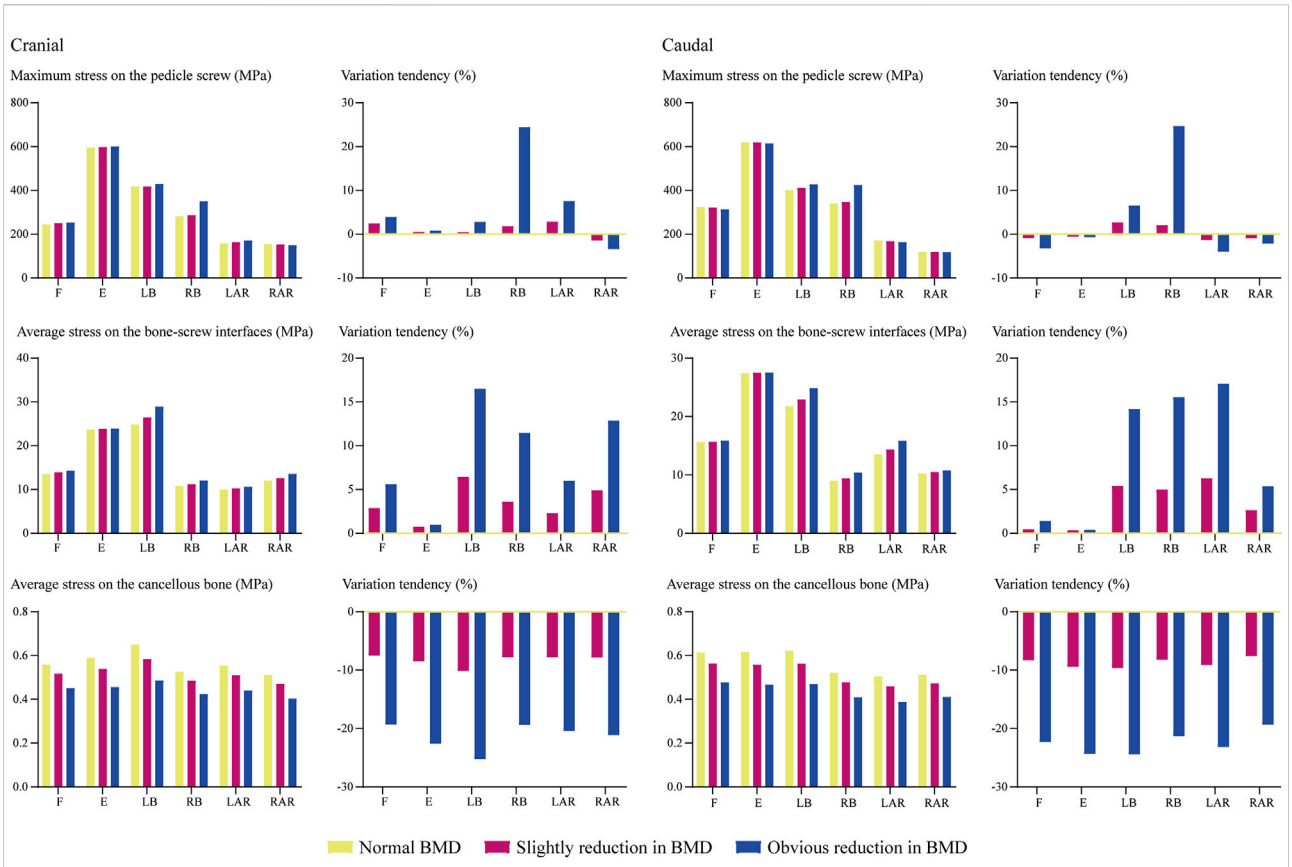

FIGURE 5
Changes in biomechanical indicators.

increase in the maximum equivalent stress of the fixation screw can be observed under bending and left lateral rotation loading conditions. A slight reduction (less than 5%) in the maximum stress of the cranial screw could only be observed under the right axial rotation loading condition with stepwise BMD reduction. In contrast, the increase in maximum stress can only be observed under bending loading conditions of the caudal screw. Additionally, with a stepwise reduction in BMD, the average equivalent stress of cancellous bones in the fixation segment was reduced step by step. In the model with slight BMD reduction, the average cancellous equivalent stress was reduced by nearly 10%, by higher than 20% in the model with significant BMD reduction (Figures 5, 6).

4 Discussion

Multiple studies have revealed that the incidence of screw loosening is high in patients with osteoporosis, and studies have proven that poor BMD of the fixation segment is an independent risk factor for screw loosening by measuring the HU values of vertebral bodies (Bredow et al., 2016; Pisano et al., 2020; Xu et al., 2020). Although few studies proved that the HU measured in the pedicle screw trajectories could make a credible prediction of screw loosening (Ishikawa et al., 2018; Sakai et al., 2018; Xu et al., 2020), no published studies identified the differences in predictive performance between HU measured by vertebral bodies and screw holding planes during the prediction of ALSR screw loosening. Meanwhile, mechanical tests identified that poor BMD would lead to loose bony yield strength and bone-screw integration (Bokov et al., 2019; Weidling et al., 2020). The resulting lower pullout strength can be recorded in pull-out tests with lower BMD (Hsu et al., 2005; Chao et al., 2008). However, whether the stress distribution changes with BMD reduction and whether this change will aggravate stress concentrations on fixation screws and bone-screw interfaces have not been verified.

This study investigates the predictive performance of HU measured in vertebral bodies and holding planes. A radiographic review of this study proved that HU values measured by these two methods were independent risk factors for screw loosening in both cranial and caudal vertebral bodies. Given that poor bony yield strength and the resulting loss of bone-screw integration are

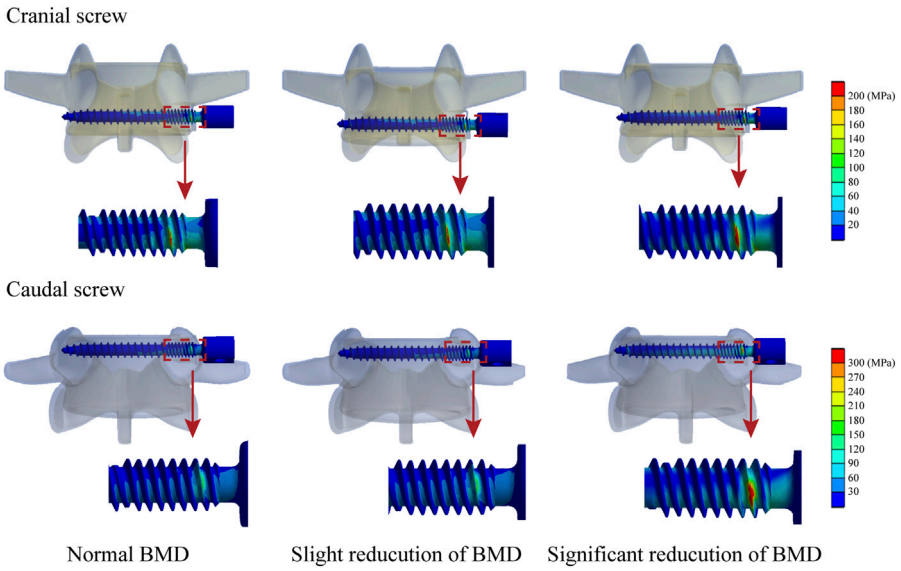

FIGURE 6
Nephograms for the maximum equivalent stress of screws under the right bending loading condition.

commonly accepted mechanisms of screw loosening in osteoporotic patients and can be well reflected by changes in HU values (Ishikawa et al., 2018; Nowak, 2019), high ICC values between vertebral bodies and screw holding planes HU identified excellent consistency between these values (Table 3). The excellent predictive performance of vertebral bodies HU on the risk of screw loosening was at least partly rooted in the excellent reflection of yield strength changes in screw holding positions.

Meanwhile, considering that regional differences in BMD and strength in cancellous bone exist (Smit et al., 1997; Wegrzyn et al., 2010), we believe HU measured in the screw holding plane can better reflect BMD reduction and related loss of bony yield strength and potential risk of bone screw integration. Consistent with this hypothesis, the predictive performance of screw holding plane HU was better than that of vertebral bodies (Figure 3 and Table 6). Given that the ALSR screw trajectory is highly adjustable, we believe that the trajectory optimization of ALSR screws based on preoperative HU measurement is feasible to optimize bone-screw integration and reduce screw loosening risk by optimizing the yield strength of screw holding positions under the premise of constant BMD in a particular osteoporotic patient.

Additionally, we verified that changes in the stress distribution in the fixation segment with BMD reduction would lead to a higher proportion of load transported by the ALSR system, resulting in higher screw and bone-screw interface stress, also initially triggering a higher risk of screw loosening. Therefore, the current results provide a new perspective for understanding the pathogenesis of screw loosening in patients with poor BMD. In other words, both reduction of screw holding position yield strength and deterioration of stress distributions were triggers for screw loosening in osteoporotic patients, and the optimization of these two factors should effectively reduce the risk of screw loosening. Regular anti-osteoporosis therapy could achieve both objectives by increasing BMD in the fixation segment (i.e., increasing the yield strength of screw fixation positions and optimizing stress distribution in the fixation segment by alleviating the pathological stress shielding effect) should be promoted in patients with lumbar screw fixation.

Changes in the fusion segment's stress distribution with BMD stepwise reduction could also provide a reasonable explanation for the clinical phenomenon observed in the radiographic review. Specifically, the screw loosening rate was higher in the cranial vertebral body, but HU values measured in vertebral bodies and screw holding planes, as significant risk factors for screw loosening, were not significantly different. As computed by the current numerical simulations, although the variation tendency of stress levels in bone-screw interfaces and cancellous bones were identical in both cranial and caudal vertebral bodies, the maximum equivalent stress step increased with BMD reduction except for the right axial rotation loading condition. In contrast, the caudal screw stress only increased under bending loading conditions. In other words, the maximum stress increased in the cranial screw

but decreased in the caudal screw under flexion, extension, and left axial rotation loading conditions. Given the exact relation between the maximum stress increase and the increase in screw loosening risk, we believe the current computational result explains the higher screw loosening risk of the ALSR fixation system in the cranial vertebral body.

To our knowledge, the most significant contribution of this study in methodology is the combination between the clinical review and numerical biomechanical simulations. Previously, these researches have been separately performed; clinical studies have observed a phenomenon without directly explaining its biomechanical mechanism; biomechanical studies have explored the potential mechanism of complications, but there is no clinical data to support this anticipation. Thus, the credibility of both types of studies is limited. In this study, the biomechanical mechanism of the observed clinical phenomenon has been directly investigated by corresponding numerical simulations. Combining these two parts is significant for better understanding a specific risk factor.

Admittedly, the current study results should be interpreted within the context of the following-mentioned limitations. Specifically, larger sample sizes of clinical data with a longer follow-up period should be obtained, and morphological changes during BMD reduction should be simulated in FEA models. However, given that screw loosening commonly occurs in the early stage of postoperative follow-up, the construction strategy of models with poor BMD has been widely reported (Ferguson and Steffen, 2003; Kealey et al., 2005; Zhang et al., 2010; Li et al., 2019), especially biomechanical changes that could well explain the result of clinical data observation. We believe the current study results are still reliable and could provide theoretical guidance for future clinical practice. Moreover, cortical bone is also important for screw fixation, but limited by the resolution of imaging data, we can not precisely measure the cortical thickness in current patients, and we admit that this is an important limitation for the study related to screw fixation strength evaluation. However, given the integration between cancellous bone and screw provide mainly screw holding strength, we believe the identification of cancellous BMD and corresponding biomechanical environment is still of great significance to deduce potential risk of screw loosening. Finally, for the lack of accurate references for the pretension of ALSR fixation, this factor has not been simulated in the current study, and we wish it can be accurately measured in our future studies.

5 Conclusion

Both vertebral bodies and "screw holding planes" HU can well predict screw loosening risk for OLIF patients with ALSR screw fixation. The predictive performance of screw holding plane HU is better than the mean HU of vertebral bodies. A higher proportion of ALSR load transmission triggers stress concentration on the screw and bone-screw interfaces in patients with poor BMD. This, together with decreased bony strength in the screw holding position, contributes to screw loosening in osteoporotic patients biomechanically. Therefore, the trajectory optimization of ALSR screws and regular anti-osteoporosis therapy may effectively reduce the risk of screw loosening.

Data availability statement

The raw data supporting the conclusions of this article will be made available by the authors, without undue reservation.

Ethics statement

The studies involving human participants were reviewed and approved by Approval for the current study protocol was obtained from the ethics committees of West China Hospital (2020-554). Written informed consent for participation was not required for this study in accordance with the national legislation and the institutional requirements.

Author contributions

Conception and design: Y-MS, J-CZ, and J-CL; Acquisition of data: Z-QY, J-CL, and Z-QS. Analysis and interpretation of imaging data: J-CL, T-HX, Z-TS, and Z-QY; Statistical analysis: T-HX, Z-QY, and J-CL, Manuscript Preparation: J-CL, and Z-QY; Manuscript modification: YS, and JZ.

Funding

This work was supported by the major Project of Science and Technology Department of Sichuan Province (2022YFS0051), and the Post-Doctor Research Project, West China Hospital, Sichuan University (2021HXBH047).

Acknowledgments

We acknowledge Xiao-Yu Zhang for the guidance of the figure preparation.

Conflict of interest

The authors declare that the research was conducted in the absence of any commercial or financial relationships that could be construed as a potential conflict of interest.

Publisher's note

All claims expressed in this article are solely those of the authors and do not necessarily represent those of their affiliated organizations, or those of the publisher, the editors and the reviewers. Any product that may be evaluated in this article, or claim that may be made by its manufacturer, is not guaranteed or endorsed by the publisher.

Supplementary material

The Supplementary Material for this article can be found online at: https://www.frontiersin.org/articles/10.3389/fbioe.2022.922848/full#supplementary-material

References

Agarwal, A., Ingels, M., Kodigudla, M., Momeni, N., Goel, V., and Agarwal, A. K. (2016). Adjacent-level hypermobility and instrumented-level fatigue loosening with titanium and PEEK rods for a pedicle screw system: An *in vitro* study. *J. Biomech. Eng.* 138 (5), 051004. doi:10.1115/1.4032965

Amaritsakul, Y., Chao, C. K., and Lin, J. (2014). Biomechanical evaluation of bending strength of spinal pedicle screws, including cylindrical, conical, dual core and double dual core designs using numerical simulations and mechanical tests. *Med. Eng. Phys.* 36 (9), 1218–1223. doi:10.1016/j.medengphy.2014.06.014

Ambati, D. V., Wright, E. K., Jr., Lehman, R. A., Jr., Kang, D. G., Wagner, S. C., and Dmitriev, A. E. (2015). Bilateral pedicle screw fixation provides superior biomechanical stability in transforaminal lumbar interbody fusion: A finite element study. *Spine J.* 15 (8), 1812–1822. doi:10.1016/j.spinee.2014.06.015

Bagheri, S. R., Alimohammadi, E., Zamani Froushani, A., and Abdi, A. (2019). Adjacent segment disease after posterior lumbar instrumentation surgery for degenerative disease: Incidence and risk factors. *J. Orthop. Surg. Hong. Kong)* 27 (2), 2309499019842378. doi:10.1177/2309499019842378

Bokov, A., Bulkin, A., Aleynik, A., Kutlaeva, M., and Mlyavykh, S. (2019). Pedicle screws loosening in patients with degenerative diseases of the lumbar spine: Potential risk factors and relative contribution. *Glob. Spine J.* 9 (1), 55–61. doi:10.1177/2192568218772302

Bredow, J., Boese, C. K., Werner, C. M., Siewe, J., Löhrer, L., Zarghooni, K., et al. (2016). Predictive validity of preoperative CT scans and the risk of pedicle screw loosening in spinal surgery. *Arch. Orthop. Trauma Surg.* 136 (8), 1063–1067. doi:10.1007/s00402-016-2487-8

Chao, C. K., Hsu, C. C., Wang, J. L., and Lin, J. (2008). Increasing bending strength and pullout strength in conical pedicle screws: Biomechanical tests and finite element analyses. *J. Spinal Disord. Tech.* 21 (2), 130–138. doi:10.1097/bsd.0b013e318073cc4b

Chuang, W. H., Kuo, Y. J., Lin, S. C., Wang, C. W., Chen, S. H., Chen, Y. J., et al. (2013). Comparison among load-, ROM-, and displacement-controlled methods used in the lumbosacral nonlinear finite-element analysis. *Spine* 38 (5), E276–E285. doi:10.1097/brs.0b013e31828251f9

Chuang, W. H., Lin, S. C., Chen, S. H., Wang, C. W., Tsai, W. C., Chen, Y. J., et al. (2012). Biomechanical effects of disc degeneration and hybrid fixation on the transition and adjacent lumbar segments. *Spine* 37 (24), E1488–E1497. doi:10.1097/brs.0b013e31826cdd93

DeLucca, J. F., Cortes, D. H., Jacobs, N. T., Vresilovic, E. J., Duncan, R. L., and Elliott, D. M. (2016). Human cartilage endplate permeability varies with degeneration and intervertebral disc site. *J. Biomechanics* 49 (4), 550–557. doi:10.1016/j.jbiomech.2016.01.007

Dreischarf, M., Zander, T., Shirazi-Adl, A., Puttlitz, C. M., Adam, C. J., Chen, C. S., et al. (2014). Comparison of eight published static finite element models of the intact lumbar spine: Predictive power of models improves when combined together. *J. Biomechanics* 47 (8), 1757–1766. doi:10.1016/j.jbiomech.2014.04.002

Fan, W., Guo, L. X., and Zhang, M. (2021). Biomechanical analysis of lumbar interbody fusion supplemented with various posterior stabilization systems. *Eur. Spine J.* 30 (8), 2342–2350. doi:10.1007/s00586-021-06856-7

Ferguson, S. J., and Steffen, T. (2003). Biomechanics of the aging spine. *Eur. Spine J.* 12 Suppl 2, S97–s103. doi:10.1007/s00586-003-0621-0

Fletcher, J. W. A., Windolf, M., Grünwald, L., Richards, R. G., Gueorguiev, B., and Varga, P. (2019). The influence of screw length on predicted cut-out failures for proximal humeral fracture fixations predicted by finite element simulations. *Arch. Orthop. Trauma Surg.* 139 (8), 1069–1074. doi:10.1007/s00402-019-03175-x

Gausden, E. B., Nwachukwu, B. U., Schreiber, J. J., Lorich, D. G., and Lane, J. M. (2017). Opportunistic use of CT imaging for osteoporosis screening and bone density assessment. *J. Bone Jt. Surg.* 99 (18), 1580–1590. doi:10.2106/jbjs.16.00749

Guo, H. Z., Tang, Y. C., Guo, D. Q., Luo, P. J., Li, Y. X., Mo, G. Y., et al. (2020). Stability evaluation of oblique lumbar interbody fusion constructs with various fixation options: A finite element analysis based on three-dimensional scanning models. *World Neurosurg.* 138, e530–e538. doi:10.1016/j.wneu.2020.02.180

Guvenc, Y., Akyoldas, G., Senturk, S., Erbulut, D., Yaman, O., and Ozer, A. F. (2019). How to reduce stress on the pedicle screws in thoracic spine? Importance of screw trajectory: A finite element analysis. *Turk Neurosurg.* 29 (1), 20–25. doi:10.5137/1019-5149.JTN.21895-17.2

Havey, R. M., Voronov, L. I., Tsitsopoulos, P. P., Carandang, G., Ghanayem, A. J., Lorenz, M. A., et al. (2012). Relaxation response of lumbar segments undergoing disc-space distraction. *Spine* 37 (9), 733–740. doi:10.1097/brs.0b013e3182323adc

He, L., Xiang, Q., Yang, Y., Tsai, T. Y., Yu, Y., and Cheng, L. (2021). The anterior and traverse cage can provide optimal biomechanical performance for both traditional and percutaneous endoscopic transforaminal lumbar interbody fusion. *Comput. Biol. Med.* 131, 104291. doi:10.1016/j.compbiomed.2021.104291

Hsieh, Y. Y., Chen, C. H., Tsuang, F. Y., Wu, L. C., Lin, S. C., and Chiang, C. J. (2017). Removal of fixation construct could mitigate adjacent segment stress after lumbosacral fusion: A finite element analysis. *Clin. Biomech.* 43, 115–120. doi:10.1016/j.clinbiomech.2017.02.011

Hsieh, Y. Y., Tsuang, F. Y., Kuo, Y. J., Chen, C. H., Chiang, C. J., and Lin, C. L. (2020). Biomechanical analysis of single-level interbody fusion with different internal fixation rod materials: A finite element analysis. *BMC Musculoskelet. Disord.* 21 (1), 100. doi:10.1186/s12891-020-3111-1

Hsu, C. C., Chao, C. K., Wang, J. L., Hou, S. M., Tsai, Y. T., and Lin, J. (2005). Increase of pullout strength of spinal pedicle screws with conical core: Biomechanical tests and finite element analyses. *J. Orthop. Res.* 23 (4), 788–794. doi:10.1016/j.orthres.2004.11.002

Ishikawa, K., Toyone, T., Shirahata, T., Kudo, Y., Matsuoka, A., Maruyama, H., et al. (2018). A novel method for the prediction of the pedicle screw stability. *Clin. Spine Surg.* 31 (9), E473–e480. doi:10.1097/bsd.0000000000000703

Jacobs, N. T., Cortes, D. H., Peloquin, J. M., Vresilovic, E. J., and Elliott, D. M. (2014). Validation and application of an intervertebral disc finite element model utilizing independently constructed tissue-level constitutive formulations that are nonlinear, anisotropic, and time-dependent. *J. Biomechanics* 47 (11), 2540–2546. doi:10.1016/j.jbiomech.2014.06.008

Kaito, T., Hosono, N., Fuji, T., Makino, T., and Yonenobu, K. (2011). Disc space distraction is a potent risk factor for adjacent disc disease after PLIF. *Arch. Orthop. Trauma Surg.* 131 (11), 1499–1507. doi:10.1007/s00402-011-1343-0

Kaito, T., Hosono, N., Mukai, Y., Makino, T., Fuji, T., and Yonenobu, K. (2010). Induction of early degeneration of the adjacent segment after posterior lumbar interbody fusion by excessive distraction of lumbar disc space. *Spi* 12 (6), 671–679. doi:10.3171/2009.12.spine08823

Kang, D. G., Lehman, R. A., Jr., Bevevino, A. J., Gaume, R. E., Purcell, R. L., Dmitriev, A. E., et al. (2014). Pedicle screw "hubbing" in the immature thoracic spine. *J. Pediatr. Orthop.* 34 (7), 703–709. doi:10.1097/bpo.0000000000000166

Kanno, H., Aizawa, T., Hashimoto, K., and Itoi, E. (2021). Novel augmentation technique of percutaneous pedicle screw fixation using

hydroxyapatite granules in the osteoporotic lumbar spine: A cadaveric biomechanical analysis. *Eur. Spine J.* 30 (1), 71–78. doi:10.1007/s00586-020-06451-2

Kealey, S. M., Aho, T., Delong, D., Barboriak, D. P., Provenzale, J. M., and Eastwood, J. D. (2005). Assessment of apparent diffusion coefficient in normal and degenerated intervertebral lumbar disks: Initial experience. *Radiology* 235 (2), 569–574. doi:10.1148/radiol.2352040437

Kim, H. J., Chun, H. J., Lee, H. M., Kang, K. T., Lee, C. K., Chang, B. S., et al. (2013). The biomechanical influence of the facet joint orientation and the facet tropism in the lumbar spine. *Spine J.* 13 (10), 1301–1308. doi:10.1016/j.spinee.2013.06.025

Kim, H. J., Kang, K. T., Chun, H. J., Lee, C. K., Chang, B. S., and Yeom, J. S. (2015a). The influence of intrinsic disc degeneration of the adjacent segments on its stress distribution after one-level lumbar fusion. *Eur. Spine J.* 24 (4), 827–837. doi:10.1007/s00586-014-3462-0

Kim, H. J., Kang, K. T., Son, J., Lee, C. K., Chang, B. S., and Yeom, J. S. (2015b). The influence of facet joint orientation and tropism on the stress at the adjacent segment after lumbar fusion surgery: A biomechanical analysis. *Spine J.* 15 (8), 1841–1847. doi:10.1016/j.spinee.2015.03.038

Kim, H., Lee, W., Choi, S., Kholinne, E., Lee, E., Alzahrani, W. M., et al. (2020). Role of additional inferomedial supporting screws in osteoporotic 3-Part Proximal humerus fracture: Finite element analysis. *Geriatr. Orthop. Surg. Rehabil.* 11, 2151459320956958. doi:10.1177/2151459320956958

Labrom, R. D., Tan, J. S., Reilly, C. W., Tredwell, S. J., Fisher, C. G., and Oxland, T. R. (2005). The effect of interbody cage positioning on lumbosacral vertebral endplate failure in compression. *Spine* 30 (19), E556–E561. doi:10.1097/01.brs.0000181053.38677.c2

Landham, P. R., Don, A. S., and Robertson, P. A. (2017). Do position and size matter? An analysis of cage and placement variables for optimum lordosis in PLIF reconstruction. *Eur. Spine J.* 26 (11), 2843–2850. doi:10.1007/s00586-017-5170-z

Li, J., Xu, C., Zhang, X., Xi, Z., Liu, M., Fang, Z., et al. (2021a). TELD with limited foraminoplasty has potential biomechanical advantages over TELD with large annuloplasty: An *in-silico* study. *BMC Musculoskelet. Disord.* 22 (1), 616. doi:10.1186/s12891-021-04504-1

Li, J., Xu, C., Zhang, X., Xi, Z., Sun, S., Zhang, K., et al. (2021b). Disc measurement and nucleus calibration in a smoothened lumbar model increases the accuracy and efficiency of *in-silico* study. *J. Orthop. Surg. Res.* 16 (1), 498. doi:10.1186/s13018-021-02655-4

Li, J., Xu, W., Zhang, X., Xi, Z., and Xie, L. (2019). Biomechanical role of osteoporosis affects the incidence of adjacent segment disease after percutaneous transforaminal endoscopic discectomy. *J. Orthop. Surg. Res.* 14 (1), 131. doi:10.1186/s13018-019-1166-1

Lu, T., and Lu, Y. (2019). Comparison of biomechanical performance among posterolateral fusion and transforaminal, extreme, and oblique lumbar interbody fusion: A finite element analysis. *World Neurosurg.* 129, e890–e899. doi:10.1016/j.wneu.2019.06.074

Matsukawa, K., Yato, Y., Imabayashi, H., Hosogane, N., Abe, Y., Asazuma, T., et al. (2016). Biomechanical evaluation of fixation strength among different sizes of pedicle screws using the cortical bone trajectory: What is the ideal screw size for optimal fixation? *Acta Neurochir.* 158 (3), 465–471. doi:10.1007/s00701-016-2705-8

Mi, J., Li, K., Zhao, X., Zhao, C. Q., Li, H., and Zhao, J. (2017). Vertebral body hounsfield units are associated with cage subsidence after transforaminal lumbar interbody fusion with unilateral pedicle screw fixation. *Clin. Spine Surg.* 30 (8), E1130–e1136. doi:10.1097/bsd.0000000000000490

Mikula, A. L., Puffer, R. C., Jeor, J. D. S., Bernatz, J. T., Fogelson, J. L., Larson, A. N., et al. (2019). Teriparatide treatment increases Hounsfield units in the lumbar spine out of proportion to DEXA changes. *J. Neurosurg. Spine*, 1–6. doi:10.3171/2019.7.SPINE19654

Morgan, E. F., Bayraktar, H. H., and Keaveny, T. M. (2003). Trabecular bone modulus-density relationships depend on anatomic site. *J. Biomechanics* 36 (7), 897–904. doi:10.1016/s0021-9290(03)00071-x

Nowak, B. (2019). Experimental study on the loosening of pedicle screws implanted to synthetic bone vertebra models and under non-pull-out mechanical loads. *J. Mech. Behav. Biomed. Mater.* 98, 200–204. doi:10.1016/j.jmbbm.2019.06.013

Oetgen, M. E., Yue, J. J., la Torre, J. J., and Bertagnoli, R. (2008). Does vertebral endplate morphology influence outcomes in lumbar total disc arthroplasty? Part II: Clinical and radiographic results as evaluated utilizing the vertebral endplate Yue-bertagnoli (VEYBR) classification. *Int. J. Spine Surg.* 2 (2), 101–106. doi:10.1016/sasj-2007-0119-rr

Okuda, S., Oda, T., Miyauchi, A., Haku, T., Yamamoto, T., and Iwasaki, M. (2006). Surgical outcomes of posterior lumbar interbody fusion in elderly patients. *J. Bone & Jt. Surg.* 88 (12), 2714–2720. doi:10.2106/jbjs.f.00186

Ottardi, C., Galbusera, F., Luca, A., Prosdocimo, L., Sasso, M., Brayda-Bruno, M., et al. (2016). Finite element analysis of the lumbar destabilization following pedicle subtraction osteotomy. *Med. Eng. Phys.* 38 (5), 506–509. doi:10.1016/j.medengphy.2016.02.002

Park, S. J., Lee, C. S., Chung, S. S., Kang, S. S., Park, H. J., and Kim, S. H. (2017). The ideal cage position for achieving both indirect neural decompression and segmental angle restoration in lateral lumbar interbody fusion (LLIF). *Clin. Spine Surg.* 30 (6), E784–e790. doi:10.1097/bsd.0000000000000406

Pearson, H. B., Dobbs, C. J., Grantham, E., Niebur, G. L., Chappuis, J. L., and Boerckel, J. D. (2017). Intraoperative biomechanics of lumbar pedicle screw loosening following successful arthrodesis. *J. Orthop. Res.* 35 (12), 2673–2681. doi:10.1002/jor.23575

Pickhardt, P. J., Pooler, B. D., Lauder, T., del Rio, A. M., Bruce, R. J., and Binkley, N. (2013). Opportunistic screening for osteoporosis using abdominal computed tomography scans obtained for other indications. *Ann. Intern Med.* 158 (8), 588–595. doi:10.7326/0003-4819-158-8-201304160-00003

Pisano, A. J., Fredericks, D. R., Steelman, T., Riccio, C., Helgeson, M. D., and Wagner, S. C. (2020). Lumbar disc height and vertebral hounsfield units: Association with interbody cage subsidence. *Neurosurg. Focus* 49 (2), E9. doi:10.3171/2020.4.focus20286

Rastegar, S., Arnoux, P. J., Wang, X., and Aubin, C. (2020). Biomechanical analysis of segmental lumbar lordosis and risk of cage subsidence with different cage heights and alternative placements in transforaminal lumbar interbody fusion. *Comput. Methods Biomechanics Biomed. Eng.* 23 (9), 456–466. doi:10.1080/10255842.2020.1737027

Renner, S. M., Natarajan, R. N., Patwardhan, A. G., Havey, R. M., Voronov, L. I., Guo, B. Y., et al. (2007). Novel model to analyze the effect of a large compressive follower pre-load on range of motions in a lumbar spine. *J. Biomechanics* 40 (6), 1326–1332. doi:10.1016/j.jbiomech.2006.05.019

Sakai, Y., Takenaka, S., Matsuo, Y., Fujiwara, H., Honda, H., Makino, T., et al. (2018). Hounsfield unit of screw trajectory as a predictor of pedicle screw loosening after single level lumbar interbody fusion. *J. Orthop. Sci.* 23 (5), 734–738. doi:10.1016/j.jos.2018.04.006

Schilling, C., Krüger, S., Grupp, T. M., Duda, G. N., Blömer, W., and Rohlmann, A. (2011). The effect of design parameters of dynamic pedicle screw systems on kinematics and load bearing: An *in vitro* study. *Eur. Spine J.* 20 (2), 297–307. doi:10.1007/s00586-010-1620-6

Schreiber, J. J., Hughes, A. P., Taher, F., and Girardi, F. P. (2014). An association can be found between hounsfield units and success of lumbar spine fusion. *HSS Jrnl* 10 (1), 25–29. doi:10.1007/s11420-013-9367-3

Smit, T. H., Odgaard, A., and Schneider, E. (1997). Structure and function of vertebral trabecular bone. *Spine* 22 (24), 2823–2833. doi:10.1097/00007632-199712150-00005

Tsouknidas, A., Sarigiannidis, S. O., Anagnostidis, K., Michailidis, N., and Ahuja, S. (2015). Assessment of stress patterns on a spinal motion segment in healthy versus osteoporotic bony models with or without disc degeneration: A finite element analysis. *Spine J.* 15 (3), S17–s22. doi:10.1016/j.spinee.2014.12.148

Tsuang, F. Y., Chen, C. H., Wu, L. C., Kuo, Y. J., Lin, S. C., and Chiang, C. J. (2016). Biomechanical arrangement of threaded and unthreaded portions providing holding power of transpedicular screw fixation. *Clin. Biomech.* 39, 71–76. doi:10.1016/j.clinbiomech.2016.09.010

Wang, W. T., Guo, C. H., Duan, K., Ma, M. J., Jiang, Y., Liu, T. J., et al. (2019). Dual pitch titanium-coated pedicle screws improve initial and early fixation in a polyetheretherketone rod semi-rigid fixation system in sheep. *Chin. Med. J. Engl.* 132 (21), 2594–2600. doi:10.1097/cm9.0000000000000335

Wegrzyn, J., Roux, J. P., Arlot, M. E., Boutroy, S., Vilayphiou, N., Guyen, O., et al. (2010). Role of trabecular microarchitecture and its heterogeneity parameters in the mechanical behavior of *ex vivo* human L3vertebrae. *J. Bone Min. Res.* 25 (11), 2324–2331. doi:10.1002/jbmr.164

Weidling, M., Oefner, C., Schoenfelder, S., and Heyde, C. E. (2020). A novel parameter for the prediction of pedicle screw fixation in cancellous bone - a biomechanical study on synthetic foam. *Med. Eng. Phys.* 79, 44–51. doi:10.1016/j.medengphy.2020.03.001

Wilson, D. C., Niosi, C. A., Zhu, Q. A., Oxland, T. R., and Wilson, D. R. (2006). Accuracy and repeatability of a new method for measuring facet loads in the lumbar spine. *J. Biomechanics* 39 (2), 348–353. doi:10.1016/j.jbiomech.2004.12.011

Xi, Z., Mummaneni, P. V., Wang, M., Ruan, H., Burch, S., Deviren, V., et al. (2020). The association between lower Hounsfield units on computed tomography and cage subsidence after lateral lumbar interbody fusion. *Neurosurg. Focus* 49 (2), E8. doi:10.3171/2020.5.focus20169

Xie, T., Wang, C., Yang, Z., Xiu, P., Yang, X., Wang, X., et al. (2020). Minimally invasive oblique lateral lumbar interbody fusion combined with anterolateral screw

fixation for lumbar degenerative disc disease. *World Neurosurg.* 135, e671–e678. doi:10.1016/j.wneu.2019.12.105

Xu, C., Huang, C., Cai, P., Fang, Z., Wei, Z., Liu, F., et al. (2022a). Biomechanical effects of pedicle screw positioning on the surgical segment in models after oblique lumbar interbody fusion: An *in-silico* study. *Ijgm* Vol. 15, 1047–1056. doi:10.2147/ijgm.s352304

Xu, C., Xi, Z., Fang, Z., Zhang, X., Wang, N., Li, J., et al. (2022b). Annulus calibration increases the computational accuracy of the lumbar finite element model. *Glob. Spine J.* 21925682221081224, 21925682221081224. doi:10.1177/21925682221081224

Xu, F., Zou, D., Li, W., Sun, Z., Jiang, S., Zhou, S., et al. (2020). Hounsfield units of the vertebral body and pedicle as predictors of pedicle screw loosening after degenerative lumbar spine surgery. *Neurosurg. Focus* 49 (2), E10. doi:10.3171/2020.5.focus20249

Yue, J. J., Oetgen, M. E., Jaramillo-de la Torre, J. J., and Bertagnoli, R. (2008). Does vertebral endplate morphology influence outcomes in lumbar disc arthroplasty? Part I: An initial assessment of a novel classification system of lumbar endplate morphology. *SAS J.* 2 (1), 16–22. doi:10.1016/s1935-9810(08)70013-6

Zhang, L., Yang, G., Wu, L., and Yu, B. (2010). The biomechanical effects of osteoporosis vertebral augmentation with cancellous bone granules or bone cement on treated and adjacent non-treated vertebral bodies: A finite element evaluation. *Clin. Biomech.* 25 (2), 166–172. doi:10.1016/j.clinbiomech.2009.10.006

Zhao, F. D., Pollintine, P., Hole, B. D., Adams, M. A., and Dolan, P. (2009). Vertebral fractures usually affect the cranial endplate because it is thinner and supported by less-dense trabecular bone. *Bone* 44 (2), 372–379. doi:10.1016/j.bone.2008.10.048

Zhao, L., Xie, T., Wang, X., Yang, Z., Pu, X., Lu, Y., et al. (2022a). Clinical and radiological evaluation of cage subsidence following oblique lumbar interbody fusion combined with anterolateral fixation. *BMC Musculoskelet. Disord.* 23 (1), 214. doi:10.1186/s12891-022-05165-4

Zhao, L., Xie, T., Wang, X., Yang, Z., Pu, X., and Zeng, J. (2022b2019). Whether anterolateral single rod can maintain the surgical outcomes following oblique lumbar interbody fusion for double-segment disc disease. Orthop surg, Zou D, Li W, deng C, du G, Xu NThe use of CT hounsfield unit values to identify the undiagnosed spinal osteoporosis in patients with lumbar degenerative diseases. *Eur. Spine J.* 28 (8), 1758–1766.

Zou, D., Sun, Z., Zhou, S., Zhong, W., and Li, W. (2020). Hounsfield units value is a better predictor of pedicle screw loosening than the T-score of DXA in patients with lumbar degenerative diseases. *Eur. Spine J.* 29 (5), 1105–1111. doi:10.1007/s00586-020-06386-8

frontiers | Frontiers in Bioengineering and Biotechnology

TYPE Original Research
PUBLISHED 02 September 2022
DOI 10.3389/fbioe.2022.953119

OPEN ACCESS

EDITED BY
Pankaj Pankaj,
University of Edinburgh,
United Kingdom

REVIEWED BY
Peter Varga,
AO Research Institute Davos,
Switzerland
Amit Roy Chowdhury,
Indian Institute of Engineering Science and Technology, Shibpur, India

*CORRESPONDENCE
Frédéric Cornaz,
frederic.cornaz@balgrist.ch

SPECIALTY SECTION
This article was submitted to Biomechanics,
a section of the journal
Frontiers in Bioengineering and Biotechnology

RECEIVED 25 May 2022
ACCEPTED 21 July 2022
PUBLISHED 02 September 2022

CITATION
Cornaz F, Farshad M and Widmer J (2022), Location of pedicle screw hold in relation to bone quality and loads. *Front. Bioeng. Biotechnol.* 10:953119. doi: 10.3389/fbioe.2022.953119

Location of pedicle screw hold in relation to bone quality and loads

Frédéric Cornaz[1,2]*, Mazda Farshad[1] and Jonas Widmer[1,2]

[1]Department of Orthopedics, Balgrist University Hospital, Zurich, Switzerland, [2]Institute for Biomechanics, ETH Zurich, Zurich, Switzerland

Introduction: Sufficient screw hold is an indispensable requirement for successful spinal fusion, but pedicle screw loosening is a highly prevalent burden. The aim of this study was to quantify the contribution of the pedicle and corpus region in relation to bone quality and loading amplitude of pedicle screws with traditional trajectories.

Methods: After CT examination to classify bone quality, 14 pedicle screws were inserted into seven L5. Subsequently, Micro-CT images were acquired to analyze the screw's location and the vertebrae were split in the midsagittal plane and horizontally along the screw's axis to allow imprint tests with 6 mm long sections of the pedicle screws in a caudal direction perpendicular to the screw's surface. Force-displacement curves in combination with the micro-CT data were used to reconstruct the resistance of the pedicle and corpus region at different loading amplitudes.

Results: Bone quality was classified as normal in three specimens, as moderate in two and as bad in two specimens, resulting in six, four, and four pedicle screws per group. The screw length in the pedicle region in relation to the inserted screw length was measured at an average of 63%, 62%, and 52% for the three groups, respectively. At a calculated 100 N axial load acting on the whole pedicle screw, the pedicle region contributed an average of 55%, 58%, and 58% resistance for the normal, moderate, and bad bone quality specimens, respectively. With 500 N load, these values were measured at 59%, 63%, and 73% and with 1000 N load, they were quantified at 71%, 75%, and 81%.

Conclusion: At lower loading amplitudes, the contribution of the pedicle and corpus region on pedicle screw hold are largely balanced and independent of bone quality. With increasing loading amplitudes, the contribution of the pedicle region increases disproportionally, and this increase is even more pronounced in situations with reduced bone quality. These results demonstrate the importance of the pedicle region for screw hold, especially for reduced bone quality.

KEYWORDS

pedicle screw, lumbar spine, instrumentation, primary stability, bone density, screw bone interface

Introduction

Dorsal pedicle screw instrumentation is one of the main techniques used for spinal fusion and spinal stabilization (Martin et al., 2019; Reisener et al., 2020). Pedicle screw based dorsal instrumentation systems have been developed into a versatile and effective method, and can be combined with a multitude of other implants, such as intervertebral cages, crosslinks, or laminar bands to achieve the aspired construct characteristics. While substantial progress has been achieved in the last few decades, insufficient screw hold and screw loosening still pose a major complication in the clinical routine in up to 50% of patients (Kim et al., 2020), which can result in pain, loss of reduction, or neurologic deficit (Ohlin et al., 1994; Röllinghoff et al., 2010; El Saman et al., 2013; Mac-Thiong et al., 2013; Glennie et al., 2015; Bredow et al., 2016; Ohba et al., 2019). Most of the time, revision surgery is the consequence.

To reduce the rate of pedicle screw loosening, alternative trajectories have been proposed, such as the cortical bone trajectory (CBT) (Santoni et al., 2009; Glennie et al., 2015) or screw augmentation methods using bone cement (Burval et al., 2007; El Saman et al., 2013; Wang et al., 2019). However, CBT screw loosening remains a relevant problem with a similar prevalence (Santoni et al., 2009; Glennie et al., 2015; Patel et al., 2016; Elmekaty et al., 2018) and bone cement augmentation poses an additional complication risk, such as cement extrusion or embolism (Becker et al., 2008; Janssen et al., 2017; Guozhi et al., 2019). More fundamental optimizing principles have been well adopted, such as maximizing screw length and diameter (Matsukawa et al., 2016), while other approaches have not been graded to outweigh the potential drawbacks in most clinical situations, such as bicortical screw placement (Spirig et al., 2021) or crosslink-augmentation (Cornaz et al., 2021).

To quantify screw hold, axial load-to-failure pullout tests (Burval et al., 2007; Aichmair et al., 2017; Lai et al., 2018), different cyclic toggling test setups simulating more physiological loading conditions (Weiser et al., 2017; Liebsch et al., 2018; Spirig et al., 2021), as well as finite element simulations (Biswas et al., 2018; Chevalier et al., 2018; Van den Abbeele et al., 2018; Widmer et al., 2020; Biswas et al., 2022) have been employed to guide surgeons, researchers, and the industry into the direction of optimized screw fixation strength. While different aspects of screw hold can be analyzed with these methods, they usually attempt to investigate the behavior of the bone-screw interaction at a "global" level. However, it appears essential to lay an additional focus on the regional distribution because large spatial differences of screw hold must be expected due to anatomical and microstructural differences along the screw's trajectory (Figure 1). This perspective could help us to understand the bone-screw interaction and guide innovation successfully towards optimized implant geometries or more effective screw trajectories.

The aim of this study was to qualitatively analyze the local support along traditional pedicle screw trajectories and to quantify the contribution of the pedicle and corpus region in relation to bone quality and loading amplitude.

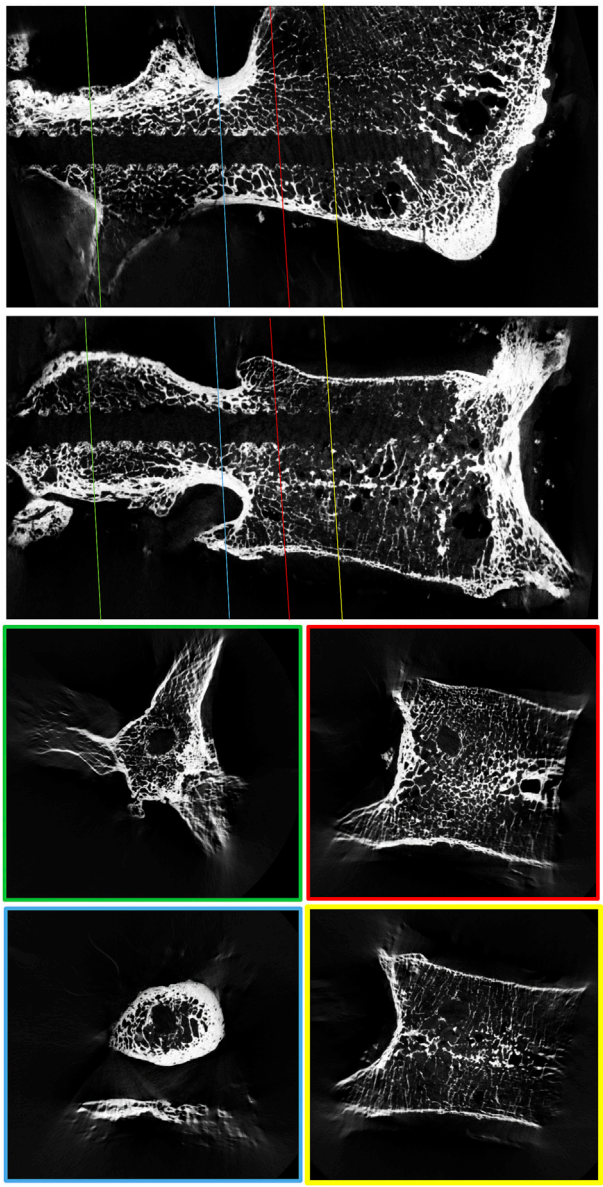

FIGURE 1
μCT reconstruction of a lumbar vertebral body to visualize the spatial variability in trabecular bone density around a 3D-printed replica of a pedicle screw.

Materials and methods

Specimen preparation

Seven L5 vertebrae of fresh frozen human cadavers were used for this study after approval by the local ethics authorities (BASEC Nr. 2017–00874). Clinical CT-scans (SOMATOM Edge Plus, Siemens Medical Solutions, Erlangen, Germany) were acquired to exclude fractures and to identify anatomical particularities, such as lumbosacral transitional anomalies. The acquisition parameters included a slice thickness of 1 mm, pixel dimensions of 0.3516 × 0.3516 mm, a peak voltage of 90–140 kVp, an x-ray tube current of 34–72 mA, and exposure times of 1,000–1,232 ms. The convolution kernel Br60s was used. To correct for the effect of different peak voltages, the grey values were approximately corrected to values corresponding to 120 kVp by using the reference values provided by the work of Afifi et al. (2020). Following the method described by Schreiber et al., the mean Hounsfield unit (HU) value of three axial elliptical regions of interest (inferior to the superior end plate, in the middle of the vertebral body and superior to the inferior end plate) was measured in the corrected CT reconstructions. The bone quality of the specimens with a mean HU value of 120 HU and larger was categorized as normal, between 90 and 119 HU as moderate (osteopenic) and below 90 HU as bad (osteoporotic) according to the reported distributions in the analyzed cohort (Schreiber et al., 2011).

After thawing, the vertebrae were skeletonized, and the pedicle screw entry points were prepared with a bone rongeur (Vaccaro et al., 2020). The pedicles were prepared with a Lenke bone probe, and the maximal insertion depth for the pedicle screw was measured. Instrumentation was performed with commercially available self-tapping polyaxial pedicle screws with a standardized diameter of 5 mm and length of 55 mm (MUST Pedicle Screw System, Medacta International SA, Castel San Pietro, Switzerland). The screws were inserted to the predefined insertion depth and the screw's rotation was brought to one of the two predefined rotational positions, to guarantee identical thread imprints at the screw's tip in all specimens. The pedicle screw was then removed, and a 3D-printed replica of the screw with a modified tail was inserted to omit metal artifacts, to improve contrast in the following micro-CT scans, and to provide mechanical reference for the screw trajectory. The 3D-printed screws were made from medical grade polyamide (P2200) and were printed using selective laser sintering (SLS) technology (P395, EOS e-Manufacturing Solutions, Munich, Germany). Insertion of the 3D-printed screw was performed with only minimal torque, preventing additional damage to the vertebral bodies. The vertebral bodies were cut in the midsagittal plane to meet the dimension limits of the specimen holder of the micro-CT scanner.

µCT imaging

µCT scans of all 14 specimens were acquired (Bruker, SkyScan 1176; PANalytical's Microfocus Tube, Source Voltage = 90 kV; Source Current = 278 µA) with a voxel size of 35.43 µm. The picture planes of the reconstructions were oriented to align with the screw's axis using dedicated software (Skyscan 1176 control software) to guarantee the same orientation of the specimens in both the µCT-scans and later biomechanical testing.

Biomechanical testing

To achieve reliable specimen fixation and adequate load distribution over a large surface area during testing, Polymethyl methacrylate (PMMA) potting (Beracryl D28 and SCS-Beracryl Monomer, Suter Kunststoffe AG, Fraubrunnen, Switzerland) was used. After wrapping the specimens in plastic foil to prevent potting intrusion (Pfeiffer et al., 1996), the tail of the 3D-printed screw replica was used by a holding apparatus to position the specimen above the potting box with the screw's trajectory horizontal and central, and with the midsagittal cut being vertical (Figure 2B). PMMA was poured to the upper rim of the potting box. After curing, the holding apparatus and the 3D-printed screws were removed, and the cranial aspect of the specimens was carefully cut with a bandsaw just cranial to the center of the pedicle screw axis (parallel to the undersurface of the potting box). With that method, the caudal screw imprint was made available for biomechanical testing (Figures 2A,C). To measure the resistance of the vertebral body perpendicular to the screw axis at different positions along the screw's trajectory, a pedicle screw of the same type as used for instrumentation was sectioned into pieces of 6 mm length with an offcut of 6 mm starting from the screw's tip. With the thread pitch of this type of pedicle screw being 3 mm, the center pieces were identical, and therefore only one center piece was required. The sections of the pedicle screws were fixed to a mounting pin to be used in the biomechanical test setup (Figure 2D). A static testing machine (Zwick/Roell Allroundline 10kN, ZwickRoell GmbH & Co. KG, Germany) was equipped with a mechanical setup, which allowed for the fixation of the potting box in the center axis of the machine, and which also allowed to move the box along the screw axis by increments of 12 mm between tests. Complementing the use of the placeholder screw as a positioning reference, the location of the threads of the screw piece was visually controlled to match the imprint in the vertebrae. After validation of the position, a punch imprint was performed at a constant rate of 0.2 mm/s, until a maximum load of 350 N for the tip piece or 500 N for the center piece was obtained. These maximal load values were chosen to guarantee overloading of the trabecular bone, while preventing failure of the cortical bone. Additional abortion criteria to protect the specimen and setup

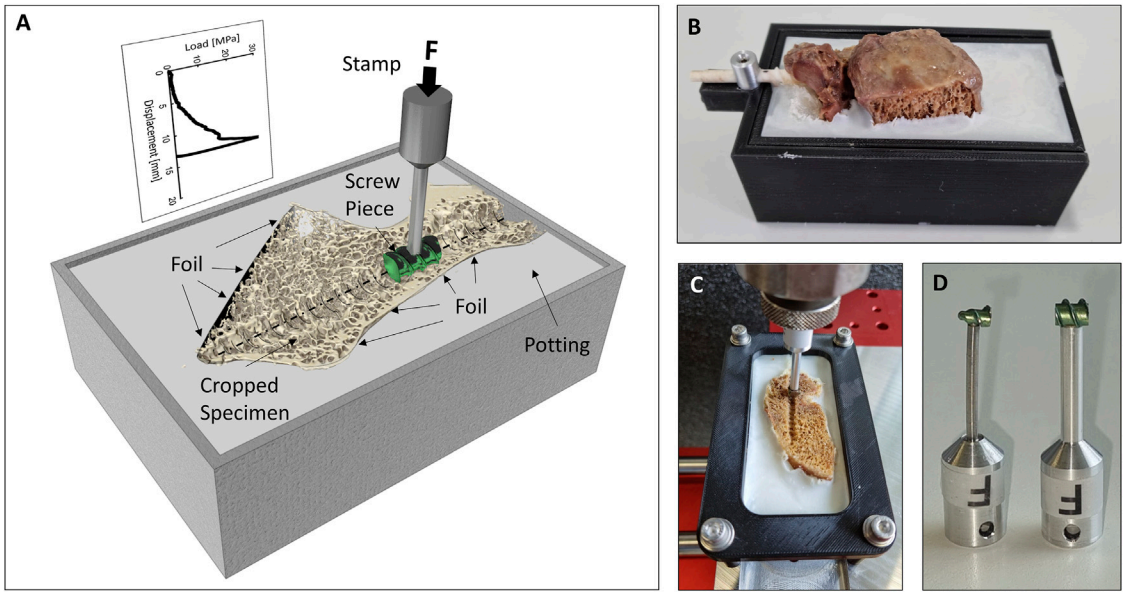

FIGURE 2
(A) Illustration of the biomechanical testing method. **(B)** Specimen after potting with the holding apparatus and the 3D-printed pedicle screw still in place. **(C)** Cropped specimen just prior to testing. **(D)** Photography of the tip (left) and center (right) screw imprint probes.

were a drop in maximal load of more than 50% or an insertion depth of more than 24 mm. The testing sequence (e.g., tip to tail) was reversed for half of the specimens to limit any systematic error due to potential effects on the adjacent testing location. Testing was performed at room temperature and the specimens were frequently strayed with phosphate buffered saline (PBS) to help prevent dehydration. To compensate for any deformation of the mechanical test setup or any motion between specimen and potting, reference measurements were conducted with the imprint stamps pushing on an aluminum plate, which has been placed on top of the specimen to allow for load distribution and to prevent any failure. The load-deflection curves from these reference measurements were used to correct the imprint measurements. Deformation of the whole setup including the sample was below 0.7 mm for a load application of 500 N.

Data analysis

The projected surface area of the two imprint probes (Figure 2D) was measured with a telecentric camera system (Edmund Optics #62–921, 182 mm WD, 0.28X, Edmund Optics Inc., Barrington, NJ, United States). This information about the projected surface area was used to convert the applied forces to stress values. The following analysis is based on the stress-displacement curves, which allow to compensate for the difference in surface area of the tip piece compared to the center piece. The parasagittal reconstructions of μCT-scans (along the screw trajectories) were used to measure the insertion length of the pedicle screw in the corpus and the pedicle region. The corpus region was defined to begin at the position of the first line perpendicular to the screw's trajectory, which intersects with the caudal endplate region and does not have contact with the posterior cortical bone. The projected surface area of the pedicle screw in the two regions was calculated.

The screw-imprint measurements were only assigned to the corpus region when they were fully localized in the corpus region (Figure 3A). The missing imprint data between the experimentally measured locations were interpolated with the neighboring stress-displacement curves of the same anatomical (Figure 3B). For sectors between two measurements of the same anatomical region, the average of these measurements was used. For a region with only one neighboring measurement of the same anatomical region, the averaged stress-deflection curve of the region was used. With that, the local stress-deflection curves along the whole screw were defined. With the known surface area of these sections, the local resisting force for any screw displacement (in the direction of the performed imprint tests) could be calculated (Figure 3C).

Assuming an average strength of 2.4 MPa (Banse et al., 2002) and a pedicle screw with a projected surface area of around 200 mm^2 (screw diameter of 5 mm and implanted screw length of 40 mm), the screw-bone interface would fail at a total loading amplitude of around 480 N. With the variability in trabecular bone strength ranging from 0.6 to 7.8 MPa (Mosekilde and

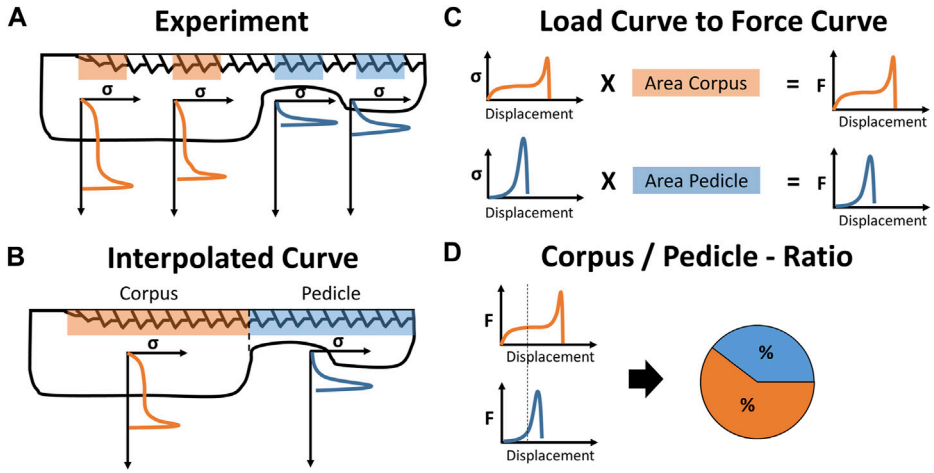

FIGURE 3
Illustration of data processing: **(A)** The experimentally derived stress-displacement curves are assigned to the corpus and pedicle region and **(B)** interpolated to a single stress-displacement curve for either anatomical region. **(C)** The projected screw surface area of both regions is used to convert the stress-values to force-values and **(D)** displacement-controlled virtual screw imprint tests are performed to calculate the load distribution between the corpus and pedicle region for specific loading conditions.

Mosekilde, 1986; Banse et al., 2002), forces of 120–1560 N could be resisted with the same pedicle screw. Therefore, total loading amplitudes of 100 N, 500 N, and 1,000 N were chosen to represent loading conditions without expected overloading (100 N), with partial overloading (500 N), and with local overloading in most cases (1000 N). The virtual screw imprint tests simulated a caudally directed displacement of the whole pedicle screw until the above-mentioned forces (100 N, 500 N, and 1,000 N) were countered by the available bone surface under the pedicle screw (Figure 3D). This method allowed to compute the screw displacement, the relative force contribution of the corpus and pedicle region, and the mean stresses at the bone surface in these two regions. These values were computed for every screw and were pooled for the three bone quality categories.

Results

The demographic characteristics of the specimens are listed in Table 1. The specimens are ordered with decreasing bone density and the same ordering is used throughout the manuscript. Bone quality was classified as normal in three specimens, as moderate in two, and as bad in two specimens, resulting in six, four, and four pedicle screws per group. Of the seven L5 vertebrae, one showed lumbosacral transitional anomaly (specimen #1, Figure 4). Because of the irregular shape of the caudal aspect of the vertebral body, the imprint tests were conducted in the cranial instead of the caudal direction for this specimen. During the imprint test of the tip piece of specimen #3 on the right-hand side (Figure 4), the test had to be stopped manually due to progressive lateral-deviation of the imprint probe. The imprint test at the most posterior testing location of specimen #1 on the right-hand side was performed with the protocol of the tip piece instead of the center piece, resulting in an imprint test with a maximum load of 350 N instead of 500 N. Analysis of the micro-CT data did not reveal any bone damage due to the insertion of the 3D-printed screw replica. All of the data was included in the evaluation.

The projected surface area of the 6 mm long screw tip piece was measured at 16.42 mm^2 and the 6 mm long center piece was measured at 29.79 mm^2. The applied maximum loads (350 and 500 N, respectively) correspond to a maximal stress of 21.3 MPa for the tip piece and 16.8 MPa for the center piece.

For a qualitative analysis of the results, the parasagittal micro-CT scans in plane with the screw trajectories are plotted in Figures 4–6 with an overlay of the pedicle screw and the stress-displacement curves at every measured location.

The implanted screw length was measured at an average of 42 mm, 36 mm, and 41 mm for the group with normal, moderate, and bad bone quality. The screw length in the pedicle region compared to the total implanted screw length was measured at averages of 63%, 62%, and 52%, which relates to an average of 68%, 68%, and 55% of the projected screw area being localized in the pedicle region for the three bone quality groups, respectively (Table 2). At a calculated 100 N axial load acting on the whole pedicle screw, the pedicle region contributed an average of 55%, 58%, and 58% resistance for the normal, moderate, and bad bone quality specimens, respectively. When this contribution is set into relation with the projected screw's surface in the pedicle region, the resistance in the pedicle region is

TABLE 1 Demographic characteristics of the specimens.

Donor #	Bone quality	Sex	Age	Height [cm]	Weight [kg]	BMI
1	Normal	Male	69	188	176.9	50
2	Normal	Male	69	183	98.9	29.6
3	Normal	Male	66	183	95.3	28.4
4	Moderate	Male	62	168	54.4	19.4
5	Moderate	Male	64	180	64.8	36.1
6	Bad	Female	59	165	50.3	18.5
7	Bad	Female	57	175	68	22.1
Mean			63.7	177.4	86.9	29.2
Standard deviation			4.3	7.8	40.6	10.3

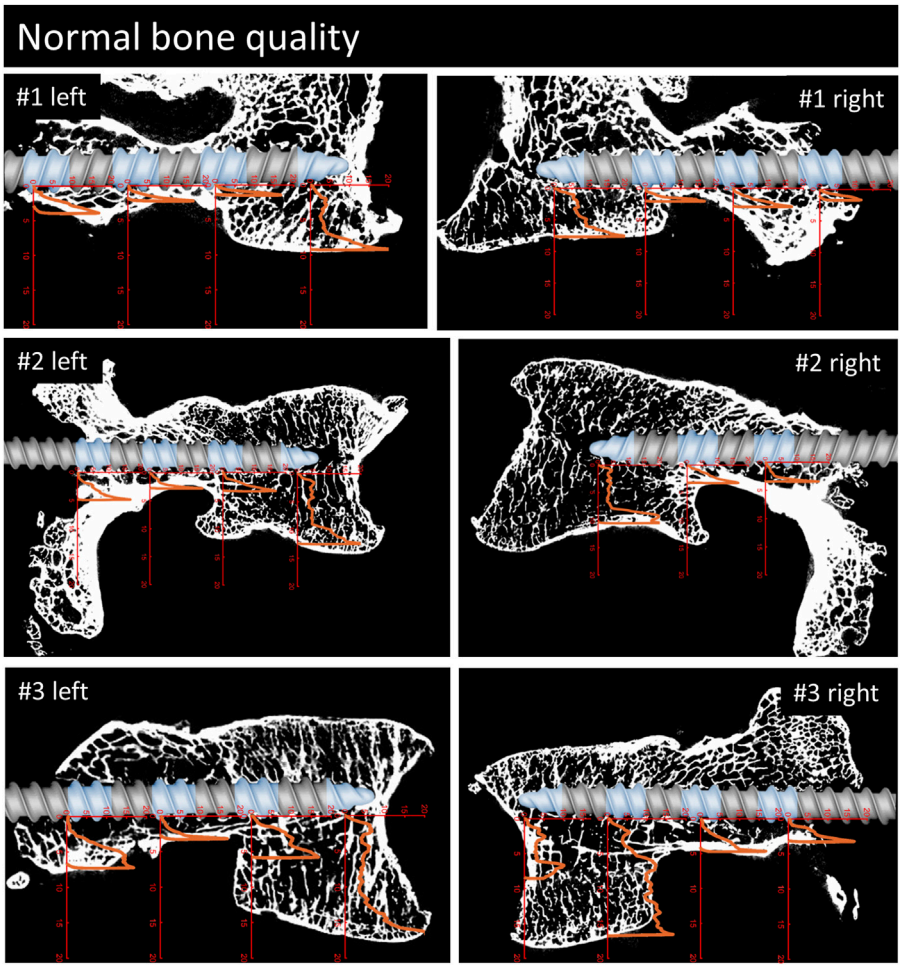

FIGURE 4
Parasagittal reconstruction of the micro-CT scans of the vertebrae with normal bone quality. An image of the pedicle screw is overlaid graphically to illustrate the position of the screw and the measurement locations (blue sections). The load [MPa]-displacement [mm] curves are depicted in orange.

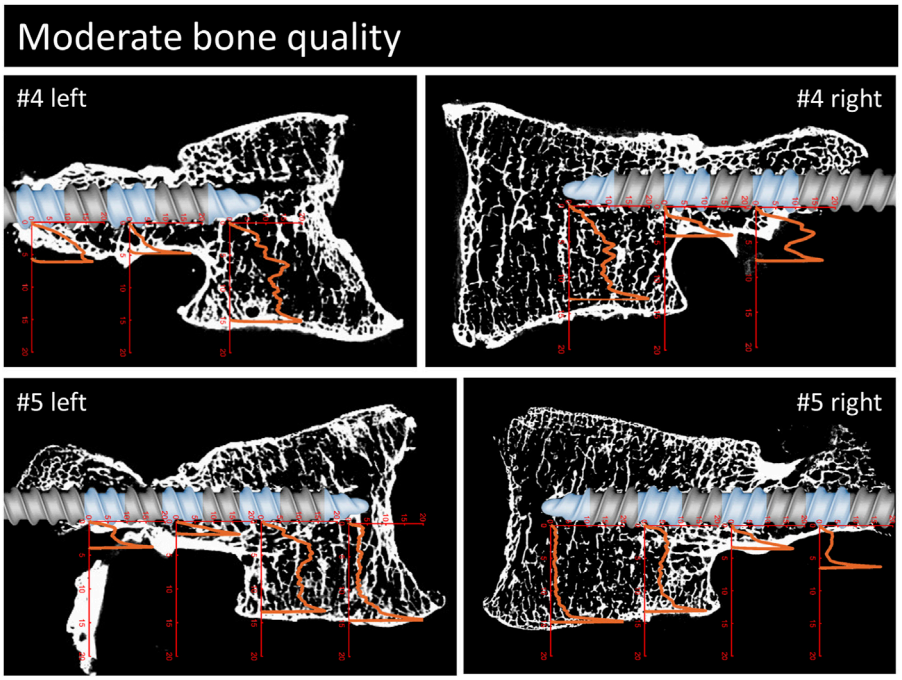

FIGURE 5
Continuation of Figure 3. Parasagittal reconstruction of the micro-CT scans of the vertebrae with moderate bone quality. An image of the pedicle screw is overlaid graphically to illustrate the position of the screw and the measurement locations (blue sections). The load [MPa]-displacement [mm] curves are depicted in orange.

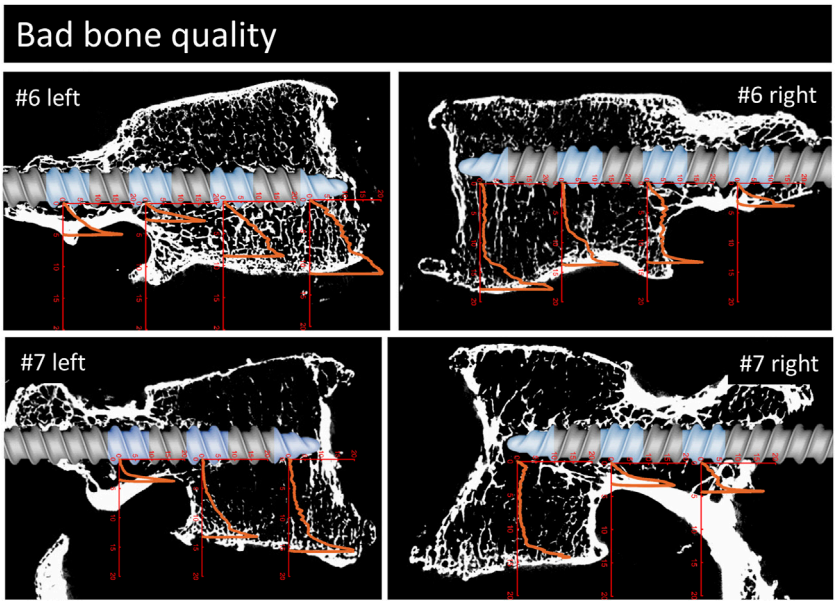

FIGURE 6
Continuation of Figures 3, 4. Parasagittal reconstruction of the micro-CT scans of the vertebrae with bad bone quality. An image of the pedicle screw is overlaid graphically to illustrate the position of the screw and the measurement locations (blue sections). The load [MPa]-displacement [mm] curves are depicted in orange.

10.3389/fbioe.2022.953119

TABLE 2 Look-up table for bone density as measured in CT, the evaluated bone quality, the length of the implanted screw, the percentage of screw length and projected screw surface area in the pedicle region, the percentage of resistance in the pedicle region as an absolute value and corrected for the projected screw surface area, the displacement values and the stress values in the pedicle and corpus region for 100 N, 500 N, and 1000 N are listed for every specimen and as averages for the three bone quality groups (HU = Hounsfield unit, PSS = projected screw surface).

Sample		Bone characteristics		Screw length	Screw in pedicle region		Resistance of pedicle region (absolute)			Resistance of pedicle region (relative to area)			Screw displacement [mm]			Stress at 100 N [MPa]		Stress at 500 N [MPa]		Stress at 1000 N [MPa]	
#	Side	Density [HU]	Quality	[mm]	Length (%)	PSS (%)	100 N	500 N	1000 N	100 N	500 N	1000 N	100 N	500 N	1000 N	Corpus	Pedicle	Corpus	Pedicle	Corpus	Pedicle
1	Right	189	Normal	42	62	66	40%	58%	63%	0.61	0.87	0.95	0.24	0.74	1.16	0.90	0.31	3.20	2.23	5.60	4.88
1	Left	189	Normal	42	67	71	67%	85%	89%	0.94	1.19	1.26	0.26	0.85	1.21	0.58	0.48	1.36	3.05	1.89	6.43
2	Right	172	Normal	36	61	66	55%	53%	77%	0.83	0.80	1.17	0.23	0.92	2.57	0.81	0.50	4.19	2.42	4.10	7.05
2	Left	172	Normal	42	62	66	49%	51%	68%	0.74	0.78	1.02	0.30	1.26	2.08	0.77	0.38	3.69	1.99	4.89	5.24
3	Right	120	Normal	42	62	66	55%	66%	70%	0.83	1.00	1.05	0.22	1.25	2.29	0.68	0.43	2.57	2.56	4.59	5.40
3	Left	120	Normal	48	67	71	65%	43%	58%	0.92	0.60	0.82	0.16	1.15	1.96	0.53	0.41	4.35	1.34	6.42	3.63
4	Right	117	Moderate	30	60	66	50%	68%	77%	0.76	1.02	1.16	0.42	1.41	2.06	1.08	0.56	3.52	3.78	5.09	8.56
4	Left	117	Moderate	30	80	88	80%	82%	87%	0.91	0.94	0.99	0.46	1.32	2.98	1.20	0.67	5.36	3.46	7.86	7.31
5	Right	113	Moderate	42	48	51	42%	43%	63%	0.82	0.84	1.23	0.16	0.92	2.57	0.61	0.42	3.00	2.14	3.88	6.32
5	Left	113	Moderate	42	62	66	60%	61%	76%	0.91	0.92	1.14	0.09	0.39	0.84	0.61	0.46	2.94	2.37	3.71	5.85
6	Right	90	Bad	46	43	46	41%	77%	85%	0.88	1.67	1.84	0.16	2.08	3.63	0.51	0.41	0.99	3.88	1.30	8.55
6	Left	90	Bad	44	41	44	47%	40%	51%	1.07	0.91	1.17	0.11	1.03	1.79	0.46	0.52	2.60	2.23	4.22	5.73
7	Right	1	Bad	36	72	78	75%	88%	95%	0.96	1.13	1.21	0.16	1.47	2.44	0.68	0.58	1.67	3.40	1.43	7.34
7	Left	1	Bad	36	50	54	67%	87%	94%	1.25	1.62	1.75	1.08	2.85	3.31	0.43	0.75	0.84	4.88	0.74	10.56
Mean for normal bone quality				42	63	68	55%	59%	71%	0.81	0.87	1.04	0.24	1.03	1.88	0.71	0.42	3.23	2.26	4.58	5.44
Mean for moderate bone quality				36	62	68	58%	63%	75%	0.85	0.93	1.13	0.28	1.01	2.11	0.87	0.53	3.70	2.94	5.13	7.01
Mean for bad bone quality				41	52	55	58%	73%	81%	1.04	1.33	1.49	0.38	1.86	2.79	0.52	0.57	1.52	3.60	1.92	8.05

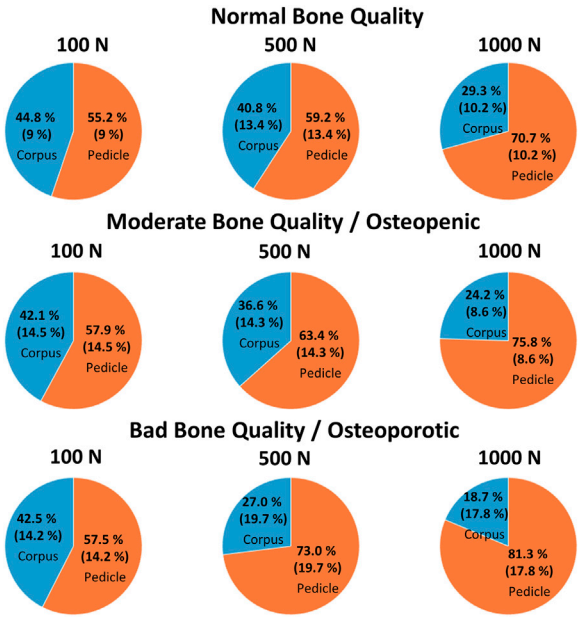

FIGURE 7
The mean (and the standard deviation) of the relative contribution of the pedicle and corpus region for normal, moderate, and bad bone quality for a total of 100 N, 500 N, and 1,000 N acting on the pedicle screw, which are illustrated using pie plots.

0.81, 0.85, and 1.04 times the resistance in the corpus region (normalization to projected surface area, Table 2). With 500 N load, the average absolute contribution of the pedicle region was 59%, 63%, and 73%, relating to a relative contribution of the pedicle region of 0.87, 0.93, and 1.33 times compared to the corpus region. With 1000 N load, the contribution of the pedicle region was quantified at 71%, 75%, and 81%, relating to the pedicle region providing 1.04, 1.13, and 1.49 times more resistance per area than the corpus region for normal, moderate, and bad bone quality, respectively. The relative contribution of the pedicle and corpus region in dependence of loading amplitude and bone quality are visualized in Figure 7. The average displacement of the screw to counter the calculated force of 100 N was 0.24 mm, 0.28 mm, and 0.38 mm for the group with normal, moderate, and bad bone quality, respectively. At 500 N force, the average displacements were 1.03 mm, 1.01 mm, and 1.86 mm and at 1000 N force, the average displacements were 1.88 mm, 2.11 mm, and 2.79 mm. Table 2 provides the main results for the individual specimens and the averaged values for the three bone quality groups.

Discussion

Pedicle screw loosening poses a relevant complication risk after posterior instrumentation of the lumbar spine. Consequently, the aim of this study was to qualitatively analyze the local support of the vertebral body along traditional pedicle screw trajectories in the caudal direction, and to quantify the contribution of the pedicle and corpus region in relation to bone quality and loading amplitude.

The overlays of the stress-displacement plots with the parasagittal micro-CT reconstructions along the screw trajectories (Figures 4–6) illustrate the local resistance of the vertebral bodies against craniocaudal loading acting on different regions of the screw. With maximal stresses of roughly 20 MPa during testing, all of the imprint tests reached the cortical shell or the endplate of the vertebral bodies. Because the ultimate strength of cancellous bone in vertebral bodies ranges from 0.6 to 7.8 MPa (Mosekilde and Mosekilde, 1986; Banse et al., 2002), this finding is in line with the expected behavior of cancellous bone under such loading conditions.

The overall shapes of the load-deflection curves can be grouped into roughly three types of behavior: curves with a rather constant stress absorbance (plateau phase) throughout a large portion of cancellous bone after an initial ramping phase, curves with a slowly progressive stress absorbance in cancellous bone after a similar initial ramping phase and finally, curves with a rather sharp increase in stress absorbance until the end of the imprint test. The first two curve types are typically found in the corpus region and the third type is primarily seen in the pedicle region. Interestingly, in situations with a large enough gap between the screw and the cortical shell, a similar plateau phase can also be seen in measurements of the pedicle region

(e.g., #1, right). The stress values at the plateau phase are assumed to be closely related to the local ultimate strength because further displacement can only be achieved through local failure of the trabecular bone structures. Therefore, the specimens with a large plateau phase in the corpus region provide a rather straightforward method to compare the stress resistance of trabecular bone in relation to bone quality. In specimens with normal bone quality, the plateau phase varies in the region of roughly 5 MPa, while in specimens with bad bone quality the plateau phase ranges at values from 1 to 3 MPa. Although general trend of lower stress absorbance in situations with reduced bone quality can clearly be seen in the presented results, some notable exceptions must be discussed: For example, the corpus region of the left side of specimen #6 shows high local bone density (as seen in the micro-CT image) and, despite the overall bone quality being labeled as bad in this specimen, the local stress resistance in this area is surprisingly good with values exceeding 10 MPa (Figure 6). In contrast, the area of the tip piece of the right side of specimen #4 resists only 1–2 MPa, even though the measured HU units of this specimen are just below the defined cut-off value for normal bone quality (117 HU, while above 120 HU normal bone quality is assumed). While these two examples demonstrate the importance of local bone density for screw hold, the general trend observed in the results with higher resistance with higher HU-units nicely shows the informative value of the rather simple and clinically applicable method to evaluate bone quality (Schreiber et al., 2011).

In the final 1–2 mm of the imprint tests, a rather steep increase in stress absorbance can be seen in virtually all measurements, independent of the location along the screw trajectory and largely unaffected by the previous shape of the load-deflection curve. This rather sharp increase in resistance is interpreted as the result of (trabecular) bone material compaction against the stable cortical shell or vertebral endplate, as well as the known increase of bone mineral density towards the cortical shell in the pedicle region (Hirano et al., 1997). In situations of minimal distance between screw and cortical shell (e.g., pedicle region of #1 left), only very small displacement values are needed to meet large resistance. This finding nicely illustrates the benefits of placing a pedicle screw close to the cortical shell which can be achieved by increasing screw diameter (larger pedicle fill) or by choosing a specific trajectory such as CBT. Another approach to achieve firm contact with the cortical shell of the pedicle region could be to use bone cement augmentation in the pedicle region. Cement augmentation of the pedicle region would further provide the advantage of reducing the potential risk of iatrogenic pedicle fracture due to the insertion of an oversized pedicle screw, and bone cement could fill the pedicle independent of its anatomical shape.

To compare the contribution of the corpus and the pedicle region quantitatively, the behavior at the measured locations was used to interpolate the missing locations along the screw, which allowed us to virtually displace the whole screw caudally and compute the relative contribution of the corpus and pedicle region, the mean stresses at the screw-bone interface of these two regions, as well as the screw's displacement.

In the situation of low loading amplitudes (100 N acting on the whole screw), no failure at the screw-bone interface is expected and differences in cortical bone stiffness can be assumed to be the primary factor for the local differences in screw support. In this situation, the contribution of the pedicle and corpus region are largely balanced, with the pedicle region providing an average of 55%–58% for all three bone quality groups (Figure 7). Interestingly, because the projected screw surface area in the pedicle is larger than the screw surface area in the corpus, the local stress resistance of the pedicle region is roughly 20% smaller compared to the corpus region in specimens with normal and moderate bone quality. In other words, the trabecular bone of the corpus provides better support than the trabecular bone of the pedicle at low loading amplitudes in this data. This finding appears contra intuitive because bone mineral density, which is known to be associated with trabecular bone strength (Keller, 1994), is typically larger at the pedicle region compared to the corpus region (Hirano et al., 1997). Furthermore, the screw's surface is closer to the cortical shell in the pedicle region, which could provide better support (and less compliance) compared to the situation in the corpus with the vertebral endplate being much further from the screw surface. One potential explanation for this finding is the consideration of the predominant loading directions of the two regions. While the primary loading direction in the corpus is craniocaudal resulting in a predominant vertical orientation of the trabecula (Bartel et al., 2006), more diverse loading directions can be postulated in the pedicle region. With the known anisotropy of trabecular bone (Bartel et al., 2006), and following Wolff's law of bone adaptation in relation to the acting stresses, the microstructure of the corpus could be better suited to counter the craniocaudally oriented loading of the screw compared to the trabecular bone of the pedicle region. Currently, much effort is invested to improve screw fixation strength by optimizing screw trajectories according to the local distribution of bone mineral density. Considering the hypothesized local differences in anisotropy of the trabecular bone in the corpus and trabecular region could help to further optimize this approach, and could even serve as the basis to develop novel implant designs to benefit from this effect.

With intermediate loading amplitudes (500 N acting on the whole screw), local failure can occur, and therefore ultimate strength of the bone can be assumed to play a more important role compared to the previously discussed loading situation. While a small increase in the support provided by the pedicle region can be observed in specimens with normal and moderate bone quality, this increase is much more accentuated in specimens with bad bone quality (Figure 7). In addition, the screw displacement in specimens with bad bone quality is more than twice as large compared to the specimens with normal or moderate bone quality. The average screw displacement of 1.86 mm in specimens with bad bone quality could potentially result in screw loosening because a radiolucency of more

than 1 mm is often used as a radiographic criterion to diagnose screw loosening (Galbusera et al., 2015). As previously discussed, one way to approach this problem is to place the pedicle screw closer to the cortical shell, by choosing a larger screw diameter (resulting in a smaller gap to the cortical shell), or by augmenting the trabecular bone of the pedicle with bone cement. With these measures, the potential screw displacement (until sufficient resistance is provided) is reduced, which could be beneficial in the prevention of screw loosening.

In the high loading amplitude situation (1000 N acting on the screw), the trends observed at the intermediate loading situation are emphasized and the relative contribution of the pedicle region is further increased to 71%, 75%, and 81%. This can be explained by the stress resistance of the pedicle region being larger than the stress resistance of the corpus region in this loading scenario. This constellation stands in contrast to the situation with 100 N loading and highlights the importance of the pedicle region for such (unphysiologically) high loading amplitudes. The load redistribution can further be seen in the changes of the local stresses from 500 N to 1000 N. At the corpus region, only a relatively small increase of the local stress can be seen (averaging at +35%), while the average increase in the pedicle region is +140%.

This work has experienced several limitations. First, the chosen loading condition is a gross simplification of the complex loading conditions that can occur during activities of daily living and represents just one specific loading scenario in which the pedicle screw is loaded perpendicular to its axis in a caudal direction. Additional loading conditions, such as bending or pull-out forces, are not represented and the consequence of different compliance along the screw axis is not included. Furthermore, simple load-to-failure tests were performed and parameters such as fatigue failure or biological adaptation such as the bone remodeling are not considered. The method that was used to interpolate the measurement data to the whole screw is associated with some uncertainty and could interfere with the results. Furthermore, screw insertion depth and with that the distribution of the projected screw surface in the corpus and pedicle region were not standardized, and therefore some variability exists between specimens (Table 2). Because the averaged values were not largely different between the groups, the effect on the data analysis should be acceptable. Nevertheless, the authors believe that thanks to this simple approach, the gained insights can be well understood and help to further our understanding of the problem of screw loosening.

Replica screw insertion and bandsaw cutting of the specimens could have induced some damage to the vertebral bodies, which could have in turn affected the measurements. Visually, there were no signs of relevant bone damage due to the specimen preparation. Because any potential damage would be affecting all measurement locations to a similar degree, the effect on the results should be minimal. To achieve reliable specimen fixation, PMMA-potting was used, which can generate elevated temperatures due to the exothermic nature of the chemical reaction (Amin et al., 2015). While these elevated temperatures might harm biological tissue, the effect on the mineralized bone material is evaluated to be of minor importance. The size of the screw pieces used for imprint testing was chosen at 6 mm to provide sufficient surface area to be more robust against very localized differences in bone density. Nevertheless, with the sharp edge at the performed cut, the failure mechanism of trabecular bone could be different from an intact pedicle screw without such edges. The distance between imprint tests was chosen at 6 mm to limit the effect on the adjacent segments. Furthermore, the testing sequence was reversed for half of the specimens to limit any systematic effect. Nevertheless, some effect on the results cannot be excluded. Based on the experimental work by Grant et al., the ultimate strength of the inferior endplate of lumbar vertebrae can be assumed to be roughly 10–15 MPa (assuming 100–150 N failure load with the indenter of 3 mm diameter) (Grant et al., 2001). Bone mineral density of the cortical shell of the pedicle region can be assumed to be at around 800 mg/cm^3 (Hirano et al., 1997), which would correspond to an ultimate strength of roughly 70 MPa (Keller, 1994; Schileo et al., 2008). This is in line with ultimate strength values for human cortical bone reported in the literature (Mirzaali et al., 2016; Wolfram and Schwiedrzik, 2016). Therefore, the cortical shell of the pedicle should be able to withstand the applied stresses; however, endplate failure or cortical shell breakthrough could occur. The absence of such failure in our data must be ascribed to the additional support given by the PMMA-embedment. Measurements with stresses exceeding the expected failure level must therefore be analyzed with prudence because the resistance of the endplate could be overestimated. Nevertheless, the increase in stress absorbance towards the endplate is assumed to be representative of reality, while the final peak values might be too high. Given that in all virtual loading scenarios (100 N, 500 N, and 1,000 N acting on the screw) the maximal stress values were below 11 MPa, this analysis should not be affected.

Conclusion

Unidirectional imprint tests of pedicle screw sections perpendicular to the screw surface have been performed to analyze the resistance along the pedicle screws following the traditional trajectory. At low loading amplitudes, the trabecular bone of the corpus region appears to provide slightly more support than the trabecular bone of the pedicle region. This observation could be the result of trabecular bone anisotropy, which could be used to further optimize screw trajectories and implant designs. At higher loading amplitudes, and especially in specimens with reduced bone quality, the contribution of the pedicle region becomes predominant, which can be ascribed to the increasing support of the cortical shell after some screw displacement towards the cortex.

To reduce the risk of screw loosening, it could be beneficial to limit the available subsidence distance until adequate resistance is met. To achieve this goal, the distance to the cortical bone could be reduced by placing the pedicle screw closer to the cortex, by selecting a larger screw diameter, or potentially by augmenting the pedicle with bone cement.

Data availability statement

The original contributions presented in the study are included in the article/Supplementary Material, and further inquiries can be directed to the corresponding author.

Ethics statement

The studies involving human participants were reviewed and approved by Kantonale Ethikkomission Zürich (KEK) Stampfenbachstrasse 121 8090 Zürich. Written informed consent for participation was not required for this study in accordance with the national legislation and the institutional requirements.

Author contributions

FC, MF, and JW contributed to conception and design of the study. FC performed the experimental work. JW performed data analysis. FC and JW wrote the first draft of the manuscript. All authors contributed to manuscript revision, read, and approved the submitted version.

Acknowledgments

The authors gratefully acknowledge the contribution of Mauro Sutter for his support with the mechanical test setup and during biomechanical testing. Imaging was performed with support of the Swiss Center for Musculoskeletal Imaging, SCMI, Balgrist Campus AG, Zürich, with special acknowledgement to Natalie Hinterholzer and Daniel Nanz.

Conflict of interest

The authors declare that the research was conducted in the absence of any commercial or financial relationships that could be construed as a potential conflict of interest.

Publisher's note

All claims expressed in this article are solely those of the authors and do not necessarily represent those of their affiliated organizations, or those of the publisher, the editors and the reviewers. Any product that may be evaluated in this article, or claim that may be made by its manufacturer, is not guaranteed or endorsed by the publisher.

References

Afifi, M. B., Abdelrazek, A., Deiab, N. A., Abd El-Hafez, A. I., and El-Farrash, A. H. (2020). The effects of CT x-ray tube voltage and current variations on the relative electron density (RED) and CT number conversion curves. *J. Radiat. Res. Appl. Sci.* 13 (1), 1–11. doi:10.1080/16878507.2019.1693176

Aichmair, A., Moser, M., Bauer, M. R., Bachmann, E., Snedeker, J. G., Betz, M., et al. (2017). Pull-out strength of patient-specific template-guided vs. free-hand fluoroscopically controlled thoracolumbar pedicle screws: a biomechanical analysis of a randomized cadaveric study. *Eur. Spine J.* 26 (11), 2865–2872. doi:10.1007/s00586-017-5025-7

Amin, D. B., Lawless, I. M., Sommerfeld, D., Stanley, R. M., Ding, B., and Costi, J. J. (2015). Effect of potting technique on the measurement of six degree-of-freedom viscoelastic properties of human lumbar spine segments. *J. Biomech. Eng.* 137 (5), 054501. doi:10.1115/1.4029698

Banse, X., Sims, T. J., and Bailey, A. J. (2002). Mechanical properties of adult vertebral cancellous bone: Correlation with collagen intermolecular cross-links. *J. Bone Min. Res.* 17 (9), 1621–1628. doi:10.1359/jbmr.2002.17.9.1621

Bartel, D. L., Davy, D. T., and Keaveny, T. M. (2006). *Orthopaedic Biomechanics: Mechanics and design in musculoskeletal systems*. Upper Saddle River, New Jersey: Prentice-Hall, 370. First edit. Prentice Hall.

Becker, S., Chavanne, A., Spitaler, R., Kropik, K., Aigner, N., Ogon, M., et al. (2008). Assessment of different screw augmentation techniques and screw designs in osteoporotic spines. *Eur. Spine J.* 17 (11), 1462–1469. doi:10.1007/s00586-008-0769-8

Biswas, J. K., Dey, S., Karmakar, S. K., Roychowdhury, A., and Datta, S. (2018). Design of patient specific spinal implant (pedicle screw fixation) using FE analysis and soft computing techniques. *Curr. Med. Imaging Former Curr. Med. Imaging Rev.* 16 (4), 371–382. doi:10.2174/1573405614666181018122538

Biswas, J. K., Kalita, K., and Roychowdhury, A. (2022). Symbolic regression metamodel-based optimal design of patient-specific spinal implant (pedicle screw fixation). *Eng. Comput.* 38 (2), 999–1014. doi:10.1007/s00366-020-01090-z

Bredow, J., Boese, C. K., Werner, C. M. L., Siewe, J., Löhrer, L., Zarghooni, K., et al. (2016). Predictive validity of preoperative CT scans and the risk of pedicle screw loosening in spinal surgery. *Arch. Orthop. Trauma Surg.* 136 (8), 1063–1067. doi:10.1007/s00402-016-2487-8

Burval, D. J., McLain, R. F., Milks, R., and Inceoglu, S. (2007). Primary pedicle screw augmentation in osteoporotic lumbar vertebrae: Biomechanical analysis of pedicle fixation strength. *Spine* 32 (10), 1077–1083. doi:10.1097/01.brs.0000261566.38422.40

Chevalier, Y., Matsuura, M., Krüger, S., Fleege, C., Rickert, M., Rauschmann, M., et al. (2018). Micro-CT and micro-FE analysis of pedicle screw fixation under different loading conditions. *J. Biomech.* 70, 204–211. doi:10.1016/j.jbiomech.2017.12.023

Cornaz, F., Widmer, J., Snedeker, J. G., Spirig, J. M., and Farshad, M. (2021). Cross-links in posterior pedicle screw-rod instrumentation of the spine: a systematic review on mechanical, biomechanical, numerical and clinical studies. *Eur. Spine J.* 30 (1), 34–49. doi:10.1007/s00586-020-06597-z

El Saman, A., Meier, S., Sander, A., Kelm, A., Marzi, I., and Laurer, H. (2013). Reduced loosening rate and loss of correction following posterior stabilization with or without PMMA augmentation of pedicle screws in vertebral fractures in the elderly. *Eur. J. Trauma Emerg. Surg.* 39 (5), 455–460. doi:10.1007/s00068-013-0310-6

Elmekaty, M., Kotani, Y., El Mehy, E., Robinson, Y., El Tantawy, A., Sekiguchi, I., et al. (2018). Clinical and radiological comparison between three different minimally invasive surgical fusion techniques for single-level lumbar isthmic and degenerative spondylolisthesis: Minimally invasive surgical posterolateral fusion versus MinimallyInvasive surgical transforaminal lumbar InterbodyFusion versus midline lumbar fusion. *Asian Spine J.* 12 (5), 870–879. doi:10.31616/asj.2018.12.5.870

Galbusera, F., Volkheimer, D., Reitmaier, S., Berger-Roscher, N., Kienle, A., and Wilke, H. J. (2015). Pedicle screw loosening: a clinically relevant complication? *Eur. Spine J.* 24 (5), 1005–1016. doi:10.1007/s00586-015-3768-6

Glennie, R. A., Dea, N., Kwon, B. K., and Street, J. T. (2015). Early clinical results with cortically based pedicle screw trajectory for fusion of the degenerative lumbar spine. *J. Clin. Neurosci.* 22 (6), 972–975. doi:10.1016/j.jocn.2015.01.010

Grant, J. P., Oxland, T. R., and Dvorak, M. F. (2001). Mapping the structural properties of the lumbosacral vertebral endplates. *Spine (Phila Pa 1976)* 26 (8), 889–896. doi:10.1097/00007632-200104150-00012

Guozhi, H., Tangchao, Y., Guoqing, D., Zhangcong, S., xian, Li Y., ye, Mo G., et al. (2019). The cement leakage in cement-augmented pedicle screw instrumentation in degenerative lumbosacral diseases: a retrospective analysis of 202 cases and 950 augmented pedicle screws. *Eur. Spine J.* 28 (7), 1661–1669. doi:10.1007/s00586-019-05985-4

Hirano, T., Hasegawa, K., Takahashi, H. E., Uchiyama, S., Hara, T., Washio, T., et al. (1997). *Structural characteristics of the pedicle and its role in screw stability*, 22, 2504–2510. doi:10.1097/00007632-199711010-00007*Spine*

Janssen, I., Ryang, Y. M., Gempt, J., Bette, S., Gerhardt, J., Kirschke, J. S., et al. (2017). Risk of cement leakage and pulmonary embolism by bone cement-augmented pedicle screw fixation of the thoracolumbar spine. *Spine J.* 17 (6), 837–844. doi:10.1016/j.spinee.2017.01.009

Keller, T. S. (1994). Predicting the compressive mechanical behavior of bone. *J. Biomech.* 27 (9), 1159–1168. doi:10.1016/0021-9290(94)90056-6

Kim, J. H., Ahn, D. K., Shin, W. S., Kim, M. J., Lee, H. Y., and Go, Y. R. (2020). Clinical effects and complications of pedicle screw augmentation with bone cement: Comparison of fenestrated screw augmentation and vertebroplasty augmentation. *Clin. Orthop. Surg.* 12 (2), 194–199. doi:10.4055/cios19127

Lai, D. M., Shih, Y. T., Chen, Y. H., Chien, A., and Wang, J. L. (2018). Effect of pedicle screw diameter on screw fixation efficacy in human osteoporotic thoracic vertebrae. *J. Biomech.* 70, 196–203. doi:10.1016/j.jbiomech.2017.10.009

Liebsch, C., Zimmermann, J., Graf, N., Schilling, C., Wilke, H. J., and Kienle, A. (2018). *In vitro* validation of a novel mechanical model for testing the anchorage capacity of pedicle screws using physiological load application. *J. Mech. Behav. Biomed. Mat.* 77, 578–585. doi:10.1016/j.jmbbm.2017.10.030

Mac-Thiong, J. M., Parent, S., Poitras, B., Joncas, J., and Hubert, L. (2013). Neurological outcome and management of pedicle screws misplaced totally within the spinal canal. *Spine* 38 (3), 229–237. doi:10.1097/brs.0b013e31826980a9

Martin, B. I., Mirza, S. K., Spina, N., Spiker, W. R., Lawrence, B., and Brodke, D. S. (2019). Trends in lumbar fusion procedure rates and associated hospital costs for degenerative spinal diseases in the United States, 2004 to 2015. *Spine (Phila Pa 1976)* 44 (5), 369–376. doi:10.1097/brs.0000000000002822

Matsukawa, K., Yato, Y., Imabayashi, H., Hosogane, N., Abe, Y., Asazuma, T., et al. (2016). Biomechanical evaluation of fixation strength among different sizes of pedicle screws using the cortical bone trajectory: What is the ideal screw size for optimal fixation? *Acta Neurochir. (Wien).* 158 (3), 465–471. doi:10.1007/s00701-016-2705-8

Mirzaali, M. J., Schwiedrzik, J. J., Thaiwichai, S., Best, J. P., Michler, J., Zysset, P. K., et al. (2016). Mechanical properties of cortical bone and their relationships with age, gender, composition and microindentation properties in the elderly. *Bone* 93, 196–211. doi:10.1016/j.bone.2015.11.018

Mosekilde, L. L., and Mosekilde, L. L. (1986). Normal vertebral body size and compressive strength: Relations to age and to vertebral and iliac trabecular bone compressive strength. *Bone* 7 (3), 207–212. doi:10.1016/8756-3282(86)90019-0

Ohba, T., Ebata, S., Oba, H., Koyama, K., and Haro, H. (2019). Risk factors for clinically relevant loosening of percutaneous pedicle screws. *Spine Surg. Relat. Res.* 3 (1), 79–85. doi:10.22603/ssrr.2018-0018

Ohlin, A., Karlsson, M., Duppe, H., Hasserius, R., and Redlund-Johnell, I. (1994). Complications after transpedicular stabilization of the spine: A survivorship analysis of 163 cases. *Spine (Phila Pa 1976)* 19 (24), 2774–2779. doi:10.1097/00007632-199412150-00007

Patel, S. S., Cheng, W. K., and Danisa, O. A. (2016). Early complications after instrumentation of the lumbar spine using cortical bone trajectory technique. *J. Clin. Neurosci.* 24, 63–67. doi:10.1016/j.jocn.2015.07.018

Pfeiffer, M., Gilbertson, L. G., Goel, V. K., Griss, P., Keller, J. C., Ryken, T. C., et al. (1996). Effect of specimen fixation method on pullout tests of pedicle screws. *Spine (Phila Pa 1976)* 21 (9), 1037–1044. doi:10.1097/00007632-199605010-00009

Reisener, M. J., Pumberger, M., Shue, J., Girardi, F. P., and Hughes, A. P. (2020). Trends in lumbar spinal fusion—a literature review. *J. Spine Surg.* 6 (4), 752–761. doi:10.21037/jss-20-492

Röllinghoff, M., Schlüter-Brust, K., Groos, D., Sobottke, R., Michael, J. W-P., Eysel, P., et al. (2010). Mid-range outcomes in 64 consecutive cases of multilevel fusion for degenerative diseases of the lumbar spine. *Orthop. Rev. (Pavia).* 2 (1), 3. doi:10.4081/or.2010.e3

Santoni, B. G., Hynes, R. A., McGilvray, K. C., Rodriguez-Canessa, G., Lyons, A. S., Henson, M. A. W., et al. (2009). Cortical bone trajectory for lumbar pedicle screws. *Spine J.* 9 (5), 366–373. doi:10.1016/j.spinee.2008.07.008

Schileo, E., Dall'Ara, E., Taddei, F., Malandrino, A., Schotkamp, T., Baleani, M., et al. (2008). An accurate estimation of bone density improves the accuracy of subject-specific finite element models. *J. Biomech.* 41 (11), 2483–2491. doi:10.1016/j.jbiomech.2008.05.017

Schreiber, J. J., Anderson, P. A., Rosas, H. G., Buchholz, A. L., and Au, A. G. (2011). Hounsfield units for assessing bone mineral density and strength: A tool for osteoporosis management. *J. Bone Jt. Surg.* 93 (11), 1057–1063. doi:10.2106/jbjs.j.00160

Spirig, J. M., Winkler, E., Cornaz, F., Fasser, M-R., Betz, M., Snedeker, J. G., et al. (2021). Biomechanical performance of bicortical versus pericortical bone trajectory (CBT) pedicle screws. *Eur. Spine J.* 30 (8), 2292–2300. doi:10.1007/s00586-021-06878-1

Vaccaro, A., Kandziora, F., Fehlings, M., and Shanmughanathan, R. (2020). Pedicle screw insertion. [Internet]. AO Surgery Reference [cited 2022 Jul 6]. Available at: https://surgeryreference.aofoundation.org/spine/trauma/thoracolumbar/basic-technique/pedicle-screw-insertion#entry-points.

Van den Abbeele, M., Valiadis, J. M., Lima, L. V. P. C., Khalifé, P., Rouch, P., and Skalli, W. (2018). Contribution to FE modeling for intraoperative pedicle screw strength prediction. *Comput. Methods Biomech. Biomed. Engin.* 21 (1), 13–21. doi:10.1080/10255842.2017.1414200

Wang, Z., Liu, Y., Rong, Z., Wang, C., Liu, X., Zhang, F., et al. (2019). Clinical evaluation of a bone cement-injectable cannulated pedicle screw augmented with polymethylmethacrylate: 128 osteoporotic patients with 42 months of follow-up. *Clinics* 74, e346. doi:10.6061/clinics/2019/e346

Weiser, L., Huber, G., Sellenschloh, K., Viezens, L., Püschel, K., Morlock, M. M., et al. (2017). Insufficient stability of pedicle screws in osteoporotic vertebrae: biomechanical correlation of bone mineral density and pedicle screw fixation strength. *Eur. Spine J.* 26 (11), 2891–2897. doi:10.1007/s00586-017-5091-x

Widmer, J., Fasser, M-R., Croci, E., Spirig, J., Snedeker, J. G., and Farshad, M. (2020). Individualized prediction of pedicle screw fixation strength with a finite element model. *Comput. Methods Biomech. Biomed. Engin.* 23 (4), 155–167. doi:10.1080/10255842.2019.1709173

Wolfram, U., and Schwiedrzik, J. (2016). Post-yield and failure properties of cortical bone. *Bonekey Rep.* 5, 1–10. doi:10.1038/bonekey.2016.60

frontiers | Frontiers in Bioengineering and Biotechnology

TYPE Original Research
PUBLISHED 09 September 2022
DOI 10.3389/fbioe.2022.949802

OPEN ACCESS

EDITED BY
Keitaro Matsukawa,
Murayama Medical Center (NHO),
Japan

REVIEWED BY
Paphon Sa-Ngasoongsong,
Mahidol University, Thailand
Dan Ioan Stoia,
Politehnica University of Timişoara,
Romania

*CORRESPONDENCE
Kuo-Chih Su,
kcsu@vghtc.gov.tw

SPECIALTY SECTION
This article was submitted
to Biomechanics,
a section of the journal
Frontiers in Bioengineering
and Biotechnology

RECEIVED 21 May 2022
ACCEPTED 18 August 2022
PUBLISHED 09 September 2022

CITATION
Wang C-C, Lee C-H, Chen K-H,
Pan C-C, Tsai M-T and Su K-C (2022),
Biomechanical effects of different
numbers and locations of screw-in
clavicle hook plates.
Front. Bioeng. Biotechnol. 10:949802.
doi: 10.3389/fbioe.2022.949802

Biomechanical effects of different numbers and locations of screw-in clavicle hook plates

Cheng-Chi Wang[1,2,3], Cheng-Hung Lee[1,4,5], Kun-Hui Chen[1,5,6], Chien-Chou Pan[1,7], Ming-Tzu Tsai[8] and Kuo-Chih Su[8,9,10]*

[1]Department of Orthopedics, Taichung Veterans General Hospital, Taichung, Taiwan, [2]Department of Health Services Administration, China Medical University, Taichung, Taiwan, [3]Department of Public Health, China Medical University, Taichung, Taiwan, [4]Department of Food Science and Technology, HungKuang University, Taichung, Taiwan, [5]Department of Post-Baccalaureate Medicine, College of Medicine, National Chung Hsing University, Taichung, Taiwan, [6]Department of Computer Science and Information Engineering, Providence University, Taichung, Taiwan, [7]Department of Rehabilitation Science, Jenteh Junior College of Medicine, Nursing and Management, Miaoli, Taiwan, [8]Department of Biomedical Engineering, HungKuang University, Taichung, Taiwan, [9]Department of Medical Research, Taichung Veterans General Hospital, Taichung, Taiwan, [10]Department of Chemical and Materials Engineering, Tunghai University, Taichung, Taiwan

Purpose: We sought to analyze the biomechanical effects which both different numbers and locations of screws have on three different clavicle hook plates, as well as any possible causes of sub-acromial bone erosion and peri-implant clavicular fractures.

Methods: This study built thirteen groups of finite element models using three different clavicle hook plates (short plates, long plates, and posterior hook offset plates) in varying numbers and locations of the screws. The von Mises stress distribution of the clavicle and hook plate, as well as the reaction force of the acromion was evaluated.

Results: The results show that inserting screws in all available screw holes on the hook plate produces a relatively large reaction force on the acromion, particularly in the axial direction of the bone plate. The fewer the screws implanted into the clavicle hook plate, the larger the area of high-stress distribution there is in the middle of the clavicle, and also, the higher the stress distribution on the clavicle hook plate.

Conclusion: This study provides orthopedic physicians with the biomechanical analysis of different numbers and locations of screws in clavicle hook plates to help minimize surgical complications.

KEYWORDS

clavicle hook plate, biomechanics, finite element analysis, acromioclavicular joint, numbers of screw, locations of screw

Introduction

Clavicle hook plates are commonly used for acromioclavicular joint dislocations and distal clavicle fractures (Di Francesco et al., 2012; Tiren et al., 2012; Kumar and Sharma, 2015; Yoon et al., 2018; Baunach et al., 2021). During surgery, after the reduction of a fracture or dislocation, the hook is applied under the acromion and the plate is fixed by screws on the clavicle. Hook plates are available in various lengths and offsets to suit different anatomies and clinical conditions. Hook plates provide a convenient and reliable method, as well as good stability for the fixation of the acromioclavicular joint (Kim et al., 2015).

Stress on both the acromion and clavicle changes after implantation of a hook plate. Common complications resulting from hook plates include sub-acromial bone erosion (Chiang et al., 2010; Hoffler and Karas, 2010; Lopiz et al., 2019) and peri-implant clavicular fractures (Charity et al., 2006; Ding et al., 2011; Lopiz et al., 2019; Ni et al., 2020; Shih et al., 2020), which are related to changes in stress on the bone after implantation. Understanding these stress changes is essential for physicians. However, there is currently no consensus on the optimal number of screws or screw locations on the plate. Sometimes the screw hole is at the fracture site, or the screw position is eccentric due to the curvature of the plate not matching the curvature of the clavicle. Therefore, not all screw holes are necessarily secured with screws. There have not yet been any clinical studies or biomechanical experiments to investigate the effects of different screw numbers and their locations.

Finite element analysis (FEA) is often used in orthopedic studies in order to analyze the biomechanical effects of different material properties and the different geometric shapes of plates (Marinescu et al., 2017; Hamandi et al., 2018; Antoniac et al., 2019). According to previous studies, lower-offset hook plates and shorter plates increase subacromial stress (Shih et al., 2015; Lee et al., 2016). A larger hook angle increases subacromial stress but reduces stress around the plate (Hung et al., 2017). Therefore, FEA is suitable for evaluating the impact a hook plate has on the shoulder after implantation.

This study conducted FEA in order to analyze the biomechanical effects of different types of hook plates in varying screw numbers and locations, as well as the possible causes of sub-acromial bone erosion and peri-implant clavicular fractures. Orthopedic physicians will be able to utilize the study results to better place screws in their appropriate positions to help reduce surgical complications.

Materials and methods

Building a simulation geometry model

This study involved building a computer model for FEA of clavicle hook plates which had been implanted in an acromioclavicular joint (Figure 1) for the purposes of investigating the effects different screw numbers and locations of different clavicle hook plates have on patients. The model used in this study was divided into four parts: the clavicle, acromion, clavicle hook plate, and screws. The models of the clavicle and acromion used CT images provided by the United States National Library of Medicine's Visible Human Project, and then used Mimics software (Mimics Medical 20.0, Materialise, Leuven, Belgium) to select the clavicle and acromion. The bone was then divided into two parts: the cortical bone and cancellous bone. In addition, this study used CAD software Solidworks 2016 (Solidworks 2016, Dassault Systemes SolidWorks Corp, Waltham, MA, United States) to build the models of the clavicle hook plates and screws.

According to the existing clavicle hook plate system used in clinical practice, three different clavicle hook plate models are then established: the short plate, long plate, and posterior hook offset plate (Figure 2). The number of screws that can be implanted in the three groups of clavicle hook plates are six-hole, eight-hole, and five-hole, respectively. Therefore, different numbers of screws were implanted in the three different models of the clavicle hook plates, which could then be further divided into thirteen groups (Figure 2). CAD software Solidworks was utilized to combine the clavicle, acromion, clavicle hook plate, and screws. Therefore, this study built a total of thirteen groups of computer finite element models. After the 3D finite element models were established, the models were imported into FEA software (ANSYS Workbench 18.0, ANSYS, Inc., Canonsburg, PA, United States) for finite element analysis simulation.

Boundary conditions and load conditions

The boundary conditions and load conditions in this study were determined by simulating the force of the sternocleidomastoid muscle when the arm picked up a teacup (the static position in front of the mouth with a cup weighing 0.5 kg in the hand) (Cronskär et al., 2015). Therefore, one load condition and two boundary conditions were given. The load condition is determined when a pull-up force is applied to the area where the sternocleidomastoid muscle attaches to the clavicle (X-axis: −1.5°N, Y-axis: 14.2°N, Z-axis: −4.2°N). The boundary condition is that the lower ends of the proximal clavicle and acromion are set to be fixed. The proximal clavicle is fixed at one point (the X-axis, Y-axis, and Z-axis displacements of this point are set to zero) so that the clavicle can rotate after being stressed (Figure 3). In addition, this study mainly simulates the clavicle hook plate implantation when the acromioclavicular ligament and the coracoclavicular ligament have been ruptured, so external force was only applied to the sternocleidomastoid muscle. In this study, the clavicle was built using CAD software. Therefore, each clavicle was placed in the same position in the computer (the clavicle position was also

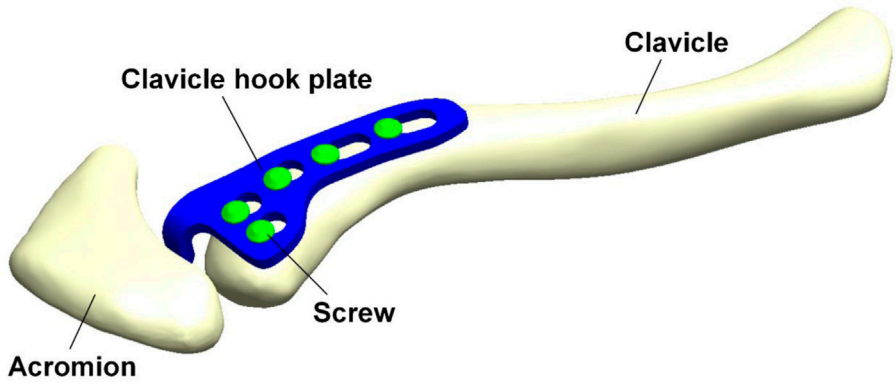

FIGURE 1
Computer model for finite element analysis of a clavicle hook plate implanted in an acromioclavicular joint.

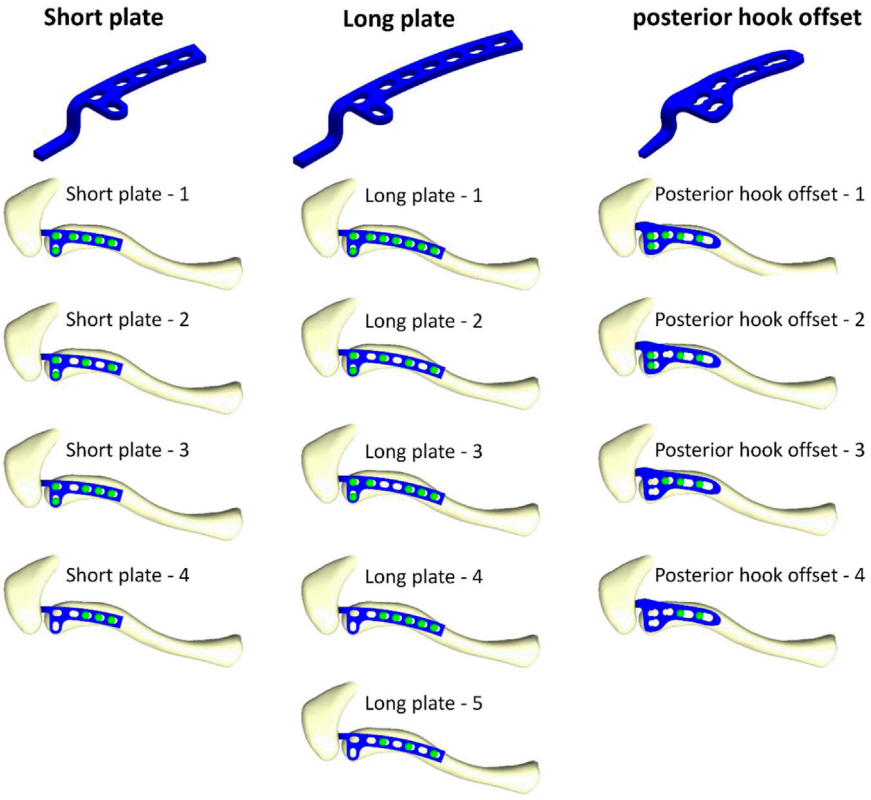

FIGURE 2
Thirteen models composed of three different clavicle hook plates, with various screw placement positions.

determined by reference to the previous study). As a result, it was possible to provide the loading conditions for each group in this study by referring to the external force from the previous study. In addition, in order to make this study closer to the actual situation, the contact between the clavicle hook plate and screws is set as "bonded," and the contact between the clavicle hook plate and acromion is set as "no separation." "No separation" means that two faces in non-separating contact are in contact only in their normal direction, allowing a slight slither between each other in the tangential direction (Lee, 2018). Such a setting can

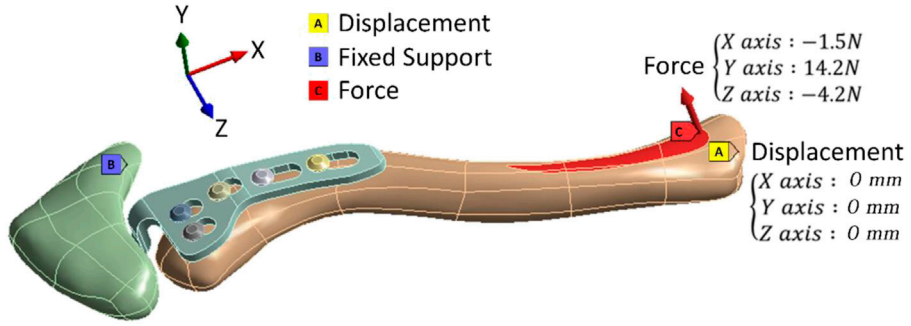

FIGURE 3
Boundary conditions and load conditions.

TABLE 1 Material properties of this study.

Material	Young's modulus (MPa)	Poisson's ratio
Cortical bone	17,000	0.3
Cancellous bone	1,000	0.3
Clavicle hook plate	200,000	0.3
Screws	118,000	0.3

simulate the actual situation of hook plate implantation being performed in the human body.

Material properties of the model

The computer model of this study consisted of four parts: the clavicle, acromion, clavicle hook plate, and screws. The material of the clavicle hook plate was simulated in titanium. All materials were assumed to be homogeneous, isotropic, and linearly elastic. According to previous studies, Young's modulus (E) and Poisson's ratio (v) were used to determine the material properties (Table 1) (Shih et al., 2015; Lee et al., 2016; Hung et al., 2017). The mesh element used in the finite element analysis computer model of this study is a tetrahedral mesh. A convergence test was performed prior to finite element analysis in order to make computer simulation data more accurate. The convergence test used in this study was mainly controlled by mesh size as the basis for convergence. The mesh sizes controlled by the convergence test were 3, 2, 1, 0.9, and 0.8 mm, respectively. After the mesh convergence test, the mesh size was 0.9 mm and the model reached 5% of the stopping criterion for the convergence test. The thirteen groups of models were meshed at a mesh size of 0.9 mm and built using quadratic tetrahedral elements (Figure 4). Therefore, it is reasonable to use the mesh model in this study to investigate the biomechanical influence of different numbers and locations of screws in clavicle hook plates. Table 2 shows the number of elements and nodes after meshing in each group.

After finite element analysis, this study observed von Mises stress in different types of clavicle hook plates involving different screw numbers and locations. The stress distribution on the clavicle hook plate and clavicle, as well as the reaction force of the acromion, was analyzed.

Results

Figure 5 shows the force reaction of the acromion. It reveals that there is a relatively small reaction force on the acromion where the screw holes near the acromion have no screws (short plate—4, long plate—4, long plate—5, posterior hook offset—3, and posterior hook offset—4). Table 3 shows the magnitude of force reaction on the acromion in the X-, Y-, and Z-axes. For the clavicle hook plates having shorter lengths (five-hole and six-hole plates), the X-axis component force increases with the number of implanted screws. The component forces in the Y-axis and the Z-axis do not differ significantly.

Figure 6 shows stress distribution on the clavicle. When more screws are implanted on the clavicle hook plate, the smaller the area of high stress on the clavicle.

Figure 7 shows stress distribution of the clavicle hook plates. It can be seen that when there are fewer screws implanted on the clavicle hook plate, high stress on the clavicle hook plate occurs.

Discussion

In this study, finite element analysis was used to investigate both the influence and biomechanical effects of different clavicle hook plates with different screw fixation methods. The results of this study can provide valuable biomechanical references for orthopedic physicians.

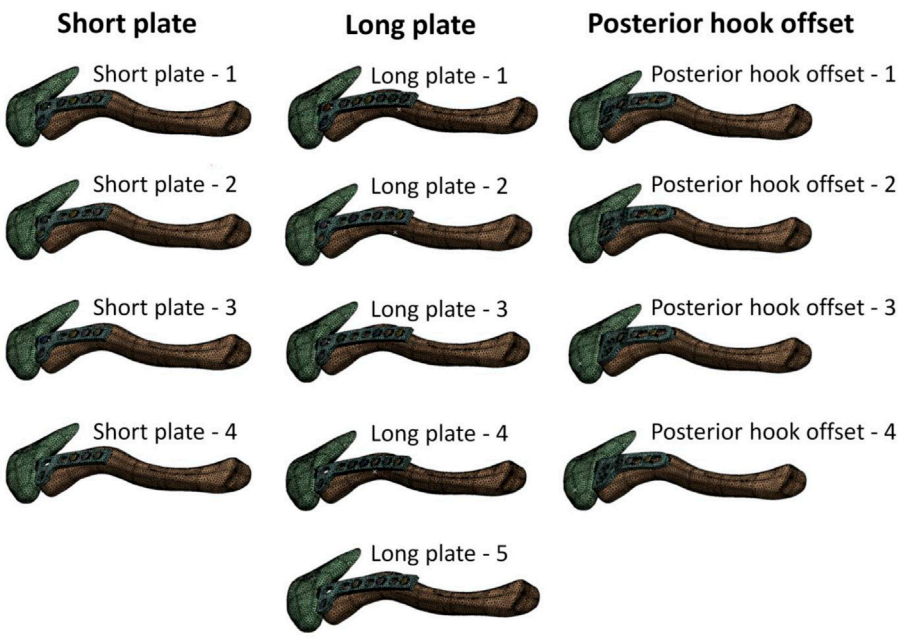

FIGURE 4
The 13 groups of models after meshing.

TABLE 2 The number of elements and nodes after meshing in each model.

	Short plate—1	Short plate—2	Short plate—3	Short plate—4	
Nodes	191,553	175,715	183,417	168,152	
Elements	105,715	96,950	101,149	92,739	
	Long plate—1	**Long plate—2**	**Long plate—3**	**Long plate—4**	**Long plate—5**
Nodes	612,485	596,956	602,359	595,918	584,471
Elements	404,098	397,039	399,433	396,073	390,504
	Posterior hook offset—1	**Posterior hook offset—2**	**Posterior hook offset—3**	**Posterior hook offset—4**	
Nodes	184,721	177,315	168,800	162,032	
Elements	101,939	97,890	93,088	89,453	

When all screw holes on the clavicle hook plate have implanted screws (group short plate—1, long plate—1, and posterior hook offset—1), there is a relatively large force reaction on the acromion. However, when observing the force reaction in each group and component forces in the X-, Y-, and Z- axes, it can be seen that the component forces in the Y-axis and Z-axis do not differ significantly. Therefore, the force reaction notably changes in the X-axis. The X-axis is parallel to the long axis of the clavicle hook plates. The greater the number of implanted screws, the more resistant force is to the external force in the X-axis direction. The X-axis component force on the acromion is based on how the bearing stress resists the force. When bearing stress = force/bearing area, then force = bearing stress × bearing area (Figure 8). When more screws are implanted, the bearing area will be larger; therefore, the external force on the X-axis of the acromion is also greater. The increased external force on the acromion increases the risk of sub-acrominal bone erosion.

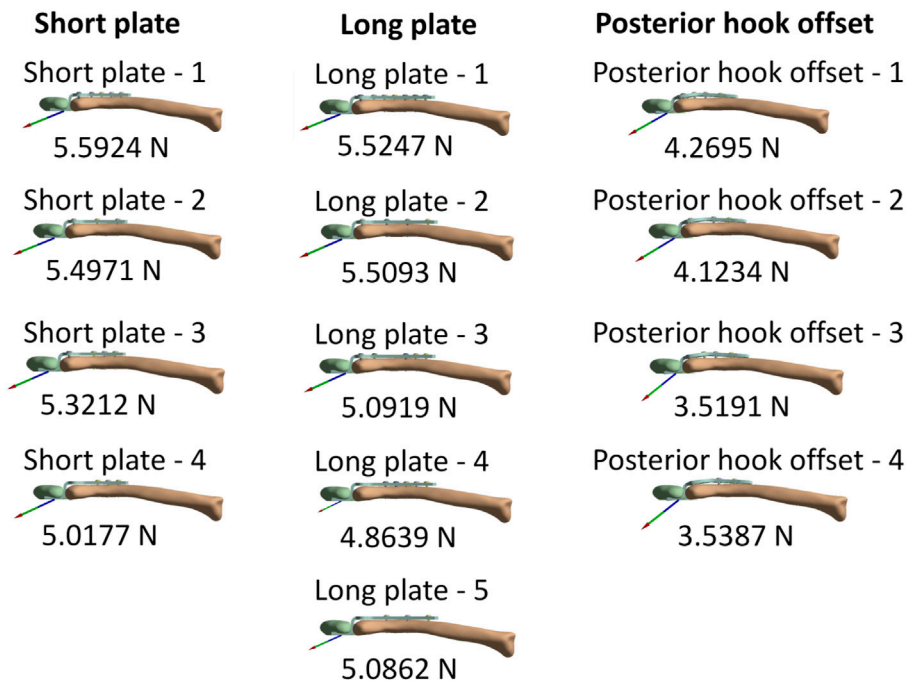

FIGURE 5
Force reaction on the acromion.

TABLE 3 Force reaction on the acromion and component forces in the X-, Y-, and Z- axes.

Force reaction (N)	X axis	Y axis	Z axis (N)	Total (N)
Short plate—1	−5.1803°N	−2.1056°N	0.073909	5.5924
Short plate—2	−5.0915°N	−2.0708°N	0.084036	5.4971
Short plate—3	−4.8796°N	−2.119°N	0.11655	5.3212
Short plate—4	−4.5425°N	−2.1171°N	0.24543	5.0177
Long plate—1	−5.1169°N	−2.0816°N	0.080534	5.5247
Long plate—2	−5.0486°N	−2.2029°N	0.10746	5.5093
Long plate—3	−4.6323°N	−2.1068°N	0.17601	5.0919
Long plate—4	−4.3756°N	−2.1037°N	0.29306	4.8639
Long plate—5	−4.6381°N	−2.0717°N	0.25604	5.0862
Posterior hook offset—1	−3.7035°N	−2.1063°N	0.27617	4.2695
Posterior hook offset—2	−3.517°N	−2.1286°N	0.31965	4.1234
Posterior hook offset—3	−2.712°N	−2.1803°N	0.52533	3.5191
Posterior hook offset—4	−2.7474°N	−2.1657°N	0.53283	3.5387

In addition, von Mises stress distribution on the clavicle was observed. Each group displayed lower stress in the area where the clavicle hook plate was implanted. The main reason for this is that after the plate was implanted, a stress-shielding effect in the area of the plate on the bone occurred. In turn, the force that the bone should bear was shielded by the implant; therefore, the clavicle bone experienced a lower stress distribution in the area covered by a plate. In addition, it was found that when the number of implanted screws was fewer in number, the greater the stress that was generated near the screws. The main reason for this is that the smaller the number of implanted screws, the smaller the contact area between the screws and the clavicle, which in turn results in higher stress. In addition, it was found that high stress was generated in the middle segment of the clavicle in each group. The main reason for this is that the cross-sectional area of the middle clavicle region is relatively small, so when the clavicle

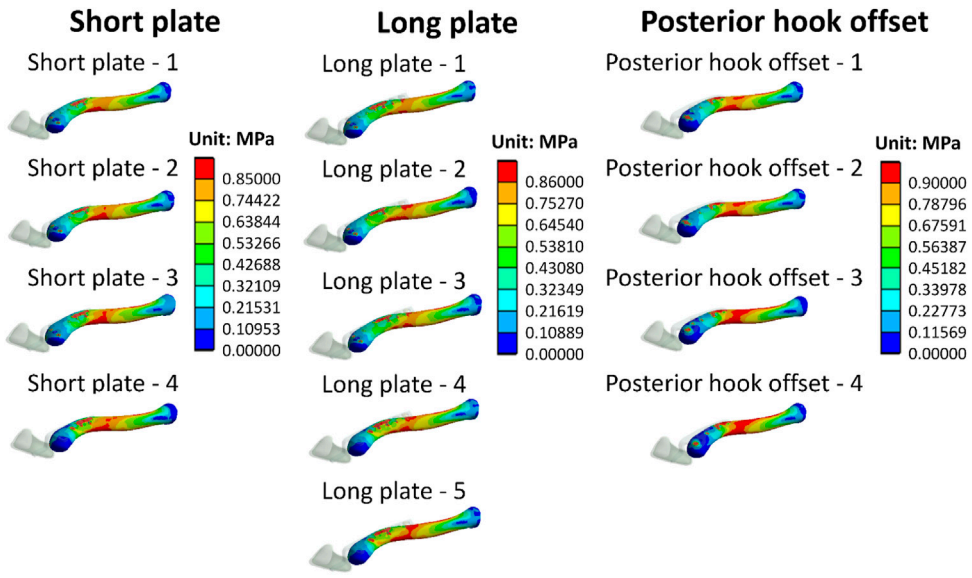

FIGURE 6
Stress distribution of clavicles.

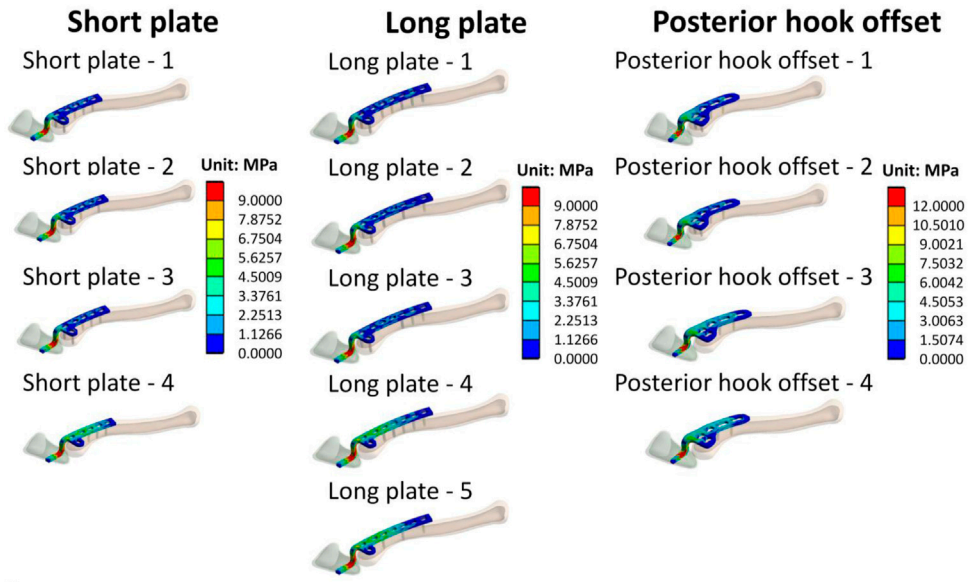

FIGURE 7
Stress distribution on clavicle hook plates.

is subjected to external force, there will be a higher stress value. In addition, it was revealed that the smaller the number of screws implanted on the clavicle hook plate (group short plate—4, long plate—5, and posterior hook offset—4), the larger the area of high-stress distribution in the middle of the clavicle. The main reason for this is that the number of implanted screws was fewer, making the overall structure unstable, in turn resulting in a large displacement on the clavicle. According to Hooke's law, stress is proportional to strain. The fewer the number of screws implanted on the clavicle hook plate, the higher the stress will be on the clavicle. The higher stress on the clavicle bone increases the risk of peri-implant clavicular fracture.

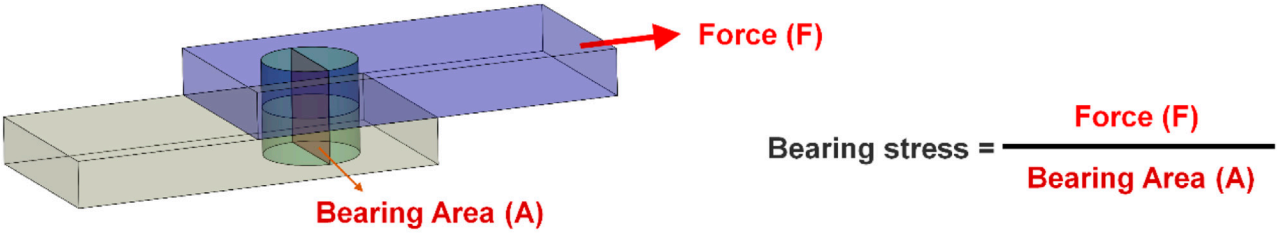

FIGURE 8
The force of bearing stress.

Stress distribution on the clavicle hook plate can be observed in Figure 7. It is shown here that each group has higher stress at the angle of the hook. The main reason for this is that it is at the corner of the geometric shape, causing the phenomenon of stress concentration. Such results are the same as those seen in previous studies (Shih et al., 2015; Lee et al., 2016; Hung et al., 2017). In addition, observing the implantation of different numbers of screws in each group, it was revealed that when the number of screws is less, there will be an area with a higher stress distribution on the clavicle hook plate. In addition, according to previous studies (Marinescu et al., 2017), the design of holes in the bone plate may cause the bone plate to break. Therefore, when designing the bone plate, unnecessary holes in the bone plate must be avoided. The main reason for this is that after the bone plate is implanted, a stress-shielding effect on the bone in the area of the bone plate occurs. Fewer the screws that are implanted, the larger the area of the plate that transmits force.

There are many limitations surrounding the finite element analysis performed in this study. The material properties are assumed to be homogeneous, isotropic, and linearly elastic. Clavicle bones are not homogeneous, isotropic, and linearly elastic. However, the focus of this study was to assess the impact of different numbers and locations of the screws in clavicle hook plates. Therefore, only the representative clavicle bone models were selected for analysis, and the bone material setup was simplified in this study. We would also like to use anisotropic material properties or different bone material properties to set up bone tissue (Cicciù et al., 2018). However, the finite element analysis of non-linear material properties is difficult to solve. Therefore, the non-linear material or different bone material properties setup used in this study may show more influencing factors on the topics covered in this study. Therefore, this study established cortical and cancellous bones on the basis of most previous finite element analysis studies (Hamandi et al., 2018). In addition, this study mainly simulates the clavicle hook plate implantation when the acromioclavicular ligament and the coracoclavicular ligament have been ruptured, so external force was only applied to the sternocleidomastoid muscle. This setting was based on previous research studies (Shih et al., 2015; Lee et al., 2016; Hung et al., 2021). In addition, the scapula model was simplified, so only the acromion was shown. The scapula model was simplified to reduce the computer calculation time. In addition, although in terms of contact setting, if there is a good setting, the research is closer to the actual situation (Chirca et al., 2021). In order to avoid increasing the parameters discussed in this study, the contact between the clavicle hook plate and acromion is set as no separation. The contact surface between the bone plate and the screw is bonded. The main purpose was to simulate the effect when the bone plate is the locking plate to avoid the factors of instability in the screw–plate contact.

Although some differences can be seen between the simulation in this study and the actual clinical situation, orthopedic physicians can still use the results to better understand the impact that different clavicle hook plates have in variable screw fixation methods on an acromioclavicular joint, as well as assist in reducing post-implantation surgical failures and complications. The study can also provide a reference for the design of new clavicle hook plates in the future.

Conclusion

Finite element analysis evaluates the biomechanical effects of different clavicle hook plates and different screw fixation methods. Our results show that inserting screws in all available screw holes on the hook plate produces a relatively large force reaction on the acromion, particularly in the axial direction of the bone plate. The fewer the screws implanted into the clavicle hook plate, the larger the area of the high stress distribution that can be seen in the middle of the clavicle, and also the higher the stress distribution on the clavicle hook plate.

Data availability statement

The raw data supporting the conclusion of this article will be made available by the authors, without undue reservation.

Author contributions

Conception and design, C-CW, C-HL, K-HC, and C-CP; methodology, K-CS; data curation, C-HW, M-TT, and K-CS; manuscript writing, C-CW, C-HL, and K-CS. All authors reviewed the manuscript.

Acknowledgments

We thank the United States National Library of Medicine's Visible Human Project for providing image source for building clavicle models in this study. We would like to thank the National Science and Technology Council of Taiwan (110-2221-E-075A-001, 111-2221-E-075A-002, 111-2314-B-075A-005), Taichung Veterans General Hospital/HungKuang University Joint Research Program (TCVGH-HK1098002), Taichung Veterans General Hospital (TCVGH-1115101C, TCVGH-1117315C) in Taiwan and the 3D Printing Research and Development Group of Taichung Veterans General Hospital for building the simulation computer model of this study.

Conflict of interest

The authors declare that the research was conducted in the absence of any commercial or financial relationships that could be construed as a potential conflict of interest.

Publisher's note

All claims expressed in this article are solely those of the authors and do not necessarily represent those of their affiliated organizations, or those of the publisher, the editors, and the reviewers. Any product that may be evaluated in this article, or claim that may be made by its manufacturer, is not guaranteed or endorsed by the publisher.

References

Antoniac, I. V., Stoia, D. I., Ghiban, B., Tecu, C., Miculescu, F., Vigaru, C., et al. (2019). Failure analysis of a humeral shaft locking compression plate—surface investigation and simulation by finite element method. *Materials* 12, 1128. doi:10.3390/ma12071128

Baunach, D., Eid, K., Ricks, M., and Borbas, P. (2021). Long-term clinical and radiological results after hook plate osteosynthesis of lateral clavicle fractures. *J. Orthop. Trauma* 35, 378–383. doi:10.1097/bot.0000000000002007

Charity, R., Haidar, S., Ghosh, S., and Tillu, A. (2006). Fixation failure of the clavicular hook plate: A report of three cases. *J. Orthop. Surg.* 14, 333–335. doi:10.1177/230949900601400320

Chiang, C.-L., Yang, S.-W., Tsai, M.-Y., and Chen, K.-H. (2010). Acromion osteolysis and fracture after hook plate fixation for acromioclavicular joint dislocation: A case report. *J. Shoulder Elb. Surg.* 19, e13–e15. doi:10.1016/j.jse.2009.12.005

Chirca, O., Biclesanu, C., Florescu, A., Stoia, D. I., Pangica, A. M., Burcea, A., et al. (2021). Adhesive-ceramic interface behavior in dental restorations. FEM study and SEM investigation. *Materials* 14, 5048. doi:10.3390/ma14175048

Cicciù, M., Cervino, G., Milone, D., and Risitano, G. (2018). FEM investigation of the stress distribution over mandibular bone due to screwed overdenture positioned on dental implants. *Materials* 11, 1512. doi:10.3390/ma11091512

Cronskär, M., Rasmussen, J., and Tinnsten, M. (2015). Combined finite element and multibody musculoskeletal investigation of a fractured clavicle with reconstruction plate. *Comput. Methods Biomech. Biomed. Engin.* 18, 740–748. doi:10.1080/10255842.2013.845175

Di Francesco, A., Zoccali, C., Colafarina, O., Pizzoferrato, R., and Flamini, S. (2012). The use of hook plate in type III and V acromio-clavicular rockwood dislocations: Clinical and radiological midterm results and MRI evaluation in 42 patients. *Injury* 43, 147–152. doi:10.1016/j.injury.2011.04.002

Ding, M., Ni, J., Hu, J., and Song, D. (2011). Rare complication of clavicular hook plate: Clavicle fracture at the medial end of the plate. *J. Shoulder Elb. Surg.* 20, e18–e20. doi:10.1016/j.jse.2011.06.005

Hamandi, F., Laughlin, R., and Goswami, T. (2018). Failure analysis of PHILOS plate construct used for pantalar arthrodesis paper II—screws and FEM simulations. *Metals* 8, 279. doi:10.3390/met8040279

Hoffler, C. E., and Karas, S. G. (2010). Transacromial erosion of a locked subacromial hook plate: Case report and review of literature. *J. Shoulder Elb. Surg.* 19, e12–e15. doi:10.1016/j.jse.2009.10.019

Hung, L.-K., Lee, C.-H., and Su, K.-C. (2021). Biomechanical analysis of clavicle hook plates with a range of posterior hook offsets implanted at different acromion positions in the acromioclavicular joint: A finite element analysis study. *Appl. Sci. (Basel).* 11 (23), 11105. doi:10.3390/app112311105

Hung, L.-K., Su, K.-C., Lu, W.-H., and Lee, C.-H. (2017). Biomechanical analysis of clavicle hook plate implantation with different hook angles in the acromioclavicular joint. *Int. Orthop.* 41, 1663–1669. doi:10.1007/s00264-016-3384-z

Kim, Y. S., Yoo, Y.-S., Jang, S. W., Nair, A. V., Jin, H., and Song, H.-S. (2015). *In vivo* analysis of acromioclavicular joint motion after hook plate fixation using three-dimensional computed tomography. *J. Shoulder Elb. Surg.* 24, 1106–1111. doi:10.1016/j.jse.2014.12.012

Kumar, N., and Sharma, V. (2015). hook plate fixation for acute acromioclavicular dislocations without coracoclavicular ligament reconstruction: A functional outcome study in military personnel. *Strateg. Trauma Limb Reconstr.* 10, 79–85. doi:10.1007/s11751-015-0228-0

Lee, C.-H., Shih, C.-M., Huang, K.-C., Chen, K.-H., Hung, L.-K., and Su, K.-C. (2016). Biomechanical analysis of implanted clavicle hook plates with different implant depths and materials in the acromioclavicular joint: A finite element analysis study. *Artif. Organs* 40, 1062–1070. doi:10.1111/aor.12679

Lee, H.-H. (2018). *Finite element simulations with ANSYS Workbench 18*. Taiwan: Chuan Hwa Book Co.

Lopiz, Y., Checa, P., García-Fernández, C., Valle, J., Vega, M. L., and Marco, F. (2019). Complications with the clavicle hook plate after fixation of Neer type II clavicle fractures. *Int. Orthop.* 43, 1701–1708. doi:10.1007/s00264-018-4108-3

Marinescu, R., Antoniac, V. I., Stoia, D. I., and Lăptoiu, D. C. (2017). Clavicle anatomical osteosynthesis plate breakage - failure analysis report based on patient morphological parameters. *Rom. J. Morphol. Embryol.* 58 (2), 593–598.

Ni, P.-L., Lin, K.-C., Chen, C.-Y., Tarng, Y.-W., Chang, W.-N., and Renn, J.-H. (2020). Peri-implant fractures following hook plate fixation for unstable distal clavicle fractures. *Orthopedics* 43, e359–e363. doi:10.3928/01477447-20200619-01

Shih, C.-M., Huang, K.-C., Pan, C.-C., Lee, C.-H., and Su, K.-C. (2015). Biomechanical analysis of acromioclavicular joint dislocation treated with clavicle hook plates in different lengths. *Int. Orthop.* 39, 2239–2244. doi:10.1007/s00264-015-2890-8

Shih, J.-T., Wu, C.-C., Wang, C.-C., Yeh, T.-T., Pan, R.-Y., Chen, C.-L., et al. (2020). Midshaft clavicle fracture following osteosynthesis with a hook plate: A retrospective case analysis. *Arch. Orthop. Trauma Surg.* 140, 1713–1718. doi:10.1007/s00402-020-03397-4

Tiren, D., van Bemmel, A. J., Swank, D. J., and van der Linden, F. M. (2012). hook plate fixation of acute displaced lateral clavicle fractures: Mid-term results and a brief literature overview. *J. Orthop. Surg. Res.* 7, 2–8. doi:10.1186/1749-799x-7-2

Yoon, B., Kim, J. Y., Lee, J.-S., and Jung, H. S. (2018). The radiologic comparison of operative treatment using a hook plate versus a distal clavicle locking plate of distal clavicle fracture. *Clin. Shoulder Elb.* 21, 227–233. doi:10.5397/cise.2018.21.4.227

frontiers | Frontiers in Bioengineering and Biotechnology

TYPE Original Research
PUBLISHED 27 September 2022
DOI 10.3389/fbioe.2022.967430

OPEN ACCESS

EDITED BY
Carl-Eric Aubin,
Polytechnique Montréal, Canada

REVIEWED BY
Peter Mitrouchev,
Université Grenoble Alpes, France
Feng Li,
Qingdao University of Science and Technology, China
Hai Hu,
Shanghai Jiao Tong University, China

*CORRESPONDENCE
Gang Huang,
huanggang@smu.edu.cn
Wenhua Huang,
Orthobiomech@163.com

†These authors have contributed equally to this work and share first authorship

SPECIALTY SECTION
This article was submitted to Biomechanics, a section of the journal Frontiers in Bioengineering and Biotechnology

RECEIVED 12 June 2022
ACCEPTED 07 September 2022
PUBLISHED 27 September 2022

CITATION
Deng Y, Zhao D, Yang Y, Ouyang H, Xu C, Xiong L, Li Y, Tan W, Huang G and Huang W (2022), Optimal design and biomechanical analysis of sandwich composite metal locking screws for far cortical locking constructs.
Front. Bioeng. Biotechnol. 10:967430.
doi: 10.3389/fbioe.2022.967430

Optimal design and biomechanical analysis of sandwich composite metal locking screws for far cortical locking constructs

Yuping Deng[1,2,3,4†], Dongliang Zhao[2,3,5†], Yang Yang[1,2,3], Hanbin Ouyang[6], Chujiang Xu[1,2], Liang Xiong[1,2], Yanbin Li[2], Wenchang Tan[3,5], Gang Huang[1,2*] and Wenhua Huang[1,2,3,4*]

[1]Department of Orthopedics and Traumatology, Integrated Hospital of Traditional Chinese Medicine, Southern Medical University, Guangzhou, China, [2]Guangdong Provincial Key Laboratory of Medical Biomechanics, School of Basic Medical Sciences, Guangdong Engineering Research Center for Translation of Medical 3D Printing Application, National Key Discipline of Human Anatomy, Southern Medical University, Guangzhou, China, [3]Institute of Biomedical Engineering, Shenzhen Bay Laboratory, Shenzhen, Guangdong, China, [4]Guangdong Medical Innovation Platform for Translation of 3D Printing Application, The Third Affiliated Hospital of Southern Medical University, Guangzhou, China, [5]State Key Laboratory of Chemical Oncogenomics, Drug Discovery Center, School of Chemical Biology and Biotechnology, Peking University Shenzhen Graduate School, Shenzhen, Guangdong, China, [6]Orthopaedic Center, Affiliated Hospital of Guangdong Medical University, Guangdong Medical University, Zhanjiang, China

In the interests of more flexible and less stiff bridge constructs to stimulate bone healing, the technique of far cortical locking has been designed to improve locked plating constructs in terms of stress concentration, stress shielding, and inhibition of issues around fracture healing. However, far cortical locking screws currently lack objective designs and anti-fatigue designs. This study investigates an optimization algorithm to form a special locking screw composed of various metals, which can theoretically achieve the maintenance of the excellent mechanical properties of far cortical locking constructs in terms of fracture internal fixation, while maintaining the biomechanical safety and fatigue resistance of the structure. The numerical results of our study indicate that the maximum von Mises stress of the optimized construct is less than the allowable stress of the material under each working condition while still achieving sufficient parallel interfragmentary motion. Numerical analysis of high cycle fatigue indicates that the optimized construct increases the safety factor to five. A high cycle fatigue test and defect analysis indicates that the sandwich locking constructs have better fatigue resistance. We conclude that the sandwich locking construct theoretically maintains its biomechanical safety and fatigue resistance while also maintaining excellent mechanical properties for fracture internal fixation.

KEYWORDS

locking screws, sandwich structure, dynamic stabilization, high-cycle fatigue, screw optimization

1 Introduction

Research over the past 50 years has consistently demonstrated that controllable axial dynamic internal fixation systems effectively promote callus formation and improve the speed and strength of fracture healing (Goodship and Kenwright 1985; Kenwright et al., 1991; Claes et al., 1998; Panagiotopoulos et al., 1999; Uhthoff et al., 2006; Bottlang et al., 2010a; Richter et al., 2015). In the development of the fracture internal fixation constructs from Arbeitsgemeinschaft fuer Osteosynthesefragen (AO) to Biological Osteosynthesis (BO), blood supply protection and interfragmentary motion is preferred over absolute stability. Secondary bone healing is induced by interfragmentary motion in the millimeter range and can be enhanced by passive or active dynamization (Perren 1979; Claes et al., 1998; Duda et al., 2002; Hente et al., 2004; Zhang et al., 2012). The stiffness of a fixation construct is a principal determinant of fracture-site motion and thereby affects the mechanism and progression by which a fracture heals. The relatively high stiffness of fixation constructs may therefore suppress flexible motion to a level insufficient for optimal promotion of secondary bone healing (Bottlang et al., 2010b; Rodriguez et al., 2016; Plumarom et al., 2019). The advent of locked plating systems has provided a new strategy for dynamic stabilization, because the locked plating construct with fixed-angle locking screws does not require compression of the fixation plate onto the bone surface (Perren et al., 1973). The Far Cortical Locking (FCL) internal fixation system developed based on the locked plating system can achieve flexible axial fixation while retaining the stability of the internal fixation construct to a certain extent (Bottlang et al., 2009). The FCL construct can achieve controlled axial movement by bending screws that lock anchored in the plate and far cortical bone, but preserve range of motion at the proximal cortical bone. A study by Bottlang et al. claimed that in ovine models, a far cortical locking group had a 36% greater callus volume ($p = 0.03$) and a 44% higher bone mineral content ($p = 0.013$) than did the locked plating group (Bottlang et al., 2010a). A clinical study reported that distal femoral fractures were stabilized by the FCL construct, with a mean healing time of 16 weeks and an incidence of nonunion of 3% (Bottlang et al., 2014).

Currently, the FCL construct has been industrialized by several companies that commercialize orthopedic implant devices and is increasingly used clinically (Bottlang et al., 2014; Adams et al., 2015; Moazen et al., 2016; Kidiyoor et al., 2019). At the same time, in clinical practice, many surgeons can use standard locking screws to achieve the adoption of FCL technology by excessive drilling or slotting of the proximal cortical layer of bone. Many experts even claim that today's FCL construct can be used as the "gold standard" for the treatment of distal femoral fractures (Bottlang et al., 2014; Plumarom et al., 2019; Wang et al., 2019). However, the flexibility of the fixation means the sacrifice of structural stability. Many scholars have put forward higher design requirements for the FCL construct: A study by Nahir et al. found that among all fracture fixation methods, the FCL construct had greater shear force than did the bicortical locking and non-locking structures, while the shear displacement is not conducive to callus growth (Habet et al., 2019). The FCL construct has a longer elastic element to reduce stiffness and provide a flexible fixation, but screw safety due to stress concentration and fatigue performance are worse than the external fixator attributed to the smaller screw diameter. During surgery, the adjacent cortical bone needs expanding to meet the requirements of FCL construct design, and the staggered and converging screw arrangement is implemented by 9° in FCL constructs to improve construct strength in torsion—this creates considerable challenges during surgery when working with a bone that has an irregular cross-section. The FCL screws are less safe and have a more significant fatigue fracture risk than do the locked plating screws that were reported in recent research (Deng et al., 2021). On the basis of these theoretical and clinically emerging concerns, several strategies to optimize the biomechanical properties of FCL constructs have been investigated. These strategies include optimizing FCL screw distribution, decreasing the plate elevation, and decreasing the plate span (Richter et al., 2015; Habet et al., 2019; Sarwar et al., 2021). While these strategies are effective for reduing structural safety hazards of FCL constructs to varying degrees, they also reduce their flexibility. What's more, currently there is no research focusing on the optimization of high cycle fatigue performance of FCL construct. Although FE-based fatigue analysis is commonly used for reliability studies in engineering, it has been relatively rare to be applied in the biomedical fields.

Composite sandwich structure, as a new type of efficient and multifunctional structure, has been widely used in various fields such as architecture, aerospace and so on because of its high designability and outstanding mechanical properties. Through reasonable selection of materials and sandwich structure design, the mechanical properties of the material structure can be effectively improved while the volume or mass of the structure can be reduced (Sarvestani et al., 2018; Hayat et al., 2019). The concept of dynamic fixation to promote fracture healing is advocated in the current internal fixation treatment of fractures, which raises concerns about the safety and durability of implanted structures. Therefore, the use of composite sandwich structure to improve the statics and fatigue resistance of implant has a wide range of application prospects in the field of medicine.

In this study, calculation of a finite element numerical simulation was proposed for performing intelligent screening and optimizing of multi-working conditions for the locking screws of the FCL constructs. While optimizing the screw section of the FCL constructs, an optimization algorithm was proposed for forming a special composite metal sandwich structure locking screw made of titanium alloy and various metals. We used Isight platform independent programming for

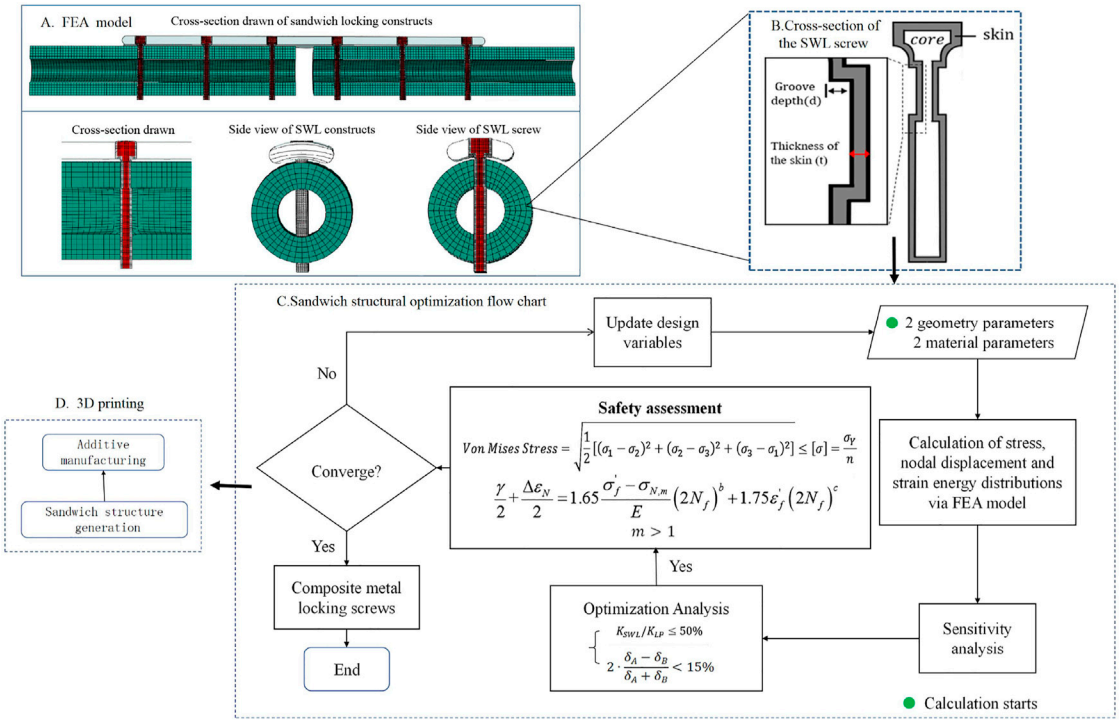

FIGURE 1
Steps for optimizing a sandwich composite metal locking screw. **(A)** Section view of optimized finite element model of sandwich locking (SWL) screw, and structure schematic diagram. **(B)** Schematic diagram of a cross-section of a composite metal screw with a sandwich structure. The core is a sandwich structure, the skin is the titanium layer structure on the surface of the screw, d is the depth of the groove of the screw at the proximal cortex, and t is the thickness of the protective structure of the surface titanium layer. **(C)** Flow chart of sandwich locking screw optimization for each design parameter, **(D)** Sandwich structure generation and additive manufacturing of the screws.

co-simulation and intelligent optimization, for static safety assessment with the allowable stress method, and for fatigue safety assessment through high-cycle fatigue analysis. What's more, the reliability of the optimization scheme was preliminarily verified by biomechanical experiment and defect analysis. The newly designed composite metal sandwich locking screw can achieve elastic fixation, progressive stiffness, uniform load distribution, and parallel interfragmentary motion of the fracture end in the far cortical locking construct, while maintaining better fatigue resistance and torsion resistance to the internal fixation construct. This study provides a more objective digital operation basis and a more ideal structure design for the application of FCL construct. This may provide a new and reliable dynamic fixation method for clinical fracture treatment.

2 Materials and methods

Our goal here is to develop a sandwich composite metal locking screw with tailored elastic modulus and morphology resulting in an optimal material selection and distribution that can achieve a reliable fatigue resistance while retaining the advantages of current FCL constructs: flexible fixation, uniform load distribution, progressive two-phase stiffening and parallel interfragmentary motion. Figure 1 illustrates the optimization steps for developing the sandwich composite metal locking screw.

2.1 Numerical model

In order to better conduct biomechanical comparative analysis and stiffness verification of internal fixation constructs, three numerical models were established in Abaqus/CAE 2018 (Dassault Systems, Velizy-Villacoublay, France) based on previous work (Deng et al., 2021): the traditional locked plating constructs, the currently adopted FCL constructs, and the sandwich locking (SWL) constructs (Figure 2).

2.1.1 Geometrical modelling and material properties

2.1.1.1 Locked plating constructs and FCL constructs

A standard femoral cross-sectional bone model with a gap of 10 mm was established based on the fracture healing model for

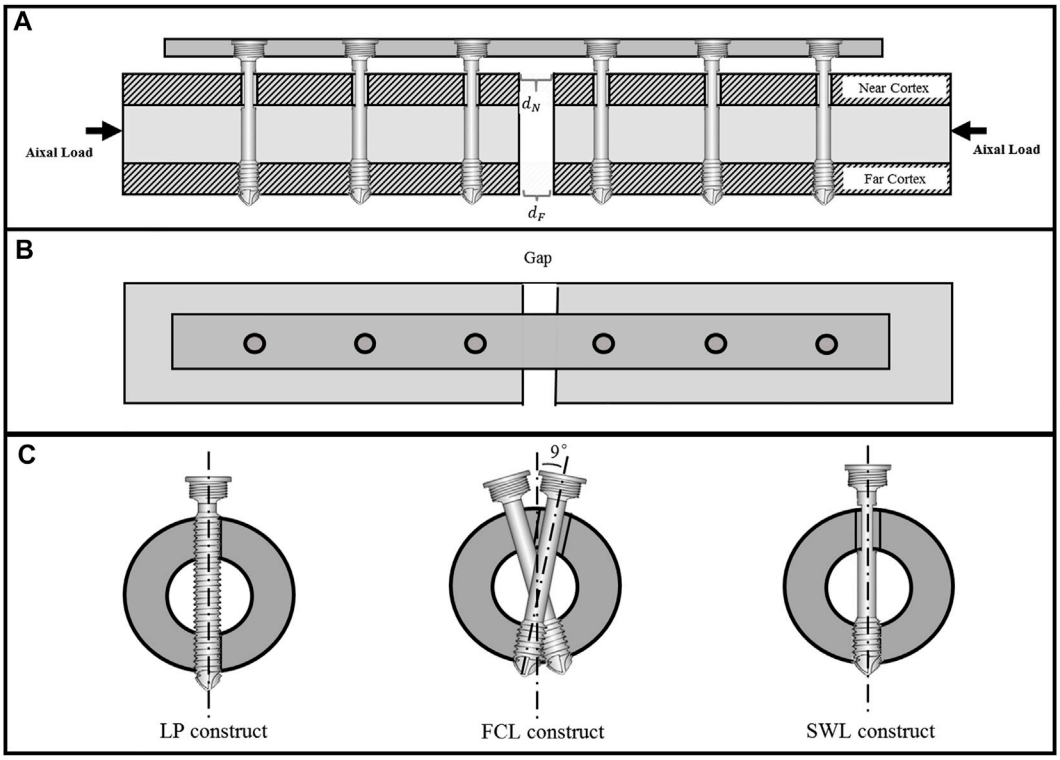

FIGURE 2
Schematic diagram of sandwich composite metal locking screw for far cortical locking construct. **(A)** Schematic diagram of the position and structural cross-section of the composite metal screw of the sandwich structure, **(B)** the top view of the structure and **(C)** the comparison diagram of locked plating (LP), far cortical locking (FCL), and sandwich locking (SWL) constructs: the proximal and distal ends of the LP are all locked, and the FCL screws are staggered by 9°; only the distal end is locked, and the proximal end is enlarged. The SWL screws are arranged in a straight line; only the distal end is locked and the proximal hole is not enlarged.

comparative analysis of internal fixation constructs. Implants were evaluated in normal femoral diaphysis surrogates to minimize inter-specimen variability (Bottlang et al., 2009; Bottlang et al., 2010b). We adopted cylindrical bone surrogates with a length of 200 mm, a diameter of 27 mm, and a wall thickness of 7 mm, modeled as linear elastic material (E = 17 GPa, ν = 0.3). The locking plate was 117 mm long, 17 mm wide, and 5.6 mm thick, and had a longitudinal curvature with a 750-mm radius. Self-tapping locking screws contained a shaft with a diameter of 3.2 mm in both locked plating and FCL constructs. Six threaded screw holes (6 mm diameter) were arranged in a staggered pattern in the FCL constructs (Figure 2C). The FCL screws for unicortical fixation in the far cortex consisted of a smooth screw midshaft with a diameter of 3.2 mm to bypass the near cortex, allowing for the elastic cantilever bending of the screw midshaft within a controlled motion envelope in the near cortex (Bottlang et al., 2009; Bottlang et al., 2010a). The plates and screws were manufactured with surgical grade titanium alloy (Ti-6Al-4V), which had a Young's Modulus of 114 GPa and Poisson's Ratio of 0.3.

2.1.1.2 SWL constructs

Two modifications were made to the currently adopted FCL constructs; all other parameters remained the same. First, the 9° staggered arrangement of screws was omitted; the second modification was to optimize the topography of the screw structure, and to design grooves where the screw was close to the near cortex. Six threaded screw-holes (6 mm diameter) were arranged in a colinear pattern (Figure 2B). The structural differences between the three constructs are shown in Figure 2C.

The cross-section of the SWL screw and the optimization variables are shown in Figure 1B. Self-tapping composite metal locking screws had a 3.2 mm diameter shaft, and were only fixed in the far cortex. The screw shaft had a 10-mm long groove close to the near cortex to bypass it, allowing for elastic cantilever bending of the unicortical screw midshaft within a controlled motion envelope in the near cortex. There was a groove close to the near cortex to change the contact form of constructs in the sandwich composite metal screw. The Ti-6Al-4V was the skin of the sandwich composite, and the thickness (t) of the skin can be optimized by the optimization method. The properties of the core material can be optimized to reduce the stiffness of the

construct, including Young's Modulus (E) and Poisson's Ratio (γ).

2.1.2 Boundary and loading conditions

Model establishment was based on axial compression tests through a proximal sphere (rigid clamp), replicating the axial loading scenario of the bench-top test (Bottlang et al., 2009; Bottlang et al., 2010b). The distal ends of the bone models were fully constrained as boundary condition. Torsion was applied around the diaphyseal shaft axis (Supplementary Figure S8). In LP constructs, screws were assumed fully bonded to the bone and the plate using the tie constraint. In FCL and SWL constructs, screws were bonded to the far cortical bone and the plate using tie constraint. Relative motion in models have been considered for friction between the screws and near cortical bone. A standard Coulomb friction coefficient of 0.3 was employed based on some of the recent studies (Eser et al., 2010; MacLeod et al., 2012). For the static loading simulations, construct stiffness in non-osteoporotic bone surrogates was assessed under axial compression and torsion by loading to 1 kN and 10 Nm, respectively. In addition to the actuator displacement (displacement of the center of mass of the proximal sphere), interfragmentary motion under axial compression was recorded at the near and far cortices (Figure 2A).

The finite element model of each construct in this study was calculated and analyzed by using the structural mesh C3D8R and the mesh independence was further discussed in the Supplementary material (Supplementary Tables S3,S4).

2.2 Sandwich structural optimization

2.2.1 Optimization objective

In our optimization, there were three intuitive optimal objects: controllable two-phase stiffness, nearly parallel interfragmentary motion and comprehensive strength.

First, the SWL constructs should reduce the stiffness of a standard locked plating construct by over 50%, and the stiffness of the normal model was 2.9 kN/mm in locked plating constructs, shown as:

$$K_{SWL}/K_{LP} \leq 50\% \tag{1}$$

Where K_{SWL} represents the stiffness of SWL constructs and K_{LP} represents the stiffness of locked plating constructs.

Second, these should induce nearly parallel motion at the near cortex and far cortex, and the difference of the displacement between the near cortex and far cortex should less than 15%:

$$2 \cdot \frac{\delta_A - \delta_B}{\delta_A + \delta_B} < 15\% \tag{2}$$

Where δ_A represents the displacement of the near cortex at the fracture ends, and δ_B represents the displacement of the far cortex at the fracture ends.

Third, the strength of the SWL constructs should meet the requirement of the safety assessment based on previous work (Deng et al., 2021). The result of optimization through the safety assessment represented the new constructs. There are two main aspects of the safety assessment: structural strength analysis based on the allowable stress, and high-cycle fatigue numerical analysis (further illustrated in the Supplementary material).

2.2.2 Design method

The flowchart of the optimization method is shown in Figure 1C. In the optimization model, there were four optimization variables, including the two material parameters (Young's Modulus (E) and the Poisson's Ratio (γ)) and two geometry parameters (the width of the groove (d) and the thickness of the titanium alloy layer (t)). However, there is not much difference between Poisson's ratio (γ) of different materials, so the small change of Poisson's ratio is not considered in the optimization process (γ is constant, $\gamma = 0.3$).

There are three steps in the optimization process. First, a random array was established for the optimization parameters (E, γ, t, d) using the Latin Hypercube method (Supplementary Table S1), and the value of the optimization objective (K, δ, σ) was obtained based on the finite element method. In the second step, the above results were used to establish the response relationship between the optimization parameters and the optimization target through the RSM method. Third, took the extremum of the von Mises stress (σ), axial stiffness (K) and displacement (δ) from the response surface relationship to get the optimized results. The value range of optimization variables are shown in Table 1. The three optimization variables were the input of the finite element model, and the algorithm applied in the optimization analysis was further illustrated in Supplementary Figure S1 in the Supplementary material (Zhou et al., 2013; López et al., 2017; Shang et al., 2019). The impact of the three optimization parameters on the optimal object was analyzed using the response surface model (RSM) method (Li et al., 2016; Patel and Gohel 2018; Li et al., 2019; Zhao et al., 2020).

2.3 Experiment validation

The established numerical simulation models were verified by statics tests and high-cycle fatigue tests, and the fatigue damage of each construct was explored through defect detection. The internal fixation system used in the mechanical experiments in this study was consistent with the geometric parameters used in the numerical model. Implants were custom manufactured by a company specializing in the production of orthopedic implants (Geasure, Changzhou, Jiangsu). Implants were evaluated in surrogate specimens of the femoral diaphysis to minimize inter-specimen variability (as further illustrated in Supplementary Figure S2 in the Supplementary material).

TABLE 1 Parameter range for the optimization of a sandwich composite metal locking screw.

	Minimum value	Maximum value	Step size
Width of the groove (d) (mm)	0	2	0.20
Thickness of titanium alloy layer (t) (mm)	0.2	1	0.25
Young's Modulus (E) (GPa)	80	262	10

Axial compression testing was performed on the three constructs (n = 5 in each group) using a biaxial universal material testing system (Instron e10000, Instron, Massachusetts, United States) (Supplementary Figure S3). For the static loading tests, an axial compression load was applied under load control with an increment of 100 N, up to 1000 N. We performed three repeated case loadings for each sample, gave each sample at least 12 min of recovery time before each load repetition, and recorded displacements and loads throughout the loading process. The structural axial stiffness of the sample was calculated from the displacement-load data, and each curve area was segmented and the slope calculated. The slope of a group of samples was the average of the slopes obtained from three repeated loads. Further, we performed high-cycle dynamic fatigue tests of 1,000,000 cycles (waveform: sine wave) at a rate of 5 Hz according to the load levels presented in Supplementary Figure S4 in the Supplementary material.

All samples were carefully collected, sorted, and cleaned, and then micro-nano tomography was performed to observe the damage location and damage mode of the samples under high cycle fatigue testing (further illustrated Supplementary Table S2 and Supplementary Figure S5 in the Supplementary material).

2.4 Outcome evaluation

To evaluate the stability and safety of the optimized and redesigned sandwich composite metal locking screws, we compared the differences in biomechanical behavior between screws in three constructs for both loading mode, including 1) construct stiffness of the fixation models for each load, and 2) the interfragmentary motion results at the near and far cortices. Axial stiffness was calculated by dividing the axial load amplitude by the actuator displacement amplitude. Torsional stiffness was calculated by dividing the torsion amplitude by the amplitude of rotation (α) around the diaphyseal axis. Torsional stiffness was multiplied by the unsupported specimen length to derive torsional rigidity. What's more, we compared the differences in biomechanical safety in three constructs for both loading mode, included 1) the von Mises stress distribution and peak values of the screws and bone models, 2) the average von Mises stress of all elements of the screws and bone models, and 3) numerical and experimental results of high-cycle fatigue test.

For statistical analysis, the average von Mises stress of all elements of the screws and bone models and the construct stiffness were compared among three groups individually, for both loading mode using one-way ANOVAs with Bonferroni post-hoc tests. For all statistical analyses, a level of significance of $\alpha = 0.05$ were used to detect significant differences.

3 Results

3.1 Optimal design results

Using the optimization method, the sandwich composite metal locking screw was designed for controllable two-phase stiffness, near parallel interfragmentary motion, and comprehensive safety. The final results of the three variables are shown below. The width of the groove (d) was 0.25 mm, and the thickness of the titanium alloy layer (t) was 0.65 mm. The Young's Modulus (E) was 98 GPa, so titanium alloy (Ti-13V-11Cr-3Al) was chosen as the core material (Young's Modulus, E = 98 GPa; Poisson's Ratio, $\gamma = 0.3$). The optimized sandwich composite metal screw is shown in Figure 3. As a preliminary proof-of-concept, the screws had been additively built with a metal 3D printer Renishaw AM 400 (Renishaw plc, United Kingdom) (further illustrated in the Supplementary Material).

3.2 The construct stiffness and displacements

The new SWL constructs have the same force-contact pattern as the FCL constructs. Table 2 summarized the construct stiffness in axial compression and torsion, and the simulation results have been verified by comparison with our experimental results and those reported in Bottlang et al. (2014). It can be seen that both the simulation results and the experimental results were highly consistent with the classical FCL construct biomechanical experimental results.

Under an axial load of 150 N, the axial compressive stiffness of the SWL construct was 0.47kN/mm, which was 83.9% lower than that for the locked plating construct (2.92 kN/mm). For axial loads greater than 150 N, the SWL construct second-phase stiffness was 3.06kN/mm and maintained a strong stiffness.

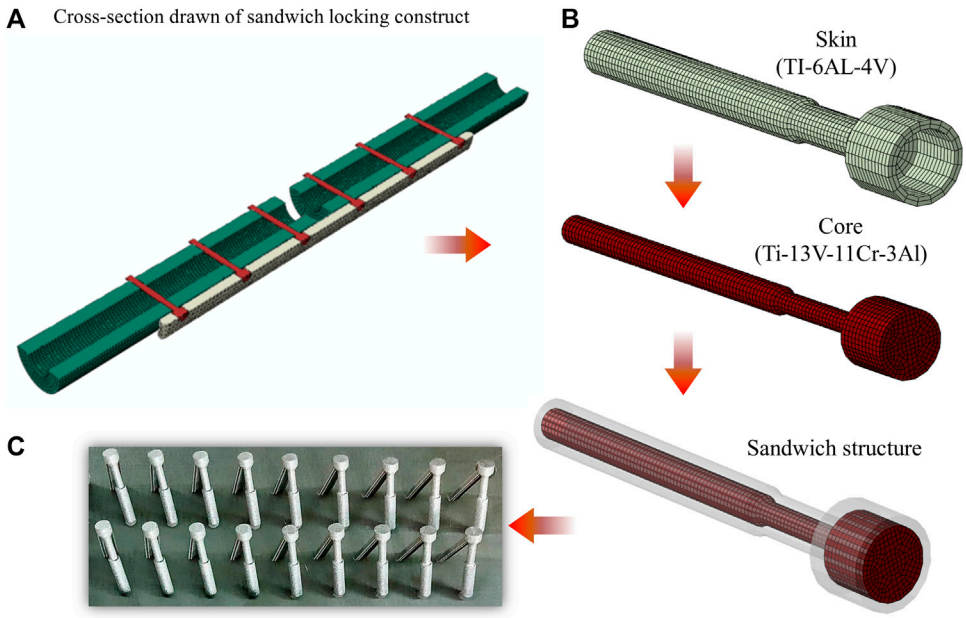

FIGURE 3
Structure schematic diagram of the optimized finite element model of the SWL screw. **(A)** Cross-section drawn of sandwich locking construct. **(B)** The best result of optimization is d = 0.25 mm, t = 0.65 mm and E = 98 GPa. Considering the influence of material compatibility, titanium alloy (Ti-13V-11Cr-3Al) was selected as the core material (Young's modulus E = 98 GPa and Poisson's ratio γ = 0.3). **(C)** Implant manufactured by 3D printing using titanium alloy (TI-6AL-4V) as a proof-of-concept.

TABLE 2 The stiffness results of each group of experiments under axial compression (0–1000 N) and torsion (0–10 Nm) loading conditions.

		Locked plating	Sandwich locking[a]	Far cortical locking[a]	*p* value[‡]
Axial stiffness (kN/mm)	Bottlang et al. (2009)	2.9 ± 0.13	——	0.36 ± 0.05/2.26 ± 0.08	<0.001/<0.001
	Our simulation	2.92	0.47/3.06	0.67/2.86	——
	Our experiment	2.90 ± 0.25	0.66 ± 0.04/3.09 ± 0.15	0.84 ± 0.19/2.19 ± 0.12	<0.001/<0.001
Torsional rigidity (Nm^2/deg)	Bottlang et al. (2009)	0.4 ± 0.03	——	0.17 ± 0.04/0.32 ± 0.01	<0.001/<0.001
	Our simulation	0.38	0.16/0.27	0.17/0.31	——

[a]The stiffness data are given as the initial value followed by the secondary value. ‡The first *p* value pertains to the comparison among the initial FCL, value, initial SWL, value and the locked plating value, and the second *p* value pertains to the comparison among the secondary FCL, value, secondary SWL, value and the locked plating value.

Axial loads above 150 N caused the sandwich composite screws to come into contact with the proximal cortical bone, which provided additional structural support, thereby increasing the secondary stiffness. In torsion, the initial torsional stiffness of the SWL construct was 64% lower than that of the locked plating construct (0.16 Nm^2/deg versus 0.38 Nm^2/deg). For torsion with torque greater than 2 Nm, the secondary stiffness of the SWL structure increased to 0.276 Nm^2/deg, which was still 13% lower than that of the FCL construct. The stiffness differences of the three constructs are shown in Figure 4A.

The groove of the sandwich composite screw changes the contact pattern between the screw and the cortical bone, so that the displacement difference between the proximal and distal ends of the fracture was small, and an approximately parallel pattern was achieved. Figure 4B showed the difference in displacement between the proximal and distal ends of cortical bone for the three constructs at 150 N. Within the initial stiffness range of the SWL construct, an axial load of 150 N induced almost parallel displacements at the fracture site, with similar displacement magnitudes at the proximal (0.301 ± 0.04 mm) and distal (0.341 ± 0.04 mm) ends of the cortical bone. The

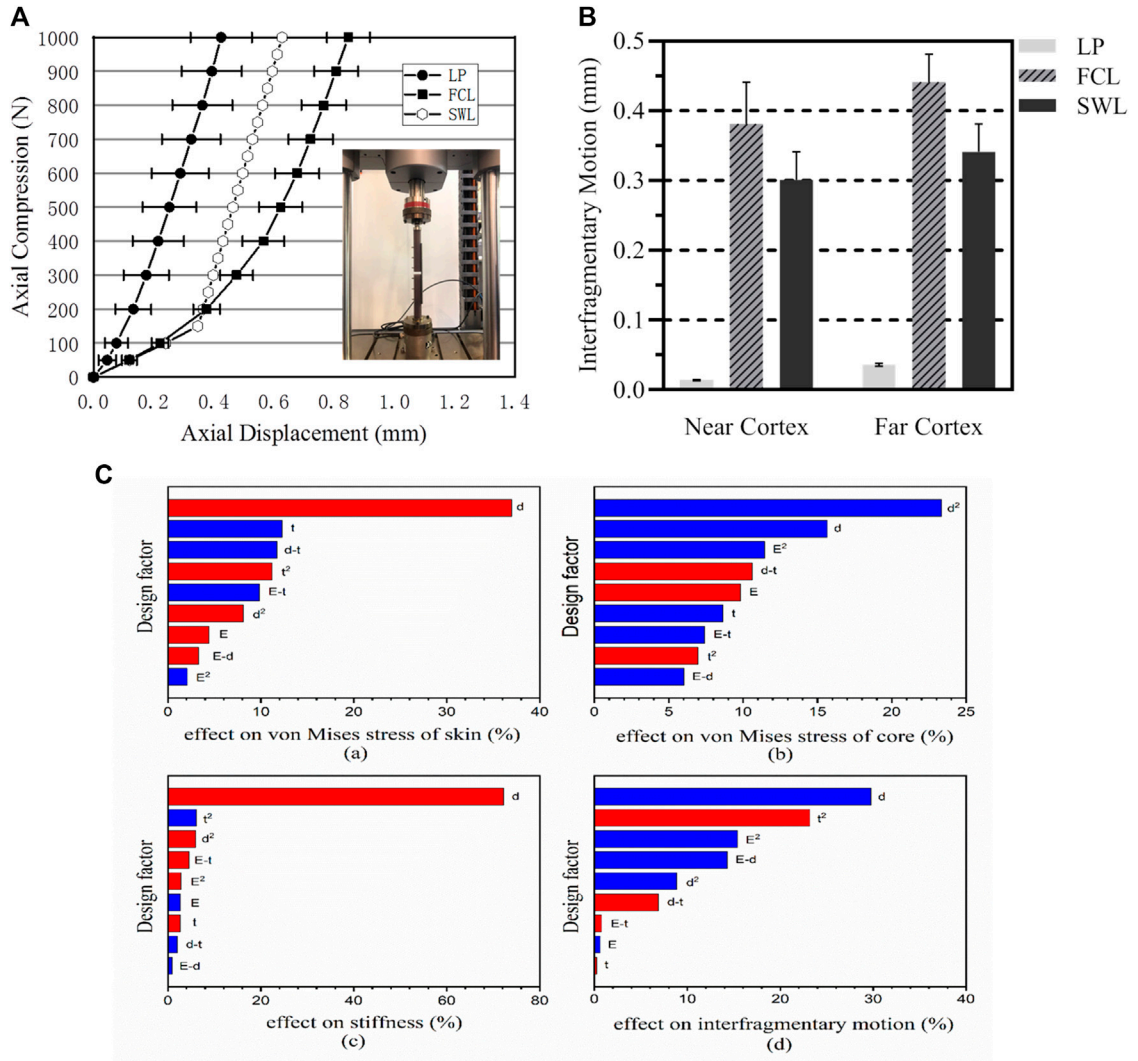

FIGURE 4
Structural displacement analysis. **(A)** Comparison of the stiffness of the three structures in the non-osteoporotic model in axial compression. **(B)** At 150 N of loading, the initial stiffness of three constructs induced comparable amounts of interfragmentary motion at the near and far cortex. LP: Locked plating constructs; FCL: Far cortical locking constructs; SWL: Sandwich locking constructs. **(C)** Factor sensitivity analysis of each design parameter.

displacement difference between the proximal and distal ends of the cortical bone in the SWL construct was 0.040 mm, which was smaller than that of the FCL construct (0.059 mm). In the locked plating construct, the corresponding displacement in the proximal cortex (0.02 ± 0.01 mm) was significantly smaller than that in the distal cortex (0.05 ± 0.02 mm) ($p < 0.01$).

3.3 The safety assessment results

As the factor of safety (n) was 2, the allowable stress can be calculated by $[\sigma] = \frac{\sigma_Y}{n} = \frac{\sigma_Y}{2}$. The allowable stresses of the two titanium alloys were $[\sigma]_{\text{Ti-6Al-4V}} = 412.5\text{MPa}$ and $[\sigma]_{\text{Ti-13V-11Cr-3Al}} = 415\text{MPa}$, respectively. The maximum value of the von Mises stress is less than the allowable stress to ensure structural safety. We evaluated the fracture risk of the screws that had the maximum deformation among the screws in each model. The maximum von Mises stresses of the screws were shown in axial compression loading and torsion, in comparison with the allowable stress (red line) (Figures 5A,B). Under the axial compressive load of 400 N, the maximum von Mises stress of the outer layer metal titanium and the core structure alloy is 300.7 and 45.8 MPa, respectively, which were all less than the allowable stress of the material. The maximum von Mises stress

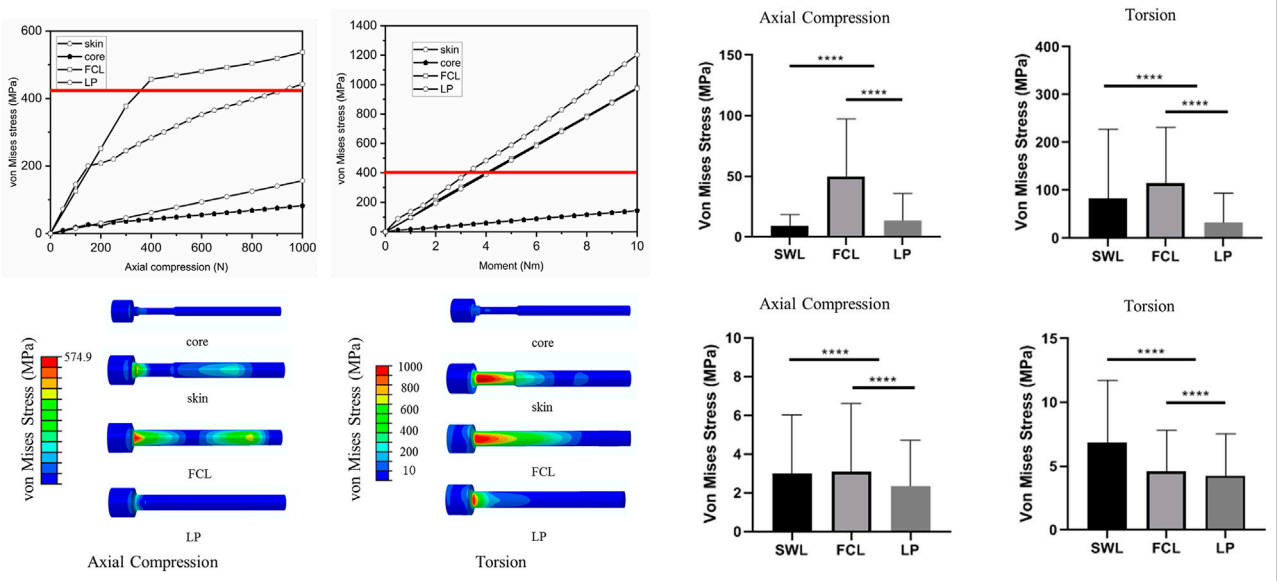

FIGURE 5
The von Mises stress results for the three constructs. **(A,B)** Under axial compression and torsion load, the maximum von Mises stress of each screw varies with load and the allowable stress of titanium alloy (red line). **(C,D)** Maximum von Mises stress cloud diagram of each screw under 1000 N axial compression and under 10 Nm. **(E–H)** The average von Mises stress of all elements of the screws **(E,F)** and bone models **(G,H)** were compared among three groups individually for each loading mode. **** means $p < 0.0001$.

of the FCL screws exceeded the allowable stress of the titanium alloy (574.9 MPa), which was 1.912 times the maximum von Mises stress of the SWL screws, so the risk of screw breakage and secondary fracture of the SWL construct was lower. For the torsional condition, under a physiological torsional load of 2 Nm, although the SWL constructs did not use a 9° staggered arrangement of screw placement, the maximum von Mises stress of the SWL was lower than the allowable stress. The maximum von Mises stress distributions of the three structural screws are shown in **Figures 5C,D,** and the von Mises stress of SWL screws was generally lower than that of the FCL screws under axial compressive load. When the axial compressive load was below 800 N or the torsion was below 3 Nm, the maximum von Mises stress of SWL screws was lower than the allowable stress. In addition, the average von Mises stresses of all elements of the screws and bone models were compared among the three groups individually for each loading mode (Figures 5E–H). At 1000 N axial compression, the average von Mises stress of all elements of the SWL construct was significantly smaller than that of the FCL constructs in both screw and bone models ($p < 0.0001$). At 10 Nm torsion, the average von Mises stress of the screw elements of the SWL construct was significantly smaller than that of the FCL construct ($p < 0.0001$). In this study, the stresses of plates in three constructs were in the safe range, far lower than the allowable stresses (Supplementary Tables S5, S6).

For the fatigue life analysis results shown in Figure 6, the area with a fatigue safety factor of one or more are the safe area of the construct, and the red part is the dangerous area, showing the area with a safety factor below one. The numerical simulation results indicated the level of fracture risk. The minimum fatigue safety factor for SWL constructs exceeded 1.7. Fatigue safety factors and fatigue life are summarized in Table 3. Compared with the FCL construct (0.2), the SWL construct increased the safety factor to 5. The fatigue life of the sandwich screws exceeded 1 million cycle loads, and the fatigue life of the bone in the SWL constructs was also greater than that in the FCL constructs.

The micro-nano tomography results were shown in Figures 6E–H, and the mechanical experimental results were in good agreement with the fatigue numerical prediction results. The results showed that all samples from the FCL group had the same damage pattern, that is, the greatest structural damage was produced in the area of the junction of the distal cortical bone screw and the artificial bone. Figures 6E,F shows the appearance of crack initiation in the area of the screw-bone interface at the far cortices. The red arrow indicated the location of structural damage under high-cycle fatigue, and the yellow line indicated the crack morphology of the structural damage. It can be seen that the FCL constructs had cracks or defects in the non-osteoporotic bone model, while no cracks or defects were detected in the locked plating constructs and SWL constructs (Figures 6G,H). Therefore, we have reason to believe that the safety of the SWL contructs meets our design requirements.

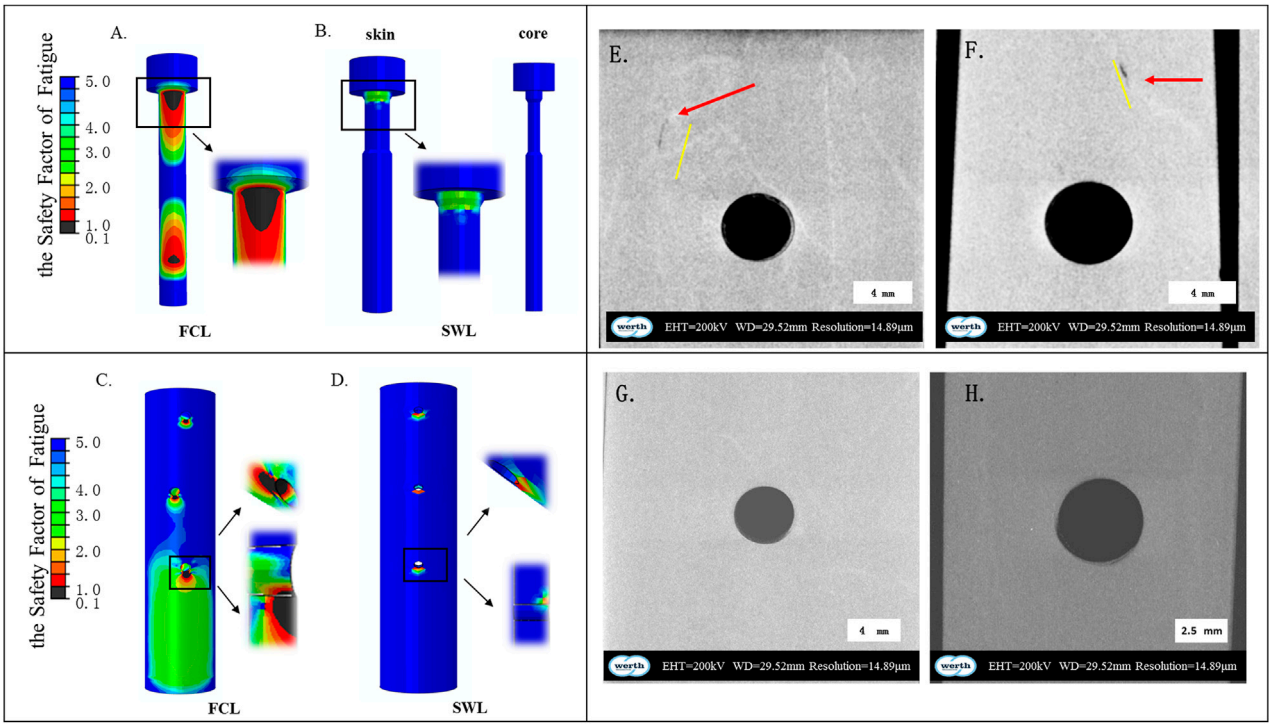

FIGURE 6
Numerical simulation and experimental results of high-cycle fatigue of three constructs. **(A–D)** High-cycle fatigue assessment and analysis based on FE-safe, the distribution cloud map of fatigue safety factors. **(E–H)** The appearance of crack initiation in the area of screw-bone interface at the far cortices: FCL construct samples **(E,F)**, LP construct samples **(G)**, SWL construct samples **(H)**.

TABLE 3 Three types of structural minimum safety factors and fatigue life prediction results.

	Far cortical locking		Locked plating		Sandwich locking		
	Bone	Screw	Bone	Screw	Bone	Screw (skin)	Screw (core)
The minimum safety Factor of fatigue (m)	0.650	0.2	2.594	5	4.731	1.7	5
Fatigue life × 1,000, 000 cycle	0.634	0.636	≫1	≫1	0.744	≫1	≫1

3.4 Design parameter sensitivity analysis

The influence of the three design parameters on the optimal objects during the optimization process was calculated. Through regularized responses on factors, it can be seen that the square term has a considerable effect on the result (over 45%). Figure 4C shows the sensitivity analysis results calculated by the RSM method, and the R-squared value was 0.9563. The red represents positive correlation and the blue negative correlations. It is evident that the width of the groove (d) had a positive effect on the von Mises stress of the outer titanium alloy, while d^2 had a negative effect on the core structure.

4 Discussion

This study provided a design method for the sandwich composite metal locking screw, and optimized a new construct with controllable two-phase stiffness, near parallel interfragmentary motion, and high fixation construct safety to promote secondary fracture healing. With the development of

sandwich structure 3D print technology (Sypeck and Wadley 2002; Sarvestani et al., 2018), we can reasonably assume that the sandwich composite metal screw is an ideal choice for dynamic fixation of fractures.

The sandwich screw is a cantilever beam with different working lengths under increasing load. The groove ensured the bone as a rigid body under a longer cantilever length, until the screw contacted with the near cortex. The larger is the width of the groove, the greater is the contact load. The above theory concurred with the sensitivity analysis shown in Figure 4C. The elasticity modulus of the core material and the depth of the groove influenced the two stiffnesses of the new constructs. Of course, the core material was mainly responsible for ensuring the safety of the construct. In considering biocompatibility and enhanced corrosion resistance, the Ti-6Al-4V was adopted as the protective skin of the sandwich screw.

In axial compression, the initial stiffness of the far cortical locking construct was 52% lower than that of the locked plating construct (Figure 4A). Secondary bone healing requires flexible fixation and relative stability to enable interfragmentary motion to stimulate callus formation (Perren 1979; Claes et al., 1998; Duda et al., 2002; Hente et al., 2004; Zhang et al., 2012; Benoit et al., 2016). The new constructs exhibited a biphasic stiffness profile with an initial stiffness and a secondary stiffness similar to the FCL construct (Bottlang et al., 2009; Deng et al., 2021). Studies demonstrated that asymmetric gap closure with locking plates caused asymmetric callus formation, with callus formation decreasing from the far cortex towards the near cortex (Bottlang et al., 2010a; Lujan et al., 2010). Clinically, the nearly parallel interfragmentary motion provided by FCL constructs should contribute to symmetric callus formation across the entire fracture site (Bottlang et al., 2014; Adams et al., 2015; Moazen et al., 2016; Kidiyoor et al., 2019). The new constructs with sandwich screws had similar parallel interfragmentary motion (Figure 4B), which may have similar symmetric callus formation. With similar biomechanical theory for FCL constructs, the new construct can theoretically promote secondary healing of fractures.

To ensure the safety of the new constructs, it is necessary to choose allowable stresses and restrict the applied load to a lower value than the construct can fully support (Casavola et al., 2011; Badalassi et al., 2014; Deng et al., 2021). Considering the inescapable microcracks of the implant and crack growth, allowable stress is a powerful instrument for assessing the implant in terms of strength theory and suitability of the metal material (Gross and Abel 2001; Sarma and Adeli 2005; Manral et al., 2020). Considering defects in the implant material and the influence of processing technology, greater design load and safe allowable stress should be adopted in the biomechanical assessment of screw failure risk (Agius et al., 2018; Anitua et al., 2018; Rahimizadeh et al., 2018; Choi et al., 2019). The fracture fixation constructs should provide sufficient biomechanical safety, particularly in terms of avoiding fatigue damage during 3–4 months of rehabilitation training. From the simulation results (Figures 6A–D), the safety of the new construct was guaranteed. From the experimental results, it can be seen that under the same conditions, the new construct had better fatigue resistance (Figures 6E–H). The high cycle fatigue numerical analysis results of this study indicated that both the bone models and the screws of FCL construct were at risk of fatigue failure under 1,000,000 cycles of cyclic loading, and fatigue life prediction analysis indicated that the fatigue failure of the bone models will occur first (Table 3). After micro-nano tomography and defect analysis of the bone models, fatigue damage was indeed found in the bone models of FCL constructs, which was consistent with the results of our fatigue numerical analysis. However, the results indicated that there was no fatigue damage of any FCL screws. It may be that the fatigue damage of the bone models released the stress on the screw, so that the screws did not suffer fatigue damage after the bone model is damaged as in numerical analysis shown. In addition, in current FCL constructs, the screws need to be arranged in a 9° staggered arrangement to ensure the torsional stiffness of the constructs, but this arrangement increases the difficulty of the surgery. Due to the design concept of the FCL constructs, to ensure that the stiffness of the first phase is small and the load when it is converted to the stiffness of the second phase is large, it is necessary to create a larger movable groove at the proximal cortical bone, which increases the complexity of the operation. The 9° staggered arrangement of the screws also means that greater trauma is added to the original fracture, further disrupting the continuity of the cortical bone. The surgical fixation plan must have universality for the various fractures of each patient with less damage to the bone.

The limitations of this study are as follows: In the model verification experiment, because at present the current technology cannot realize the grafting and 3D printing of 0.65-mm Ti-6Al-4V on titanium alloy (Ti-13V-11Cr-3Al), we only used the SWL screws made of core material titanium alloy (Ti-13V-11Cr-3Al). However, the SWL model in this study is in an ideal condition that Ti-6A1-4V can fully bond with Ti-13V-11Cr-3Al. This combined structure relies on the manufacturing level and needs more fabricating cost. The current metal 3D printing technology is still difficult to achieve fine grafting and printing on complex 3D structures. Thus, the use of this new structure depends on the development of the manufacturing process. In addition, this study was based on an ideal fracture model on cylindrical bone models and did not represent the various complex situations of actual clinical fractures (such as more complex fracture lines and force lines).

In conclusion, in this study, the finite numerical simulation calculation was used to intelligently optimize the locking screws of the FCL construct under multiple working conditions. The SWL construct theoretically maintains its biomechanical safety and fatigue resistance while maintaining excellent mechanical properties for fracture internal fixation. The newly designed composite metal sandwich locking screw can theoretically achieve elastic fixation, progressive stiffness, uniform load distribution, and parallel interfragmentary motion of the fracture end in the far cortical locking construct, while maintaining better fatigue resistance and torsion resistance to the internal fixation construct. Additional studies are required to assess SWL screws performance in combined loading modes and to determine if SWL constructs effectively promote secondary bone healing *in vivo*.

Data availability statement

The original contributions presented in the study are included in the article/Supplementary Material, further inquiries can be directed to the corresponding authors.

Author contributions

YD completed the experiment and wrote the manuscript. ZD wrote sections of the manuscript. YY performed the statistical analysis. HW and TW directed the design test and reviewed the manuscript. The rest of the authors put forward valuable opinions in the whole subject design. All authors contributed to the article and approved the submitted version.

Funding

This research is funded by National Natural Science Foundation of China (21773199 and 31972915). Sanming Project of Medicine in Shenzhen (SZSM201612019). Shenzhen Bay Laboratory Initial Funding (21300021). Southwest Medical University High-Level Talents (Zhong Shizhen Team) Special Support Program. Science and Technology Planning Project of Guangdong Province (2018B090944002, 2021A05243).

Conflict of interest

The authors declare that the research was conducted in the absence of any commercial or financial relationships that could be construed as a potential conflict of interest.

Publisher's note

All claims expressed in this article are solely those of the authors and do not necessarily represent those of their affiliated organizations, or those of the publisher, the editors and the reviewers. Any product that may be evaluated in this article, or claim that may be made by its manufacturer, is not guaranteed or endorsed by the publisher.

Supplementary material

The Supplementary Material for this article can be found online at: https://www.frontiersin.org/articles/10.3389/fbioe.2022.967430/full#supplementary-material

References

Adams, J. D., Jr, Tanner, S. L., and Jeray, K. J. (2015). Far cortical locking screws in distal femur fractures. *Orthopedics* 38 (3), e153–e156. doi:10.3928/01477447-20150305-50

Agius, D., Kourousis, K. I., and Wallbrink, C. (2018). A review of the as-built SLM Ti-6Al-4V mechanical properties towards achieving fatigue resistant designs. *Metals* 8 (1), 75. doi:10.3390/met8010075

Anitua, E., Flores, C., Piñas, L., and Alkhraisat, M. H. (2018). Frequency of technical complications in fixed implant prosthesis: The effect of prosthesis screw emergence correction by computer-aided design/computer-aided manufacturing. *J. Oral Implantol.* 44 (6), 427–431. doi:10.1563/aaid-joi-d-17-00229

Badalassi, M., Biolzi, L., Royer-Carfagni, G., and Salvatore, W. (2014). Safety factors for the structural design of glass. *Constr. Build. Mat.* 55, 114–127. doi:10.1016/j.conbuildmat.2014.01.005

Benoit, A., Mustafy, T., Londono, I., Aubin, C. E., and Villemure, I. (2016). *In vivo* dynamic compression has less detrimental effect than static compression on newly formed bone of a rat caudal vertebra. *J. Musculoskelet. Neuronal Interact.* 16 (3), 211–220.

Bottlang, M., Doornink, J., Fitzpatrick, D. C., and Madey, S. M. (2009). Far cortical locking can reduce stiffness of locked plating constructs while retaining construct strength. *J. Bone Jt. Surgery-American Volume* 91 (8), 1985–1994. doi:10.2106/jbjs.h.01038

Bottlang, M., Doornink, J., Lujan, T. J., Fitzpatrick, D. C., Marsh, J. L., Augat, P., et al. (2010a). Effects of construct stiffness on healing of fractures stabilized with locking plates. *J. Bone Jt. Surg.* 92 (2), 12–22. doi:10.2106/jbjs.j.00780

Bottlang, M., Fitzpatrick, D. C., Sheerin, D., Kubiak, E., Gellman, R., Zandschulp, C. V., et al. (2014). Dynamic fixation of distal femur fractures using far cortical locking screws: A prospective observational study. *J. Orthop. Trauma* 28 (4), 181–188. doi:10.1097/01.bot.0000438368.44077.04

Bottlang, M., Lesser, M., Koerber, J., Doornink, J., von Rechenberg, B., Augat, P., et al. (2010b). Far cortical locking can improve healing of fractures stabilized with locking plates. *J. Bone Jt. Surg.* 92 (7), 1652–1660. doi:10.2106/jbjs.i.01111

Casavola, C., Pappalettere, C., and Pluvinage, G. (2011). Fatigue resistance of titanium laser and hybrid welded joints. *Mat. Des.* 32 (5), 3127–3135. doi:10.1016/j.matdes.2010.12.002

Choi, N. H., Yoon, H. I., Kim, T. H., and Park, E. J. (2019). Improvement in fatigue behavior of dental implant fixtures by changing internal connection design: An *in vitro* pilot study. *Materials* 12 (19), 3264. doi:10.3390/ma12193264

Claes, L. E., Heigele, C. A., Neidlinger-Wilke, C., Kaspar, D., Seidl, W., Margevicius, K. J., et al. (1998). Effects of mechanical factors on the fracture healing process. *Clin. Orthop. Relat. Res.* 355, S132–S147. doi:10.1097/00003086-199810001-00015

Deng, Y., Ouyang, H., Xie, P., Wang, Y., Yang, Y., Tan, W., et al. (2021). Biomechanical assessment of screw safety between far cortical locking and locked plating constructs. *Comput. Methods Biomech. Biomed. Engin.* 24 (6), 663–672. doi:10.1080/10255842.2020.1844882

Duda, G. N., Sollmann, M., Sporrer, S., Hoffmann, J. E., Kassi, J. P., Khodadadyan, C., et al. (2002). Interfragmentary motion in tibial osteotomies stabilized with ring fixators. *Clin. Orthop. Relat. Res.* 396, 163–172. doi:10.1097/00003086-200203000-00025

Eser, A., Tonuk, E., Akca, K., and Cehreli, M. C. (2010). Predicting time-dependent remodeling of bone around immediately loaded dental implants with different designs. *Med. Eng. Phys.* 32 (1), 22–31. doi:10.1016/j.medengphy.2009.10.004

Foux, A., Yeadon, A. J., and Uhthoff, H. K. (1997). Improved fracture healing with less rigid plates: A biomechanical study in dogs. *Clin. Orthop. Relat. Res.* 339, 232–245. doi:10.1097/00003086-199706000-00032

Goodship, A. E., and Kenwright, J. (1985). The influence of induced micromovement upon the healing of experimental tibial fractures. *J. Bone Jt. Surg. Br. volume* 67 (4), 650–655. doi:10.1302/0301-620x.67b4.4030869

Gross, S. T., and Abel, E. W. (2001). A finite element analysis of hollow stemmed hip prostheses as a means of reducing stress shielding of the femur. *J. Biomech.* 34 (8), 995–1003. doi:10.1016/s0021-9290(01)00072-0

Habet, N., Elkins, J., Peindl, R., Killen, C., and Lack, W. D. (2019). Far cortical locking fixation of distal femur fractures is dominated by shear at clinically relevant bridge spans. *J. Orthop. Trauma* 33 (2), 92–96. doi:10.1097/bot.0000000000001341

Hayat, M. D., Singh, H., He, Z., and Cao, P. (2019). Titanium metal matrix composites: An overview. *Compos. Part A Appl. Sci. Manuf.* 121, 418–438. doi:10.1016/j.compositesa.2019.04.005

Hente, R., Füchtmeier, B., Schlegel, U., Ernstberger, A., and Perren, S. M. (2004). The influence of cyclic compression and distraction on the healing of experimental tibial fractures. *J. Orthop. Res.* 22 (4), 709–715. doi:10.1016/j.orthres.2003.11.007

Kenwright, J., Richardson, J. B., Cunningham, J. L., White, S. H., Goodship, A. E., Adams, M. A., et al. (1991). Axial movement and tibial fractures. A controlled randomised trial of treatment. *J. Bone Jt. Surg. Br. volume* 73 (4), 654–659. doi:10.1302/0301-620x.73b4.2071654

Kidiyoor, B., Kilaru, P., Rachakonda, K. R., Joseph, V. M., Subramaniam, G. V., Sankineani, S. R., et al. (2019). Clinical outcomes in periarticular knee fractures with flexible fixation using far cortical locking screws in locking plate: A prospective study. *Musculoskelet. Surg.* 103 (2), 149–153. doi:10.1007/s12306-018-0553-9

Li, C., Xiao, Q., Tang, Y., and Li, L. (2016). A method integrating Taguchi, RSM and MOPSO to CNC machining parameters optimization for energy saving. *J. Clean. Prod.* 135, 263–275. doi:10.1016/j.jclepro.2016.06.097

Li, K., Yan, S., Zhong, Y., Pan, W., and Zhao, G. (2019). Multi-objective optimization of the fiber-reinforced composite injection molding process using Taguchi method, RSM, and NSGA-II. *Simul. Model. Pract. Theory* 91, 69–82. doi:10.1016/j.simpat.2018.09.003

López, C., Bacarreza, O., Baldomir, A., Hernandez, S., and H. Ferri Aliabadi, M. (2017). Reliability-based design optimization of composite stiffened panels in post-buckling regime. *Struct. Multidiscipl. Optim.* 55 (3), 1121–1141. doi:10.1007/s00158-016-1568-1

Lujan, T. J., Henderson, C. E., Madey, S. M., Fitzpatrick, D. C., Marsh, J. L., and Bottlang, M. (2010). Locked plating of distal femur fractures leads to inconsistent and asymmetric callus formation. *J. Orthop. Trauma* 24 (3), 156–162. doi:10.1097/bot.0b013e3181be6720

MacLeod, A. R., Pankaj, P., and Simpson, A. H. R. (2012). Does screw–bone interface modelling matter in finite element analyses? *J. biomechanics* 45 (9), 1712–1716. doi:10.1016/j.jbiomech.2012.04.008

Manral, A. R. S., Gariya, N., Bansal, G., Singh, H. P., and Rawat, A. (2020). Computational stress analysis of Chicken Feather Fibre (CFF) with Epoxy-Resin matrix composite material. *Mater. Today Proc.* 26, 2805–2810. doi:10.1016/j.matpr.2020.02.582

Moazen, M., Leonidou, A., Pagkalos, J., Marghoub, A., Fagan, M. J., and Tsiridis, E. (2016). Application of far cortical locking technology in periprosthetic femoral fracture fixation: A biomechanical study. *J. Arthroplasty* 31 (8), 1849–1856. doi:10.1016/j.arth.2016.02.013

Panagiotopoulos, E., Fortis, A. P., Lambiris, E., and Kostopoulos, V. (1999). Rigid or sliding plate. A mechanical evaluation of osteotomy fixation in sheep. *Clin. Orthop. Relat. Res.* 358, 244–249. doi:10.1097/00003086-199901000-00029

Patel, S. B., and Gohel, J. V. (2018). Optimization of sol–gel spin-coated Cu2ZnSnS4 (CZTS) thin-film control parameters by RSM method to enhance the solar cell performance. *J. Mat. Sci.* 53 (17), 12203–12213. doi:10.1007/s10853-018-2464-4

Perren, S. M., Allgöwer, M., Cordey, J., and Russenberger, M. (1973). Developments of compression plate techniques for internal fixation of fractures. *Prog. Surg.* 12, 152–179. doi:10.1159/000394905

Perren, S. M. (1979). Physical and biological aspects of fracture healing with special reference to internal fixation. *Clin. Orthop. Relat. Res.* 138, 175–196.

Plumarom, Y., Wilkinson, B. G., Marsh, J. L., Willey, M. C., An, Q., Gao, Y., et al. (2019). Radiographic healing of far cortical locking constructs in distal femur fractures: A comparative study with standard locking plates. *J. Orthop. Trauma* 33 (6), 277–283. doi:10.1097/bot.0000000000001464

Rahimizadeh, A., Nourmohammadi, Z., Arabnejad, S., Tanzer, M., and Pasini, D. (2018). Porous architected biomaterial for a tibial-knee implant with minimum bone resorption and bone-implant interface micromotion. *J. Mech. Behav. Biomed. Mat.* 78, 465–479. doi:10.1016/j.jmbbm.2017.11.041

Richter, H., Plecko, M., Andermatt, D., Frigg, R., Kronen, P. W., Klein, K., et al. (2015). Dynamization at the near cortex in locking plate osteosynthesis by means of dynamic locking screws: An experimental study of transverse tibial osteotomies in sheep. *J. Bone Jt. Surgery-American Volume* 97 (3), 208–215. doi:10.2106/jbjs.m.00529

Rodriguez, E. K., Zurakowski, D., Herder, L., Hall, A., Walley, K. C., Weaver, M. J., et al. (2016). Mechanical construct characteristics predisposing to non-union after locked lateral plating of distal femur fractures. *J. Orthop. Trauma* 30 (8), 403–408. doi:10.1097/bot.0000000000000593

Sarma, K. C., and Adeli, H. (2005). Comparative study of optimum designs of steel high rise building structures using allowable stress design and load and resistance factor design codes. *Pract. Period. Struct. Des. Constr.* 10 (1), 12–17. doi:10.1061/(asce)1084-0680(2005)10:1(12)

Sarvestani, H. Y., Akbarzadeh, A. H., Mirbolghasemi, A., and Hermenean, K. (2018). 3D printed meta-sandwich structures: Failure mechanism, energy absorption and multi-hit capability. *Mat. Des.* 160, 179–193. doi:10.1016/j.matdes.2018.08.061

Sarwar, A., Gee, A., Bougherara, H., Kuzyk, P. R., Schemitsch, E. H., and Zdero, R. (2021). Biomechanical optimization of the far cortical locking technique for early healing of distal femur fractures. *Med. Eng. Phys.* 89, 63–72. doi:10.1016/j.medengphy.2021.02.003

Shang, X., Chao, T., Ma, P., and Yang, M. (2019). An efficient local search-based genetic algorithm for constructing optimal Latin hypercube design. *Eng. Optim.* 52, 271–287. doi:10.1080/0305215x.2019.1584618

Sypeck, D. J., and Wadley, H. N. G. (2002). Cellular metal truss core sandwich structures. *Adv. Eng. Mat.* 4 (10), 759–764. doi:10.1002/1527-2648(20021014)4:10<759::aid-adem759>3.0.co;2-a

Uthoff, H. K., Poitras, P., and Backman, D. S. (2006). Internal plate fixation of fractures: Short history and recent developments. *J. Orthop. Sci.* 11 (2), 118–126. doi:10.1007/s00776-005-0984-7

Wang, R., Zhang, H., Cui, H., Fan, Z., Xu, K., Liu, P., et al. (2019). Clinical effects and risk factors of far cortical locking system in the treatment of lower limb fractures. *Injury* 50 (2), 432–437. doi:10.1016/j.injury.2018.09.013

Wilkinson, B. G., Marsh, J. L., Willey, M. C., An, Q., Gao, Y., Karam, M. D., et al. (2019). Radiographic healing of far cortical locking constructs in distal femur fractures: A comparative study with standard locking plates. *J. Orthop. Trauma* 33 (6), 277–283. doi:10.1097/bot.0000000000001464

Zhang, X., Vandamme, K., Torcasio, A., Ogawa, T., Van Lenthe, G. H., Naert, I., et al. (2012). *In vivo* assessment of the effect of controlled high- and low-frequency mechanical loading on peri-implant bone healing. *J. R. Soc. Interface* 9 (72), 1697–1704. doi:10.1098/rsif.2011.0820

Zhao, D., Niu, P., Sun, X., Yin, Z., Tan, W., and Huo, Y. (2020). Mechanical difference of left ventricle between rabbits of myocardial infarction and hypertrophy. *J. Biomechanics* 111, 110021. doi:10.1016/j.jbiomech.2020.110021

Zhou, J., Wang, B., Lin, J., and Fu, L. (2013). Optimization of an aluminum alloy anti-collision side beam hot stamping process using a multi-objective genetic algorithm. *Archives Civ. Mech. Eng.* 13 (3), 401–411. doi:10.1016/j.acme.2013.01.008

Frontiers in
Bioengineering and Biotechnology

Accelerates the development of therapies, devices, and technologies to improve our lives

A multidisciplinary journal that accelerates the development of biological therapies, devices, processes and technologies to improve our lives by bridging the gap between discoveries and their application.

Discover the latest Research Topics

See more →

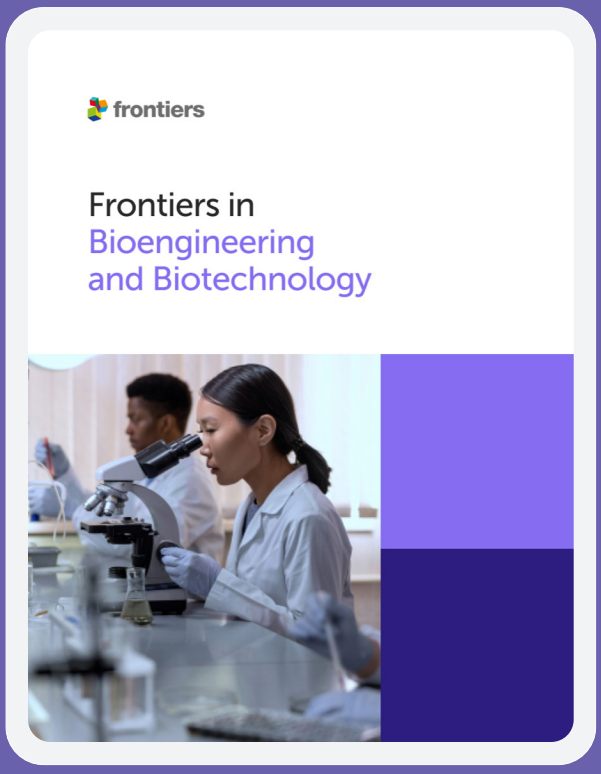

Frontiers

Avenue du Tribunal-Fédéral 34
1005 Lausanne, Switzerland
frontiersin.org

Contact us

+41 (0)21 510 17 00
frontiersin.org/about/contact